NEW THEORETICAL IDEAS IN COSMOLOGY DRIVEN BY HIGH PRECISION OBSERVATIONS.

by

Manoj Kumar Yennapureddy

A Dissertation Submitted to the Faculty of the

DEPARTMENT OF PHYSICS

In Partial Fulfillment of the Requirements
For the Degree of

DOCTOR OF PHILOSOPHY

In the Graduate College

THE UNIVERSITY OF ARIZONA

2019

THE UNIVERSITY OF ARIZONA
GRADUATE COLLEGE

As members of the Dissertation Committee, we certify that we have read the dissertation prepared by Manoj Kumar Yennapureddy
entitled New theoretical ideas in cosmology driven by high precision observations.
and recommend that it be accepted as fulfilling the dissertation requirement for the Degree of Doctor of Philosophy.

Fulvio Melia — Date: 30 April 2019

Elliott Cheu — Date: 30 April 2019

Arvider Sandhu — Date: 30 April 2019

Sean Fleming — Date: 30 April 2019

Final approval and acceptance of this dissertation is contingent upon the candidate's submission of the final copies of the dissertation to the Graduate College.
I hereby certify that I have read this dissertation prepared under my direction and recommend that it be accepted as fulfilling the dissertation requirement.

Dissertation Director: Fulvio Melia — Date: 30 April 2019

ACKNOWLEDGEMENTS

First and foremost, I would like to thank my advisor, Fulvio Melia, for his constant support, encouragement and patient mentorship over the past few years. The discussion and interactions I had with him greatly influenced my scientific thinking and shaped me as a scientist. I much enjoyed these discussions with him, which always provided insights in solving the research problems I had. I thank him for patiently listening through my research problems and offering suggestions which led to the solutions for the problems. I owe thanks to my committee members Elliot Cheu, Arvinder Sandhu and Sean Fleming for being on my committee. I thank Prof. Shufang Su, who has helped me in understanding QFT and Standard model physics, the independent study under her helped understand the standard model particle physics. I am grateful for all my teachers, particularly to Anupama and Sreedhar, who instigated scientific interests in me. I still do remember lighting the bulb by generating electricity through potatoes, this was the first moment of love towards science. I want to thank Prof. D. V. Rao, who encouraged and supported me in pursuit of my Scientific dreams. I also thanks to Pedro, Maxwell, Tom and Gardie for their warm welcome into the department.

I would like to thank my friends Kiran, Rafi, Kartheek and Anudeep with whom I had enormous fun during my undergraduate years at the Rajiv Gandhi University of Knowledge Technologies. I owe many thanks to my dearest friends Varun who has been a constant supporter throughout of my life. I also owe thanks to my friends Dinesh, Sai, Mahesh, Anil and Pramod who have supported and helped me along the way. It is always good to have an excellent scientific discussion with friends and colleagues, on this occasion, I owe thanks to Shiva Teja, with whom I had exciting scientific discussions and debates.

Above all, I would like to thank my parents Samba Reddy (Dad) and Sujatha (Amma), aunt Samba Laxmi (athamma) who have been incredibly supportive through my graduate studies. They have strived a lot in providing quality education throughout my childhood. And I finally thank my sister Soumya for being supportive throughout my graduate studies.

I would like to thank Govt. of Telangana and Tarknath Das foundation for funding my graduate studies.

DEDICATION

This Thesis and work is dedicated to my Mom (Amma) for her enormous love.

Table of Contents

LIST OF FIGURES

Appendix-A

Appendix-B

LIST OF TABLES

Chapter - 3

Chapter - 7

Appendix - A

Appendix - B

Abstract

The standard ΛCDM cosmological was successful in accounting for the predictions of light elements in the Universe and anisotropies in the Cosmic Microwave Background (CMB). However, the recent high precision data has indicated the presence of fundamental problems in the ΛCDM such as missing large angle correlation in CMB and the early appearance of supermassive black holes and galaxies. In this thesis, using the Hubble diagram of HII galaxies, angular diameter distance inferred from strong gravitational lenses, H(z) inferred from cosmic chronometer and angular diameter distance inferred from quasar cores, we show that R_h=ct an alternative FRW cosmology with zero active mass condition is favored better over ΛCDM. Also, using the linear perturbation theory based on interacting dark matter - dark energy model we show that the predicted halo mass function in R_h=ct universe is consistent with the observations throughout redshifts $10 > z > 4$. Whereas the standard ΛCDM cosmological model is inconsistent with observations, in particular, it underpredicts the number of halos by more than four orders of magnitude. Additionally, the structure formation in ΛCDM is strongly dependent on the inflationary mechanism to account for the generation of scale-invariant primordial fluctuations. The inflationary mechanism drives all the modes to exist and re-enter the horizon. In particular, the small-scale modes enter the horizon during the radiation dominated epoch whereas large-scale modes enter the horizon during matter dominated epoch, thus providing a mechanism for different growth rates at different epochs. Whereas the R_h=ct universe does not have such a complicated mechanism as the model does not have a horizon problem and does not incorporate inflation into its expansion history, so modes never exit the horizon. Moreover, the growth of structures in R_h=ct does not require different handling of small- and large-scale modes. The R_h=ct model with its simple structure formation mechanism fits the observations quite well, whereas ΛCDM with its complicated mechanism underpredicts the number of halos by at least four orders of magnitude. All the tests thus far completed have shown support favoring R_h=ct better than over ΛCDM indicating R_h=ct universe is far more viable than ΛCDM cosmological model.

CHAPTER 1

Introduction

1.1 Introduction to standard cosmological model

The standard ΛCDM cosmological model is based on General relativity and Friedmann-Robertson-Walker metric. General relativity is the framework which describes gravity as manifestation due to the geometry of the spacetime. The geometry of the spacetime is encoded in the form of a metric which should be provided as an input to Einstein equations to describe the dynamics of the universe. The most general metric can be written as

$$ds^2 = g_{\mu\nu}dx^\mu dx^\nu = g_{00}dt^2 + 2g_{0i}dtdx^i + g_{ij}dx^i dx^j \tag{1.1}$$

To determine the form of g_{ij} and g_{00} we need to invoke the symmetries of the Universe, which can only be obtained through observations. The large-scale galaxy surveys have indicated that the universe is isotropic when averaged over large-scales. We extend this further and assume the existence of the cosmological principle which states that the universe is isotropic to any free-falling observer. Moreover, if the universe is isotropic to all observers, then it must also be homogeneous which implies the universe will appear the same everywhere when observed over large-scales. If the universe is spatially homogeneous and isotropic, then the universe can be described by time-ordered sequences of three-dimensional spatial slices, each of these slices has to be homogeneous and isotropic. Moreover, if the universe is isotropic then the g_{0i} term in the metric has to be zero; otherwise, there will be spatial velocities preferring a particular direction which contradicts our assumption. Then the reduced metric can be written as

$$ds^2 = g_{00}dt^2 - a^2(t)\gamma_{ij}dx^i dx^j \tag{1.2}$$

where a(t) is the scale factor and $x^i = (x^1, x^2, x^3)$ are comoving coordinates and $x^i_{phy} = a(t)x^i$ represents the physical coordinate. Then the physical velocity can be obtained as follows

$$v^i_{phy} \equiv \frac{dx^i_{phy}}{dt} = a(t)\frac{dx^i}{dt} + \frac{\dot{a}}{a}x^i = v^i_{pec} + Hx^i_{phy} \tag{1.3}$$

where v^i_{pec} is the peculiar velocity measured by a comoving observer who follows the Hubble flow, where Hx^i_{phy} is the Hubble flow. The metric, when written in polar coordinates, can be expressed as follows

$$ds^2 = g_{00}dt^2 - a^2(t)\left[\frac{dr^2}{1-kr^2} + r^2 d\Omega^2\right] \tag{1.4}$$

where k represents the curvature of the universe, k= 0, 1, -1 describes flat, closed and open universes respectively. In the context of ΛCDM, the g_{00} term in the above equation has been forced to one, but this can happen only under a specific condition which we will mention in the next section, for now, assume $g_{00} = 1$. Then we get

$$ds^2 = dt^2 - a^2(t)\left[\frac{dr^2}{1-kr^2} + r^2 d\Omega^2\right] \tag{1.5}$$

The above metric is called the Friedmann-Robertson-Walker metric. As it is evident that the above metric is nonstatic due to its time dependence arising in the form of a(t). Moreover, a(t) multiplies the comoving coordinates, any proper (physical) distances will change in proportions to 'a(t)' i.e

$$x(t) = a(t)r \tag{1.6}$$

The FRW (Friedmann-Robertson-Walker) metric contains two unknowns which are k and a(t), the information regarding these two unknowns should be obtained using Einstein Equations

$$G^\alpha_\beta = R^\alpha_\beta - \frac{1}{2}\delta^\alpha_\beta R = 8\pi G T^\alpha_\beta \tag{1.7}$$

To determine both k and a(t) we need to specify the form of Energy-momentum tensor T^α_β. As we have assumed that the universe is both homogeneous and isotropic, then T^i_0 must be zero and the spatial components should be diagonal with $T^1_1 = T^2_2 = T^3_3$. Moreover, we assume the source is ideal fluid without any gradients of temperature, number density and bulk velocity. Then the energy-momentum tensor can be written as

$$T^\alpha_\beta = (\rho + \mathcal{P})u^\alpha u_\beta - \mathcal{P}\delta^\alpha_\beta \tag{1.8}$$

where ρ is the energy density of all the constituents in the universe and $\mathcal{P}$ is the pressure contribution from all the constituents of the universe. The nature of these constituents can be specified through the relationship between $\mathcal{P}$ and ρ in the form of an equation of state $\mathcal{P} = \mathcal{P}(\rho)$. Moreover, in the comoving frame the energy-momentum tensor can be written as $T^\alpha_\beta = diag[\rho(t), -\mathcal{P}(t), -\mathcal{P}(t), -\mathcal{P}(t)]$. Then computing the G^α_β is straight forward where G^i_0 term vanishes and G^i_j term is proportional to a unit matrix. The $G_{00} = 8\pi G T_{00}$ term is given by

$$\left(\frac{\dot{a}}{a}\right)^2 + \frac{k}{a^2} = \frac{8\pi G}{3}\rho \tag{1.9}$$

and the spatial term can be written as

$$\frac{2\ddot{a}}{a} + \left(\frac{\dot{a}}{a}\right)^2 + \frac{k}{a^2} = -8\pi G\mathcal{P} \tag{1.10}$$

The above two equations are called Friedmann's first and second equations respectively. These equations when combined with the equation of the state $\mathcal{P} = \mathcal{P}(\rho)$ will completely specify a(t) and ρ(t). Moreover the first and second Friedmann's equations can be combined together to give

$$\frac{\ddot{a}}{a} = -\frac{4\pi G}{3}(\rho + 3\mathcal{P}) \tag{1.11}$$

And finally using the conservation of energy momentum tensor i.e. $\nabla_\mu T^{\mu\nu} = 0$ we get

$$\dot{\rho} = -3\frac{\dot{a}}{a}(\rho + \mathcal{P}) \tag{1.12}$$

In the above equation it has to be noted that ρ represents the total energy density of the universe and similarly, $\mathcal{P}$ represents the total pressure due to all the constituents of species present in the universe. Now consider the case with the standard ΛCDM cosmological model which has a radiation domination phase in the early universe followed by matter domination and quite lately dark energy domination. During the radiation dominated phase, matter was in negligible amount comparatively with radiation (photons), so ignoring the matter contribution to the total ρ and $\mathcal{P}$ and using $\mathcal{P}_r = \frac{1}{3}\rho_r$ in Eq(17) we get

$$\rho_r \propto a^{-4} \tag{1.13}$$

During the matter domination phase, radiation was quite negligible thus ignoring its contribution to total ρ and using $\mathcal{P}_m = 0$ in the Eq(17) will give

$$\rho_m \propto a^{-3} \tag{1.14}$$

And finally during the dark energy domination, both the radiation and matter content are quite negligible ignoring their contribution to the total ρ and $\mathcal{P}$ in Eq(17) and using $\mathcal{P}_\Lambda = -\rho_\Lambda$ we get

$$\rho_\Lambda \propto constant \tag{1.15}$$

Now considering Eq(14) today and defining $H_0 = \left(\frac{\dot{a}}{a}\right)_0$ as Hubble constant and normalizing the scale factor to one today, we get

$$k^2 = \frac{8\pi G}{3}\rho_0 - H_0^2 \tag{1.16}$$

Hence the spatial curvature k of the universe can be determined by measuring the H_0 and the total energy density ρ_0 of the universe observed today. The ρ_0 and H_0 determined using the Planck measurements [1] of CMB have indicated that our universe is spatially flat and $\rho_0 = \frac{3c^2}{8\pi G H_0^2}$ which is termed as the critical density ρ_c. Hence using k=0 and Eq(14-20) in Eq(14) will give

$$H^2 = H_0^2\Big(\Omega_r a^{-4} + \Omega_m a^{-3} + \Omega_\Lambda\Big) \tag{1.17}$$

where we have defined $\Omega_i = \frac{\rho_i}{\rho_c}$. Hence the standard ΛCDM model has at least five parameters which are determined through observation. These free parameters include H_0 which measures the expansion rate today, Ω_m which measures the matter content of the universe, Ω_Λ which measures the dark energy content of the universe, w_{de} the equation of state of dark energy and the parameter which partitions matter into baryonic and dark matter. Any sceptic can argue that the success of ΛCDM in accounting the observation over the past decade is due to its flexibility to optimize these free parameters. Surprising, when these parameters are optimized by fitting observations particularly the CMB [2-4] over a Hubble time, the results indicate that the universe has expanded by an amount equal to the amount under constant expansion, despite the fact that the presence of radiation dominated, matter dominated and dark energy dominated phases in ΛCDM had produced periods of deceleration and acceleration. When stated simply the average acceleration of the universe over a Hubble time is zero within measurement errors. The average acceleration of the universe being zero implies $\langle \rho/\mathcal{P} \rangle = -1/3$. What is even more surprising is that in the context of ΛCDM, the condition $\langle \rho/\mathcal{P} \rangle = -1/3$ can be achieved only once throughout its entire history and this is happening right now when we are observing. In addition to this with the advent of high precision data, the problems with ΛCDM cosmological models are coming into light.

1.2 **Problems with Standard cosmological model**

The standard ΛCDM cosmological model was primarily accounted for its success in accounting for the observed temperature $T_0 = 2.7K$ [5] of the Cosmic Microwave Background and its anisotropies [5], the abundance of light elements such as Hydrogen and Helium [6-7], and finally the matter power spectrum [8]. The past two decades are exciting periods in cosmology as an enormous amount of data has been gathered from both space and ground-based observations. These observations have improved our understanding of the Universe. In particular, the test of the standard model based on Type Ia supernovae [9,10] has indicated the presence of dark energy with negative pressure. In addition to the galaxy rotation curves, galaxy surveys have pointed a need for the presence of the weakly interacting non-baryonic matter termed as the

cold dark matter [11]. With the CMB and Type Ia supernovae, the ΛCDM cosmological has been established to contain approximately 70% of dark energy, 27% of dark matter and 3% of baryonic matter.

1.2.1 Cosmic Lithium Problem

The light elements such as **H**, ^{4}**He**, Deuterium, ^{3}**He**, ^{9}**Be** and ^{7}**Li** are produced in standard ΛCDM within first 3 minutes of the Big Bang. The BBN has played a major role in the success of ΛCDM. The exact amount of these light elements produced through BBN depends on the relative amounts of matter and radiation in the early universe.

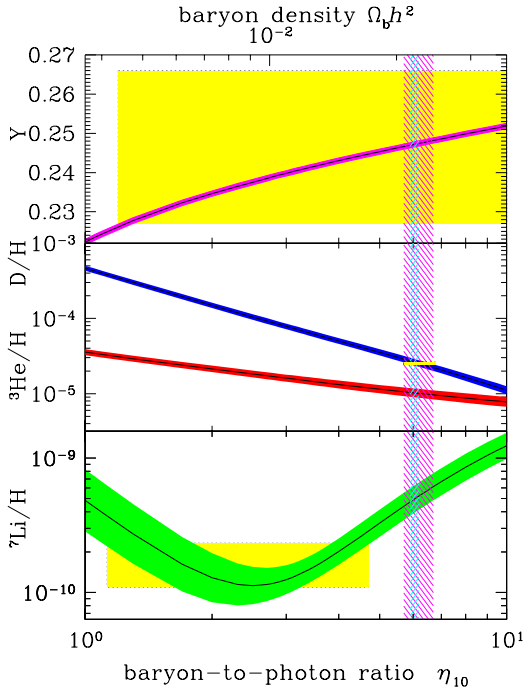

Figure 1.1: The abundances of ^{4}**He**, D, ^{3}**He**, and ^{7}**Li** as predicted by the standard model of Big-Bang nucleosynthesis — the bands show the 95% CL range. Boxes indicate the observed light element abundances. (Adopted from ref. [12])

This relative amount, the photon-to-baryon ratio which has been measured from cosmic microwave background [5] was used to predict the abundances of light elements. The predictions of deuterium [13] and ^{4}**He** [6-7] are in very good agreement with observations, but the first year WMAP results have indicated a factor of 2-3 between prediction and observations of ^{7}**Li** abundances [3] as shown in Fig 1.1. The atmospheres of many stars have indicated a much lower abundance of lithium than predicted by ΛCDM, a discrepancy termed as "cosmic lithium problem" [14]. Moreover, this discrepancy has worsened over time; this discrepancy stands at the factor of 3 - 4 corresponding to 5σ discrepancy.

1.2.2 **Missing large angular correlation problem in cmb**

The standard ΛCDM cosmological model has successfully accounted for the Cosmic Microwave Background temperature and its anisotropies. However, the all sky-map measurements reported by Cosmic Background Explorer (COBE) [5], Wilkinson Microwave Anisotropy Probe (WMAP) [3] and Planck [1] have indicated apparent alignment of the largest modes of CMB anisotropy and low angular correlations on the largest scales (see Fig 1.2). These anomalies are in conflict with the predictions of ΛCDM cosmological model. Although this anomaly could be possibly explained due to cosmic variance within standard ΛCDM model. However, if these anomalies are real, then they hint for a necessity to modify the standard model or perhaps even new physics. The primary reasons for this are that these CMB fluctuations are thought of as precursors of the fluctuations which grew due to gravitational instabilities leading to the formation of large-scale structures in the Universe. In particular, the absence of large-angle correlations in CMB indicates the existence of a maximum fluctuation size at the time of recombination. Then the existence of a maximum fluctuation size will be in conflict with the prediction of inflation, a mechanism through which primordial fluctuations of all sizes ($0 < \lambda < \text{inf}$) are produced. If this anomaly is not due to the cosmic variance, then the absence of large-angle correlation will rule out inflation with at least 8σ confidence [15], but without inflation, ΛCDM model will not be able to account for the uniformity of the CMB temperature across the sky. Hence the absence of large-angle correlations if not due to the cosmic variance [16] will imply a necessity to modify the standard ΛCDM model.

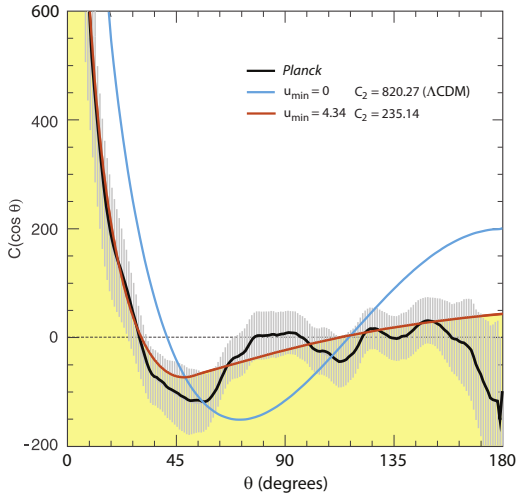

Figure 1.2: Angular correlation function measured with Planck(dark solidcurve), and associated 1errors (grey), compared with(blue) the prediction of the conventional inflationary ΛCDM, in which u_{min}=0 and C_2 is optimized using the power spectrum, and (red) truncated inflation, or a non-inflationary cosmology, with anoptimized lower limit u_{min}=4.34 and C_2=235.14 (Adopted from ref. [17])

1.2.3 Discrepancy between inferred H_0 from CMB and local H_0

In addition to the large-angle correlation problem in CMB, the recent high precision measurements of local H_0 from Type Ia supernovae and sound horizon observed from the cosmic microwave background radiation have indicated 4.4σ discrepancy [18,19]. In particular, the parameters of the ΛCDM model are optimised for the CMB measurements and local Type Ia measurements independently of each other. It was intially believed that this tension could be due to systematics in the observations. However, recent high measurements of H_0 within 1.9% accuracy has indicated that this problem is real. This discrepancy can only be mitigated by the early appearance of dark energy or probably new physics beyond the standard model.

1.2.4 Problems with structure fromation timeline in ΛCDM

The third pillar on which ΛCDM was based on its successful ability to account for the shape of the observed matter power spectrum today [8]. However, the high precision data which came into light in the past decade have indicated a conflict in the timeline of structure formation in ΛCDM. In particular, the discovery of SDSS010013.02+280225.8 ultra luminous quasar at redshift z = 6.3 [20], has worsened the problem of supermassive black hole growth rate and evolution in the early universe in the context of ΛCDM cosmological model [21]. Besides, each of the 50 previously discovered quasars at redshifts z ¿ 6 contains a black hole with approximately 10^9 $M_\odot$ (see ref. [19] and citation therein). In the context of CDM, the formation of Pop III stars might have occurred by redshift z = 20 - 30 [22,23] corresponding to a time of 200 Myrs, then the subsequent transition to Pop II stars will take at least 100 Myrs because the gas expelled by the first generation stars have to cool and recollapse [24,25]. This Pop II stars would have acted as seeds for black holes. If the early black holes grew according to Eddington's rate, then it would take at least 930 Myrs. However, the observed quasar at redshift z = 6.3 corresponds to 880 Myrs in ΛCDM which is in tension with the observations. There are two possibilities to reconcile this problem, 1) the black holes might have grown with two-three times that of Eddingtons limit, but this kind of growth rate was not observed in the local Universe or 2) Pop III stars should have formed earlier thus reconciling the problem.

Besides, the structure formation timeline in ΛCDM predicts that at redshifts z = 4 - 8 most massive galaxies should be transitioning from initial halo assembly to baryonic evolutions. However, the recent CANDELS and SPINTZER surveys have found that these massive halos have formed earlier than predicted by CDM implying The Impossibly Early Galaxy Problem [27] (see Fig 1.3). Although attempts made to reconcile this problem have indicated that 0.8 dex change in $\frac{M_{Halo}}{L_{UV}}$ is required. However, such a drastic change could come about only with a complete absence of dark matter at redshift 8, or if essentially100% of the baryons condensed

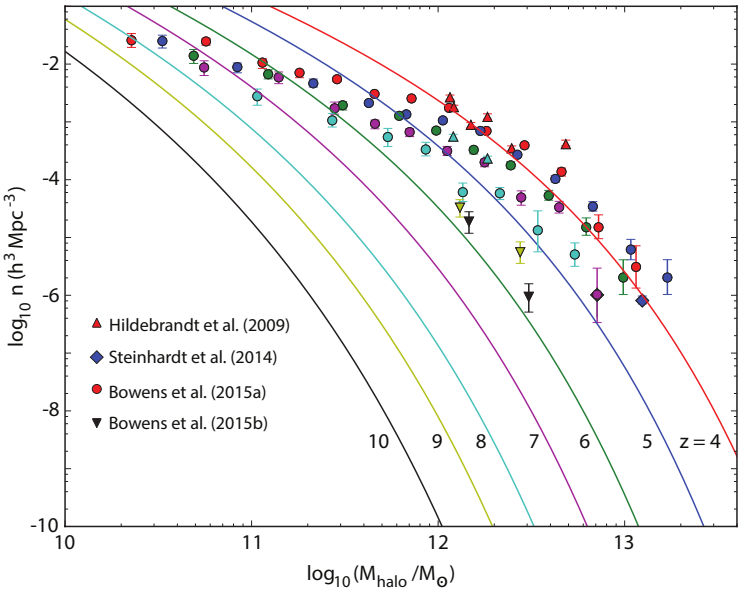

Figure 1.3: Halo mass function inferred from galaxy surveys, as a function of mass andredshift: z= 4 (red), 5 (blue), 6 (green), 7 (magenta), 8 (cyan), 9 (yellow),and 10(black). Solid curves represent the theoretical halo number density predicted by ΛCDM in this same redshift range (Adapted from ref. [26,27])

into stars at higher redshifts. Both of these scenarios constitute implausible physics, such as the need to convert all of the baryons into stars instantly upon halo virilization [27]. Other attempted remedies have equally unlikely requirements. So perhaps a better way to characterize the problem with the halo mass function is to say that it can only be made consistent with expectations of standard the model with the adoption of unlikely, new physics.

1.3 Introduction to the $R_h = ct$ Universe

As mentioned earlier, when the parameters of the ΛCDM are optimized for CMB, the results indicate that $\langle \rho/\mathcal{P} \rangle = -1/3$ implying average acceleration as zero, and this could only happen in its entire history. Perhaps this result indicates a reevaluation in the establishment of ΛCDM and as it turns out this result should hold throughout the history of the Universe when one forces $g_{tt} = 1$ [28]. Besides, the frame in which FRW metric is applicable must be in free fall as $g_{00} = 1$, but when compared this metric with the Schwarzschild metric it will be clearly evident that an observer in this comoving frame should not see any gravitational effects. Thus, one can immediately ask a question, is the FRW metric justified for any a(t) or are there any constraints on a(t)? It turns out there exists certain conditions under which the metric is applicable. This condition can be obtained easily by starting with a more generally applicable spherically metric which can be written as

$$ds^2 = e^{2\Phi/c^2}c^2dt^2 - e^{\lambda}dr^2 - R^2d\Omega^2 \tag{1.18}$$

where $d\Omega^2 = d\theta^2 + sin^2\theta d\phi^2$ and Φ, λ and R are functions of r,t whose functional form has to be determined by solving Einstein equations given by eq(12). The energy conservation $\nabla_\beta T^{\alpha\beta} = 0$ yields Euler equation

$$\frac{\partial\Phi}{\partial r} = -\frac{\mathcal{P}'c^2}{\rho + \mathcal{P}} \tag{1.19}$$

and the conservation of energy equation

$$\dot{\rho} = -3\left(\frac{\dot{R}}{R}\right)(\rho + \mathcal{P}) \tag{1.20}$$

And finally the dynamical equation

$$e^{-\Phi/c^2}\frac{\partial}{\partial t}\left(e^{-\Phi/c^2}\dot{R}\right) = -c^2\left[\frac{1 + U^2 - 2Gm/(c^2R)}{\rho + \mathcal{P}}\right]\left(\frac{\partial\mathcal{P}}{\partial R}\right)_t - \frac{Gmc^2 + 4\pi GR^3\mathcal{P}}{c^2R^2} \tag{1.21}$$

The above equations are entirely general, and they are applicable for any spherically symmetric distribution of mass-energy described as a perfect fluid. Now enforcing symmetries of the universe, i.e. homogeneity and isotropy, it is quite evident that the following condition has to enforced for the sake of homogeneity

$$\frac{\partial\Phi(r,t)}{\partial r} = 0 \tag{1.22}$$

The above equation satisfies only if $\mathcal{P}' = 0$ (see Eq(29)), confirming that the pressure is homogeneous, then recasting the reduced dynamical equation into the form of first Friedmann equation we get

$$\left(\frac{\dot{a}}{a}\right)^2 = \frac{8\pi G}{3c^2}\rho e^{2\Phi/c^2} - \frac{kc^2}{a^2}e^{2\Phi/c^2} \tag{1.23}$$

Then the acceleration equation can be written as

$$\left(\frac{\ddot{a}}{a}\right) - \left(\frac{\dot{a}}{a}\right)\frac{\dot{\Phi}}{c^2} = -\frac{4\pi G}{3c^2}e^{2\phi/c^2}(\rho + \mathcal{P}) \tag{1.24}$$

The above equation can also be written as

$$\frac{\partial}{\partial t}\left[\ln\left(\dot{a}^2e^{-2\Phi/c^2}\right)\right] = -\frac{kc^2}{a\dot{a}}\left(1 + \frac{3\mathcal{P}}{\rho}\right)e^{2\Phi/c^2} - \frac{\dot{a}}{a}\left(1 + \frac{3\mathcal{P}}{\rho}\right) \tag{1.25}$$

The solution to this equation can be written as

$$e^{2\Phi(t)/c^2} = h\dot{a}^2e^{\mathcal{I}(t)} \tag{1.26}$$

where

$$\mathcal{I}(t) = \int_0^t dt' \frac{8\pi G}{3c^2 H} e^{\Phi/c^2}(\rho + 3\mathcal{P}) \tag{1.27}$$

where $H \equiv e^{-\Phi/c^2}(\dot{a}/a)$ is the Hubble constant. In order to force Φ as constant, we must have $\mathcal{I} \to 0$, which results in zero active mass condition given as $\rho + 3\mathcal{P} = 0$. More importantly, Φ must only be a function of 't' in order to respect the homogeneous condition which we assumed earlier. As Φ is only a function of 't' one may choose a gauge such that $g_{tt} = 1$, but in doing so one is forcing into a free-falling frame corresponding to an acceleration free environment. If we use the zero active mass condition in Eq(16) we end up with

$$\ddot{a} = 0 \tag{1.28}$$

whose solution will be given as

$$a(t) = \frac{t}{t_0} \tag{1.29}$$

where t_0 is the integration constant and represents the age of the universe.

This thesis is organized as follows in Chapter-2 we describe the model independent test between ΛCDM and $R_h = ct$ universe using HII galaxy Hubble diagram, then in Chapter-3 we describe the model independent test between ΛCDM and $R_h = ct$ universe using strong gravitational lenses, and in Chapter-4 we adress "The Impossibly Early Galaxy Problem" in the context of the $R_h = ct$ universe, in Chapter-5 develop the structure formation theory in $R_h = ct$ universe by introducting interacting dark energy-dark matter model consistent with $R_h = ct$ universe and finally in Chapter-6 we address the "Impossibly Early Galaxy problem" using the growth solutions obtained from Chapter-5 to describe the structure formation in $R_h = ct$ universe. And finally in Appendix-A and B we describe the model independent tests between ΛCDM and $R_h = ct$ using cosmic chronometers and angular diameter distances obtained from quasars.

References:

[1] Planck Collaboration, Ade, P.A.R., Aghanim, N. et al., “Planck 2015 results. XIII. Cosmological parameters”, A&A, 594 , A13 (2016)

[2] Bennet, C. L et al., “First Year Wilkinson Microwave Anisotropy Probe (WMAP) Observations: Foreground emission,” Astrophys. J. Suppl, 148 , 97 (2003)

[3] Spergel, D. N. et al., “First Year Wilkinson Microwave Anisotropy Probe (WMAP) Observations:Determination of cosmological parameters,” Astrophys. J. Suppl, 148 , 175 (2003)

[4] Ade, P. A. R. et al. (Planck Collaboration), “Planck 2013 results (XXIII): Isotropy and statistics of the CMB,” Astron. Astrophys. 571 , A23 (2014)

[5] Wright, E. L., Bennett, C. L., Gorski, K., Hinshaw, G. & Smoot, G. F., “Angular Power Spectrum of the Cosmic Microwave Background Anisotropy seen by the COBE DMR” , ApJL, 464 , L21 (1996)

[6] Mukhanov, V., “ Nucleosynthesis without a computer”, Int. J. Theor. Phys, 43 , 669, 2004

[7] Izotov, Y.I et al., “ Helium abundances in the most metal deficient blue compact galaxies”, Astrophys. J, 527 , 757, 1999

[8] Tegmark, M., Zaldariraga, M., “Separating the early universe from late universe: cosmological parameter estimation beyond black box”, Phys.Rv.D, 66 , 10, 2002

[9] S. Perlmutter et al., “Measurements of W and L from 42 high-redshift supernovae”, Astrophys. J, 517 , 565 (1999)

[10] A. G. Riess et al., “Observational evidence from supernovae for an accelerating universe and a cosmological constant”, Astron.J, 116 , 1009 (1998)

[11] De Swart, J. G., Bertone, G., Van Dongen, J., “How Dark matter came to matter”, Natu. Astro, 01 , 59 (2017)

[12] B. D. Fields, P. Molaro and S. Sarkar., “Big-Bang Nucleosynthesis”, 2014 (arXiv:1412.1408)

[13] Kirkman, D et al., “ The cosmological baryon density from the deuterium to hydrogen towards QSO absorption system: D/H towards Q1243+3047”, Astrophys. J. Supp, 149 , 1 (2003)

[14] Field, B. D., “The primordial Lithium Problem”, Ann. Rev. Nucle. Phys, 61 , 1 (2011)

[15] Melia, F., “Angular correlation of the cosmic microwave background in the R h = ct Universe”, A&A, 561 , 80 (2014)

[16] Bennet, C. L et al., “Nine-year Wilkinson Microwave Anisotropy Probe (WMAP) Observations: Final Maps and Results”, Astrophy. J. Supp, 208 , 20B (2013)

[17] F. Melia and M. Lopez-Corredoira, “Evidence of a truncated spectrum in the angular correlation function of the cosmic microwave background”, A&A, 610, A87 (2018)

[18] Reiss, A. G et al., “A 2.4% determination of the local value of the Hubble constant”, ApJ, 826 , 56R (2016)

[19] Reiss, A. G., Casertano, S., Yuan, W., Macri, L. M., Scolnic, D., “Large Magellanic Cloud Cepheid Standards Provide a 1% Foundation for the Determination of the Hubble Constant and Stronger Evidence for Physics Beyond LambdaCDM”, (arXiv:1903.07603) (2019)

[20] Wu X-B et al., “An ultraluminous quasar with a twelve-billion-solar-mass black hole at redshift 6.30”, Nature, 518 , 512 (2015)

[21] Melia, F., McClintock, T. M., “Supermassive Black Holes in the early universe”, Proceedings of the Royal Society A, 471 , 0449 (2015)
[22] Abel, T., Bryan, G. L., Norman, M. L., “The formation of the first star in the universe”,Science, 295 ,93–98 (2002)
[23] Bromm, V., Coppi P. S., Larson R. B., “The formation of the first stars. I. The primordial star-forming cloud”,Astrophys. J, 564 , 23–51 (2002)[22] Yoshida, N., Bromm, V., Hernquist, L.,“The era of massive population III stars: cosmological implications and self-termination”,Astrophys. J, 605 , 579–590 (2004)
[24] Johnson, J. L., Greif, T. H., Bromm, V., “Local radiative feedback in the formation of the first protogalaxies”,Astrophys. J, 665 , 85–95 (2007)
[25] Steinhardt, C. L., Capak, P., Masters, D., Speagle, J. S., “The Impossibly Early Galaxy Problem”, ApJ, 84 , 21S (2016)
[26] M. K. Yennapureddy and F. Melia, “A Cosmological Solution to the Impossibly Early Galaxy Problem”, PDU, 20, 65 (2018)
[27] Melia, F., “Physical Basis for the symmetries in the Friedmann-Robertson-Walker metric”, Front. Phys, 11 , 4 (2016)
[28] Misner, C. W., Sharp, D. H., “Relativistic equation for adiabatic, spherically symmetric gravitational collapse”, Phys. Rev, 136 , 571 (1964)
[29] Thompson, I. H., Whitrow, G. F., “Time-dependent internal solutions for spherically symmetrical bodies in general relativity (I): Adiabatic collapse”, MNRAS, 136 , 207 (1967)

CHAPTER-2

Reconstruction of the HII galaxy Hubble diagram using Gaussian processes

Manoj K. Yennapureddy, Fulvio Melia

Published In: Journal of Cosmology and Astroparticle Physics
DOI:10.1088/1475-7516/2017/11/029

In the previous chapter, we have described the homogeneous universe in standard ΛCDM and R_h=ct cosmological models. Also, mentioned the fact that the FRW metric is valid only when the zero-active mass condition is imposed as an additional constraint on the cosmological models. Hence it is evident that the standard ΛCDM model cosmological model is inconsistent with the zero active mass condition. Due to the presence of zero active mass condition, the R_h=ct universe expands linearly throughout its history whereas the standard ΛCDM model has an early decelerated expansion followed by accelerated expansion history. The fact that these two cosmological models have different expansion rate can be used as a probe to test these cosmological models using observations. In this chapter, using the fact that HII galaxies can be used as standard candles due to the strong correlation between the luminosity in the Balmer emission lines and their ionized gas velocity dispersion to test ΛCDM and R_h=ct cosmologies using Gaussian Processes in a model-independent approach.

Using the Gaussian process, we construct the Hubble diagram based solely on the HII galaxies data without any pre-assumption of any model or parametric form. The prime benefit of this approach is that, in the end, neither of the models being tested may be the correct cosmology, so the GP reconstructed function is an overall better representation of the data than what either model can provide. Then using the area statistics, we quantify the results of the comparisons between R_h=ct and ΛCDM cosmological models. Our analysis based on GP and area statistics has indicated that the predicted fit in R_h=ct fits the data with approximately 69% probability whereas the corresponding probability for ΛCDM is less than 1%. These results indicate that the prediction of R_h=ct lies within about 1σ of the reconstructed curve whereas ΛCDM is excluded at over 2.6σ confidence.

Journal of Cosmology and Astroparticle Physics
An IOP and SISSA journal

Reconstruction of the HII galaxy Hubble diagram using Gaussian processes

Manoj K. Yennapureddy[a] **and Fulvio Melia**[b,1]

[a]Department of Physics, The University of Arizona, Tucson, AZ 85721, U.S.A.
[b]Department of Physics, the Applied Math Program and Steward Observatory, The University of Arizona, Tucson, AZ 85721, U.S.A.

E-mail: manojy@email.arizona.edu, fmelia@email.arizona.edu

Received May 28, 2017
Revised September 20, 2017
Accepted November 9, 2017
Published November 20, 2017

Abstract. The Hubble diagram constructed using HII galaxies (HIIGx) and Giant extragalactic HII regions (GEHR) as standard candles already extends beyond the current reach of Type Ia SNe. A sample of 156 HIIGx and GEHR sources has been used previously to compare the predictions of ΛCDM and $R_h = ct$, the results of which suggested that the HIIGx and GEHR sources strongly favour the latter over the former. But this analysis was based on the application of parametric fits to the data and the use of information criteria, which disfavour the less parsimonious models. In this paper, we advance the use of HII sources as standard candles by utilizing Gaussian processes (GP) to reconstruct the distance modulus representing these data without the need to pre-assume any particular model, none of which may in the end actually be the correct cosmology. In addition, this approach tightly constrains the 1σ confidence region of the reconstructed function, thus providing a better tool with which to differentiate between competing cosmologies. With this approach, we show that the *Planck* concordance model is in tension with the HII data at more than 2.5σ, while $R_h = ct$ agrees with the GP reconstruction very well, particularly at redshifts $\gtrsim 10^{-3}$.

Keywords: galaxy evolution, active galactic nuclei, astrophysical fluid dynamics, stars

ArXiv ePrint: 1711.03454

[1]John Woodruff Simpson Fellow.

https://doi.org/10.1088/1475-7516/2017/11/029

JCAP11(2017)029

Contents

JCAP11(2017)029

1 Introduction

HII galaxies (HIIGx) and Giant extragalactic HII regions (GEHR) share certain characteristics, including similar optical spectra and massive star formation [1], and prominent Balmer emission lines in Hα and Hβ produced by surrounding hydrogen gas ionized by the massive star clusters [2–5]. It has been noted that the luminosity $L(\mathrm{H}\beta)$ in Hβ in these systems is strongly correlated with the ionized gas velocity dispersion σ [4], presumably because both the number of ionizing photons and the turbulent velocity of the gas increase with the mass in the starburst component [6, 7]. This strong correlation and a relatively small dispersion in the relationship between $L(\mathrm{H}\beta)$ and σ makes it possible to consider and use these galaxies (and HII regions) as standard candles [1, 6–17].

The first attempt to use HIIGx and GEHR as cosmological tracers was made by Melnick et al. [8], who used the $L(\mathrm{H}\beta)$ - σ correlation to estimate the Hubble constant H_0. Most recently, Terlevich et al. [17] optimized the cosmological parameters in the standard model using 156 sources, including 25 high-z HIIGx, 107 local HIIGx, and 24 GEHR, demonstrating that these parameter values are consistent with those obtained through the analysis of Type Ia SNe.

Broadening the reach of the $L(\mathrm{H}\beta)$ - σ correlation, Wei et al. [18] investigated whether the current sample of HIIGx could be used — not only to optimize the parameters of any given model, but also — to compare competing models, such as ΛCDM and the $R_\mathrm{h} = ct$ universe [19–25]. Using maximum likelihood estimation (MLE), these authors confirmed that the parameters in flat ΛCDM optimized with the HIIGx and GEHR correlation (e.g., yielding $\Omega_\mathrm{m} = 0.40^{+0.09}_{-0.09}$, where $\Omega_\mathrm{m} \equiv \rho_\mathrm{m}/\rho_c$ is the normalized matter energy density ρ_m in terms of the critical density today, $\rho_c \equiv 3c^2H_0^2/8\pi G$) are generally consistent with their *Planck* values [26], though they went further and argued that the Akaike (AIC), Kullback (KIC) and Bayes (BIC) Information Criteria tend to favour the $R_\mathrm{h} = ct$ model over ΛCDM, with likelihoods $\sim 94.8\%$ versus $\sim 5.2\%$ for AIC, $\sim 96.8\%$ versus $\sim 3.2\%$ for KIC, and $\sim 98.8\%$ versus $\sim 1.2\%$ for BIC. When additional parameters are optimized using this approach, the respective probabilities are skewed even more in favour of $R_\mathrm{h} = ct$.

This comparison of ΛCDM and $R_\mathrm{h} = ct$ using HIIGx and GEHR data has confirmed and strengthened similar results obtained previously with other types of observation. These have included: type Ia SNe [27, 28], based on the framework established by Perlmutter et al. [29], Riess et al. [30], and Schmidt et al. [31]; gamma-ray bursts [32], based on correlations and ideas first proposed by Dai et al. [33] and Ghirlanda et al. [34]; high-z quasars [35–39];

cosmic chronometers [37, 40], using an idea first explored by Jimenez & Loeb [41] and Simon et al. [42]; age measurements of passively evolving galaxies [43], founded on principles laid out by Alcaniz & Lima [44] and Lima & Alcaniz [45]; gravitational lenses [46–48], Type Ic superluminous SNe (e.g., refs. [49, 50]) and the aforementioned HIIGx and GEHR [18].

In this paper, we advance the use of HIIGx and GEHR as standard candles in yet another significant and broadly meaningful way. All of the previous applications of the $L(\mathrm{H}\beta)$ - σ correlation have been based on the use of parametric fits inferred from specifically chosen models. One of the principal limitations of this approach is that none of the selected models may actually be the correct cosmology. Here, we use another statistical method developed recently to reconstruct the function representing the data without the pre-assumption of any model, based instead on utilizing Gaussian processes (GP; see, e.g., ref. [51]). The GP method has the flexibility of reconstructing a function that best fits the data without the assumption of any parametric form at all, thereby making model comparisons more reliable and robust.

2 Observational data and model comparisons

The data sample used in this paper consists of 25 high-z HII galaxies, 107 local HII galaxies, and 24 giant extra galactic HII regions, comprising 156 sources in total (Terlevich et al. 2015). Of these 156 sources, the 107 local HII galaxies lie in the redshift range $0.01 \lesssim z \lesssim 0.2$ [16].

For these sources, the luminosity versus ionized gas velocity correlation [15–17] is given as

$$\log L(\mathrm{H}\beta) = \alpha \log \sigma(\mathrm{H}\beta) + \kappa \,, \tag{2.1}$$

where σ is the velocity dispersion of the Hβ line, and α and κ are constants representing the slope and intercept. In general, the values of these parameters have to be optimized simultaneously with the cosmological parameters to avoid circularity issues, but they appear to be very insensitive to the underlying cosmology. Wei et al. [18] carried out this optimization procedure by combining κ and the Hubble constant H_0 together as

$$\delta = -2.5\kappa - 5\log H_0 + 125.2 \,, \tag{2.2}$$

and found that regardless of which model one assumes, α and δ deviate by at most only a tiny fraction of their 1σ errors from one application to the next. For simplicity, we shall therefore use the averages of the optimized values reported by Wei et al. [18], which are $\alpha = 4.87^{+0.11}_{-0.08}$ and $\delta = 32.42^{+0.42}_{-0.33}$. To give a concrete sense of what this means in practice, one would get $\alpha = 4.86^{+0.08}_{-0.07}$ and $\delta = 32.38^{+0.29}_{-0.29}$ for $R_\mathrm{h} = ct$ and $\alpha = 4.89^{+0.09}_{-0.09}$ and $\delta = 32.49^{+0.35}_{-0.35}$ for ΛCDM, if one were to re-optimize them separately. In the spirit of what we are trying to do here, i.e., reconstructing the correlation function independently of any model, we shall therefore adopt the average values for all the cases we consider.

Using the $L(\mathrm{H}\beta)$ - σ correlation, one can obtain the distance modulus for an HII galaxy as

$$\mu_\mathrm{obs} = -\delta + 2.5\big[\alpha \log \sigma(\mathrm{H}\beta) - \log F(\mathrm{H}\beta)\big] \,. \tag{2.3}$$

By comparison, the theoretical distance modulus is given as

$$\mu_\mathrm{th} = 5\log\left[\frac{\tilde{D}_L(z)}{Mpc}\right] , \tag{2.4}$$

where $\tilde{D}_L(z)$ is expressed as $\tilde{D}_L(z) = H_0 D_L(z)$, in terms of the Hubble constant H_0 and the luminosity distance $D_L(z)$, which depends on the cosmological model. The expressions

JCAP11(2017)029

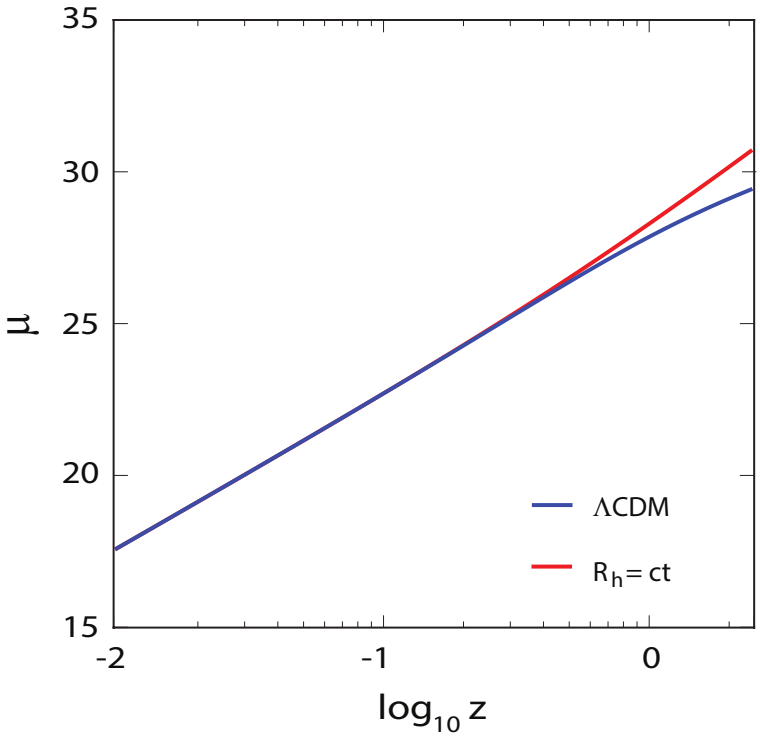

Figure 1. The theoretically predicted distance modulus as a function of redshift for $R_{\rm h} = ct$ (red) and the concordance ΛCDM model (blue). While the two models are indistinguishable for $z \lesssim 0.3$, they deviate significantly at higher redshifts.

for $D_L^{\Lambda{\rm CDM}}(z)$ and $D_L^{R_{\rm h}=ct}(z)$ are given in ref. [18]. These two luminosity distances are indistinguishable at low redshift, but deviate from each other progressively with increasing z, as one may see in figure 1, which shows the distance modulus given by equation (2.4), for each of the two models.

3 Gaussian processes and the HII galaxy Hubble diagram

Adapting the GP code developed by Seikel et al. [51], we reconstruct the function $\mu_{\rm obs}$ in equation (2.3) representing the 156 HII galaxy sources in Terlevich et al. [17], without pre-assuming any model or its parametric form of the distance modulus. The GP method uses some of the attributes of a Gaussian distribution, though the former utilizes a distribution over functions obtained using GP, while the latter represents a random variable. The reconstruction of a function $f(x)$ at x using GP creates a Gaussian random variable with mean $\mu(x)$ and variance $\sigma(x)$. The function reconstructed at x using GP, however, is not independent of that reconstructed at $\tilde{x} = (x + dx)$, these being related by a covariance function $k(x, \tilde{x})$. Although one can use many possible forms of k, we use one that depends on the distance between x and $\tilde{x}$, i.e., the squared exponential covariance function defined as

$$k(x, \tilde{x}) = \sigma_f^2 \exp\left(-\frac{(x-\tilde{x})^2}{2\Delta^2}\right) . \tag{3.1}$$

JCAP11(2017)029

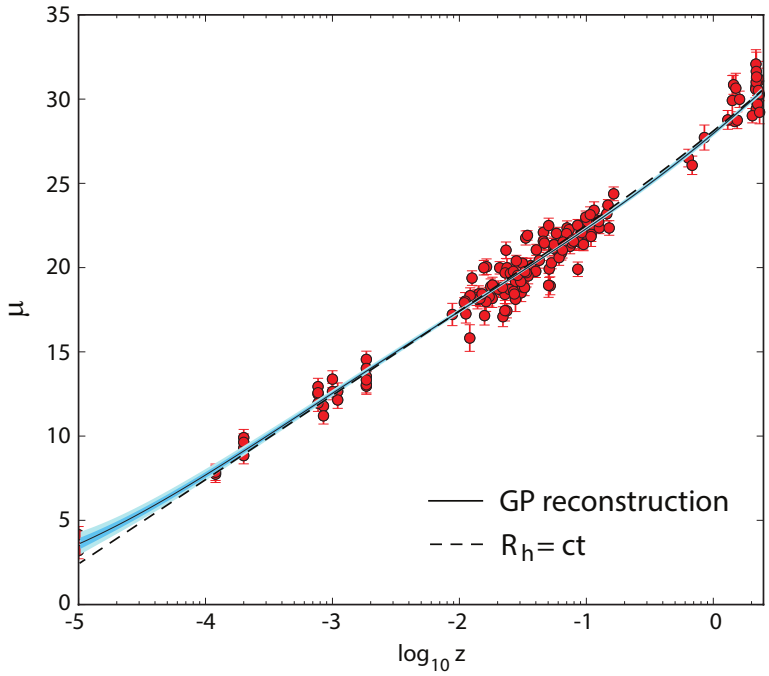

Figure 2. The thin solid curve (black) indicates the reconstructed distance modulus $\mu_{\rm obs}(z)$, using Gaussian processes, for all 156 of the currently available HII-region/Galaxy data, shown as red circles with 1σ error bars. The dark blue swath represents the 1σ confidence region, while light blue is 2σ. Also shown in this figure is the distance modulus predicted by the $R_{\rm h} = ct$ universe (dashed). The paucity of data at very low redshifts leads to a less precise determination of the measured $\mu_{\rm obs}(z)$, indicated by the widening 1σ and 2σ confidence regions, but the comparison between the two curves for $z > 10^{-4}$ is excellent.

Note that this function depends on two hyperparameters, σ_f and Δ, where σ_f indicates a change in the y-direction and Δ represents a distance over which a significant change in the x-direction occurs. Overall, these two hyperparameters characterize the smoothness of the function k, and are trained on the data using a maximum likelihood procedure, which leads to the reconstructed $\mu_{\rm obs}$ function in equation (2.3).

One of the principal features of the GP approach that we highlight in this application to the HII Galaxy Hubble diagram concerns the estimation of the 1σ confidence region attached to the reconstructed $\mu_{\rm obs}$ function. The 1σ confidence region depends on both the actual errors of individual data points, $\sigma_{\mu_{\rm obs}}$, on the optimized hyperparameter σ_f, and on the product $K_* K^{-1} K_*^T$ (see ref. [51]), where K_* is the covariance matrix at the point of estimation x_*, calculated using the given data at x_i, according to

$$K_* = [k(x_1, x_*), k(x_2, x_*), \ldots, k(x_i, x_*)] \, . \tag{3.2}$$

K is the covariance matrix for the original dataset. Note that the dispersion at point x_i will be less than $\sigma_{\mu_{\rm obs}}$ when $K_* K^{-1} K_*^T > \sigma_f$, i.e., when for that point of estimation there is a large correlation between the data. From the above equation it is clear that the correlation between any two points x and $\tilde{x}$ will be large only when $x - \tilde{x} < \sqrt{2}\Delta$. This condition, however, is satisfied most frequently for the HII Galaxy data used in our study, which results in a GP estimated 1σ confidence region that is smaller than the errors in the original data. Since the

JCAP11(2017)029

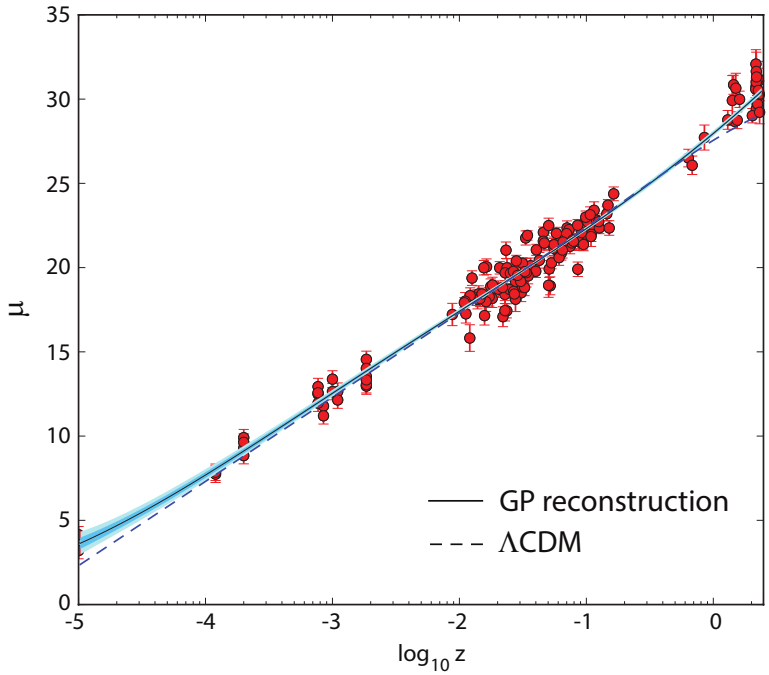

Figure 3. Same as figure 2, except now showing the GP reconstructed $\mu_{\rm obs}(z)$ curve in comparison with the prediction of ΛCDM. Unlike $R_{\rm h} = ct$, the standard model's prediction deviates significantly from the GP reconstructed $\mu_{\rm obs}(z)$ curve at $z \gtrsim 0.1$, as quantified by the cumulative probability distribution shown in figure 4 below, based on the area differential between the two curves.

$\sigma_{\mu_{\rm obs}}$ of the data are relatively small, the reconstructed 1σ regions are correspondingly small as well, as one may see in figures 2 and 3. This feature is critical to understanding why the GP approach for reconstructing the $L(\mathrm{H}\beta)$ - σ correlation yields a powerful diagnostic for comparing competing models. We refer the reader to ref. [51] for further details.

4 Discussion

The reconstructed $\mu_{\rm obs}$ function (solid), along with its 1σ (dark blue), and 2σ (light blue) confidence regions, is shown in figures 2 and 3, together with the 156 sources (with errors) used to derive it. In these figures, we also show the theoretically predicted distance modulus (dashed) for $R_{\rm h} = ct$ (figure 2) and ΛCDM (figure 3). It is quite evident that the distance modulus predicted by $R_{\rm h} = ct$ is an excellent match to the reconstructed $\mu_{\rm obs}(z)$ function, while the prediction of ΛCDM is an equally good fit at low redshifts, but a very poor fit for $z \gtrsim 0.3$.

As we are comparing two continuous functions, i.e., $\mu_{\rm obs}(z)$ with either $\mu_{R_h=ct}$ or $\mu_{\Lambda CDM}$, we estimate each model's probability of being correct using an area minimization statistic used more commonly in other fields, e.g., medical diagnostics [52]. In this approach, we create 500 mock samples of HII data according to

$$\mu_i(z) = \mu_{\rm obs}(z) + r\sigma_{\mu_{\rm obs}} \ , \tag{4.1}$$

where $\mu_{\rm obs}$ are the actual measurements shown in figures 2 and 3 and $\sigma_{\mu_{\rm obs}}$ are their associated errors, while r is assumed to be a Gaussian random variable with zero mean and a variance

JCAP11(2017)029

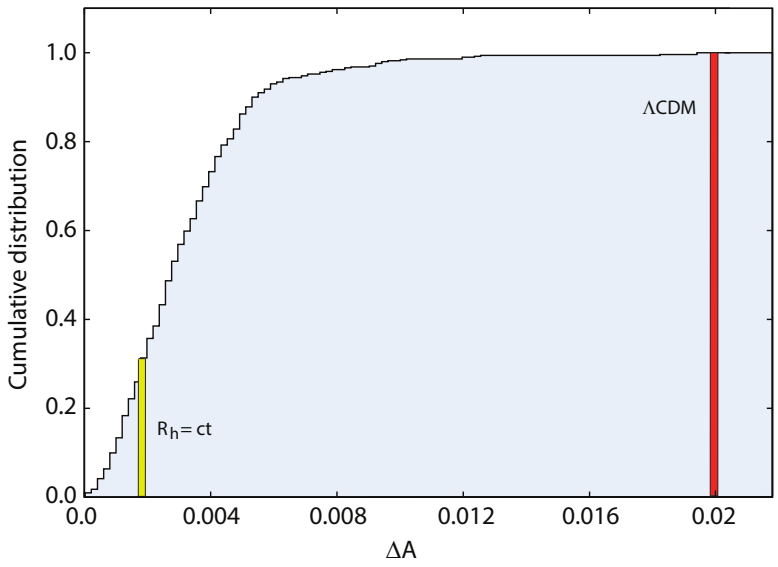

Figure 4. Cumulative probability distribution (normalized to 1) of the differential area calculated for $\mu(z)$, based on mock samples constructed via Gaussian randomization of the measured $\mu(z_i)$ values (see figures 2 and 3). The $R_{\rm h} = ct$ model is shown with a yellow bar, corresponding to an area differential of 0.0018, with a probability $\sim 69\%$. The ΛCDM model is shown with a red bar, corresponding to an area differential of 0.02, with a probability $\lesssim 1\%$.

of 1. Then we use $\mu_i(z)$ together with the $\sigma_{\mu_{\rm obs}}$ errors to reconstruct the function $\mu_{\rm mock}(z)$ corresponding to each mock sample, and finally we calculate the normalized absolute area difference between $\mu_{\rm mock}(z)$ and the GP reconstructed function of the actual data using

$$\Delta A = \frac{\int_{z_{\rm min}}^{z_{\rm max}} dz' \left| \mu_{\rm mock}(z') - \mu_{\rm obs}(z') \right|}{\int_{z_{\rm min}}^{z_{\rm max}} dz' \, \mu_{\rm obs}(z')} \, . \tag{4.2}$$

We repeat this procedure 500 times to build a distribution of frequency versus area differential ΔA, and from it construct the cumulative probability distribution shown in figure 4. Also shown in this figure is the normalized area differential (0.0018) for $R_{\rm h} = ct$, corresponding to a probability of $\sim 69\%$. A close inspection of figure 2 reveals that the main contribution to this area differential comes from the very low-z region, where a relative paucity of sources mitigates the accuracy with which the $\mu_{\rm obs}(z)$ function may be reconstructed. By comparison, the normalized area differential for ΛCDM is 0.02, corresponding to a probability $\lesssim 1\%$. For this model, most of the contribution to the area differential comes from the high-z measurements, which are of principal interest to our model comparison in this paper.

As discussed in section 3 above, one of the strengths of the GP method for reconstructing the function representing the data is the relatively small uncertainty in the result, as illustrated by the rather tight 1σ and 2σ bands shown in figures 2 and 3. This is what allows a comparison of this curve with the predictions of models being tested to select the preferred cosmology with a high degree of confidence. The cumulative probability plot in figure 4 shows that the predicted fit in $R_{\rm h} = ct$ is closer to the GP reconstruction than that of 69% of all the mock realizations, while the best-fit curve in ΛCDM does worse than $\sim 99\%$ of the

JCAP11(2017)029

possible variations. Another way to think of this is that, while the prediction of $R_{\rm h} = ct$ lies within about 1σ of the reconstructed curve, ΛCDM is excluded at over 2.6σ.

This outcome refutes some of the conclusions drawn, e.g., in ref. [53], where the analysis was also based on the use of Gaussian Processes to reconstruct an observed function. But there are actually two issues to discuss in any such comparison. These authors did indeed also use a GP approach for the analysis of redshift-dependent data, but their focus was on the Hubble constant $H(z)$. They reconstructed the expansion rate, as given by H, whereas we are using the HII galaxy Hubble diagram, which provides the distance modulus as a function of redshift. These are two very different kinds of observation. Ultimately they must be related, of course, but our reconstructed function is of a redshift-dependent distance, while theirs is of the redshift-dependent expansion rate.

The second issue has to do with which model is favoured by the data. Their analysis is now quite dated. Updates to that work have appeared in refs. [37, 40, 54]. A central question is which data ought to be used for the $H(z)$ analysis. As we now understand, mixing measurements of $H(z)$ based on BAO measurements with those extracted from cosmic chronometers, as was done in this earlier work, introduces significant biases and systematic uncertainties. The limitation of BAO measurements is that one must pre-assume a particular model in order to disentangle the effects of redshift-space distortions from the actual cosmological redshift variation across a galaxy cluster. Most of the BAO measurements rely on the use of ΛCDM to carry out this step, making the data, including $H(z)$, model-dependent. In order to carry out a truly model-independent comparison between different models based on $H(z)$, one must therefore restrict the analysis solely to the cosmic chronometer measurements. And when one does this, the outcome of the model selection changes from ΛCDM to $R_{\rm h} = ct$, as described more fully in these subsequent publications.

As we say, however, the present paper does not deal with $H(z)$ measurements, so this broader discussion concerning which model is favoured by the expansion-rate measurements does not apply here, though our results in this paper are fully consistent with these earlier model comparisons based on the Hubble constant $H(z)$. As far as we know, the present paper presents the first application of GP processes to the Hubble diagram constructed from HII galaxies.

5 Conclusion

Broadly speaking, the results of our analysis in this paper confirm and strengthen the earlier conclusion drawn from a comparison of $R_{\rm h} = ct$ and ΛCDM based on a maximization of the likelihood function using the predicted distance modulus in these models to fit the data [18]. That analysis took into account the different number of model parameters to arrive at a relative probability estimated using various information criteria.

The analysis of HIIGx and GEHR data with Gaussian processes, which we have used exclusively in this paper, constitutes a powerful complementary diagnostic for several reasons. First, there is no need to pre-assume a parametric form of the distance modulus, based on specific cosmological models, in order to analyze the data. The principal benefit of this approach is that, in the end, neither of the models being tested may be the correct cosmology, so the GP reconstructed function is an overall better representation of the data than what either model can provide. Second, the manner with which the GP approach identifies the functions that fairly represent the data produces a 1σ confidence region significantly tighter than the error one may infer on the basis of a simple χ^2 or MLE evaluation. This is the reason why the recon-

JCAP11(2017)029

structed function in figures 2 and 3, and its associated 1σ and 2σ confidence regions, can differentiate between models such as $R_{\rm h} = ct$ and ΛCDM so powerfully, as quantified in figure 4.

On the basis of our analysis, ΛCDM does not fare very well when compared to the reconstructed $\mu_{\rm obs}(z)$ function, irrespective of whether or not it is being compared to $R_{\rm h} = ct$. Even if we were to consider its predicted distance modulus directly in the context of the cumulative distribution (figure 4) constructed from the data, the resultant probability is smaller than $\sim 2.6\sigma$. By comparison, the prediction of $R_{\rm h} = ct$ is virtually indistinguishable from the reconstructed $\mu_{\rm obs}(z)$ function, deviating from it only slightly at very low redshifts, where a relative paucity of data weakens the precision with which the reconstruction may be made. Quite tellingly, the reconstructed function strongly prefers $R_{\rm h} = ct$ over ΛCDM at high redshifts, where the cosmological model comparison is most important.

Through the use of Gaussian processes in this paper, we have strengthened the case for using the $L(\mathrm{H}\beta)$ - σ correlation seen in HIIGx and GEHR data as a standard candle for testing cosmological models even beyond the current reach (i.e., $z \lesssim 1.8$) of Type Ia SNe. This argument will become even more compelling as the systematic uncertainties in the $L(\mathrm{H}\beta)$ - σ correlation are better understood. These uncertainties include the size of the burst, the age of the burst, the oxygen abundance of HIIGx, and the internal extinction correction [55].

A major issue that needs to be addressed in future work concerns a possible uncertainty in the initial mass function (IMF), or the possibility that it may vary with redshift. Since the $L(\mathrm{H}\beta)$ - σ relation correlates the ionizing flux produced by the massive stars to the velocity field in the potential well created primarily by the gas and lower mass stars, any systematic variation of the IMF affects the mass-to-light ratio and, therefore, the slope and zero point of the correlation function [16]. There is hope that at least some of these uncertainties may be reduced further with the help of upcoming observations using the K-band Multi Object Spectrograph at the Very Large Telescope. This survey should produce a larger sample of high-z HIIGx, providing much better and competitive constraints on the cosmological parameters and the comparison of competing models [17].

Acknowledgments

We are grateful to the anonymous referee for pointing out several improvements that have led to a better presentation of the results. FM is also grateful to the Instituto de Astrofísica de Canarias in Tenerife and to Purple Mountain Observatory in Nanjing, China for their hospitality while part of this research was carried out. FM is also grateful for partial support to the Chinese Academy of Sciences Visiting Professorships for Senior International Scientists under grant 2012T1J0011, and to the Chinese State Administration of Foreign Experts Affairs under grant GDJ20120491013.

References

[1] J. Melnick, M. Moles, R. Terlevich and J.-M. Garcia-Pelayo, *Giant HII regions as distance indicators. I — relations between global parameters for the local calibrators*, *Mon. Not. Roy. Astron. Soc.* **226** (1987) 849.

[2] L. Searle and W.L.W. Sargent, *Inferences from the composition of two dwarf blue galaxies*, *Astrophys. J.* **173** (1972) 25.

[3] J. Bergeron, *Characteristics of the blue stars in the dwarf galaxies I ZW* 18 *and II ZW* 40, *Astrophys. J.* **211** (1977) 62.

JCAP11(2017)029

[4] R. Terlevich and J. Melnick, *The dynamics and chemical composition of giant extragalactic HII regions*, *Mon. Not. Roy. Astron. Soc.* **195** (1981) 839.

[5] D. Kunth and G. Östlin, *The most metal-poor galaxies*, *Astron. Astrophys. Rev.* **10** (2000) 1 [astro-ph/9911094] [INSPIRE].

[6] J. Melnick, R. Terlevich and E. Terlevich, *HII galaxies as deep cosmological probes*, *Mon. Not. Roy. Astron. Soc.* **311** (2000) 629 [astro-ph/9908346] [INSPIRE].

[7] E.R. Siegel, R. Guzmán, J.P. Gallego, M. Orduña López and P. Rodríguez Hidalgo, *Towards a precision cosmology from starburst galaxies at $z > 2$*, *Mon. Not. Roy. Astron. Soc.* **356** (2005) 1117 [astro-ph/0410612] [INSPIRE].

[8] J. Melnick, R. Terlevich and M. Moles, *Giant HII regions as distance indicators. II — application to HII galaxies and the value of the Hubble constant*, *Mon. Not. Roy. Astron. Soc.* **235** (1988) 297.

[9] O. Fuentes-Masip, C. Muñoz-Tuñón, H.O. Castañeda and G. Tenorio-Tagle, *On the size and luminosity versus velocity dispersion correlations from the giant HII regions in the irregular galaxy NGC* 4449, *Astron. J.* **120** (2000) 752.

[10] G.L. Bosch, E. Terlevich and R. Terlevich, *Narrowband CCD photometry of giant HII regions*, *Mon. Not. Roy. Astron. Soc.* **329** (2002) 481 [astro-ph/0109421] [INSPIRE].

[11] E. Telles, *HII galaxies*, *ASP Conf. Proc.* **297** (2003) 143.

[12] V. Bordalo and E. Telles, *The L-σ relation of local HII galaxies*, *Astrophys. J.* **735** (2011) 52 [arXiv:1104.4719] [INSPIRE].

[13] M. Plionis et al., *A strategy to measure the dark energy equation of state using the HII galaxy Hubble relation and X-ray AGN clustering: preliminary results*, *Mon. Not. Roy. Astron. Soc.* **416** (2011) 2981 [arXiv:1106.4558] [INSPIRE].

[14] D. Mania and B. Ratra, *Constraints on dark energy from HII starburst galaxy apparent magnitude versus redshift data*, *Phys. Lett.* **B 715** (2012) 9 [arXiv:1110.5626] [INSPIRE].

[15] R. Chávez et al., *Determining the Hubble constant using giant extragalactic HII regions and HII galaxies*, *Mon. Not. Roy. Astron. Soc.* **425** (2012) L56 [arXiv:1203.6222] [INSPIRE].

[16] R. Chávez et al., *The L-σ relation for massive bursts of star formation*, *Mon. Not. Roy. Astron. Soc.* **442** (2014) 3565 [arXiv:1405.4010] [INSPIRE].

[17] R. Terlevich et al., *On the road to precision cosmology with high-redshift HII galaxies*, *Mon. Not. Roy. Astron. Soc.* **451** (2015) 3001 [arXiv:1505.04376] [INSPIRE].

[18] J.-J. Wei, X.-F. Wu and F. Melia, *The HII galaxy Hubble diagram strongly favors $R_{\rm h} = ct$ over ΛCDM*, *Mon. Not. Roy. Astron. Soc.* **463** (2016) 1144 [arXiv:1608.02070] [INSPIRE].

[19] F. Melia, *The edge of infinity: supermassive black holes in the universe*, Cambridge University Press, New York U.S.A., (2003), pg. 158.

[20] F. Melia, *The cosmic horizon*, *Mon. Not. Roy. Astron. Soc.* **382** (2007) 1917 [arXiv:0711.4181] [INSPIRE].

[21] F. Melia, *The $R_{\rm h} = ct$ universe without inflation*, *Astron. Astrophys.* **553** (2013) A76 [arXiv:1206.6527] [INSPIRE].

[22] F. Melia, *A physical basis for the symmetries in the Friedmann-Robertson-Walker metric*, *Front. Phys. (Beijing)* **11** (2016) 119801 [arXiv:1601.04991] [INSPIRE].

[23] F. Melia, *The linear growth of structure in the $R_{\rm h} = ct$ universe*, *Mon. Not. Roy. Astron. Soc.* **464** (2017) 1966 [arXiv:1609.08576] [INSPIRE].

[24] F. Melia and M. Abdelqader, *The cosmological spacetime*, *Int. J. Mod. Phys.* **D 18** (2009) 1889 [arXiv:0907.5394] [INSPIRE].

JCAP11(2017)029

[25] F. Melia and A. Shevchuk, *The $R_h = ct$ universe*, *Mon. Not. Roy. Astron. Soc.* **419** (2012) 2579 [arXiv:1109.5189] [INSPIRE].

[26] PLANCK collaboration, P.A.R. Ade et al., *Planck* 2013 *results. XXIII. Isotropy and statistics of the CMB*, *Astron. Astrophys.* **571** (2014) A23 [arXiv:1303.5083] [INSPIRE].

[27] F. Melia, *Fitting the Union*2.1 *SN sample with the $R_h = ct$ universe*, *Astron. J.* **144** (2012) 110 [arXiv:1206.6289] [INSPIRE].

[28] J.-J. Wei, X.-F. Wu, F. Melia and R.S. Maier, *A comparative analysis of the supernova legacy survey sample with ΛCDM and the $R_h = ct$ universe*, *Astron. J.* **149** (2015) 102 [arXiv:1501.02838] [INSPIRE].

[29] SUPERNOVA COSMOLOGY PROJECT collaboration, S. Perlmutter et al., *Discovery of a supernova explosion at half the age of the universe and its cosmological implications*, *Nature* **391** (1998) 51 [astro-ph/9712212] [INSPIRE].

[30] SUPERNOVA SEARCH TEAM collaboration, A.G. Riess et al., *Observational evidence from supernovae for an accelerating universe and a cosmological constant*, *Astron. J.* **116** (1998) 1009 [astro-ph/9805201] [INSPIRE].

[31] SUPERNOVA SEARCH TEAM collaboration, B.P. Schmidt et al., *The high Z supernova search: measuring cosmic deceleration and global curvature of the universe using type-IA supernovae*, *Astrophys. J.* **507** (1998) 46 [astro-ph/9805200] [INSPIRE].

[32] J.-J. Wei, X.-F. Wu and F. Melia, *The gamma-ray burst Hubble diagram and its implications for cosmology*, *Astrophys. J.* **772** (2013) 43 [arXiv:1301.0894] [INSPIRE].

[33] Z.G. Dai, E.W. Liang and D. Xu, *Constraining Ω_m and dark energy with gamma-ray bursts*, *Astrophys. J.* **612** (2004) L101 [astro-ph/0407497] [INSPIRE].

[34] G. Ghirlanda, G. Ghisellini, D. Lazzati and C. Firmani, *Gamma-ray bursts: new rulers to measure the universe*, *Astrophys. J.* **613** (2004) L13 [astro-ph/0408350] [INSPIRE].

[35] F. Melia, *High-z quasars in the $R_h = ct$ universe*, *Astrophys. J.* **764** (2013) 72 [arXiv:1301.0017] [INSPIRE].

[36] F. Melia, *The high-z quasar Hubble diagram*, *JCAP* **01** (2014) 027 [arXiv:1312.5798] [INSPIRE].

[37] F. Melia and T.M. McClintock, *A test of cosmological models using high-z measurements of $H(z)$*, *Astron. J.* **150** (2015) 119 [arXiv:1507.08279] [INSPIRE].

[38] G. Kauffmann and M. Haehnelt, *A unified model for the evolution of galaxies and quasars*, *Mon. Not. Roy. Astron. Soc.* **311** (2000) 576 [astro-ph/9906493] [INSPIRE].

[39] J.S.B. Wyithe and A. Loeb, *Self-regulated growth of supermassive black holes in galaxies as the origin of the optical and X-ray luminosity functions of quasars*, *Astrophys. J.* **595** (2003) 614 [astro-ph/0304156] [INSPIRE].

[40] F. Melia and R.S. Maier, *Cosmic chronometers in the $R_h = ct$ universe*, *Mon. Not. Roy. Astron. Soc.* **432** (2013) 2669 [arXiv:1304.1802] [INSPIRE].

[41] R. Jimenez and A. Loeb, *Constraining cosmological parameters based on relative galaxy ages*, *Astrophys. J.* **573** (2002) 37 [astro-ph/0106145] [INSPIRE].

[42] J. Simon, L. Verde and R. Jimenez, *Constraints on the redshift dependence of the dark energy potential*, *Phys. Rev.* **D 71** (2005) 123001 [astro-ph/0412269] [INSPIRE].

[43] J.-J. Wei, X.-F. Wu, F. Melia, F.-Y. Wang and H. Yu, *The age-redshift relationship of old passive galaxies*, *Astron. J.* **150** (2015) 35 [arXiv:1505.07671] [INSPIRE].

[44] J.S. Alcaniz and J.A.S. Lima, *New limits on Ω_Λ and Ω_m from old galaxies at high redshift*, *Astrophys. J.* **521** (1999) L87 [astro-ph/9902298] [INSPIRE].

JCAP11(2017)029

[45] J.A.S. Lima and J.S. Alcaniz, *Constraining the cosmic equation of state from old galaxies at high redshift*, *Mon. Not. Roy. Astron. Soc.* **317** (2000) 893 [astro-ph/0005441] [INSPIRE].

[46] J.-J. Wei, X.-F. Wu and F. Melia, *A comparison of cosmological models using time delay lenses*, *Astrophys. J.* **788** (2014) 190 [arXiv:1405.2388] [INSPIRE].

[47] F. Melia, J.-J. Wei and X.-F. Wu, *A comparison of cosmological models using strong gravitational lensing galaxies*, *Astron. J.* **149** (2015) 2 [arXiv:1410.0875] [INSPIRE].

[48] M.K. Yennapureddy and F. Melia, *Cosmological tests with strong gravitational lenses using Gaussian processes*, *Astron. J.* submitted, (2017).

[49] C. Inserra and S.J. Smartt, *Superluminous supernovae as standardizable candles and high redshift distance probes*, *Astrophys. J.* **796** (2014) 87 [arXiv:1409.4429] [INSPIRE].

[50] J.-J. Wei, X.-F. Wu and F. Melia, *Testing cosmological models with type Ic super luminous supernovae*, *Astron. J.* **149** (2015) 165 [arXiv:1503.06378] [INSPIRE].

[51] M. Seikel, C. Clarkson and M. Smith, *Reconstruction of dark energy and expansion dynamics using Gaussian processes*, *JCAP* **06** (2012) 036 [arXiv:1204.2832] [INSPIRE].

[52] E.R. DeLong, D.M. DeLong and D.L. Clarke-Pearson, *Comparing the areas under two or more correlated receiver operating characteristic curves: a nonparametric approach*, *Biometrics* **44** (1988) 837.

[53] M. Bilicki and M. Seikel, *We do not live in the $R_h = ct$ universe*, *Mon. Not. Roy. Astron. Soc.* **425** (2012) 1664 [arXiv:1206.5130] [INSPIRE].

[54] J.-J. Wei, F. Melia and X.-F. Wu, *Impact of a locally measured H_0 on the interpretation of cosmic-chronometer data*, *Astrophys. J.* **835** (2017) 270 [arXiv:1612.08491] [INSPIRE].

[55] R. Chávez et al., *Constraining the dark energy equation of state with HII galaxies*, *Mon. Not. Roy. Astron. Soc.* **462** (2016) 2431 [arXiv:1607.06458] [INSPIRE].

JCAP11(2017)029

CHAPTER-3

Cosmological tests with strong gravitational lenses using Gaussian Processes

Manoj K. Yennapureddy, Fulvio Melia

Published In: European Physical Journal C
DOI:10.1140/epjc/s10052-018-5746-8

In the previous chapter, using HII galaxies as standard candles, we have shown that ΛCDM is excluded with 2.6σ confidence whereas R_h=ct universe is within 1σ confidence of the reconstructed curve using Gaussian Process. In this chapter, we continue to test the predictions of R_h=ct universe and ΛCDM cosmological model using strong gravitational lenses. Strong gravitational lensing occurs when the source, lens and observer are sufficiently well aligned in such a way that the deflections of light due to intervening galaxies (lens) forms an Einstein's ring, using which one can infer the angular diameter distances to the lenses. These angular diameter distance have a strong dependence on the expansion rate of the universe thus can be used to distinguish R_h=ct and ΛCDM cosmological models.

In this chapter, using the Gaussian processes by employing angular diameter distances inferred from strong gravitational lenses we show the likelihood of R_h=ct universe fitting the data is far better than the ΛCDM cosmological model. Though these statistics are still quite limited, it is nonetheless informing us that the differentiation between models improves as the number of sources increases. Also, at least for R_h=ct, the probability of its predictions matching the GP reconstructed functions generally increases as the size of the lens sample grows.

Eur. Phys. J. C (2018) 78:258
https://doi.org/10.1140/epjc/s10052-018-5746-8

THE EUROPEAN PHYSICAL JOURNAL C

CrossMark

Regular Article - Theoretical Physics

Cosmological tests with strong gravitational lenses using Gaussian processes

Manoj K. Yennapureddy[1,a], **Fulvio Melia**[2,b]

[1] Department of Physics, The University of Arizona, Tucson, AZ 85721, USA
[2] Department of Physics, the Applied Math Program, and Department of Astronomy, The University of Arizona, Tucson, AZ 85721, USA

Received: 6 December 2017 / Accepted: 19 March 2018 / Published online: 24 March 2018

Abstract Strong gravitational lenses provide source/lens distance ratios $\mathcal{D}_{\rm obs}$ useful in cosmological tests. Previously, a catalog of 69 such systems was used in a one-on-one comparison between the standard model, ΛCDM, and the $R_{\rm h} = ct$ universe, which has thus far been favored by the application of model selection tools to many other kinds of data. But in that work, the use of model parametric fits to the observations could not easily distinguish between these two cosmologies, in part due to the limited measurement precision. Here, we instead use recently developed methods based on Gaussian Processes (GP), in which $\mathcal{D}_{\rm obs}$ may be reconstructed directly from the data without assuming any parametric form. This approach not only smooths out the reconstructed function representing the data, but also reduces the size of the 1σ confidence regions, thereby providing greater power to discern between different models. With the current sample size, we show that analyzing strong lenses with a GP approach can definitely improve the model comparisons, producing probability differences in the range $\sim$ 10–30%. These results are still marginal, however, given the relatively small sample. Nonetheless, we conclude that the probability of $R_{\rm h} = ct$ being the correct cosmology is somewhat higher than that of ΛCDM, with a degree of significance that grows with the number of sources in the subsamples we consider. Future surveys will significantly grow the catalog of strong lenses and will therefore benefit considerably from the GP method we describe here. In addition, we point out that if the $R_{\rm h} = ct$ universe is eventually shown to be the correct cosmology, the lack of free parameters in the study of strong lenses should provide a remarkably powerful tool for uncovering the mass structure in lensing galaxies.

1 Introduction

The degree to which light from high-redshift quasars is deflected by intervening galaxies can be calculated precisely if one has enough information concerning the distribution of mass within the gravitational lens [1,2]. Depending on the mass of the galaxy, and the alignment between source, lens, and observer, gravitational lenses may be classified either as macro (with sub-classes of strong and weak lensing) or micro lensing systems. Strong lensing occurs when the source, lens, and observer are sufficiently well aligned that the deflection of light forms an Einstein ring. Using the angle of deflection, one may derive the radius of this ring, from which one may then also compute the angular diameter distance to the lens. This distance, however, is model dependent. Hence, together with the measured redshift of the source, this angular diameter distance may be used to discriminate between various cosmological models (see, e.g., Ref. [3–7]).

In this paper, we use a recent compilation of 118 [8] plus 40 [9] strong lensing systems, with good spectroscopic measurements of the central velocity dispersion based on the Sloan Lens ACS (*SLACS*) Survey [4,10,11], and the Lenses Structure and Dynamics (*LSD*) Survey (see, e.g., refs. [12,13]), to conduct a comparative study between ΛCDM [14,15] and another Friedmann–Robertson–Walker (FRW) cosmology known as the $R_{\rm h} = ct$ universe [16,17]. Over the past decade, such comparative tests between this alternative model and ΛCDM have been carried out using a wide assortment of data, most of them favouring the former over the latter (for a summary of these tests, see Table 1 in ref. [18]). These studies have included high z-quasars [19], gamma-ray bursts [15], Type Ia SNe [21,22], and cosmic chronometers [23]. The $R_{\rm h} = ct$ model is characterized by a total equation of state $p = -\rho/3$, in terms of the total pressure p and density ρ in the cosmic fluid.

The results of these comparative tests are not yet universally accepted, however, and several counterclaims have

F. Melia: John Woodruff Simpson Fellow.

[a] e-mail: manojy@email.arizona.edu
[b] e-mail: fmelia@email.arizona.edu

been made in recent years. One may loosely group these into four general categories: (1) that the gravitational radius (and therefore also the Hubble radius) R_h is not really physically meaningful [24–26]; (2) that the zero active mass condition $\rho + 3p = 0$ at the basis of the $R_h = ct$ cosmology is inconsistent with the actual constitutents in the cosmic fluid [27]; (3) that the $H(z)$ data favour ΛCDM over $R_h = ct$ [25,28]; and (4) that Type Ia SNe also favour the concordance model over $R_h = ct$ [25,28,29]. These works, and papers published in response to them [17,23,30–33], have generated an important discussion concerning the viability of $R_h = ct$ that we aim to continue here. In Sect. 7 below, we will discuss at greater length the need to use truly model-independent data in these tests, basing their analysis on sound statistical practices. Such due diligence is of utmost importance in any serious attempt to compare different cosmologies in an unbiased fashion.

The test most directly relevant to the work reported here was carried out using strong lenses by Ref. [7], who based their comparison on parametric fits from the models themselves, and concluded that both cosmologies account for the data rather well. The precision of the measurements used in that application, however, was not good enough to favour either model over the other. In this paper, we revisit that sample of strong lensing systems and use an entirely different approach for the comparison, based on Gaussian Processes (GP) to reconstruct the function representing the data non-parametrically. In so doing, the angular diameter distance to the lensing galaxies is determined without pre-assuming any model, providing a better comparison of the competing cosmologies using a functional area minimization statistic described in Sect. 5. An obvious benefit of this approach is that a reconstructed function representing the data may be found regardless of whether or not any of the models being tested is actually the correct cosmology.

In Sect. 2 of this paper, we describe the lensing equation used in cosmological tests, and we then describe the data used with this application in Sect. 3. The Gaussian processes and the cosmological models being tested here are summarized in Sect. 4. The area minimization statistic is introduced in Sect. 5, and we explain how this is used to obtain the model probabilities. We end with our conclusions in Sect. 6.

2 Theory of lensing

In work with strong lensing, the observed images are typically fitted using a singular isothermal ellipsoid approximation (SIE) for the lens [34]. The projected mass distribution at redshift z_l is assumed to be elliptical, with semi-major axis θ_2 and semi-minor axis θ_1. Often, an even simpler approximation suffices, and we make use of it in this paper: we use a singular isothermal sphere (SIS) for the lens model, in which the semi-major and semi-minor axes are equal, i.e., $\theta_1 = \theta_2$. To provide context for this approach, we first describe SIE lens model and afterwards restrict it further by setting $\theta_1 = \theta_2$. The lens equation [35] that relates the position β in the source plane to the position θ in the image plane is given by

$$\beta = \theta - \nabla_\theta \Phi, \tag{1}$$

where Φ is the lensing potential of the SIE given as [36]

$$\Phi = \theta_E \sqrt{(1-\epsilon)\,\theta_1^2 + (1+\epsilon)\,\theta_2^2}, \tag{2}$$

and ϵ is the ellipticity related to the eccentricity according to

$$e = \sqrt{\frac{1-\epsilon}{1+\epsilon}}. \tag{3}$$

In Eq. (2), θ_E is the Einstein radius, defined as

$$\theta_E = 4\pi \left(\frac{\sigma_v}{c}\right)^2 \mathcal{D}, \tag{4}$$

where σ_v is the velocity dispersion within the lens and

$$\mathcal{D} \equiv \frac{D_A(z_l, z_s)}{D_A(0, z_s)}. \tag{5}$$

Notice that Eq. (4) is independent of the Hubble constant H_0. Nonetheless, one must still measure σ_v, the total velocity dispersion of stellar and dark matter. Obtaining this quantity is challenging because it is not the average line-of-sight velocity dispersion weighted with surface-brightness. The velocity dispersion of the SIS (σ_{SIS} or σ_v), may be related to the central velocity dispersion σ_0, which is obtained from the stellar velocity dispersion with one-eighth the effective optical radius (see, e.g., Refs. [4,5]). Though this works quite well for massive elliptical galaxies, which are indistinguishable kinematically from an SIE within one effective radius, σ_{SIS} and σ_0 are actually not equal. Dark matter is dynamically hotter than bright stars so the velocity dispersion of the former must be greater than that of the latter [37]. Treu et al. [4] studied the homogeneity of early-type galaxies using the large samples of lenses identified by the Sloan Lenses ACS Survey (SLACS; [10,38]) and found that $f_{SIS} \equiv \langle \sigma_{SIS}/\sigma_0 \rangle = 1.010 \pm 0.017$ when fitting the geometry of multiple images. Similar results were found in Ref. [39], who examined the ratio of stellar velocity dispersion to σ_{SIS} for different anisotropy parameters. The accumulation of evidence therefore suggests that $f_{SIS} = 1.01$, and this is the value we adopt for this study. Thus, following Ref. [40], we write the Einstein Radius as

$$\theta_E = 4\pi \left(\frac{\sigma_{SIS}}{c}\right)^2 \mathcal{D}, \tag{6}$$

where

$$\sigma_{SIS} = f_{SIS}\,\sigma_0. \tag{7}$$

The data based on Eq. (6) will be used to compare our two cosmological models in this paper. The errors associated with individual measurements of $\mathcal{D}$ are calculated from the error propagation equation,

$$\sigma_{\mathcal{D}} = \mathcal{D}_{\rm obs}\left[\left(\frac{\sigma_{\theta_{\rm E}}}{\theta_{\rm E}}\right)^2 + 4\left(\frac{\sigma_{\sigma_0}}{\sigma_0}\right)^2 + 4\left(\frac{\sigma_f}{f_{SIS}}\right)^2\right]^{1/2}, \tag{8}$$

containing $\theta_{\rm E}$, σ_0, $f_{SIS} = 1.01$ and $\sigma_f = 0.017$. We follow Grillo et al. [5] and set $\sigma_{\theta_{\rm E}} = 0.05\,\theta_{\rm E}$ and $\sigma_{\sigma_0} = 0.05\,\sigma_0$. The overall dispersion in $\mathcal{D}$ is expected to be $\sigma_{\mathcal{D}} \sim 0.11\mathcal{D}_{\rm obs}$.

3 Data

The compilation we use here contains 158 strong lensing systems. These have excellent spectroscopic measurements of the central velocity dispersion, obtained using the Sloan Lens ACS (SLACS) Survey [4,10,11] and the Lenses Structure and Dynamics (LSD) survey [12,13]. One can also find some of the original contributions to these datasets in Refs. [41–48]. The velocity dispersion (and its aforementioned error $\sim 5\%$) are obtained from Sloan Digital Sky Survey Database (SDSS).

Given that two distances are involved for each lens-source pairing, the GP method calls for a reconstruction of $\mathcal{D}(z_l, z_s)$ in two dimensions. This will only be feasible, however, when the sample is large enough to yield enough statistics to warrant this full approach. For now, even with 158 strong lensing systems, we are constrained to consider small redshift ranges, effectively reducing the problem to a one-dimensional reconstruction in each sub-division. Because the data are less dispersed in the lens plane, where $0.1 < z_l < 0.5$, and scattered much more in the source plane, $0.3 < z_s < 3.0$, we carry out the reconstruction within thin redshift-shells of sources, turning $D_{\rm obs}(z_l, z_s)$ into a one-dimensional function of z_l for what is essentially a fixed z_s. To minimize the scatter in source redshifts, we use a bin size less than 0.025 and choose those bins that have at least five data points within them, allowing us to reconstruct $D_{\rm obs}(z_l, z_s)$ using GP for each of the selected bins. In our sample of 158 strong-lensing systems, these criteria therefore allow us to assemble five different redshift bins, with anywhere from 5 to 9 lens-source pairs in each of them. These strong lenses are displayed in Tables 1, 2, 3, 4 and 5. Note that for the purpose of GP reconstruction in one dimension, we assume that all the sources in redshift bin $(z_s, z_s + \Delta z)$ have the same average redshift $z_s + \Delta z/2$.

4 Gaussian processes and model comparisons

Adapting the code developed by Seikel et al. [51] for Gaussian Processes in python, we reconstruct $\mathcal{D}_{\rm obs}(z_l, \langle z_s\rangle)$ for each of the sub-samples in Tables 1, 2, 3, 4 and 5, without assuming any model a priori. The GP method uses some of the attributes of a Gaussian distribution, though the former utilizes a distribution over functions obtained using GP, while the latter represents a random variable. The reconstruction of a function $f(x)$ at x using GP creates a Gaussian random variable with mean $\mu(x)$ and variance $\sigma(x)$. The function reconstructed at x using GP, however, is not independent of that reconstructed at $\tilde{x} = (x + dx)$, these being related by a covariance function $k(x, \tilde{x})$. Although one can use many possible forms of k, we use one that depends on the distance between x and $\tilde{x}$, i.e., the squared exponential covariance function defined as

$$k(x, \tilde{x}) = \sigma_f^2 \exp\left(-\frac{(x-\tilde{x})^2}{2\Delta^2}\right). \tag{9}$$

Note that this function depends on two hyperparameters, σ_f and Δ, where σ_f indicates a change in the y-direction and Δ represents a distance over which a significant change in the x-direction occurs. Overall, these two hyperparameters characterize the smoothness of the function k, and are trained on the data using a maximum likelihood procedure, which leads to the reconstructed $\mathcal{D}_{\rm obs}(z_l, \langle z_s\rangle)$ function for each source redshift shell centered on z_s. For this paper, we have found that these hyperparameter values are 0.144 and 0.661, respectively.

One of the principal features of the GP approach that we highlight in this application to strong lenses concerns the estimation of the 1σ confidence region attached to the reconstructed $\mathcal{D}_{\rm obs}(z_l, \langle z_s\rangle)$ curves. The 1σ confidence region depends on both the actual errors of individual data points, $\sigma_{\mathcal{D}i}$, on the optimized hyperparameter σ_f (see Eq. 9) and on the product $K_* K^{-1} K_*^T$ (see Ref. [51]), where K_* is the covariance matrix at the point of estimation x_*, calculated using the given data at x_i, according to

$$K_* = [k(x_1, x_*), k(x_2, x_*), \ldots, k(x_i, x_*)]. \tag{10}$$

K is the covariance matrix for the original dataset. Note that the dispersion at point x_i will be less than $\sigma_{\mathcal{D}i}$ when $K_* K^{-1} K_*^T > \sigma_f$, i.e., when for that point of estimation there is a large correlation between the data. From Eq. (9) it is clear that the correlation between any two points x and $\tilde{x}$ will be large only when $x - \tilde{x} < \sqrt{2}\Delta$. This condition, however, is satisfied most frequently for the strong lenses used in our study, which results in GP estimated 1σ confidence regions that are smaller than the errors in the original data. We refer the reader to Ref. [51] for further details.

Table 1 Strong gravitational lensing systems with $0.45 < z_s < 0.475$

Galaxy	z_l	$\theta_{\rm E}$ (arc s)	σ_0 (km s^{-1})	$\mathcal{D}_{\rm obs}\, f_{SIS} = 1.010$	$\sigma_{\mathcal{D}}$	$\mathcal{D}_{R_{\rm h}=ct}$	$\mathcal{D}_{\Lambda{\rm CDM}}$	Refs.[a]
SDSS J1134 + 6027	0.1528	1.10	239 ± 12	0.6689	0.735	0.634	0.652	10
SDSS J1403 + 0006	0.1888	0.83	213 ± 17	0.635	0.069	0.553	0.573	10
SDSS J2300 + 0022	0.2285	1.25	305 ± 19	0.446	0.0512	0.460	0.479	1–9
SDSS J0956 + 5100	0.2405	1.32	318 ± 17	0.4536	0.0498	0.441	0.459	1–9
SDSS J0935 − 0003	0.3475	0.87	396 ± 35	0.192	0.0211	0.222	0.234	10,11

[a]References: (1) [50]; (2) [46]; (3) [49]; (4) [47]; (5) [48]; (6) [4]; (7) [11]; (8) [5]; (9) [6]; (10) [12]; (11) [13]

Table 2 Strong gravitational lensing systems with $0.46 < z_s < 0.485$

Galaxy	z_l	$\theta_{\rm E}$ (arc s)	σ_0(km s^{-1})	$\mathcal{D}_{\rm obs}\, f_{SIS} = 1.010$	$\sigma_{\mathcal{D}}$	$\mathcal{D}_{R_{\rm h}=ct}$	$\mathcal{D}_{\Lambda{\rm CDM}}$	Refs.[a]
SDSS J1134 + 6027	0.1528	1.10	239 ± 12	0.6689	0.735	0.634	0.652	10
SDSS J1403 + 0006	0.1888	0.83	213 ± 17	0.635	0.069	0.553	0.573	10
SDSS J1402 + 6321	0.2046	1.39	290 ± 16	0.5743	0.063	0.526	0.546	1–9
SDSS J1205 + 4910	0.2150	1.22	281 ± 14	0.5368	0.059	0.504	0.524	10
SDSS J2300 + 0022	0.2285	1.25	305 ± 19	0.446	0.0512	0.460	0.479	1–9
SDSS J0956 + 5100	0.2405	1.32	318 ± 17	0.4536	0.0498	0.441	0.459	1–9
SDSS J0935 − 0003	0.3475	0.87	396 ± 35	0.192	0.0211	0.222	0.234	10,11

[a]Reference: (1) [50]; (2) [46]; (3) [49]; (4) [47]; (5) [48]; (6) [4]; (7) [11]; (8) [5]; (9) [6]; (10) [12]; (11) [13]

Table 3 Strong gravitational lensing systems with $0.5 < z_s < 0.525$

Galaxy	z_l	$\theta_{\rm E}$ (arc s)	σ_0 (km s^{-1})	$\mathcal{D}_{\rm obs}\, f_{SIS} = 1.010$	$\sigma_{\mathcal{D}}$	$\mathcal{D}_{R_{\rm h}=ct}$	$\mathcal{D}_{\Lambda{\rm CDM}}$	Refs.[a]
SDSS J1451 − 0239	0.1254	1.04	223 ± 14	0.726	0.079	0.718	0.735	10,11
SDSS J2303 + 1422	0.1553	1.64	271 ± 16	0.775	0.0852	0.654	0.673	1–9
SDSS J1627 − 0053	0.2076	1.21	295 ± 13	0.482	0.052	0.552	0.573	1–9
SDSS J1142 + 1001	0.2218	0.98	221 ± 22	0.697	0.0766	0.509	0.529	10,11
SDSS J0109 + 1500	0.2939	0.69	251 ± 19	0.3807	0.0418	0.389	0.407	10
SDSS J0216 − 0813	0.3317	1.15	349 ± 24	0.3287	0.0361	0.320	0.336	1–9

[a]References: (1) [50]; (2) [46]; (3) [49]; (4) [47]; (5) [48]; (6) [4]; (7) [11]; (8) [5]; (9) [6]; (10) [12]; (11) [13]

Table 4 Strong gravitational lensing systems with $0.51 < z_s < 0.535$

Galaxy	z_l	$\theta_{\rm E}$ (arc s)	σ_0 (km s^{-1})	$\mathcal{D}_{\rm obs}\, f_{SIS} = 1.010$	$\sigma_{\mathcal{D}}$	$\mathcal{D}_{R_{\rm h}=ct}$	$\mathcal{D}_{\Lambda{\rm CDM}}$	Refs.[a]
SDSS J2321 − 0939	0.0819	1.57	245 ± 70	0.9082	0.0999	0.816	0.829	1–9
SDSS J1451 − 0239	0.1254	1.04	223 ± 14	0.726	0.079	0.718	0.735	10,11
SDSS J0959 + 0410	0.1260	1.00	229 ± 13	0.6616	0.07277	0.723	0.740	1–9
SDSS J1538 − 5817	0.1428	1.00	189 ± 12	0.9717	0.106	0.687	0.705	10,11
SDSS J2303 + 1422	0.1553	1.64	271 ± 16	0.775	0.0852	0.654	0.673	1–9
SDSS J1627 − 0053	0.2076	1.21	295 ± 13	0.482	0.052	0.552	0.573	1–9
SDSS J0959 + 4416	0.2369	0.96	244 ± 19	0.5597	0.0615	0.501	0.521	10
SDSS J0109 + 1500	0.2939	0.69	251 ± 19	0.3807	0.0418	0.389	0.407	10
SDSS J0216 − 0813	0.3317	1.15	349 ± 24	0.3287	0.0361	0.320	0.336	1–9

[a]References: (1) [50]; (2) [46]; (3) [49]; (4) [47]; (5) [48]; (6) [4]; (7) [11]; (8) [5]; (9) [6]; (10) [12]; (11) [13]

Table 5 Strong gravitational lensing systems with $0.52 < z_s < 0.545$

Galaxy	z_l	$\theta_{\rm E}$ (arc s)	σ_0 (km s^{-1})	$\mathcal{D}_{\rm obs}\ f_{SIS} = 1.010$	$\sigma_{\mathcal{D}}$	$\mathcal{D}_{R_{\rm h}=ct}$	$\mathcal{D}_{\Lambda{\rm CDM}}$	Refs.[a]
SDSS J1420 + 6019	0.0629	1.04	206 ± 5	0.851	0.0936	0.858	0.869	1–9
SDSS J2321 − 0939	0.0819	1.57	245 ± 70	0.9082	0.0999	0.816	0.829	1–9
SDSS J1451 − 0239	0.1254	1.04	223 ± 14	0.726	0.079	0.718	0.735	10, 11
SDSS J0959 + 0410	0.1260	1.00	229 ± 13	0.6616	0.07277	0.723	0.740	1–9
SDSS J1538 − 5817	0.1428	1.00	189 ± 12	0.9717	0.106	0.687	0.705	10, 11
SDSS J1627 − 0053	0.2076	1.21	295 ± 13	0.482	0.052	0.552	0.573	1–9
SDSS J0959 + 4416	0.2369	0.96	244 ± 19	0.5597	0.0615	0.501	0.521	10
SDSS J0109 + 1500	0.2939	0.69	251 ± 19	0.3807	0.0418	0.389	0.407	10
SDSS J0216 − 0813	0.3317	1.15	349 ± 24	0.3287	0.0361	0.320	0.336	1–9

[a]References: (1) [50]; (2) [46]; (3) [49]; (4) [47]; (5) [48]; (6) [4]; (7) [11]; (8) [5]; (9) [6]; (10) [12]; (11) [13]

The principal goal of this paper is to use a GP reconstruction of the $\mathcal{D}_{\rm obs}(z_l, \langle z_s \rangle)$ functions in order to compare the predictions of the ΛCDM and $R_{\rm h} = ct$ cosmological models. The standard model contains radiation (photons and neutrinos), matter (baryonic and dark) and dark energy in the form of a cosmological constant. This blend of constituents, currently dominated by dark energy, is producing a phase of accelerated expansion, following an earlier period of deceleration when radiation was dominant. In terms of today's critical density $\rho_c \equiv 3c^2 H_0/8\pi G$ and Hubble constant H_0, the Hubble expansion rate in this cosmology depends on the matter density, $\Omega_{\rm m} \equiv \rho_{\rm m}/\rho_c$, radiation density, $\Omega_{\rm r} \equiv \rho_{\rm r}/\rho_c$ and dark energy density, $\Omega_{\rm de} \equiv \rho_{\rm de}/\rho_c$, with the constraint $\Omega_{\rm m} + \Omega_{\rm r} + \Omega_{\rm de} = 1$. Since $\Omega_{\rm r}$ is negligible in the current era, we ignore radiation and use $\Omega_{\rm de} = 1 - \Omega_{\rm m}$. For all the calculations, we use the parameters optimized by Planck, with $\Omega_{\rm m} = 0.272$, and $\Omega_{\rm de} = 0.728$. Thus, one deduces from the Friedmann equation that in ΛCDM

$$H(z) = H_0\sqrt{\Omega_{\rm m}(1+z)^3 + \Omega_{\rm de}}. \tag{11}$$

The angular diameter distance between redshifts z_1 and z_2 is given as

$$D(z_1, z_2) = \frac{1}{1+z_2}\int_{z_1}^{z_2} dz\, \frac{c}{H(z)}. \tag{12}$$

Therefore, substituting for $H(z)$ from Eq. (11), one gets

$$D_A^{\Lambda{\rm CDM}}(z_1, z_2) = \frac{c}{H_0}\frac{1}{(1+z_2)} \times \int_{z_1}^{z_2}\left[\Omega_{\rm m}(1+z)^3 + \Omega_{\rm de}\right]^{-1/2} dz. \tag{13}$$

The $R_{\rm h} = ct$ universe [16,17,52–54] is also an FRW cosmology with radiation (photons and neutrinos), matter (baryonic and dark) and dark energy, with radiation and dark energy dominating the early Universe, and matter and dark energy dominating the current era [55]. But while it is similar to ΛCDM in this regard, it has an additional constraint on the total equation of state, i.e., $\rho + 3p = 0$, the so-called zero active mass condition, where ρ and p are the total energy density and pressure, respectively. With this additional constraint, the $R_{\rm h} = ct$ universe always expands at a constant rate, which depends on only one parameter – the Hubble constant H_0. Using the Friedmann equation with zero active mass, we find that

$$H^{R_{\rm h}=ct}(z) = H_0(1+z), \tag{14}$$

and from Eq. (12), we therefore find that

$$D_A^{R_{\rm h}=ct}(z_1, z_2) = \frac{c}{H_0}\frac{1}{(1+z_2)}\ln\left(\frac{1+z_2}{1+z_1}\right). \tag{15}$$

5 The area minimization statistic

Now that we are dealing with a comparison between two continuous functions, i.e., $\mathcal{D}_{\rm obs}$ with either $\mathcal{D}^{\Lambda{\rm CDM}}$ or $\mathcal{D}^{R_{\rm h}=ct}$ (each derived from Eq. 5 using Eqs. 13 and 15), we cannot use discrete sampling statistics, such as weighted least squares, for the comparison of different models. The reason is that sampling at random points to obtain the squares of differences between model and reconstructed curve would lose information between these points, whose importance cannot be ascertained prior to the sampling. To overcome this deficiency, we introduce a new statistic, based on a previous application [56,57], which we call the "Area Minimization Statistic" to estimate each model's probability of being consistent with the data. Our principal assumption is that the measurement errors are Gaussian, which we use to generate a mock sample of GP reconstructed curves representing the possible variation of $\mathcal{D}$ away from $\mathcal{D}_{\rm obs}$. We do this by

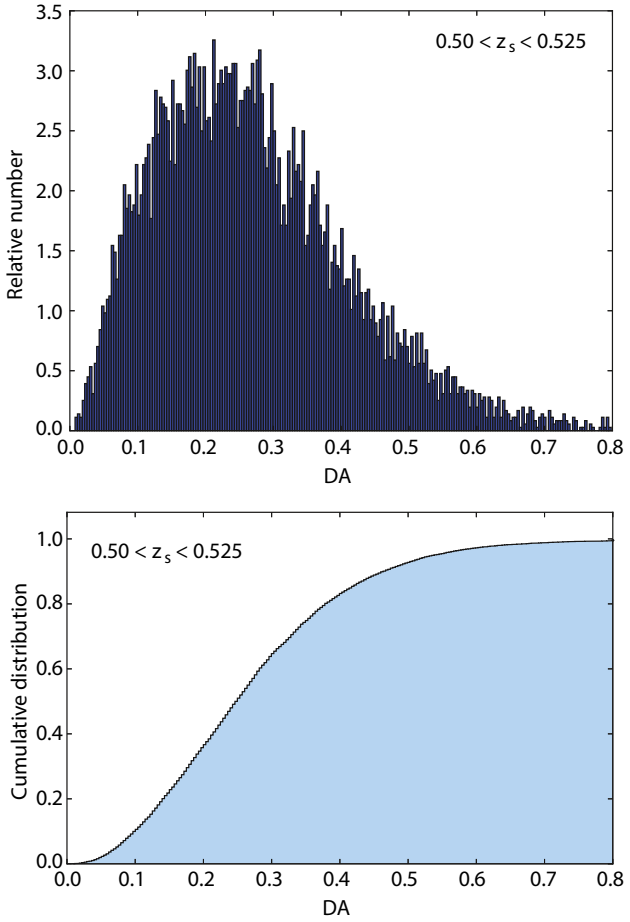

Fig. 1 Top panel: the distribution of frequency versus area differential DA for a mock sample with source shell $0.5 < z_s < 0.525$; and bottom panel: its corresponding cumulative probability distribution

employing the Gaussian randomization

$$\mathcal{D}_i(z_l, \langle z_s\rangle) = \mathcal{D}_{i,\,\mathrm{obs}}(z_l, \langle z_s\rangle) + r\sigma_{\mathcal{D}_i}, \tag{16}$$

where $\mathcal{D}_{i,\,\mathrm{obs}}(z_l, \langle z_s\rangle)$ are the actual measurements as a function of z_l for each source shell $\langle z_s\rangle$. $\sigma_{\mathcal{D}_i}$ are the actual observed errors and r is a Gaussian random variable with zero mean and a variance of 1. Next, these $\mathcal{D}_i(z_l, \langle z_s\rangle)$ are used together with the errors $\sigma_{\mathcal{D}_i}$ to reconstruct the function $\mathcal{D}_{\mathrm{mock}}(z_l, \langle z_s\rangle)$ corresponding to each mock sample, and finally we calculate the weighted absolute area difference between $\mathcal{D}_{\mathrm{mock}}(z_l, \langle z_s\rangle)$ and the GP reconstructed function of the actual data according to

$$DA = \int_{z_{\mathrm{min}}}^{z_{\mathrm{max}}} dz_l \left(\frac{\left|\mathcal{D}_{\mathrm{mock}}(z_l, \langle z_s\rangle) - \mathcal{D}_{\mathrm{obs}}(z_l, \langle z_s\rangle)\right|}{\sigma(z_l)} \right). \tag{17}$$

In this expression, z_{min} and z_{max} are the minimum and maximum redshifts, respectively, of the data range. We repeat this procedure 10,000 times to build a distribution of frequency versus area differential DA, and from it construct the cumulative probability distribution. In Fig. 1 we show these quantities for the illustrative source shell $0.50 < z_s < 0.525$ (the frequency is shown in the top panel, and the cumulative probability distribution is on the bottom). This procedure generates a 1-to-1 mapping between the value of DA and the frequency with which it arises. With the additional assumption that curves with a smaller DA are a better match to $\mathcal{D}_{\mathrm{obs}}$, one can then use the cumulative distribution to estimate the probability that the difference between a model's prediction and the reconstructed curve is merely due to Gaussian randomness. When comparing a model's prediction to the data, we therefore calculate its DA and use our 1-to-1 mapping to determine the probability that its inconsistency with the data is just due to variance, rather than the model being wrong. These are the probabilities we then compare to determine which model is more likely to be correct. This basic concept is common to many kinds of statistical approaches, though none of the existing ones can be used when comparing two continuous curves, as we have here.

The reconstructed curves for our five subsamples are shown in the left-hand panels of Fig. 2. These correspond to the five source redshift shells in Tables 1, 2, 3, 4 and 5. The corresponding cumulative probability distributions are plotted in the right-hand panels, which also locate the DA values for $R_{\mathrm{h}} = ct$ (yellow) and ΛCDM (red). The probabilities associated with these differential areas are summarized in Table 6. Along with the reconstructed functions, the left-hand panels also show the corresponding 1σ (dark) and 2σ (light) confidence regions provided by the GP, and the theoretical predictions in ΛCDM (dashed) and $R_{\mathrm{h}} = ct$ (dotted). As we highlighted earlier, the functions $\mathcal{D}_{\mathrm{obs}}(z_l, \langle z_s\rangle)$ have been reconstructed without pre-assuming any parametric form, so in principle they represent the actual variation of $\mathcal{D}$ with redshift, regardless of whether or not either of the two models being tested here is the correct cosmology.

The overall impression one gets from the results displayed in Fig. 2 and summarized in Table 6 is that, for every source redshift shell sampled here, the probability of $R_{\mathrm{h}} = ct$ being consistent with the GP reconstructed function $\mathcal{D}_{\mathrm{obs}}$ is ∼10–30% higher than that for ΛCDM. Future surveys will greatly grow the sample of sources available for this type of analysis, differentiating between these two models with greater confidence.

6 Conclusions

In this paper, we have introduced the GP reconstruction approach to strong lensing studies, though clearly the avail-

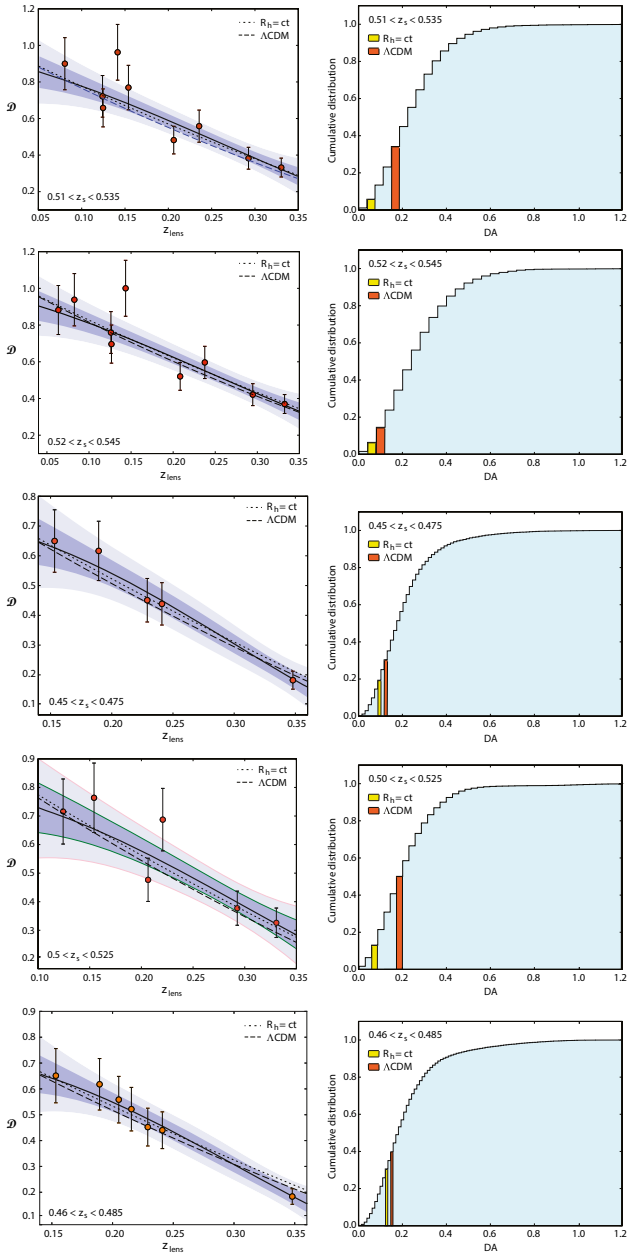

Fig. 2 Left panels **a**, **c**, **e**, **g**, **i** The solid curve in each plot indicates the reconstructed $\mathcal{D}_{\rm obs}$ function using Gaussian processes, for the source redsfhit ranges (0.51, 0.535), (0.52, 0.545), (0.45, 0.475), (0.5, 0.525), and (0.46, 0.485). The dotted curve indicates the predicted $\mathcal{D}$ in the $R_{\rm h} = ct$ universe and the dashed curve indicates the corresponding $\mathcal{D}$ in ΛCDM. In each of these figures, dark blue represents the 1σ confidence region, and light blue is 2σ. Right panels **b**, **d**, **f**, **h**, **j** The corresponding cumulative probability distributions

able sample is still not large enough for us to make full use of this method. As noted earlier, one of the principal benefits of this technique is that the function (in this case $\mathcal{D}_{\rm obs}$) representing the data may be obtained without the assumption of any parametric form associated with particular models. This allows one to test different models against the actual $\mathcal{D}_{\rm obs}$, rather than against each other's predictions, neither of which may be a good representation of the measurements. In addition, GP provide 1σ and 2σ confidence regions for the reconstructed functions more in line with the population as a whole, rather than individual data points, greatly restricting the ability of 'incorrect' models to adequately fit the observations due to otherwise large measurement errors.

This is reflected in the probabilities quoted in Table 6 for the two models we have examined here. Unlike previous model comparisons based on the use of parametric fits to the strong-lensing data, we now find that $R_{\rm h} = ct$ is favoured over ΛCDM with consistently higher likelihoods in all five source redshift shells we have assembled for this work. Though these statistics are still quite limited, it is nonetheless telling that the differentiation between models improves as the number of sources within each shell increases. Also, at least for $R_{\rm h} = ct$, the probability of its predictions matching the GP reconstructed functions generally increases as the size of the lens sample grows. The outcome of this work underscores the importance of using unbiased data and sound statistical methods when comparing different cosmological models. As a counterexample, consider the use of $H(z)$ measurements based on BAO observations instead of cosmic chronometers [28], constituting an unwitting use of model-dependent measurements to test competing models. Such an approach ignores the significant limitations in all but the three most recent BAO measurements [58,59] for this type of work. Previous applications of the galaxy two-point correlation function to measure the BAO scale were contaminated with redshift distortions associated with internal gravitational effects [59]. To illustrate the significance of these limitations, and the impact of the biased BAO measurements of $H(z)$, note how the model favoured by the data switches from ΛCDM to $R_{\rm h} = ct$ when only the unbiased measurements are used [61].

A second counterexample is provided by the merger of disparate sub-samples of Type Ia SNe to improve the statistical analysis. We have already published an in-depth explanation of the perils associated with the blending of data with different systematics for the purpose of model selection [62], but let us nonetheless consider a brief synopsis here. The Union2.1 catalog [63,64] includes $\approx$ 580 SN detections, though each sub-sample has its own systematic and intrinsic uncertainties. The conventional approach minimizes an overall χ^2, while each sub-sample is assigned an intrinsic dispersion to ensure that $\chi^2_{\rm dof} = 1$ [28,29]. Instead, the statistically correct approach would estimate the unknown intrinsic dispersions simultaneously with all other parameters [62,65]. Quite tellingly, the outcome of the model selection is reversed when one switches from the improper statistical approach to the correct one. To emphasize how

Table 6 Model comparison using strong gravitational lenses with Gaussian processes

Source redshift range	Number of lenses	$R_h = ct$ probability (%)	ΛCDM probability (%)	Figures
0.51–0.535	9	94.23	65.82	2a, b
0.52–0.545	9	93.59	85.48	2c, d
0.46–0.485	7	69.43	60.29	2e, f
0.50–0.525	6	86.96	49.91	2g, h
0.45–0.475	5	80.65	69.68	2i, j

critical this reversal is in the case of ΛCDM, one simply needs to compare the outcome of using a merged supersample with that produced with a large, single homogeneous sample, such as the Supernova Legacy Survey Sample [66].

Within this context, we highlight the fact that the features of the GP reconstruction approach in the study of strong lenses are promising because, in spite of the fact that the use of these systems to measure cosmological parameters has been with us for over a decade (see, e.g., Refs. [4–6,67]), the results of this effort have thus far been less precise than those of other kinds of observations. For the large part, these earlier studies were based on the use of parametric fits to the data, but it is quite evident (e.g., from Figs. 1 and 2 in Ref. [7]) that the scatter in $\mathcal{D}_{\rm obs}$ about the theoretical curves generally increases significantly as $D_A(z_l, z_s) \to D_A(0, z_s)$. That is, measuring $\mathcal{D}$ incurs a progressively greater error as the distance to the gravitational lens becomes a smaller fraction of the distance to the quasar source. This has to do with the fact that $\theta_{\rm E}$ changes less for large values of z_s/z_l so, for a fixed error in the Einstein angle, the measurement of $\mathcal{D}_{\rm obs}$ becomes less precise. As we have demonstrated in this paper, the analysis of strong lensing systems based on a GP reconstruction of $\mathcal{D}_{\rm obs}$ improves our ability to distinguish between different models, albeit by a modest amount given the current sample.

Upcoming survey projects, such as the Dark Energy Survey (DES; [68]), the Large Synoptic Survey Telescope (LSST; [69]), the Joint Dark Energy Mission (JDEM; [70]), and the Square Kilometer Array (SKA; e.g., Ref. [71]), are expected to greatly grow the size of the lens sample. The ability of GP reconstruction methods to differentiate between models will increase in tandem with this growth. Several sources of uncertainty still remain, however, including the actual mass distribution within the lens. And since such errors appear to be more restricting for lens systems with large values of z_s/z_l, a priority for future work should be the identification of strong lenses with small angular diameter distances between the source and lens relative to the distance between the lens and observer.

Acknowledgements FM is grateful to the Instituto de Astrofísica de Canarias in Tenerife and to Purple Mountain Observatory in Nanjing, China for their hospitality while part of this research was carried out. FM is also grateful for partial support to the Chinese Academy of Sciences Visiting Professorships for Senior International Scientists under Grant 2012T1J0011, and to the Chinese State Administration of Foreign Experts Affairs under Grant GDJ20120491013.

Funded by SCOAP[3].

References

1. M. Bartelmann, P. Schneider, AA **345**, 17 (1999)
2. A. Refreiger, ARAA **41**, 645 (2003)
3. T. Futamase, S. Yoshida, PThPh **105**, 887 (2001)
4. T. Treu, L.V.E. Koopmans, A.S. Bolton, S. Burles, L.A. Moustakas, ApJ **640**, 662 (2006)
5. C. Grillo, M. Lombardi, G. Bertin, AA **477**, 397 (2008)
6. M. Biesiada, A. Piórkowska, B. Malec, MNRAS **406**, 1055 (2010)
7. F. Melia, J.-J. Wei, X.-F. Wu, AJ **149**, 2 (2015)
8. S. Cao et al., ApJ **806**, 185 (2015)
9. Y. Shu et al., ApJ **851**, 48 (2017)
10. A. Bolton, S.M. Burles, L.V.E. Koopmans, T. Treu, L.M. Moustakas, ApJ **638**, 703 (2006)
11. L.V.E. Koopmans, T. Treu, A.S. Bolton, S. Burles, L.A. Moustakas, ApJ **649**, 599 (2006)
12. A.S. Bolton, S.M. Burles, L.V.E. Koopmans et al., ApJ **682**, 964 (2008)
13. E.R. Newton, P.J. Marshall, T. Treu, SLACS collaboration. ApJ **734**, 104 (2011)
14. A .G. Riess et al., AJ **116**, 1009 (1998)
15. S. Perlmutter et al., Nature **391**, 51 (1998)
16. F. Melia, MNRAS **382**, 1917 (2007)
17. F. Melia, A. Shevchuk, MNRAS **419**, 2579 (2012)
18. F. Melia, MNRAS **464**, 1966 (2017)
19. F. Melia, ApJ **764**, 72 (2013)
20. J.-J. Wei, X. Wu, F. Melia, ApJ **772**, 43 (2013)
21. J.-J. Wei, X.-F. Wu, F. Melia, R.S. Maier, AJ **149**, 102 (2015)
22. F. Melia, J.-J. Wei, R. S. Maier, X. Wu, EPL (2017) **(submitted)**
23. F. Melia, R.S. Maier, MNRAS **432**, 2669 (2013)
24. P. van Oirschot, J. Kwan, G.F. Lewis, MNRAS **404**, 1633 (2010)
25. M. Bilicki, M. Seikel, MNRAS **425**, 1664 (2012)
26. G.F. Lewis, P. van Oirschot, MNRAS Lett. **423**, 26 (2012)
27. G.F. Lewis, MNRAS **432**, 2324 (2013)

28. D.L. Shafer, Phys. Rev. D **91**, 103516 (2015)
29. D. Rubin & B. Hayden B., ApJL **833**, 5 (2016) **(id. L30)**
30. O. Bikwa, F. Melia, A.S.H. Shevchuk, MNRAS **421**, 3356 (2012)
31. F. Melia, JCAP **09**, 029 (2012)
32. F. Melia, Astrophys. Sp. Sci. **356**, 393 (2015)
33. F. Melia, MNRAS **446**, 1191 (2015)
34. K.U. Ratnatunga, R.E. Griffiths, E.J. Ostrander, AJ **117**, 2010 (1999)
35. P. Schneider, J. Ehlers, E.E. Falco, *Gravitational lenses* (Springer, Berlin, 1992)
36. R. Kormann, P. Schneider, M. Bartelmann, AA **284**, 285 (1994)
37. R.E. White, D.S. Davis, BAAS **28**, 1323 (1996)
38. A.S. Bolton, S.M. Burles, L.V.E. Koopmans, T. Treu, L.M. Moustakas, ApJL **624**, L21 (2005)
39. G. van de Ven, P.G. van Dokkum, M. Franx, MNRAS **344**, 924 (2003)
40. S. Cao, Y. Pan, M. Biesiada, W. Godlowski, Z.-H. Zhu, JCAP **3**, 16 (2012)
41. P. Young, J.E. Gunn, J. Kristian, J.B. Oke, J.A. Westphal, ApJ **241**, 507 (1980)
42. J. Huchra, M. Gorenstein, S. Kent et al., AJ **90**, 691 (1985)
43. J. Lehar, G.I. Langston, A. Silber, C.R. Lawrence, B.F. Burke, AJ **105**, 847 (1993)
44. C.D. Fassnacht, D.S. Womble, G. Neugebauer et al., ApJL **460**, L103 (1996)
45. J.L. Tonry, AJ **115**, 1 (1998)
46. L.V.E. Koopmans, T. Treu, ApJ **568**, 5 (2002)
47. L.V.E. Koopmans, T. Treu, ApJ **583**, 606 (2003)
48. T. Treu, L.V.E. Koopmans, ApJ **611**, 739 (2004)
49. T. Treu, L.V.E. Koopmans, MNRAS **343**, 29 (2003)
50. T. Treu, L.V.E. Koopmans, ApJ **575**, 87 (2002)
51. M. Seikel, C. Clarkson, M. Smith, JCAP **06**, 036S (2012)
52. F. Melia, M. Abdelqader, IJMPD **18**, 1889 (2009)
53. F. Melia, Front. Phys. **11**, 119801 (2016)
54. F. Melia, Front. Phys. **12**, 129802 (2017)
55. F. Melia, M. Fatuzzo, MNRAS **456**, 3422 (2016)
56. M.K. Yennapureddy, F. Melia, JCAP **11**, 029Y (2017)
57. F. Melia, M.K. Yennapureddy, JCAP **02**, 034M (2018)
58. L. Anderson et al., MNRAS **441**, 24 (2014)
59. T. Delubac et al., AA **574**, A59 (2015)
60. M. López-Corredoira, ApJ **781**, 96 (2014) **(id. 96)**
61. F. Melia, M. López-Corredoira, IJMPD **26**, 1750055 (2017)
62. J.-J. Wei, X. Wu, F. Melia, R.S. Maier, AJ **149**, 102 (2015)
63. M.R. Kowalski, ApJ **686**, 749 (2008)
64. N. Suzuki et al., ApJ **746**, 85 (2012)
65. A.G. Kim, PASP **123**, 230 (2011)
66. M. Betoule et al., AA **568**, 22 (2014)
67. M. Biesiada, B. Malec, A. Piórkowska, RAA **11**, 641 (2011)
68. J. Frieman, Dark energy survey collaboration. BAAS **36**, 1462 (2004)
69. A. Tyson, R. Angel, The new era of wide field astronomy. ASP conference series, vol. 232. Ed. R. Clowes, A. Adamson, G. Bromage. San Francisco: ASP, p. 347 (2001)
70. A. Tyson, ASP conference series, vol. 339, Observing dark energy, Ed. S. C. Wolff, T. R. Lauer, p. 95 (2005)
71. J. McKean, N. Jackson, S. Vegetti, M. Rybak, S. Serjeant, L.V.E. Koopmans, R. B. Metcalf, C. Fassnacht, P. J. Marshall, M. Pandey-Pommier, In: Proceedings of advancing astrophysics with the square kilometre array (AASKA14). 9–13 June 2014. Giardini Naxos, Italy (2015)

CHAPTER-4

A Cosmological Solution to the Impossibly Early Galaxy Problem

Manoj K. Yennapureddy, Fulvio Melia

Published In: Physics of the Dark Universe
DOI:10.1016/j.dark.2018.03.003

In the previous two chapters, we have tested the R_h=ct universe, and ΛCDM cosmological models based on their prediction assuming the universe is homogeneous. However, observations indicate that our universe is not homogeneous; it does contain structures such as galaxies which represent the non-homogeneous universe. Any cosmological model which describes the universe should also predict the formation of structures and the timeline of their formation. In the past decade with the advent of high precision observations it became evident that the standard ΛCDM cosmology was not able to account for the early appearance of supermassive black holes and galaxies. Moreover, the surprisingly early appearance of massive galaxies challenges the standard model, and the halo mass function estimated from galaxy surveys at $z \gtrsim 4$ appears to be inconsistent with the predictions of ΛCDM, giving rise to what has been termed ‘‘The Impossibly Early Galaxy Problem.”

In this chapter, we use the linear perturbation theory to infer the growth of structures using which we address “The Impossibly Early Galaxy Problem”. The results of this chapter indicate that the growth of the structures in R_h=ct is consistent with observations. The predicted halo mass function in R_h=ct universe fits the observations at low redshifts from z = 4 to 7, but it overpredicts one to two orders of magnitude at high redshifts. This inconsistency might be due to the break down of our solutions obtained through the linear perturbation theory presented in this chapter.

Physics of the Dark Universe 20 (2018) 65–71

Contents lists available at ScienceDirect

Physics of the Dark Universe

journal homepage: www.elsevier.com/locate/dark

A cosmological solution to the Impossibly Early Galaxy Problem

Manoj K. Yennapureddy [a], Fulvio Melia [b,*,1]

[a] Department of Physics, The University of Arizona, AZ 85721, USA
[b] Department of Physics, The Applied Math Program, and Department of Astronomy, The University of Arizona, AZ 85721, USA

ARTICLE INFO

Article history:
Received 26 October 2017
Received in revised form 18 March 2018
Accepted 19 March 2018

Keywords:
Cosmological parameters
Cosmological observations
Cosmological theory
Dark energy
Galaxies
Large-scale structure

ABSTRACT

To understand the formation and evolution of galaxies at redshifts $0 \lesssim z \lesssim 10$, one must invariably introduce specific models (e.g., for the star formation) in order to fully interpret the data. Unfortunately, this tends to render the analysis compliant to the theory and its assumptions, so consensus is still somewhat elusive. Nonetheless, the surprisingly early appearance of massive galaxies challenges the standard model, and the halo mass function estimated from galaxy surveys at $z \gtrsim 4$ appears to be inconsistent with the predictions of ΛCDM, giving rise to what has been termed "The Impossibly Early Galaxy Problem" by some workers in the field. A simple resolution to this question may not be forthcoming. The situation with the halos themselves, however, is more straightforward and, in this paper, we use linear perturbation theory to derive the halo mass function over the redshift range $0 \lesssim z \lesssim 10$ for the $R_h = ct$ universe. We use this predicted halo distribution to demonstrate that both its dependence on mass and its very weak dependence on redshift are compatible with the data. The difficulties with ΛCDM may eventually be overcome with refinements to the underlying theory of star formation and galaxy evolution within the halos. For now, however, we demonstrate that the unexpected early formation of structure may also simply be due to an incorrect choice of the cosmology, rather than to yet unknown astrophysical issues associated with the condensation of mass fluctuations and subsequent galaxy formation.

1. Introduction

The structures we see today are believed to have grown gravitationally from tiny fluctuations in the primordial density field. Current theory holds that perturbations started to collapse once their density exceeded a certain critical value, forming bound objects that then assembled together with the surrounding gas and dust to form stars, galaxies and clusters. With dark matter particles decoupling first from the radiation, the early stages of structure formation proceeded principally through the condensation of dark matter halos. Baryonic particles subsequently accreted into the potential valleys created in this fashion once they themselves decoupled from the relativistic background.

The physics responsible for the formation of galaxies in this scenario is still not completely understood, but there is general consensus concerning the rate at which halos formed, specifically their number density distribution as a function of mass and redshift [1–3]. This halo mass function (as it is more commonly known) was first derived analytically by Press & Schechter [4] using several simplifying assumptions, including a spherically symmetric collapse model and a Gaussian initial density field. But though this analysis predicts a reasonable distribution, it nonetheless also underpredicts the number of high-mass halos and overpredicts the low-mass ones compared to detailed numerical simulations. More recently, Sheth & Tormen [1] have shown that this discrepancy may be mitigated by adopting an ellipsoidal collapse model rather than spherical. Even so, these analytical and semi-analytical approaches have for the most part been tested only against numerical simulations. Unfortunately, while Press–Schechter underpredicts the number of high-mass halos, Sheth–Tormen apparently overpredicts them, though a correction factor based on the linear growth rate may have been found. We shall describe this effect following Eq. (21) below. It is more difficult to test these semi-analytic approaches using actual observations because halos cannot be seen directly. The predicted halo distribution must be compared to the data indirectly, through the observation of the galaxy mass function, with an added assumption concerning the evolutionary relationship between them.

The observed halo formation was recently assessed [5] using several previous analyses to compare different techniques for relating the halo and galaxy distributions. For this purpose, these authors employed high redshift surveys in the redshift range $z \sim 4$–8, principally The Cosmic Assembly Near-infrared Deep Extragalactic Survey (CANDELS [6,7]) and the Spitzer Large Area Survey with

* Corresponding author.
E-mail addresses: manojy@email.arizona.edu (M.K. Yennapureddy), fmelia@email.arizona.edu (F. Melia).
[1] John Woodruff Simpson Fellow.

https://doi.org/10.1016/j.dark.2018.03.003
2212-6864/

Hyper-Suprime-Cam (SPLASH [8]), to probe the galaxy luminosity and mass functions, from which the halo distribution may be derived. CANDELS is well suited to find the lower-mass galaxies because it represents a survey over a small area, whereas SPLASH has broad sky coverage and can therefore probe the more massive galaxies.

Obtaining the halo distribution and masses from the galaxy distribution presents quite a challenge. The best way to obtain halo masses from the spatial distribution of galaxies is via galaxy clustering methods [9,10], which do not assume any physical properties of the galaxies themselves, though they must assume a model for the dark matter concentration. Other techniques use the relationship between the luminosity and stellar masses, obtained from template fitting [11]. For example the "abundance matching technique" [12] relates one of the key features in the luminosity or mass function, such as the knee, to a feature in the halo mass function, and then matches the galaxy density and dark-matter halo density to derive halo masses over the whole mass range. Alternatively, one may also assume that the relations derived at low redshift using luminosity to dark-matter mass ratios still apply at high redshifts.

But though each of these techniques yields somewhat different outcomes in a quantitative sense, they all agree qualitatively [5]. These earlier findings show quite emphatically that the halo distribution estimated from galaxies at $z \gtrsim 4$ in the CANDELS and SPLASH surveys is inconsistent with the evolution of the halo mass function and the galaxy luminosity and mass functions predicted by standard ΛCDM [9,10,13,12]—a situation termed "The Impossibly Early Galaxy Problem" [5]. Various possible remedies were considered by these authors to reconcile the observed and predicted halo mass distributions, including possible errors introduced in calibrating the data using relations derived at lower redshifts, which may not be applicable for $z \gtrsim 4$. None of the remedies worked, however. If anything, this extended study showed that the high-redshift galaxies appear normal, suggesting that the relations derived at lower redshifts are probably also applicable at these higher redshifts.

The tension between the predictions of ΛCDM and the 'measured' halo mass function may be resolved with a better understanding of the underlying physics, e.g., regarding start formation and galaxy evolution. On the other hand, the current uncertain situation may simply be an indication that there are insurmountable problems with the use of ΛCDM as the background cosmology. In this paper, we will proceed under this assumption—i.e., that the problems elucidated by Steinhardt et al. [5] are real, and seek to find a solution to the surprisingly early formation of massive halos. To balance the discussion, however, we acknowledge the fact that this point of view is not universally accepted—a situation largely due to uncertainties in the simulations used to fully interpret the data and halo mass function.

Understanding the evolution of galaxies and their observational signatures, such as their UV luminosity or their redshift-dependent clustering, necessarily relies on modelling dark-matter evolution [14], and cosmological hydrodynamical simulations [15,16], complemented by analytical and semi-analytical calculations [17,18]. Complications arise in part because the observed UV luminosity function depends strongly on redshift (at least from $z \sim 4$ to 10), and various combinations of inputs and assumptions produce degenerate results [19,20]. It is fair to say that the degree of tension between the observations and predictions of the standard model depends on one's point of view.

But as noted, there are good reasons to suspect that real problems with the formation of structure do exist in the standard model. Some of these have to do with the unusually early appearance of supermassive black holes at $z \sim 6$–7 [21,22] and galaxies at $z \sim 10$–12 (see refs. cited in [23]). In addition, a rather compelling case may be made that a problem exists [5] based on the following points: (1) the halo mass function at $0 \lesssim z \lesssim 8$ is inferred using 3 or 4 different techniques, not just one, and all of the results agree at least qualitatively; (2) the fact that these techniques all require a blending of observational and simulational (i.e., model-dependent) factors to arrive at a mutually consistent picture measure that it is difficult to understand exactly what the results mean, because such an approach is very compliant to the assumptions one makes. For example, abundance matching forces agreement between observation and theory even in the absence of a strong physical motivation for the underlying model. The uncertainties (e.g., in how to match star-forming galaxy UV luminosities with halo formation in both mass and time) leave unresolved questions concerning how galactic evolution impacts our understanding of halo evolution. Nonetheless, forcing consistency between the observations and predictions of the standard model comes at a considerable cost.

One may understand this situation as follows. Much of the analysis in this paper is based on the 'standard' ratio of halo to stellar-mass, which arises from two considerations: First is the expectation that 10% of the baryonic matter condensed into stars [24]. Second, is the ratio of dark matter to baryonic matter, which is observed to be about 6:1 [25]. As we shall detail below, Steinhardt et al. [5] attempted to reconcile the disparity between theory and observation by introducing several modifications to the underlying physical processes. In order to fit the derived halo mass function in ΛCDM, however, they found that only a change by 0.8 dex in the ratio of dark matter to baryonic matter would suffice. But such a drastic change could come about only with a complete absence of dark matter at redshift 8, or if essentially 100% of the baryons condensed into stars at higher redshifts. Both of these scenarios constitute implausible physics, such as the need to convert all of the baryons into stars instantly upon halo virialization [5]. Other attempted remedies have equally unlikely requirements. So perhaps a better way to characterize the problem with the halo mass function is to say that it can only be made consistent with expectations of the standard model with the adoption of unlikely, new physics.

Given the unsettled debate concerning the formation and evolution of galaxies, we stress that our focus in this paper is not to model the galaxies themselves. We merely use some key observations of galactic profiles to infer the mass and time evolution of halos which, in principle, constitutes a much simpler, cleaner objective. For a complete assessment of problems with the formation of structure, it will eventually be necessary to study both the formation of halos and the galaxies within them, but this is a much more challenging analysis than we are attempting here. Such elaborate simulations for the formation and clustering of galaxies are outside the scope of the present paper. The outcome of this subsequent work will be reported elsewhere.

In the present context, the difficulty that ΛCDM has in accounting for the observed halo mass function has much in common with the growing tension between the measured cosmological growth rate, $b\sigma_8(z)$, and its value predicted by the standard model, particularly in the redshift range $0 < z < 1$, where a significant curvature expected in the functional form of $b\sigma_8(z)$ is absent in the data [26]. Admittedly, the errors in the measured values of $b\sigma_8(z)$ are still too large to rule out any model, but this is precisely why a comparison of the measured halo mass function with theory is very probative. If it turns out that *both* the halo distribution at high redshift and $b\sigma_8(z)$ at lower redshift are in tension with the growth of structure expected in standard cosmology, a compelling argument can be made that an alternative expansion scenario must be seriously considered. In this paper, we therefore compare the measured halo mass function, not only with the prediction of ΛCDM, but

also with that expected in the alternative Friedmann–Robertson–Walker (FRW) cosmology known as the $R_h = ct$ universe [27–31]. It was a direct one-on-one comparison between these two models that highlighted the greater consistency of the growth rate data with $R_h = ct$ than with ΛCDM [26]. As we shall see shortly, the measured halo mass function also provides strong support for $R_h = ct$ and, if the tension between the predictions of ΛCDM and the data fail to be resolved, may also eventually argue that $R_h = ct$ is favoured over the standard model.

2. The halo mass function in ΛCDM

Let us first see how the halo mass function predicted by the standard model fares in comparison with the data. Throughout this paper, we use the number density and halo mass calibrated in Ref. [5] (and references cited therein) based on the CANDELS and SPLASH surveys. These data, along with seven theoretical curves calculated within the redshift range $z = 4$–10, are shown in Fig. 1. The theoretical curves in this figure are based on the halo mass function estimates of Sheth & Tormen [1], using the HMFCalc code developed in Ref. [32]. The standard model parameters are assumed to have their *Planck* values, $(h, \Omega_m, \Omega_\Lambda) = (0.704, 0.272, 0.728)$ [25]. Some of these data points were obtained using the clustering technique and the photometric spectral energy distribution (SED) based on template fitting. A ratio $M_H/M_* \sim 70$ [24] was used to convert the stellar mass function M_* to a halo mass M_H. For the data points obtained using the UV luminosity function, a conversion $M_H/M_\odot \approx 120 L_{UV}/L_\odot$ was used to convert UV luminosity to stellar mass and then to halo mass.

The assumption of a constant ratio $M_H/M_* \sim 70$ (and correspondingly for the UV luminosity) can have a strong influence on the analysis in this paper, so it is appropriate to question its reliability. The situation today is somewhat unfortunate in this regard, given that adequate data are lacking to determine empirically what these ratios are—indeed, whether they are even constant with redshift. And simulations carried out by several groups do not appear to produced fully consistent outcomes. We ourselves do not have a position in this discussion, and eagerly await a resolution in order to put our calculations on firmer ground. For the time being, our goal is to find the most reasonable compromise, while maintaining a manageable approach to avoid tainting our results with excessive (possibly incorrect) detail.

There is some evidence that this ratio is more or less constant based on fits to the inferred halo to stellar mass ratio at lower redshifts, as explained in Ref. [24], but its adoption is not universally accepted. There has been some debate [33,34,10,35,36] regarding whether or not these numbers remain unchanged at higher redshifts. Not surprisingly, there is therefore disagreement between various researchers regarding whether or not the halo to stellar mass relation should be parametrized in terms of both mass and redshift, rather than just the mass or redshift on its own. For example, Refs. [37,17] used both mass and redshift, a conclusion supported by the simulations of Finkelstein et al. [12], who reported that the halo to stellar mass in their calculations evolves with both mass and redshift. For example, their results showed that, at constant UV luminosity, the stellar-to-halo mass ratio increases with z. This trend was also inferred in Ref. [24], where the halo mass function was parametrized in terms of z. But on the other side of this debate, Refs. [38,39] reported that the median stellar mass to halo mass relation does not evolve strongly in the redshift range $5 \lesssim z \lesssim 12$. Some additional uncertainty was generated by the work in Ref. [18], where quite a different approach was used to match the observations with theory. These workers abandoned the need for continuous evolution altogether, and instead allowed mass to be both added and subtracted in order to allow the halo mass function to match the available data at each redshift.

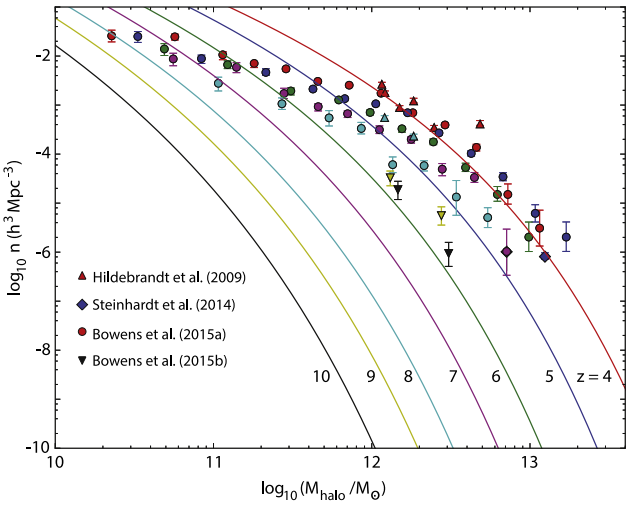

Fig. 1. Halo mass function inferred from galaxy surveys, as a function of mass and redshift: $z = 4$ (red), 5 (blue), 6 (green), 7 (magenta), 8 (cyan), 9 (yellow), and 10 (black). Solid curves represent the theoretical halo number density predicted by ΛCDM in this same redshift range, based on the estimates of Ref. [1] and calculated with the HMFCalc code of Ref. [32].
Source: Adapted from Ref. [5].

There may be an explanation for why there exist two camps in this discussion. It is certainly true that the ratio of halo mass to luminosity varies in the simulations of Refs. [12,39,38,40,41], who reported an evolution in both UV luminosity and redshift. Others have pointed out several caveats, however, mostly having to do with the fact that these conclusions are based primarily on theoretical modelling. But one cannot always be certain that all of the necessary physics has been included. Many physical processes appear to be missing in these simulations, though one does not know for sure how serious any one of them can be. These include non-equilibrium cooling, photo heating, radiative transfer effects, and Pop III star formation, all of which may affect these scaling relations.

Given this uncertain situation, we will follow the analysis in Ref. [5], whose data we are adopting in this paper, in which the halo mass was parametrized solely on z. This results in constant ratios, as are apparently observed at lower redshifts. These authors argue that a break down of this condition at higher redshifts, as suggested by some (perhaps most) simulations, would cause other observational signatures to manifest themselves in the evolution of growth. But no such effects have been observed, lending some support to the assumption of a constant value of these ratios with increasing redshift. These authors considered other possible changes to reconcile the problem, such as varying the Initial Mass Function (IMF), evolving dust corrections, merging and time delays, but to find consistency between theory and observations, they were drawn to unphysical conditions, some of which we described in the Introduction. They concluded that to explain the observed mismatch between the inferred and predicted halo mass function, one has to allow for a rapid evolution in the IMF or a halo to stellar mass ratio that evolves very rapidly. This appears to be unrealistic, given that no such features have been verified observationally.

A quantitative assessment of the degree to which our results (discussed below) would change with an alternative choice of ratios shows that an increase in the correlation $M_H/M_\odot \approx 120 L_{UV}/L_\odot$ by 10% would still permit a reasonable fit (within one order of magnitude) to the halo mass function at high mass and redshift for $R_h = ct$, but it would not improve the situation for ΛCDM. A decrease by 40% of this ratio would still allow a reasonable fit at high redshift for ΛCDM, though not for $R_h =$

ct. Our results below will show that the differences in outcome between the two models is so large that variations in quantities such as the M_H/M_* and $M_H/M_\odot \approx 120 L_{UV}/L_\odot$ ratios are unlikely to be responsible for the full measure of tension between ΛCDM and the measured halo mass function.

It is quite evident in Fig. 1 that the theoretical predictions of ΛCDM are inconsistent with the observational data. The ΛCDM model predicts a sharp evolution in the density of massive halos beyond redshift 4, but as one can see from this figure, the number density of halos is far greater than predicted at these high redshifts. We shall see shortly that, whereas ΛCDM is left without any viable explanation for the measured growth rate and halo mass function, both of these problems are resolved in the $R_h = ct$ cosmology. In the next section, we will discuss the growth of perturbations in $R_h = ct$ and use this result to derive the halo mass function assuming the ellipsoidal collapse model of Sheth & Tormen [1] for the overdense regions.

3. Linear perturbation theory and halo mass function in $R_h = ct$

3.1. Linear perturbation growth

The initial density field grew as a result of self-gravity, while the Hubble expansion and pressure effects diluted it. Which of these factors dominated at any given time determined the evolution of the initial density fluctuations. To follow the evolution in density, one must solve the relativistic perturbed equations because the matter may be coupled to relativistic components, including radiation. Much of the ground work for this theory has been laid out in Ref. [26], and we here adopt some of the principal results of that work to trace out the evolution of the perturbations $\delta \equiv \delta\rho/\rho \leqslant 1$, where the density and pressure are written

$$\rho = \rho_0 + \delta\rho \ , \tag{1}$$

$$p = p_0 + \delta p \ . \tag{2}$$

These fluctuations perturb the metric $g_{\alpha\beta}$ and stress–energy tensor $T_{\alpha\beta}$, all of which are included in the set of linearized relations derived from Einstein's equations. Many of the details of this derivation have appeared previously in Refs. [42–52]. For example, it is not difficult to show that in the covariant Lagrangian approach, where the proper time and cosmic time are related via the gauge transformation

$$\frac{d\tau}{dt} = 1 - \frac{\delta p}{\rho + p} \ , \tag{3}$$

one has [48,51]

$$\frac{d\delta\rho}{dt} = -3H_0\delta\rho - 3\delta H(\rho_0 + P_0) \ . \tag{4}$$

In addition, perturbations to the metric result in

$$\frac{d\delta H}{dt} + 2H_0\delta H + \frac{4\pi G}{3c^2}\rho_0\delta + \frac{v_s^2}{3(1+w)}D^2\delta = 0 \ , \tag{5}$$

where δH is the corresponding perturbation to the Hubble constant, i.e., $H(t) = H_0(t) + \delta H(t)$, and w is the equation of state parameter, defined as $p = w\rho$. Also, $v_s^2 \equiv \partial p/\partial\rho$ is the sound speed squared.

The $R_h = ct$ cosmology satisfies the zero active mass condition, $\rho + 3p = 0$, at all times, so the Universe is dominated by dark energy and (baryonic + dark) matter at low redshifts ($z \lesssim 10$), and by dark energy and radiation in the early Universe. Since we are only considering redshifts $z \lesssim 10$ in this paper, we focus exclusively on the growth of linear perturbations in the matter and dark energy dominated era. We further assume that dark energy acts as a smooth background, so the perturbations are strictly due to fluctuations in the matter density. As discussed in Ref. [29], the zero active mass condition requires us to retain the leading second order terms as well, which are usually unimportant relative to the first order terms.

The fluctuation growth is characterized by the following expressions:

$$\dot\delta = -H_0\delta - 2\delta H - 3\delta H\delta \ , \tag{6}$$

$$\ddot\delta + 3H_0\dot\delta - \frac{3}{2}(\dot\delta^2 - H_0\delta\dot\delta + H_0^2\delta^2) = v_s^2 D^2\delta \ . \tag{7}$$

As is well known, the second term on the left-hand side represents the dilution due to Hubble expansion, while the third term represents growth due to the gravitational instability. The right-hand side accounts for the effects of pressure within the perturbed fluid, sometimes producing acoustic oscillations. But notice that with the zero active mass condition, the gravitational growth term is zero to first order. This is the most significant difference between the ΛCDM and $R_h = ct$ predictions. While the growth equation in the standard model implies a strong gravitational instability and, therefore, a strong evolution of the halo mass function with redshift (see Fig. 1), $\delta(t)$, and hence the halo growth rate, are much weaker functions of redshift in $R_h = ct$.

We may find a relatively straightforward solution to Eq. (7) by utilizing the weak dependence of $\delta(t)$ on t. If we adopt the ansatz

$$\delta(t) \sim t^\alpha \ , \tag{8}$$

with $|\alpha| \ll 1$, then the third term on the left-hand side of Eq. (7) gives

$$\frac{3}{2}(\dot\delta^2 - H_0\delta\dot\delta + H_0^2\delta^2) = \frac{1}{t^2}(\alpha^2\delta^2 - \alpha\delta^2 + \delta^2) \approx Bt^{-2}\alpha \tag{9}$$

(where B is itself much smaller than 1), so that

$$\ddot\delta + 3H_0\dot\delta - \frac{B}{t^2}\delta = v_s^2 D^2\delta \ . \tag{10}$$

We may then follow the conventional procedure of solving this equation using modal analysis with the Fourier decomposition

$$\delta_k(t) = \int \delta(x^\alpha) e^{i\mathbf{k}.\mathbf{x}} d^3x \ . \tag{11}$$

Since, in addition, one has $a(t) = t/t_0$ and $H_0(t) = 1/t$ in $R_h = ct$, we find that

$$\frac{d^2\delta_k}{dt^2} + \frac{3}{t}\frac{d\delta_k}{dt} - \frac{B}{t^2}\delta_k = -\frac{k^2}{a^2}v_s^2\delta_k \ . \tag{12}$$

In the redshift range $z \lesssim 10$, the Universe is dominated by matter and dark energy, so one may ignore the contribution of radiation and write $\rho \approx \rho_m + \rho_{de}$. Also, since the perturbation is assumed to contain only matter, $v_s \approx 0$, and therefore

$$\ddot\delta_k + \frac{3}{t}\dot\delta_k - \frac{B}{t^2}\delta_k = 0 \ . \tag{13}$$

This equation has a polynomial solution,

$$\delta_k(t) = (C_1 t^{-2} + C_2 t^{B/2}) \tag{14}$$

where C_1 and C_2 are constants that depend on the initial conditions. The first term describes a decaying mode, whereas the second term is the growing – actually, quasi-steady – mode. Ignoring the decaying mode, we have

$$\delta_k(t) \approx \delta_k(t_0)\left(\frac{t}{t_0}\right)^{B/2} \tag{15}$$

or, equivalently,

$$\delta_k(z) = \delta_k(0)(1+z)^{-B/2} \ . \tag{16}$$

Using a spherical top-hat window function $W_R(x)$ to filter the fluctuations $\delta(x)$ on a scale of radius R, the variance of the fluctuations is given as

$$\sigma_R^2(R,z) \equiv \frac{b^2(z)}{2\pi^2}\int_0^\infty k^2 P(k) W^2(k,R) dk \ , \tag{17}$$

where $b(z)$ is the usual growth factor which, from Eq. (16), may be written as

$$b(z) = (1+z)^{-B/2} \ . \tag{18}$$

The top-hat filter in Fourier-space is given by

$$W(k,R) = \frac{3\Big[\sin(kR) - kR\cos(kR)\Big]}{(kR)^3} \ . \tag{19}$$

Since one can readily see from Eq. (9) that $|B| \ll 1$, it is clear that the fluctuations grow very slowly at low redshifts. This is the principal feature that makes the predictions of $R_h = ct$ consistent with the $b\sigma_8$ data at $z \lesssim 1$, while ΛCDM predicts a significant curvature in this function that is not confirmed by the observations.

3.2. The halo mass function

One can address questions concerning the fraction of matter bound in structures and their distribution using the halo mass function, first derived by Press and Schechter [4] assuming spherical collapse and a Gaussian initial density field. It is well known, however, that the Press–Schechter mass function overpredicts the number of high-mass halos and underpredicts the number of low-mass ones. This problem can be resolved using an ellipsoidal collapse model, rather than spherical, producing the Sheth–Tormen mass function [1], given as

$$f(\sigma) = A\sqrt{\frac{2a}{\pi}}\left[1+\left(\frac{\sigma^2}{a\delta_c^2}\right)^p\right]\frac{\delta_c}{\sigma}\exp\left[-\frac{a\delta_c^2}{2\sigma^2}\right] , \tag{20}$$

where $A = 0.3222$ is a normalization constant, $a = 0.707$ and $p = 0.3$. This mass function is related to the number density of halos with masses less than M as follows:

$$f(\sigma) = \frac{M}{\rho_0(z)}\frac{dn(M,z)}{d\ln\sigma^{-1}} \ , \tag{21}$$

where σ is the variance of the fluctuations in Eq. (17).

A quantitative assessment of the merits of Press–Schechter versus Sheth–Tormen is hard to come by because tests of these analytic functions necessarily rely on numerical simulations, rather than actual model-independent measurements. However, in their Bolshoi simulation completed just a few years ago, Klypin et al. [53] examined in detail how the Sheth–Tormen prediction compares with their results as a function of mass and redshift. They found that discrepancies were small, i.e., less than ∼10%, at $z \approx 0$ for masses in the range $\sim(5\times10^9$–$5\times10^{14})\ M_\odot$. But the Sheth–Tormen analytic function over-predicts the halo abundance at higher redshifts. For example, at $z \sim 6$, Sheth–Tormen over-predicts the number of halos by about 50% compared to the simulation for masses $\sim10^{11}$–$10^{12}\ M_\odot$. This prediction worsens by an order of magnitude at $z \sim 10$.

In the context of ΛCDM, a remedy for this defect is to include a multiplicative (correction) factor (introduced in Ref. [53]) that brings the Sheth–Tormen approximation to $\lesssim 10\%$ deviation compared to the simulations for masses $\sim(5\times10^9$–$5\times10^{14})\ M_\odot$, and redshifts $0 \lesssim z \lesssim 10$:

$$F(b[z]) = \frac{(5.501b[z])^4}{1+(5.500b[z])^4} \ , \tag{22}$$

where $b(z)$ is the growth factor in Eq. (18) (normalized to 1 at $z = 0$). But as we have pointed out, $b(z)$ is a very slowly-growing function of z in the $R_h = ct$ universe, so the impact of such a correction factor is minimal at best. Since an actual numerical simulation analogous to Bolshoi has not yet been carried out for $R_h = ct$, one does not know yet whether the discrepancies seen for ΛCDM persist here. Perhaps the much weaker dependence of $b(z)$ on z mitigates the over-prediction seen for the standard model. For the purpose of this paper, given (1) that the results published in Ref. [5] (and reproduced in Fig. 1) are based on the Sheth–Tormen approximation without a correction factor, and (2) that the linear growth rate $b(z)$ changes very little with redshift in $R_h = ct$, thus making the correction factor $F(b)$ virtually ineffective, we will continue to use the Sheth–Tormen result in Eq. (21) without the possibly important modification introduced in Eq. (22). This issue will be revisited in future work once a full numerical simulation analogous to Bolshoi will have been carried out for $R_h = ct$.

In terms of the impact of this approach on the respective results in ΛCMD and $R_h = ct$ are concerned, one can see right away from Fig. 1 that reducing the Sheth–Tormen prediction for the number of halos at high mass only makes things worse compared to the data shown in this plot, since the standard model's prediction already falls well below the measurements. For $R_h = ct$, on the other hand, we shall see in Fig. 2 below that the theoretical prediction is very good for the lower masses, but misses progressively more and more towards the high-mass end. The deviation at a halo mass $\sim10^{13}\ M_\odot$ is a factor of 10–20, suggestively close to the over-prediction found in [53]. It will be interesting indeed to see in future work if a correction factor similar to that in Eq. (22) brings the results of $R_h = ct$ completely in line with the data at all masses.

An additional caveat with our assumptions in this paper is that simulations produce results that are not always consistent with each other when different 'halo finders' are used to identify the mass condensations. The recently performed Bolshoi calculations [53] indicate that Sheth–Tormen (used in our analysis) over-predicts the number of halos found in Bolshoi at $z = 8.8$ by a factor of 4–6 when the Spherical Over (SO) density halo finder algorithm is used, whereas Sheth–Tormen is actually consistent with the results based on the Friends of Friends (FOF) algorithm. Worse, the inferred number and mass distributions are inconsistent with each other in the simulation when the results of FOF are compared with those of SO. Bolshoi found that both algorithms identified the same distinct halos, but FOF assigned larger masses to some of them. On average, the masses of halos found with FOF was 1.4 times larger than those based on SO for the same halos. Masses obtained using FOF and SO tend to be consistent at lower redshifts, but deviate from each other at higher redshifts. Noting this as a potential problem to address in future, more elaborate treatments of the analysis we attempt here, we also acknowledge the fact that these inconsistencies are still small compared to other potential systematic issues entering our investigation, such as the poorly known star formation rate and galaxy evolution models used in the 'measurement' of the halo mass function. We will therefore proceed without attempting to address these issues here.

4. A cosmological resolution of the impossibly early galaxy problem

Before comparing the predicted halo mass function with the observations, we must recalibrate the data to take into account the differences in differential comoving volume between the two models. This is most easily done using the following expressions for the comoving distance:

$$D_{\rm com}^{\Lambda\rm CDM} = \frac{c}{H_0}\int_0^z \frac{du}{\sqrt{\Omega_{\rm m}(1+u)^3 + \Omega_{\rm r}(1+u)^4 + \Omega_\Lambda}} \ , \tag{23}$$

and

$$D_{\rm com}^{R_h=ct} = \frac{c}{H_0}\ln(1+z) \ . \tag{24}$$

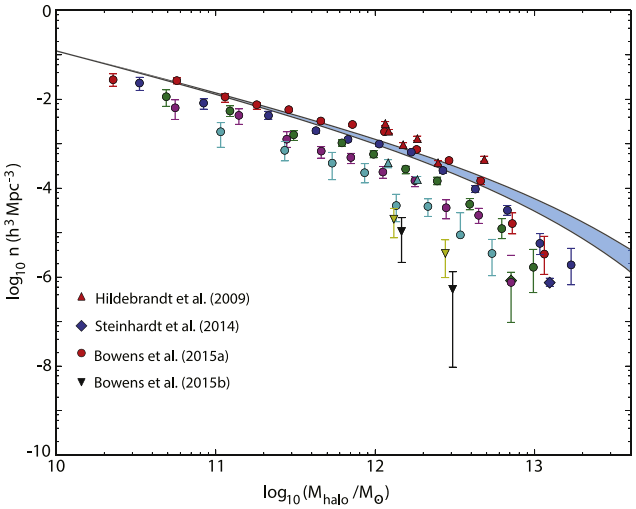

Fig. 2. Same as Fig. 1, except that the data have been recalibrated for the $R_h = ct$ universe using the ratio of differential comoving volumes in Eq. (24). The solid curves represent the halo mass function for $R_h = ct$ calculated from Eqs. (20) and (21), using a normalization $b\sigma_8(0) = 0.43$ and 0.37. These two values bracket the 1σ variation of the optimized fit to recently published redshift space distortion measurements of the cosmological growth rate [26], which produced the value $b\sigma_8(0) = 0.40 \pm 0.03$, with b the growth factor in Eq. (18). Given the very weak dependence of $\delta_k(z)$ on redshift (Eq. (16)), the halo mass function in this model is essentially independent of z in the range 4–10.

Note that here H_0 refers to the Hubble constant today. The conversion factor to recalibrate the data is then simply

$$\frac{dV_{\rm com}^{\Lambda{\rm CDM}}/dz}{dV_{\rm com}^{R_h=ct}/dz} = \left(\frac{D_{\rm com}^{\Lambda{\rm CDM}}}{D_{\rm com}^{R_h=ct}}\right)^2 \frac{dD_{\rm com}^{\Lambda{\rm CDM}}/dz}{dD_{\rm com}^{R_h=ct}/dz}\,. \tag{25}$$

The impact of this recalibration may be gauged via a comparison of the data plotted in Figs. 1 and 2. Within the redshift range $0 \lesssim z \lesssim 10$, the differential comoving volumes in $R_h = ct$ and ΛCDM differ by less than ∼10%. One sees similarly small shifts in n between these two plots.

A second factor one must take into account while calculating the halo distribution is the value of $\sigma_8(0)$, which is used to normalize the power spectrum. Based solely on fits to the linear growth rate at $z \lesssim 1$ [26], $b\sigma_8(0)$ in $R_h = ct$ is inferred to have the value 0.40 ± 0.03. The solid curves shown in Fig. 2 are calculated with the normalizations $b\sigma_8(0) = 0.37$ and 0.43, bracketing the 1σ variation of the best fit. The consistency between the halo mass function at $z \sim 4$–7 and the linear growth rate at $z \lesssim 1$ [26] should not be underestimated. The fact that these two quite different sets of measurements – the growth rate at $z \lesssim 1$ and the halo mass function at $z \sim 4$–7 – are mutually consistent with the expansion and growth rates predicted by $R_h = ct$ is a big factor in favour of this model.

Having said this, it is nonetheless also true that $R_h = ct$ overpredicts the number of halos towards the high mass end, as one can see from the right-hand side of Fig. 2. Several factors may be contributing to this: (1) As noted earlier, the Bolshoi simulation indicates that the Sheth–Tormen mass function overpredicts the number of halos at high mass and high redshift, at least in the context of ΛCDM. If an analogous result holds in $R_h = ct$, this might be the cleanest explanation for the theoretical overprediction seen in this figure. To be certain of this effect, however, we must await the completion of a full Bolshoi-like simulation with $R_h = ct$ as the background cosmology. (2) The number of halos inferred at high mass and high redshift may be incomplete due to observational selection effects and/or an incompleteness in the galaxy surveys. In this scenario, the apparent overprediction of halos at high mass and high redshift may get resolved with future observations. (3) As discussed above, the equations we have used in this paper to explore the linear growth rate of fluctuations may break down at $z \gtrsim 10$ due to the increasing role of radiation, which we have ignored until now. A more sophisticated analysis will be required at high redshifts to handle a more realistic growth rate calculation.

By comparison, the predicted halo mass function in ΛCDM misses the data everywhere on two counts: first, the shape of $n(M_{\rm halo})$ is not a good match to the observed distribution; ΛCDM predicts a steep function, in significant tension with the measurements at all redshifts. Second, ΛCDM predicts a strong evolution of the halo mass function with redshift, notably underpredicting the observed density at high redshifts by many orders of magnitude, while at the same time overpredicting their density at lower redshifts. Coupled to the standard model's inability to properly account for the observed flat linear growth rate at $z \lesssim 1$, our results in this paper suggest that the growth of structure in the standard model is inconsistent with the data, at least out to $z \sim 10$.

There are several caveats to this conclusion, however. First, the steepness of the function predicted by ΛCDM is largely due to the assumption of a constant light to mass ratio in the conversion of luminosity to mass. The same assumption does not adversely affect $R_h = ct$, but perhaps the tension with ΛCDM may be alleviated (at least partially) with a more complicated relation between light and mass that produces a shallower mass function. As we have discussed previously, ΛCDM does not directly predict this function, relying instead on theoretical adjustments to fit the data. It is more a question of whether these adjustments produce other signatures that may or may not be in tension with the observations. In other words, what we see in Fig. 1 is essentially a rescaling of the galaxy luminosity function, not a direct measurement of the halo mass function, and this rescaling relies on several pieces of poorly understood physics. Eventually, it will be necessary to carry out a comprehensive simulation that couples the cosmological halo evolution with the physics of galaxy formation in order for us to be more certain regarding the translation of galaxy data into a reliable halo mass function. A second caveat is that even in $R_h = ct$ the halo mass function deviates significantly from the predicted value for $z > 7$, as we have discussed above. The fact that both models show significant deviations at the high mass, high redshift end of the halo distribution may therefore be an indication that at least some of the tension with the data is related to the poorly known underlying physics, rather than it merely being an indication that the issue lies solely with the cosmology.

5. Conclusion

Some evidence suggests a disparity between the halo mass function predicted by ΛCDM and the actual measurements of this quantity. This work has been motivated by its lack of anticipated strong evolution in redshift and a significant steepening of the distribution with increasing mass. The observed halo mass function is relatively flat, pointing to a much higher density at the high-mass end, and a correspondingly lower density of halos with smaller masses. In addition, the halo distribution appears to be evolving much more slowly than is required by the standard model, at least for redshifts $z \lesssim 10$.

In earlier work, we used recently published redshift space distortion measurements of the cosmological growth rate, $b\sigma_8(z)$, at redshifts $z \lesssim 1$, to show that the linear evolution of perturbations in the $R_h = ct$ cosmology appears to be a better match to the data than the current standard model. In that work, we found an optimized growth rate $b\sigma_8(0) = 0.40 \pm 0.03$. Interestingly, the halo mass function in $R_h = ct$, normalized using this value, fits the measured halo distribution very well, certainly much better than ΛCDM does. Of course, one must still be wary of these results, given

that the halo masses cannot be measured directly. Nonetheless, since the various techniques used to translate the observed galaxy mass distribution into a halo mass function all agree qualitatively on the outcome, the mutual consistency between the halo fits at $z \sim 4$–10 and the linear growth rate fit at $z \lesssim 1$, suggests that the formation of structure predicted by $R_h = ct$ is a better fit to the observations than that expected in ΛCDM.

Although our focus in this paper has been exclusively on the formation and evolution of halos, the surprising nature of the halo mass function has also been characterized as a breakdown in the theory of galaxy formation at high redshifts. But this conclusion is actually not new. It has been known for several years that the observed high-z quasars and galaxies must have formed much too quickly when viewed with the timeline afforded them by the standard model [21,23,22]. For example, in order to understand the emergence of $\sim 10^9\ M_\odot$ black holes earlier than $z \sim 6$–7 in ΛCDM, one must assume that black-hole growth either began with anomalously large seeds ($M > 10^5\ M_\odot$), or proceeded at super-Eddington rates, neither of which has ever been seen—here locally, or at high redshifts. Yet in $R_h = ct$, the timeline is just right to have allowed these high-z objects to form according to well known and understood astrophysical principles.

Our analysis of the halo mass function in this paper constitutes another important confirmation of the expansion scenario predicted by the $R_h = ct$ cosmology. But there is much work yet to be done with the formation of structure in this model. Though $R_h = ct$ accounts for the observed halo distribution very well for masses $M \lesssim 10^{12}\ M_\odot$, its predictions deviate from the observations by one to two orders of magnitude at the highest mass end. Though this is still much less extreme than the situation one confronts in ΛCDM, this divergence suggests several possible explanations that need to be explored. These include (1) the linear growth rate seen at low redshifts in $R_h = ct$ may need modification at $z \gtrsim 10$. This would not be surprising, given that the current theory is based on the dominance of matter and dark energy in the cosmic fluid. But at high redshifts, the growing relevance of radiation cannot be ignored; and (2) The relations used to infer the halo masses from large galaxy surveys ought to be revisited. Attempts at mitigating the disparity between theory and observation in ΛCDM had very little impact. They may be more successful in the case of $R_h = ct$, since the current tension exists solely for $M \gtrsim 10^{12}\ M_\odot$. The halo mass function for masses lower than this agrees with theory very well.

Eventually, a complete study of galaxy formation and clustering in $R_h = ct$ needs to be carried out in concordance with the evolution of the halo mass function. Hopefully, this self-consistent approach will mitigate at least several of the uncertainties still hindering the interpretation of halo properties from the actual measurement of the galaxy luminosity function and spectrum. Currently, there is still too much freedom in combining various physical influences on galaxy evolution to arrive at a unique picture of structure formation at redshifts $z \lesssim 10$.

Acknowledgements

We are very grateful to the anonymous referee for suggesting several important improvements to the presentation of our results in this paper. FM is grateful to the Instituto de Astrofísica de Canarias in Tenerife and to Purple Mountain Observatory in Nanjing, China for their hospitality while part of this research was carried out. FM is also grateful for partial support to the Chinese Academy of Sciences Visiting Professorships for Senior International Scientists under grant 2012T1J0011, and to the Chinese State Administration of Foreign Experts Affairs under grant GDJ20120491013.

References

[1] R.K. Sheth, H.J. Mo, G. Tormen, Mon. Not. R. Astron. Soc. 323 (1) (2001) 1.
[2] V. Springel, S.D.M. White, A. Jenkins, et al., Nature 435 (2005) 629.
[3] M. Vogelsberger, S. Genel, V. Springel, et al., Mon. Not. R. Astron. Soc. 444 (2014) 1518.
[4] W. Press, P. Schechter, Astrophys. J. 187 (1974) 425.
[5] C.L. Steinhardt, P. Capak, D. Masters, J.S. Speagle, Astrophys. J. 824 (2016) 1.
[6] N.A. Grogin, D.D. Kocevski, S.M. Faber, et al., Astrophys. J. Suppl. 197 (2011) 35.
[7] A.M. Koekemoer, S. Faber, H. Ferguson, et al., Astrophys. J. Suppl. 197 (2011) 36.
[8] P. Capak, et al., Spitzer Proposal ID 13058 (2016sptz.prop13058C), 2016.
[9] H. Hildebrandt, J. Pielorz, T. Erben, et al., Astron. Astrophys. 498 (2009) 725.
[10] K.-S. Lee, H.C. Ferguson, T. Wiklind, et al., Astrophys. J. 752 (2012) 66.
[11] O. Ilbert, H.J. McCracken, O. Le Févre, et al., Astron. Astrophys. 556 (2013) A55.
[12] S.L. Finkelstein, M. Song, P. Behroozi, et al., Astrophys. J. 814 (2015) 95.
[13] K.I. Caputi, O. Ilbert, C. Laigle, et al., Astrophys. J. 810 (2015) 73.
[14] C.G. Lacey, C.M. Baugh, C.S. Frenk, A.J. Benson, Mon. Not. R. Astron. Soc. 412 (2011) 1828.
[15] K. Finlator, B.D. Oppenheimer, R. Davé, Mon. Not. R. Astron. Soc. 410 (2011) 1703.
[16] D. Waters, S.M. Wilkins, T. Di Matteo, Y. Feng, R. Croft, D. Nagai, Mon. Not. R. Astron. Soc. 461 (2016) L51.
[17] P.S. Behroozi, J. Silk, Astrophys. J. 799 (2015) id 32.
[18] N. Mashian, P.A. Oesch, A. Loeb, Mon. Not. R. Astron. Soc. 455 (2016) 2101.
[19] R.J. Bouwens, G.D. Illingworth, P.A. Oesch, et al., Astrophys. J. 803 (2015) 34.
[20] R.J. Bouwens, P.A. Oesch, I. Labbe, et al., Astrophys. J. 830 (2015) id 67.
[21] F. Melia, Astrophys. J. 764 (2013) 72.
[22] F. Melia, T.M. McClintock, Proc. R. Soc. Lond. Ser. A Math. Phys. Eng. Sci. 471 (2015) 20150449.
[23] F. Melia, Astron. J. 147 (2014) 120.
[24] A. Leauthaud, J. Tinker, K. Bundy, et al., Astrophys. J. 744 (2012) 159.
[25] Planck Collaboration, P.A.R. Ade, N. Aghanim, et al., Astron. Astrophys. 594 (2016) id A13.
[26] F. Melia, Mon. Not. R. Astron. Soc. 464 (2017) 1966.
[27] F. Melia, Mon. Not. R. Astron. Soc. 382 (2007) 1917.
[28] F. Melia, Front. Phys. 11 (2016) 118901.
[29] F. Melia, Front. Phys. 12 (2017) 129802.
[30] F. Melia, M. Abdelqader, IJMP-D 18 (2009) 1889.
[31] F. Melia, A. Shevchuk, Mon. Not. R. Astron. Soc. 419 (2012) 2579.
[32] S.G. Murray, C. Power, A.S.G. Robotham, A&C 3 (2013) 23.
[33] C. Conroy, J.E. Gunn, M. White, Astrophys. J. 699 (2009) 486.
[34] D. Schaerer, S. de Barros, Astron. Astrophys. 515 (2010) A73.
[35] D.P. Stark, M.A. Schenker, R. Ellis, B. Robertson, R. McLure, J. Dunlop, Astrophys. J. 763 (2013) 129.
[36] J.S. Speagle, C.L. Steinhardt, P.L. Capak, J.D. Silverman, Astrophys. J. 214 (2014) 15.
[37] H. Trac, R. Cen, P. Mansfield, Astrophys. J. 813 (2015) 54T.
[38] Ma Xiangcheng, Philip F. Hopkins, Shea Garrison-Kimmel, et al., arxiv: 170606605M, 2017.
[39] Mauro Stefanon, Rychard J. Bouwens, Ivo Labbé, Astrophys. J. 843 (2017) 36S.
[40] Daniel Ceverino, Simon C.O. Glover, Ralf S. Klessen, Mon. Not. R. Astron. Soc. 470 (2017) 2791C.
[41] Brian W. Oshea, John H. Wise, Hao Xu, et al., Astrophys. J. 807 (2015) 12O.
[42] S. Weinberg, Gravitation and Cosmology, Wiley, NY, 1972.
[43] L.D. Landau, E.M. Lifshitz, The Classical Theory of Fields, Pergamon Press, Oxford, 1975.
[44] P.J.E. Peebles, The Large-Scale Structure of the Universe, Princeton University Press, NY, 1980.
[45] P.J.E. Peebles, Principles of Physical Cosmology, Princeton University Press, NY, 1993.
[46] W.H. Press, E.T. Vishniac, Astrophys. J. 239 (1980) 1.
[47] E.W. Kolb, M. Turner, The Early Universe, Addison-Wesley, Reading MA, 1990.
[48] T. Padmanabhan, Structure Formation in the Universe, Cambridge University Press, Cambridge, England, 1993.
[49] P. Coles, F. Lucchin, Cosmology: The Origin and Evolution of Cosmic Structure, Wiley, NY, 1995.
[50] J.A. Peacock, Cosmological Physics, Cambridge University Press, Cambridge, England, 1999.
[51] A.R.D. Liddle, K.A. Lyth, Cosmological Inflation and Large-Scale Structure, Cambridge University Press, Cambridge, England, 2000.
[52] C.G. Tsagas, A. Challinor, R. Maartens, Phys. Rep. 465 (2008) 61.
[53] A.A. Klypin, S. Trujillo-Gomez, J. Primack, Astrophys. J. 740 (2011) 102.

CHAPTER-5

Structure Formation and Matter Power Spectrum in the R_h=ct Universe

Manoj K. Yennapureddy, Fulvio Melia

Submitted: Physical Review D

In the previous chapter, we have shown using linear perturbation theory the predicted halo mass function in the R_h=ct universe is consistent with observation for redshifts $z < 7$, but it overpredicts over one to two orders of magnitude at high redshifts. These might be due to the break down of the linear perturbation developed in the previous chapter at higher redshifts. In developing the linear perturbation theory in the previous chapter, we have assumed that dark energy is homogeneous and does not clump.

In this chapter, we develop the structure formation theory assuming that dark matter and dark energy interact and clump. Using the perturbation theory for interacting dark matter - dark energy models we obtain the matter power spectrum in the R_h=ct universe and show that it is consistent with the observations. Moreover, we show that the growth of structure in R_h=ct is simple, streamlined and does not require different handling of small modes compared to the larger ones. Whereas ΛCDM must rely on the unproven and as yet unverified physics of inflation to account for the generation of scale-invariant primordial fluctuations and a mechanism for driving the modes to exit and re-enter the horizon, thus creating an intricate mechanism for producing observed matter power spectrum.

Structure formation and the matter power-spectrum in the $R_{\rm h} = ct$ universe

M. K. Yennapureddy*

Department of Physics, The University of Arizona, AZ 85721, USA

F. Melia†

Department of Physics, The Applied Math Program,

and Department of Astronomy, The University of Arizona, AZ 85721, USA

Abstract

Inflationary ΛCDM is quite successful accounting for the observed matter power spectrum. Inflation drives quantum fluctuations beyond the Hubble horizon, freezing them out before they re-enter as classicalized perturbations at later times. Small-scale modes re-enter first,during the radiation dominated epoch and subsequently decay, while large-scale modes re-enter during the matter dominated epoch and grow. This distinction shapes the matter power spectrum, and provides observational evidence in support of the standard model. In this paper, we demonstrate that another mechanism, based on the fluctuation growth in the $R_{\rm h} = ct$ universe, itself an FLRW cosmology with the added constraint of zero active mass (i.e., $\rho + 3p = 0$), also accounts very well for the observed matter power spectrum, so this feature is not unique to ΛCDM. In $R_{\rm h} = ct$, mode growth varies according to fluctuation size in such a way as to shape the matter power spectrum consistently with the observations, but there is no complicated epoch dependence as one finds in ΛCDM.

PACS numbers: 04.20.Ex, 95.36.+x, 98.80.-k, 98.80.Jk

*Electronic address: manojy@email.arizona.edu

†John Woodruff Simpson Fellow; Electronic address: fmelia@email.arizona.edu

I. INTRODUCTION

Our current view of cosmic evolution holds that large-scale structure originated from primordial quantum fluctuations, believed to have been seeded by an inflationary field in the early Universe [1–6].According to this theory, quantum fluctuations classicalized and grew due to self-gravity to form the inhomogeneous Universe we see today. The existence of these inhomogeneities in the CMB and matter power spectrum [7–9] has become quite evident with the advent of high precision measurements. Moreover, the observation of galaxy rotation curves [10–12] and weak lensing measurements [13–17] have indicated a necessity for the existence of dark matter. Hence primordial fluctuations must include dark and baryonic matter, and radiation. Dark matter is assumed to be collisionless and non-interacting, so its fluctuations grew due to self-gravity only, without the suppression from radiation pressure. Once dark matter perturbations grew beyond a critical limit, they formed bound objects [18]. In contrast, baryons could not form bound objects in the early Universe because their growth was suppressed by the radiation to which they were coupled. As the baryons gradually decoupled from the radiation, however, they accreted into the potential wells created by dark matter to form the large-scale structure we see in the Universe today. This scenario—in which dark matter participated in the formation of structure in the early Universe—is indispensable to ΛCDM. Without the dark matter, structure formation would have been delayed by the baryon-radiation coupling, creating an inconsistency with the observations.

But the high precision data coming down the pipeline over the past decade have created a conflict with the timeline of structure formation in ΛCDM, even with the contribution due to dark matter. In particular, the discovery of SDSS010013.02+280225.8, an ultraluminous quasar at redshift $z = 6.3$ [19], has exacerbated the problem of supermassive black-hole growth and evolution in the early Universe [20]. Almost all of the 122 previously discovered quasars at redshifts $z \approx 6$ [21–37] have a black hole with mass $\sim 10^9\ M_\odot$, challenging the standard model's predicted timeline, which would have afforded them less than 900 Myr to grow after the big bang, but likely even less than ~ 500 Myr since the onset of Population II star formation. In the context of ΛCDM, the formation of Pop III stars might have occurred by redshift $z \approx 20$ [38–41], corresponding to a time of 200 Myrs. Then the subsequent transition to Pop II stars would have taken at least 100 Myrs because the gas expelled by the first generation stars had to cool and recollapse [42, 43]. These Pop II stars would have

acted as seeds for black holes. If the early black holes grew according to the Eddington rate, it would have taken at least 930 Myrs for them to reach their observed mass. The observed quasar at redshift $z = 6.3$, however, would have been 880 Myrs old in ΛCDM, which is not consistent with how these objects grew. Two possibilities have been proposed to reconcile this problem: 1) the black holes might have grown with highly anomalous accretion rates, but this phenomenon is not observed anywhere in the Universe; 2) Pop III stars might have formed earlier than expected, thus partially reconciling the problem. But this too doesn't appear to be reasonable, according to various simulations [44–55]. In addition, the structure formation timeline in ΛCDM predicts that at redshifts $z = 4 - 8$ most massive galaxies should have been transitioning from an initial halo assembly to baryonic evolution. But the recent Cosmic Assembly Near-infrared Deep Extragalactic Survey (CANDELS [56, 57]) and Spitzer Large Area Survey with Hyper-Suprime-Cam (SPLASH [58]) surveys have found that these massive halos formed much earlier than predicted by ΛCDM, giving to rise to what some have called 'The Impossibly Early Galaxy Problem' [59–61]. Attempts to reconcile this problem have indicated that a ~ 0.8 dex change is required in the halo to stellar mass ratio over this redshift range, though such a drastic change could come about only with a complete absence of dark matter at redshift 8 or with essentially 100% of the baryons condensing into stars at higher redshifts [59]. Both of these scenarios constitute implausible physics, such as the need to convert all of the baryons into stars instantly upon halo virialization (see [59] and references cited therein). Other attempted remedies, such as an evolution of the halo mass to light ratio, could reconcile the problem, but could only happen if the initial mass function were top-heavy. Studies have shown that the ratio of halo mass to light should remain the same, at least within the redshift range ($4 \leq z \leq 8$).

In this paper, we present the formation of structure in $R_{\rm h} = ct$ [62–67], an alternative Friedmann-Lemaître-Robertson-Walker (FLRW) cosmology with zero active mass [66, 67]. The linear expansion in this model afforded sufficient time for supermassive objects to form, thus solving the 'too early' appearance of massive quasars [20]. Even more importantly, we recently showed that the growth rate in this model accounts very well for the (otherwise too) early appearance of massive halos and galaxies [60, 61].

In § 2, we summarize the basis for the two cosmological models we consider here (i.e., ΛCDM and $R_{\rm h} = ct$). Then, in §§ 3–5, we shall derive the necessary mathematical formalism for the formation of structure in the $R_{\rm h} = ct$ universe, and describe the evolution of the

matter power spectrum in §§ 6–8. Our conclusions will be presented in § 9.

II. THE COSMOLOGICAL MODELS

A. Inflationary ΛCDM

The standard model contains dark energy, dark matter, radiation and baryons as the primary constituents. The existence of dark energy is inferred from the distance-redshift relation of Type Ia SNe [68–70], while the presence of dark matter is inferred from the galaxy rotation [10–12] and weak lensing [13–16] measurements, as noted earlier. Its current energy budget is dominated by dark energy ($\sim 70\%$; [71]), possibly in the form of a cosmological constant with an equation-of-state $w_{\rm de} \equiv p_{\rm de}/\rho_{\rm de} = -1$. The dark-matter component contributes an additional $\sim 27\%$ of the energy budget, and is primarily responsible for the formation and growth of large-scale structures. The rest of the energy density ($\sim 3\%$) is in the form of baryons, with a negligible contribution from radiation.

The early ΛCDM universe was radiation dominated, producing a phase of decelerated expansion, leading to the well-known temperature horizon problem. The standard model is therefore strongly dependent on an early inflationary expansion, lasting from 10^{-35} to 10^{-32} s, in order to mitigate such internal inconsistencies [1]. In more recent times, however, the principal benefit of inflation has been viewed as the mechanism it fosters for the creation and growth of quantum fluctuations [2–5] that might haved subsequently grown into large-scale inhomogeneities. As stated earlier, the currently held view is that the classicalised version of these quantum fluctuations produced large-scale structure. Although, the actual mechanism of classicalisation has remained elusive [6, 72–76], it is thought that primordial modes were driven beyond the Hubble horizon by inflation, frozen and turned into classical modes. They re-entered the horizon once the Hubble radius grew sufficiently. This exit and entry of modes across the horizon is quite critical, playing a vital role in producing the matter power spectrum that we shall describe in more detail in § 7.

B. The $R_{\rm h} = ct$ Universe

Our primary focus in this paper is to demonstrate how the $R_{\rm h} = ct$ universe also provides a mechanism for producing the observed matter power spectrum. This is an FLRW cosmology

constrained by the zero active mass condition, which results in an expansion with an apparent (or gravitational) radius always equal to ct [62–67, 77]. It too assumes the presence of dark energy, radiation and baryonic and dark matter. The primary difference between ΛCDM and $R_{\rm h} = ct$ is that the latter is constrained by the equation-of-state $\rho + 3p = 0$ [66, 67], where p is the total pressure and ρ is the total energy density. Numerous comparative tests examining which of the two models, ΛCDM or $R_{\rm h} = ct$, is favoured by the data have been carried out over the past decade. These include high-z quasars [65, 78–80, 82, 98], gamma ray bursts [83–85], cosmic chronometers [20, 82, 86, 87, 97], Type Ia SNe [64, 68–70, 88], Type Ic superluminous SNe [89, 90], and the age measurements of passively evolving galaxies [91–93], and strong gravitational lensing [81, 94, 95].

In all such one-on-one comparisons completed thus far, model selection tools show that the data favour $R_{\rm h} = ct$ over ΛCDM [20, 80, 85, 88, 90, 93, 96–98]. What is particularly attractive about this alternative FLRW cosmology is that it did not have an early decelerated or accelerated phase, so it has no horizon problem [96]. An inflationary phase is not needed in the $R_{\rm h} = ct$ universe, removing the need to find a self-consistent theory of inflation, which has thus far eluded us for over three decades. The early $R_{\rm h} = ct$ universe was dominated by dark energy and radiation, in the fractions $\sim 80\%$ and $\sim 20\%$ of the total energy density, respectively [99]. The late $R_{\rm h} = ct$ universe is dominated by dark energy and matter, comprising 2/3 and 1/3 of the energy density, respectively. In addition, since the ratio of horizon size to proper mode size always remains constant in the $R_{\rm h} = ct$ universe, modes never cross the horizon. Thus, the mechanism for generating the matter power spectrum in $R_{\rm h} = ct$ is completely different than that in ΛCDM.

III. PERTURBED EINSTEIN EQUATIONS IN FLRW

We begin by deriving the perturbed Einstein equations for an arbitrary FLRW metric and then use them in the $R_{\rm h} = ct$ universe to obtain the growth rate and power spectrum at various epochs. All the modes remain sub-horizon in $R_{\rm h} = ct$, but one has to use relativistic perturbation theory rather than Newtonian theory because the cosmic fluid in $R_{\rm h} = ct$ is always dominated by dark energy. We proceed by perturbing the general FLRW metric

[100–110], which we write in the form

$$ds^2 = a^2(\eta)\Big[-(1-\bar{h}_{00})\,d\eta^2 + 2\bar{h}_{0\alpha}\,d\eta\,dx^\alpha + (\delta_{\alpha\beta}+2\bar{h}_{\alpha\beta})\,dx^\alpha\,dx^\beta\Big]\,, \tag{1}$$

where $a(\eta)$ is the scale factor in terms of the conformal time η. The components of the tensor $\bar{h}$ are the perturbations to the homogeneous FLRW metric. The indices α and β run from 1 to 3. Using the conventional scalar-vector-tensor decomposition, we write $\bar{h}_{00}$, $\bar{h}_{0\alpha}$ and $\bar{h}_{\alpha\beta}$ as follows

$$\bar{h}_{00} = 2\Phi\,, \tag{2}$$

$$\bar{h}_{0\alpha} = w_\alpha = w_\alpha^\perp + \partial_\alpha\phi^\parallel\,, \tag{3}$$

and

$$\bar{h}_{\alpha\beta} = \Big[-\psi\delta_{\alpha\beta} + \Big(\nabla_\alpha U_\beta^\perp + \nabla_\beta U_\alpha^\perp\Big) + \Big(\nabla_\alpha\nabla_\beta - \frac{1}{3}\delta_{\alpha\beta}\nabla^2\Big)\Phi_1 + h_{\alpha\beta}^{\perp\perp}\Big]\,, \tag{4}$$

with $\psi = h^\alpha{}_\alpha$ and $h_\alpha^{\perp\perp\alpha} = 0$. All these metric perturbations are highly coordinate dependent, so one cannot automatically attribute any physical meaning to the perturbed components of the metric.

For infinitesimal coordinate transformations, such as $\bar{x}^i = x^i + \xi^i$, the decomposed perturbed metric components transform as follows

$$\bar{\Phi} = \Phi - \frac{1}{a}\frac{da}{d\eta}\xi^0\,, \tag{5}$$

$$\bar{\phi}^\parallel = \phi^\parallel + \xi^0 - \frac{d\xi}{d\eta}\,, \tag{6}$$

$$\bar{w}_\alpha^\perp = w_\alpha^\perp - \frac{d\xi_\alpha^\perp}{d\eta}\,, \tag{7}$$

$$\bar{\psi} = \psi + \frac{1}{a}\frac{da}{d\eta}\xi^0 + \frac{1}{3}\nabla^2\xi\,, \tag{8}$$

$$\bar{\Phi}_1 = \Phi_1 - \xi\,, \tag{9}$$

$$\bar{U}_\alpha^\perp = U_\alpha^\perp - \frac{1}{2}\xi_\alpha^\perp\,, \tag{10}$$

and

$$\bar{h}_{\alpha\beta}^{\perp\perp} = h_{\alpha\beta}^{\perp\perp}\,. \tag{11}$$

To use these perturbed components, one may either choose a particular observer (i.e., a particular set of coordinates), resort to a particular gauge, or work with Bardeen's four gauge independent variables [111]. It is evident from Equations (5)–(11) that there are

seven independent metric perturbations, implying seven degrees of freedom, but there are only four gauge-invariant variables. So when choosing a particular gauge, one must fix 3 degrees of freedom. In this work, we follow the first approach by choosing the Newtonian gauge and fix three independent metric perturbations as follows (with $\phi^{\parallel} = \Phi_1 = U_\alpha^\perp = 0$):

$$\Phi_A = \Phi + \frac{1}{a}\frac{\partial[a(\phi^{\parallel} - \frac{d\Phi_1}{d\eta})]}{\partial\eta} \,, \tag{12}$$

$$\Phi_H = \frac{1}{a}\frac{da}{d\eta}(\phi^{\parallel} - \frac{d\Phi_1}{d\eta}) - \psi - \frac{1}{3}\partial^\alpha\partial_\alpha\Phi_1 \,, \tag{13}$$

$$\psi_\alpha = w_\alpha^\perp - 2\frac{dU_\alpha^\perp}{d\eta} \,, \tag{14}$$

and

$$h_{\alpha\beta}^\perp = h_{\alpha\beta}^\perp \,. \tag{15}$$

After setting three metric perturbations to zero (in the Newtonian gauge), one ends up with

$$\Phi_A = \Phi \,, \tag{16}$$

$$\Phi_H = -\psi \,, \tag{17}$$

$$\psi_\alpha = w_\alpha^\perp \,, \tag{18}$$

and

$$\bar{h}_{\alpha\beta}^\perp = h_{\alpha\beta}^\perp \,. \tag{19}$$

It is quite evident from the above equations that, in the Newtonian gauge, the independent metric perturbations are in fact the Bardeen variables. This is the primary reason for choosing this gauge. Then the perturbed metric is given as

$$ds^2 = a^2(\eta)\Big[-(1+2\Phi)\,d\eta^2 + 2w_\alpha^\perp\,d\eta\,dx^\alpha + \left\{(1-2\psi)\delta_{\alpha\beta} + 2h_{\alpha\beta}^{\perp\perp}\right\}\,dx^\alpha\,dx^\beta\Big] \,. \tag{20}$$

It is well known that the vector perturbations die away as the Universe expands, and since our primary motivation in this paper is to compute the power spectrum and evolution of the perturbed dark-matter density field, we shall ignore both the vector and tensor perturbations for this work. The metric with only the scalar perturbations is then given as

$$ds^2 = a^2(\eta)\Big[-(1+2\Phi)\,d\eta^2 + (1-2\psi)\delta_{\alpha\beta}\,dx^\alpha\,dx^\beta\Big] \,, \tag{21}$$

which may be used to compute the Ricci tensor with the following components:

$$R_{00} = \nabla^2\Phi + 3\frac{d^2\psi}{d\eta^2} + 3\mathcal{H}\left[\frac{d\Phi}{d\eta} + \frac{d\psi}{d\eta}\right] - 3\frac{d\mathcal{H}}{d\eta} \ , \tag{22}$$

$$R_{0\alpha} = 2\partial_\alpha\frac{d\psi}{d\eta} + 2\mathcal{H}\partial_\alpha\Phi \ , \tag{23}$$

$$\begin{aligned} R_{\alpha\beta} \ = \ & \left[\frac{d\mathcal{H}}{d\eta} + 2\mathcal{H}^2 - \frac{d^2\psi}{d\eta^2} + \nabla^2\psi - 2\left(\frac{d\mathcal{H}}{d\eta} + 2\mathcal{H}^2\right)(\psi+\Phi)\right. \\ & \left. -\mathcal{H}\frac{d\Phi}{d\eta} - 5\mathcal{H}\frac{d\psi}{d\eta}\right]\delta_{\alpha\beta} + \partial_\alpha\partial_\beta(\psi+\Phi) \ , \end{aligned} \tag{24}$$

the Ricci scalar,

$$a^2\mathcal{R} = 6\left(\frac{d\mathcal{H}}{d\eta} + \mathcal{H}^2\right) - 2\nabla^2\Phi + 4\nabla^2\psi - 12\left(\frac{\mathcal{H}}{d\eta} + \mathcal{H}^2\right)\Phi - 6\frac{d^2\psi}{d\eta^2} - 6\mathcal{H}\left(\frac{d\Phi}{d\eta} + 3\frac{d^2\psi}{d\eta^2}\right) \ , \tag{25}$$

and also the Einstein tensor,

$$G_{00} = 3\mathcal{H}^2 + 2\nabla^2\psi - 6\mathcal{H}\frac{d\psi}{d\eta} \ , \tag{26}$$

$$G_{0\alpha} = 2\partial_\alpha\frac{d\psi}{d\eta} + 2\mathcal{H}\partial_\alpha\Phi \ , \tag{27}$$

$$\begin{aligned} G_{\alpha\beta} \ = \ & -\left(2\frac{d\mathcal{H}}{d\eta} + \mathcal{H}^2\right)\delta_{\alpha\beta} + \left[\nabla^2(\Phi-\psi) + 2\frac{d^2\psi}{d\eta^2} + 2\left(2\frac{d\mathcal{H}}{d\eta} + \mathcal{H}^2\right)(\psi+\Phi)\right. \\ & \left. +2\mathcal{H}\frac{d\Phi}{d\eta} + 4\mathcal{H}\frac{d\psi}{d\eta}\right]\delta_{\alpha\beta} + \partial_\alpha\partial_\beta(\psi+\Phi) \ . \end{aligned} \tag{28}$$

In these expressions, $\mathcal{H}$ is the Hubble parameter written as $\frac{a'}{a}$.

A. The Perturbed Stress-Energy Tensor

The perturbed stress-energy tensor for a perfect fluid may be written

$$T^a{}_b = (\rho + \delta\rho + p + \delta p)(u^a + \delta u^a)(u_b + \delta u_b) + (p + \delta p)\delta^a_b \ , \tag{29}$$

where ρ and $\delta\rho$ are the total, and perturbed, energy density of the Universe contributed by all the species, p and δp are the total, and perturbed, pressure contributed by all the species, and u_a and δu_a are the total, and perturbed, four-velocity. Then, using $g_{ab}\,u^a u^b = -1$, the perturbed velocity components are

$$\delta u^0 = -\frac{\Phi}{a} \ , \tag{30}$$

and

$$\delta u^{\alpha} = \frac{v^{\alpha}}{a} \ , \tag{31}$$

and we use the scalar-vector-decomposition to put $v_{\alpha} = \partial_{\alpha} v + v_{\alpha}^{\perp}$.

Working out the spatial components of Einstein's equation, i.e., $G_{\alpha\beta} = 8\pi\, G g_{\alpha c} T^{c}_{\beta}$, we get

$$\Bigg[\nabla^2(\Phi - \psi) + 2\frac{d^2\psi}{d\eta^2} + 2\bigg(2\frac{d\mathcal{H}}{d\eta} + \mathcal{H}^2\bigg)(\psi + \Phi) + 2\mathcal{H}\frac{d\Phi}{d\eta} + 4\mathcal{H}\frac{d\psi}{d\eta}\Bigg]\delta_{\alpha\beta}$$
$$+\partial_{\alpha}\partial_{\beta}(\psi + \Phi) = 8\pi G a^2 \Bigg[\delta p - 2\psi p\Bigg]\delta_{\alpha\beta} \ . \tag{32}$$

When $\alpha \neq \beta$, we get $\psi = -\Phi$, and using this condition for the rest of the components in Einstein's equation, we find that

$$2\frac{d^2\Phi}{d\eta^2} + 4\bigg(2\frac{d\mathcal{H}}{d\eta} + \mathcal{H}^2\bigg)\Phi + 6\mathcal{H}\frac{d\Phi}{d\eta} = 8\pi G a^2(\delta p - 2p\Phi) \ , \tag{33}$$

$$2\nabla^2\Phi - 6\mathcal{H}\frac{d\Phi}{d\eta} = 8\pi G a^2(\delta\rho + 2\rho\Phi) \ , \tag{34}$$

and

$$2\partial_{\alpha}\frac{d\Phi}{d\eta} + 2\mathcal{H}\partial_{\alpha}\Phi = 8\pi G a^2(\rho + p)v_{\alpha} \ , \tag{35}$$

where $v_{\alpha} = \partial_{\alpha} v + v_{\alpha}^{\perp}$.

Finally, using a wave decomposition with a Fourier series, defined for an arbitrary function as

$$F_k = \frac{1}{(2\pi)^3}\int F(x)\, e^{i\vec{k}\cdot\vec{x}}\, d^3x \ , \tag{36}$$

we get

$$k^2\Phi_k + 3\mathcal{H}\bigg(\frac{d\Phi_k}{d\eta} + \mathcal{H}\Phi_k\bigg) = 4\pi\, G a^2 \delta\rho_k \ . \tag{37}$$

$\delta\rho_k$ in the above equation comprises of the components which deviate from ideal cosmic fluid. In the case of ΛCDM $\delta\rho_k$ comprises of dark matter, baryons, neutrinos and radiation, whereas in the case of $R_h = ct$ Universe, this term comprises of dark matter, dark energy, baryons, neutrinos and radiation.

IV. THE PERTURBED BOLTZMANN EQUATIONS IN ΛCDM

Equation (37) describes the evolution of the perturbed gravitational potential Φ with a source term $\delta\rho$ driving its growth. To solve it, one must determine the evolution equation

for $\delta\rho$ as well. In principle $\delta\rho$ represents the total perturbed energy density of the universe, comprised of perturbations of individual species that clump above the smooth background. In this section, we shall obtain the evolution equations for individual species by perturbing their corresponding Boltzmann equations.

The Boltzmann equation for a given species (i.e., dark matter, baryons, radiation, etc.) describes the evolution of its distribution function in the 8-dimensional phase space with 4-dimensions representing the four space-time coordinates, x^i, and the other four comprising the 4-momentum, p^i. Using the additional constraint $g_{ij}p^ip^j = -m^2$, this 8-dimensional phase space is reduced to 7-dimensions. In this work, we choose the four spacetime coordinates, x^i, the magnitude of the 3-momentum, $p \equiv |\vec{p}|$, and its direction, $\hat{p}^\mu$, as the independent variables. From Liouville's theorem, one obtains the following equation for the evolution of the distribution function $f_s(x^i, p, \hat{p}^\mu)$ (for species 's'):

$$\frac{df_s}{d\lambda} = \frac{\partial f_s}{\partial x^0}\frac{\partial x^0}{\partial \lambda} + \frac{\partial f_s}{\partial x^\mu}\frac{\partial x^\mu}{\partial \lambda} + \frac{\partial f_s}{\partial p}\frac{\partial p}{\partial \lambda} + \frac{\partial f_s}{\partial \hat{p}^\mu}\frac{\partial \hat{p}^\mu}{\partial \lambda} = C[f_s] \ , \tag{38}$$

where λ and $C[f_s]$ are the affine parameter and the source/collision term for this species, respectively. We define $P^i = dx^i/d\lambda$, so that $dx^0/d\lambda = P^0$. Thus, dividing the above equation by P^0, and neglecting the fourth term that is of second order, one gets

$$\frac{df_s}{d\eta} = \frac{\partial f_s}{\partial \eta} + \frac{\partial f_s}{\partial x^\mu}\frac{P^\mu}{P^0} + \frac{\partial f_s}{\partial p}\frac{\partial p}{\partial \eta} = \frac{C[f_s]}{P^0} \ , \tag{39}$$

where η is the conformal time, in terms of the expansion factor $a(t)$ and cosmic time t. Using $P^\mu/P^0 = (p/E)\hat{p}^\mu$ (where E is the energy) and geodesic equation, we may write the above equation as follows:

$$\frac{dp}{d\eta} = -\mathcal{H}p + E\hat{p}^\mu\partial_\mu\frac{h_{00}}{2} - \frac{p}{2}\frac{dh_{\mu\nu}}{d\eta}\hat{p}^\mu\hat{p}^\nu \ , \tag{40}$$

where $h_{\mu\nu}$ are the perturbed metric coefficients. Then substituting Equation (40) into Equation (39), we get

$$\frac{df_s}{d\eta} + \frac{p\hat{p}^\mu}{E}\frac{\partial f_s}{\partial x^\mu} + p\bigg(-\mathcal{H} + \frac{E}{p}\hat{p}^\mu\partial_\mu\frac{h_{00}}{2} - \frac{1}{2}h'_{\mu\nu}\hat{p}^\mu\hat{p}^\nu\bigg)\frac{\partial f_s}{\partial p} = \frac{a}{E}(1-\Phi)C[f_s] \ . \tag{41}$$

In arriving at this equation, we have substituted $P_0 = \frac{E}{a}(1+\Phi)$, in terms of the perturbed gravitational potential, Φ.

Next, we partition the distribution function into its unperturbed, $\bar{f}_s$, and perturbed, $\mathcal{F}_s$, components:

$$f_s(\eta, x^i, p, \hat{p}^i) = \bar{f}_s(\eta, x^i, p, \hat{p}^i) + \mathcal{F}_s(\eta, x^i, p, \hat{p}^i) \ . \tag{42}$$

Thus, multiplying Equation (41) by the energy and integrating over momentum space, and collecting the zeroth-order terms, one gets

$$\int \frac{d^3p}{(2\pi)^3} E(p) \frac{d\bar{f}_s}{d\eta} - \int \frac{d^3p}{(2\pi)^3} \mathcal{H} p E(p) \frac{\partial \bar{f}_s}{\partial p} = \int \frac{d^3p}{(2\pi)^3} a C[f_s] \ . \tag{43}$$

In the context of ΛCDM, the quantity $C[f_s]$ is zero because the particle number is conserved during the phase of fluctuation growth. Therefore, integrating the second term on the left-hand side by parts and neglecting the boundary term, we arrive at the expression

$$\int \frac{d^3p}{(2\pi)^3} E(p) \frac{d\bar{f}_s}{d\eta} + 3\mathcal{H} \int \frac{d^3p}{(2\pi)^3} \left(E + \frac{p^2}{3E} \right) \bar{f}_s = 0 \ . \tag{44}$$

This equation may be reduced further by using the following definitions of density and pressure:

$$\rho_s = \int \frac{d^3p}{(2\pi)^3} E(p) \bar{f}_s \ , \tag{45}$$

and

$$\mathcal{P}_s = \int \frac{d^3p}{(2\pi)^3} \frac{p^2}{3E} \bar{f}_s \ . \tag{46}$$

If we now apply Equations (44-46) to the dark matter fluctuation, we arrive at the expression

$$\frac{d\rho_{\rm dm}}{d\eta} + 3\mathcal{H}(\rho_{\rm dm} + \mathcal{P}_{\rm dm}) = 0 \ . \tag{47}$$

We multiply Equation (41) by $E(p)$ and again integrate over momentum space using the definition of ρ and $\mathcal{P}$, but now collecting the first order terms:

$$\frac{d(\delta\rho_{\rm dm})}{d\eta} + (\rho_{\rm dm} + \mathcal{P}_{\rm dm}) \partial_\mu v^\mu_{\rm dm} + 3\mathcal{H}(\delta\rho_{\rm dm} + \delta\mathcal{P}_{\rm dm}) + 3(\rho_{\rm dm} + \mathcal{P}_{\rm dm}) \frac{d\Phi}{d\eta} = 0 \ . \tag{48}$$

We define $\delta_{\rm dm} \equiv \delta\rho_{\rm dm}/\rho_{\rm dm}$ and set both $\mathcal{P}_{\rm dm}$ and $\delta\mathcal{P}_{\rm dm}$ equal to zero. Then,

$$\frac{d\delta_{\rm dm}}{d\eta} = \frac{1}{\rho_{\rm dm}} \frac{d(\delta\rho_{\rm dm})}{d\eta} - \frac{\delta_{\rm dm}}{\rho_{\rm dm}} \frac{d\rho_{\rm dm}}{d\eta} \ . \tag{49}$$

Substituting this expression into Equation (48) and decomposing them into Fourier modes, we find that

$$\frac{d\delta_{{\rm dm},\,k}}{d\eta} = -k u_{dm,k} - 3\frac{d\Phi_k}{d\eta} \ . \tag{50}$$

In arriving at this equation, we have also used $\partial_\mu v^\mu_k = k u_{dm,k}$, where $u_{dm,k}$ is the velocity perturbation of dark matter.

Now, taking the second moment of Equation (41) by multiplying it with $p\hat{p}^\mu$ and contracting with $i\hat{k}_\mu$, and then integrating it over momentum, we get

$$\frac{d(\rho_{\rm dm} u_{{\rm dm},\,k})}{d\eta} + 4\mathcal{H}\rho_{\rm dm} u_{{\rm dm},\,k} + k\rho_{\rm dm}\Phi_k = 0 \ , \tag{51}$$

where $u_{\mathrm{dm},\,k}$ is the k^{th} velocity perturbation of dark matter. Again substituting for $d\rho_{\mathrm{dm}}/d\eta$ in this equation, we get

$$\frac{du_{\mathrm{dm},\,k}}{d\eta} = -\frac{1}{a}\frac{da}{d\eta}u_{\mathrm{dm},\,k} - k\Phi_k \ . \tag{52}$$

V. THE PERTURBED BOLTZMANN EQUATIONS IN $R_{\mathrm{h}} = ct$

The early $R_{\mathrm{h}} = ct$ universe consisted of $\approx 80\%$ dark energy and $\approx 20\%$ radiation, with a small contamination of matter [99]. At late times, these fractions change to $\approx 67\%$ dark energy and 33% matter. A coupling between dark matter and dark energy is therefore unavoidable in this model, since particle number is not conserved. The Boltzmann equations in this model will therefore be considerably different from those in ΛCDM. The pertinent equations were derived earlier in [61], but we summarize the procedure here for consistency and convenience.

Starting with Equation (41), an integration over momentum space yields

$$\int \frac{d^3p}{(2\pi)^3}E(p)\frac{d\bar{f}_s}{d\eta} + 3\mathcal{H}\int \frac{d^3p}{(2\pi)^3}\left(E + \frac{p^2}{3E}\right)\bar{f}_s = \int \frac{d^3p}{(2\pi)^3}aC[f_s] \ , \tag{53}$$

where the principal difference between this result and Equation (44) is that $C[f_s]$ on the righthand side is zero for ΛCDM, but not for $R_{\mathrm{h}} = ct$. The interaction term cannot be zero in the latter due to the coupling between dark energy and dark matter. Then, using the definition of density and pressure for dark matter (from Equations 45 and 46), one gets

$$\frac{d\rho_{\mathrm{dm}}}{d\eta} + 3\mathcal{H}\rho_{\mathrm{dm}} = \int \frac{d^3p}{(2\pi)^3}aC[f_{\mathrm{dm}}] \ . \tag{54}$$

The aforementioned transition in densities, e.g., $\rho_{\mathrm{de}} \approx 0.8\rho_{\mathrm{c}}$ after the Big Bang to $\approx 2\rho_{\mathrm{c}}/3$ more recently, and analogously for radiation and matter, may be modeled simply using a straightforward empirical expression,

$$\rho_{\mathrm{dm}} = (\rho_{\mathrm{c}}/3a^2)\exp\left[-\frac{a_*}{a}\frac{(1-a)}{(1-a_*)}\right] , \tag{55}$$

to reflect the fact that, in $R_{\mathrm{h}} = ct$, the Universe transitioned from a radiation/dark-energy dominated early phase to a matter/dark-energy dominated one at late times. In the above expression, ρ_{c} is the critical density today, and a_* represents the scale factor at matter radiation equality. Using this expression, one may easily evaluate the collision/source term,

$$C[\bar{f}_{\mathrm{dm}}] = \frac{\mathcal{H}E}{a}\bar{f}_{\mathrm{dm}} + \frac{\mathcal{H}E}{a^2}\bar{f}_{\mathrm{dm}}\left(\frac{a_*}{1-a_*}\right) , \tag{56}$$

which describes the interaction between dark energy and dark matter. A fraction of dark energy must be transformed (possibly via decay) into dark matter. Thus, the corresponding collision term for dark energy is

$$C[\bar{f}_{\rm de}] = -\frac{\mathcal{H}E}{a}\bar{f}_{\rm dm} - \frac{\mathcal{H}E}{a^2}\bar{f}_{\rm dm}\left(\frac{a_*}{1-a_*}\right) . \tag{57}$$

Returning now to Equation (41), with the use of Equation (56), we find for dark matter that

$$\frac{df_{\rm dm}}{d\eta}+\frac{p\hat{p}^\mu}{E}\frac{\partial f_{\rm dm}}{\partial x^\mu}+p\left(-\mathcal{H}+\frac{E}{p}\hat{p}^\mu\partial_\mu\frac{h_{00}}{2}-\frac{1}{2}h'_{\mu\nu}\hat{p}^\mu\hat{p}^\nu\right)\frac{\partial f_{\rm dm}}{\partial p} = \left[\mathcal{H}f_{\rm dm}+\frac{\mathcal{H}}{a}f_{\rm dm}\left(\frac{a_*}{1-a_*}\right)\right](1-\Phi) . \tag{58}$$

We take the first moment of this equation by multiplying it with $E(p)$ and integrating over momentum space. Collecting the first order terms yields

$$\frac{d(\delta\rho_{\rm dm})}{d\eta}+(\rho_{\rm dm}+\mathcal{P}_{\rm dm})\partial_\mu v^\mu_{\rm dm}+3\mathcal{H}(\delta\rho_{\rm dm}+\delta\mathcal{P}_{\rm dm})+3(\rho_{\rm dm}+\mathcal{P}_{\rm dm})\frac{d\Phi}{d\eta} = \left[\mathcal{H}+\frac{\mathcal{H}}{a}\left(\frac{a_*}{1-a_*}\right)\right](\delta\rho_{\rm dm}-\rho_{\rm dm}\Phi) . \tag{59}$$

We also have, from the definition of $\delta_{\rm dm}$ and $\mathcal{P}_{\rm dm} = \delta\mathcal{P}_{\rm dm} = 0$ for dark matter, that

$$\frac{d\delta_{\rm dm}}{d\eta} = \frac{1}{\rho_{\rm dm}}\frac{d(\delta\rho_{\rm dm})}{d\eta} - \frac{\delta_{\rm dm}}{\rho_{\rm dm}}\frac{d\rho_{\rm dm}}{d\eta} . \tag{60}$$

And substituting for $d(\delta\rho_{\rm dm})/d\eta$ in this equation, and isolating the Fourier mode k, we find that

$$\frac{d\delta_{{\rm dm},\,k}}{d\eta} = -ku_{dm,k} - 3\frac{d\Phi_k}{d\eta} - \mathcal{H}\left[1+\frac{a_*}{a(1-a_*)}\right]\Phi_k . \tag{61}$$

Then, taking the second moment of Equation (58) by multiplying it with $p\hat{p}^\mu$, contracting it with $i\hat{k}_\mu$, and integrating over momentum space, we find

$$\frac{d(\rho_{\rm dm}u_{{\rm dm},\,k})}{d\eta} + 4\mathcal{H}\rho_{\rm dm}u_{{\rm dm},\,k} + k\Phi_k\rho_{\rm dm} = \mathcal{H}\left[1+\frac{a_*}{a(1-a_*)}\right]\rho_{\rm dm}u_{{\rm dm},\,k} . \tag{62}$$

Substituting for $d\rho_{\rm dm}/d\eta$ we thus get

$$\frac{du_{{\rm dm},\,k}}{d\eta} = -\frac{1}{a}\frac{da}{d\eta}u_{{\rm dm},\,k} - k\Phi_k . \tag{63}$$

A similar procedure allows to derive the analogous equation for dark energy. Using the interaction term in Equation (57), we may write

$$\frac{df_{\rm de}}{d\eta}+\frac{p\hat{p}^\mu}{E}\frac{\partial f_{\rm de}}{\partial x^\mu}+p\left(-\mathcal{H}+\frac{E}{p}\hat{p}^\mu\partial_\mu\frac{h_{00}}{2}-\frac{1}{2}h'_{\mu\nu}\hat{p}^\mu\hat{p}^\nu\right)\frac{\partial f_{\rm de}}{\partial p} = -\mathcal{H}(1-\Phi)\left[1+\frac{a_*}{a(1-a_*)}\right]f_{\rm dm} , \tag{64}$$

where $f_{\rm de}$ is the distribution function for dark energy. Then, partitioning $f_{\rm de}$ into its unperturbed ($\bar{f_{de}}$) and perturbed ($\mathcal{F}_{de}$) components, we find

$$\frac{d\mathcal{F}_{\rm de}}{d\eta}+\frac{p\hat{p}^{\mu}}{E}\frac{\partial\mathcal{F}_{\rm de}}{\partial x^{\mu}}-\mathcal{H}p\frac{\partial\mathcal{F}_{\rm de}}{\partial p}+p\left(\frac{E}{p}\hat{p}^{\mu}\partial_{\mu}\frac{h_{00}}{2}-\frac{1}{2}h^{'}_{\mu\nu}\hat{p}^{\mu}\hat{p}^{\nu}\right)\frac{\partial\bar{f}_{\rm de}}{\partial p}=-\mathcal{H}\left[1+\frac{a_{*}}{a(1-a_{*})}\right]\left(\mathcal{F}_{\rm dm}-\Phi\bar{f}_{\rm dm}\right). \tag{65}$$

Taking the first momentum of this equation and isolating them into Fourier modes gives

$$\frac{d\delta\rho_{\rm de}}{d\eta}+\rho_{\rm de}(1+w_{\rm de})\partial_{\mu}v^{\mu}_{de}+3\mathcal{H}\delta\rho_{\rm de}\left(1+\frac{\delta\mathcal{P}_{\rm de}}{\delta\rho_{\rm de}}\right)+3\frac{d\Phi}{d\eta}\rho_{\rm de}(1+w_{\rm de})=-\mathcal{H}\left[1+\frac{a_{*}}{a(1-a_{*})}\right](-\rho_{\rm dm}\Phi+\delta\rho_{\rm dm}). \tag{66}$$

From the definition of $\delta_{\rm de}=\delta\rho_{\rm de}/\rho_{\rm de}$ and the inferred equation-of-state $\mathcal{P}_{\rm de}=-\rho_{\rm de}/2$ (Melia 2009) for dark energy, we may write

$$\frac{d\delta_{\rm de}}{d\eta}=\frac{1}{\rho_{\rm de}}\frac{d\delta\rho_{\rm de}}{d\eta}-\frac{\delta\rho_{\rm de}}{\rho^{2}_{\rm de}}\frac{d\rho_{\rm de}}{d\eta} \tag{67}$$

so that, combining Equations (66) and (67), we get

$$\frac{d\delta_{\rm de}}{d\eta}=-\frac{1}{2}\partial_{\mu}v^{\mu}_{de}-3\mathcal{H}\delta_{\rm de}\left(\frac{1}{2}+\frac{\delta\mathcal{P}_{\rm de}}{\delta\rho_{\rm de}}\right)-\frac{3}{2}\frac{d\Phi}{d\eta}+\mathcal{H}\left[1+\frac{a_{*}}{a(1-a_{*})}\right]\frac{\rho_{\rm dm}}{\rho_{\rm de}}(\delta_{\rm de}-\delta_{\rm dm}+\Phi). \tag{68}$$

We do not yet know the sound speed for the coupled dark matter/dark energy fluid, so we characterize it as follows:

$$c_{s}^{2}\equiv\frac{\delta\mathcal{P}}{\delta\rho}=\frac{\delta\mathcal{P}_{\rm de}}{\delta\rho_{\rm dm}+\delta\rho_{\rm de}}=\frac{\delta\mathcal{P}_{\rm de}/\delta\rho_{\rm de}}{(1+\delta\rho_{\rm dm}/\delta\rho_{\rm de})} \tag{69}$$

and, assuming adiabatic fluctuations, we shall put

$$\frac{\delta\mathcal{P}_{\rm de}}{\delta\rho_{\rm de}}=c_{s}^{2}\left[1+\frac{2\rho_{\rm dm}}{\rho_{\rm de}}\right]. \tag{70}$$

For the sake of simplicity, we assume the sound speed to be a constant limited to the range $0<(c_{s}/c)^{2}<1$. We have found that the actual value of this constant has a negligible impact on the solutions to the above equations since the ratio of dark matter density to dark energy is always much smaller than 1 in the $R_{\rm h}=ct$ universe, and we therefore adopt the simple fraction $c_{s}^{2}=c^{2}/2$ throughout this work. Thus, using Equations (68) and (70), we get

$$\frac{d\delta_{\rm de,k}}{d\eta}=-\frac{k}{2}u_{{\rm de},\,k}-\delta_{\rm de,k}\left(\frac{3\mathcal{H}}{2}+3\mathcal{H}c_{s}^{2}+\frac{6\mathcal{H}c_{s}^{2}\rho_{\rm dm}}{\rho_{\rm de}}\right)-\frac{3}{2}\frac{d\Phi_{k}}{d\eta}+\mathcal{H}\left[1+\frac{a_{*}}{a(1-a_{*})}\right]\frac{\rho_{\rm dm}}{\rho_{\rm de}}(\delta_{\rm de,k}-\delta_{\rm dm,k}+\Phi_{k}). \tag{71}$$

Finally, taking the second moment of Equation (65), we find that

$$\frac{du_{{\rm de},\,k}}{d\eta}=-\frac{5\mathcal{H}}{2}u_{{\rm de},\,k}-k\Phi_{k}+2kc_{s}^{2}\left[1+\frac{2\rho_{\rm dm}}{\rho_{\rm de}}\right]\delta_{\rm de,k}+\mathcal{H}\left[1+\frac{a_{*}}{a(1-a_{*})}\right]\frac{\rho_{\rm dm}}{\rho_{\rm de}}(u_{{\rm de},\,k}-2u_{{\rm dm},\,k}). \tag{72}$$

VI. THE OBSERVED MATTER POWER SPECTRUM

The matter power spectrum is obtained using several steps and a combination of data from the CMB, and the Ly-α forest, together with a model-dependent transfer function, that must be calculated individually for each cosmology. For the sake of clarity, we begin by summarizing these key factors in the process.

A. The Cosmic Microwave Background

First and foremost, all of the data are model dependent, and must be recalibrated when changing background cosmologies. For the concordance model parameter values, the CMB measurements are shown as blue, orange and black circular dots in Figure 3. The actual CMB observations are converted into a power spectrum using the approach of [112]. The CMB angular power for multipole ℓ may be written

$$C_\ell = \int_{-\infty}^{\infty} W_\ell(k) P_*(k)\, d\ln k \ , \tag{73}$$

where $W_\ell(k)$ is the transfer function that depends on the cosmic matter budget and the reionisation optical depth, and $P_*(k)$ is the primordial power spectrum, assumed for simplicity, to be $P_*(k) \propto k$. These CMB measurements are mapped into the k-space of the matter power spectrum using the approach of [112], the measured CMB data points d_i (in the case of CMB they are C_ℓ) are mapped into the probability distribution using the following equation

$$d_i = \int_{-\infty}^{\infty} \mathcal{P}_i(k) d\ln k \ , \tag{74}$$

where $\mathcal{P}_i$ is the probability distribution (see [112]), in Fig 3, the CMB data points are placed horizontally at the k-value corresponding to the median of this distribution, with a horizontal error bar ranging from the 20th to the 80th percentile of this distribution, representing a 1 σ range. They are then plotted at a vertical position given by

$$P_{\Lambda\rm CDM}(k) \simeq T^2_{\Lambda\rm CDM}(k_{\rm eff}) P_*(k) \ , \tag{75}$$

where $k_{\rm eff}$ is the horizontal location of the median of the window function and $T_{\Lambda\rm CDM}(k)$ is the matter transfer function in ΛCDM. In order to use these data for the $R_{\rm h} = ct$ universe, they must be recalibrated using the appropriate matter transfer function, according to the

expression

$$P_{R_{\rm h}=ct}(k) = P_{\Lambda{\rm CDM}}(k)\frac{T^2_{R_{\rm h}=ct}(k)}{T^2_{\Lambda{\rm CDM}}(k)} \ . \tag{76}$$

The CMB data points recalibrated for $R_{\rm h} = ct$ are shown (also as blue, orange and black circular dots) in Figure 6.

B. The Ly-α Forest

The Ly-α forest (red triangles in Figs. 3 and 6) is produced by absorption seen in high redshift quasar spectra, associated with neutral hydrogen present in a continuously fluctuating photo-ionized intergalactic medium. Simulations show that the underlying mass density is related to the optical depth of the Ly-α absorption, which allows the Ly-α forest to be used as a proxy for the matter power spectrum. The gas traced by Ly-α is modestly overdense compared to the cosmic mean, so if all the relevant physics can be simulated, one may construct the underlying matter power spectrum from the observed spectrum. The TreeSPH hydrodynamical simulation that simulates the observed Ly-α forest indicates that the optical depth τ is proportional to the density of neutral hydrogen, according to the expression

$$\tau(x) = A\rho_b(x)^\beta \ , \tag{77}$$

where x is the line of sight distance towards the quasar and A is the amplitude that depends on the cosmology and physical state of the gas. This amplitude A is obtained by matching the simulated and observed Ly-α forests. But given that the simulation depends on the assumed background cosmology, the value of A is itself model dependent. There are several caveats in obtaining the matter power spectrum from these data, however. In particular, the hydro-simulations with a dark matter only prescription may not have included all of the relevant physics, and it is not clear how the uncertainties in the reionisation history, the ionizing background and its fluctuations propagate into the reconstruction of $P(k)$. These data may therefore not be as reliable as the others for model selection purposes.

Nevertheless, we here attempt to overcome this model dependence as much as possible. The model dependence of the amplitude in the power spectrum arises from the process of matching the observed and simulated spectra. Thus, in order to properly compare the data with the predicted matter power spectrum in $R_{\rm h} = ct$, one must carry out similar

simulations with this model as the background cosmology. These simulations have not been performed yet, however, so we shall rely on a statistical argument to calibrate the matter power spectrum obtained from the Ly-α forest. The power spectrum obtained from the CMB and the Ly-α forest belong to the same sample, so one can use the t-test to examine whether the matter power spectrum obtained from the Ly-α forest through simulations is consistent with that obtained from the CMB. One may then also use the t-test to calibrate the matter power spectrum obtained from Ly-α by ensuring consistency with the spectrum obtained from CMB.

The matter power spectrum from the Ly-α forest may be calibrated using a two-step process. First, we optimize the polynomial function $f(k) = a_1 k^{-1} + b_1 k^{-2} + c_1 k^{-3} + D_1$, where a_1, b_1, c_1 and D_1 are constants, by minimizing the χ^2 in fitting the matter power spectrum from CMB. A second optimization procedure is followed using a polynomial $g(k) = a_2 k^{-1} + b_2 k^{-2} + c_2 k^{-3} + D_2$ to fit the matter power spectrum from Ly-α, yielding the constants a_2, b_2, c_2 and D_2 via χ^2 minimization. A relative calibration between these two is obtained by varying the normalization constant D_2 until the p-value obtained from the t-test lies above the 95% confidence level. Using this approach, we find that the p-values for ΛCDM and $R_{\rm h} = ct$ are, respectively, $\approx 99.8\%$ and $\approx 98.7\%$.

VII. THE MATTER POWER SPECTRUM IN ΛCDM

In ΛCDM, dark energy is a cosmological constant, contributing to the smooth background but not the fluctuations. Thus, $\delta\rho$ in Equation (37) is comprised primarily of matter, though radiation ($\delta\rho_\gamma$) may contribute as well. But in this paper, we follow convention and consider only dark matter growth, so the radiation does not condense into the fluctuations. Like dark energy, it contributes only to the smooth background. The equations describing the growth of dark matter fluctuations in ΛCDM may therefore be written (see Equations 37, 50 and 52)

$$\frac{d\Phi_k}{d\eta} = -\left(1 + \frac{k^2}{3\mathcal{H}^2}\right)\mathcal{H}\Phi_k + \frac{4\pi G a^2 \rho_{\rm m}}{3\mathcal{H}}\delta_{\rm m} \ , \tag{78}$$

$$\frac{d\delta_{{\rm dm},\,k}}{d\eta} = -k u_k - 3\frac{d\Phi_k}{d\eta} \ , \tag{79}$$

and

$$\frac{du_{{\rm dm},\,k}}{d\eta} = -\frac{1}{a}\frac{da}{d\eta}u_{{\rm dm},\,k} - k\Phi_k \ . \tag{80}$$

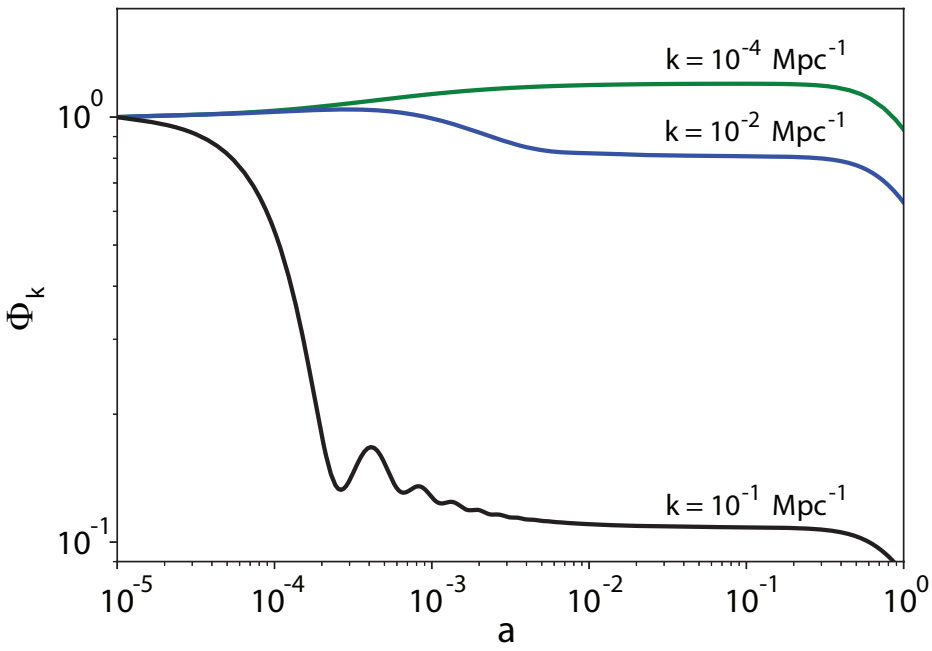

FIG. 1: Numerical solution of the perturbed potential, Φ, in ΛCDM, for modes $k = 10^{-4}$, 10^{-2} and 10^{-1} Mpc^{-1}.

Equation (82) describes the evolution of the gravitational potential. The second term on the right-hand side in this expression represents the self-gravity driving the fluctuation growth, while the first is due to the so-called Hubble friction that suppresses growth. Equations (83) and (84) describe the evolution of the matter fluctuations and their velocity. We solve these coupled first order differential equations starting with $\delta_m = \frac{3}{2}\Phi$ and $u = \frac{1}{2}k\eta\Phi$, following the initial conditions used in the Cosmological Initial Conditions and Microwave Anisotropy Codes (COSMICS [113]). As noted earlier, the expansion history in ΛCDM includes an exponential acceleration that drives the modes across the Hubble horizon. They then freeze and later re-enter as the Universe continues to expand. The small-scale modes re-enter during the radiation-dominated phase, while the large-scale modes re-enter when matter dominates. The modes re-enter across the Hubble horizon at different times, so the starting time when classical growth begins depends on their proper wavelength (or, equivalently, on their comoving wavenumber k). Hence we choose the initial (conformal) time at the beginning of the fluctuation growth to be $\eta = \min[10^{-3}k^{-1}, 10^{-1}h^{-1}Mpc]$ (see COSMICS [113]). The solution to these equations is plotted in Figures 1 and 2. Figure 1 shows

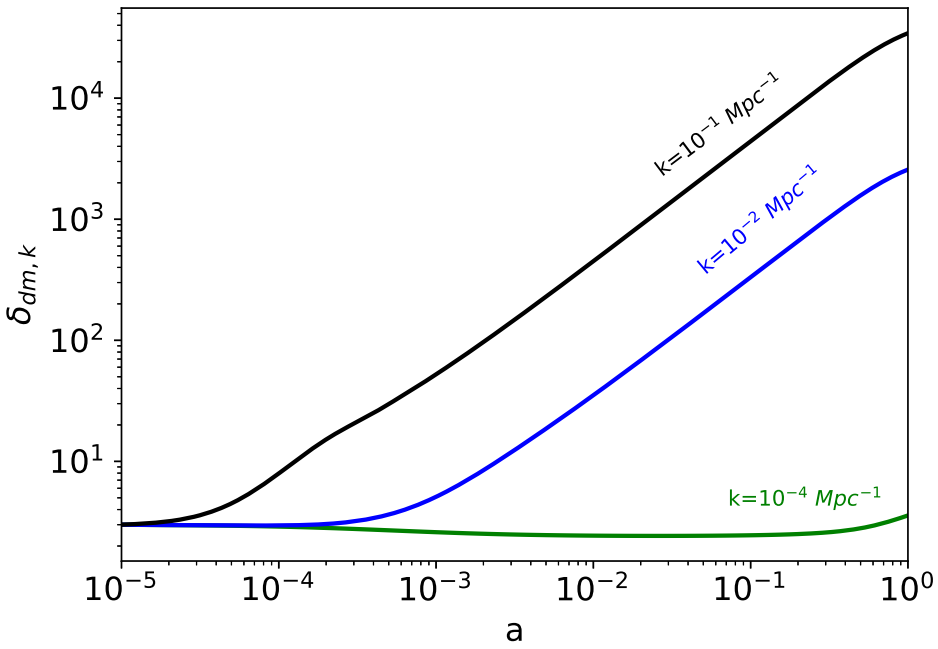

FIG. 2: Numerical solution of the matter fluctuation $\delta_{\mathrm{dm},k}$ in ΛCDM, for modes $k = 10^{-4}$, 10^{-2} and 10^{-1} Mpc^{-1}.

the evolution of the gravitational potential Φ_k, consistent with (1) that all the modes are frozen outside the horizon, (2) that the small-scale modes that re-enter the horizon during the radiation-domination expansion decay at first, and grow only when matter starts to dominate, and (3) that the large-scale modes remain frozen outside the horizon during the radiation-dominated phase, and re-enter when matter dominates and grow continuously thereafter.

Using the transfer function defined as $T(k,a) = \Phi_k(a)/\Phi_k(a_i)$ (see [114]), we then compute the matter power spectrum $P(k) = AP_*(k)T^2(k,a)$, in terms of the primordial power spectrum $P_*(k)$ generated by inflation, and the normalization factor A. The computed matter power spectrum is shown in Figure 3, along with the power spectrum observed in the CMB, and Ly-α. As noted earlier, the small-scale modes, $k \gtrsim 0.02$ Mpc^{-1}, re-enter the horizon during the radiation-dominated expansion and then decay, as one may see to the right in Figure 3. The large-scale modes, $k \lesssim 0.02$ Mpc^{-1}, re-enter the horizon when matter is dominant and then grow. To appreciate the behavior to the right of the peak in this plot, consider two typical modes k_1 and k_2 with $k_1 > k_2$. The first mode has a shorter wave-

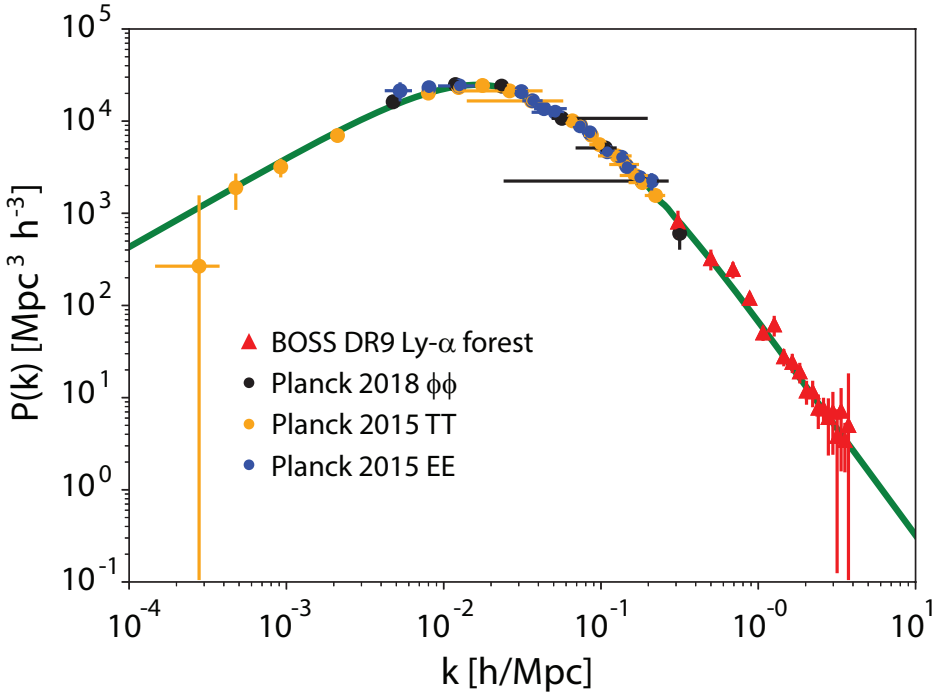

FIG. 3: The matter power spectrum observed in the CMB (orange, blue and black dots), and the Ly-α survey (red triangles), compared with the power spectrum predicted by ΛCDM (solid black curve), where h is the parameter $H_0/(100\ \mathrm{km\ s^{-1}\ Mpc^{-1}})$. Throughout this work, we assume the value $h = 0.6732$, consistent with the latest *Planck* measurements [71].

length and therefore re-enters before the second one. Mode k_1 thus suffers a greater decay due to the large Hubble friction. Hence mode k_1 has less power than mode k_2. Starting from the small modes and progressing towards the larger ones, the power increases until $k \approx 0.02\ \mathrm{Mpc}^{-1}$, which corresponds to the mode that re-enters the Hubble horizon exactly at matter-radiation equality. Modes with $k \lesssim 0.02\ \mathrm{Mpc}^{-1}$ don't decay and instead grow during the matter-dominant era. In principle, these modes should all have the same power if the primordial power spectrum is completely scale invariant, but Figure 3 indicates that the power declines as we progress towards even larger mode wavelengths, to the left of $k \approx 0.02$ Mpc^{-1}. This happens because the primordial power spectrum $P_* = Ak^{n_s}$ is not exactly scale invariant; it has a scalar spectral index $n_s = 0.967$. Clearly, the turning point in the power spectrum is highly sensitive to the energy content in the form of matter and radiation. Any adjustment to these quantities will alter the location of the matter-radiation equality and therefore change the shape of the matter power spectrum.

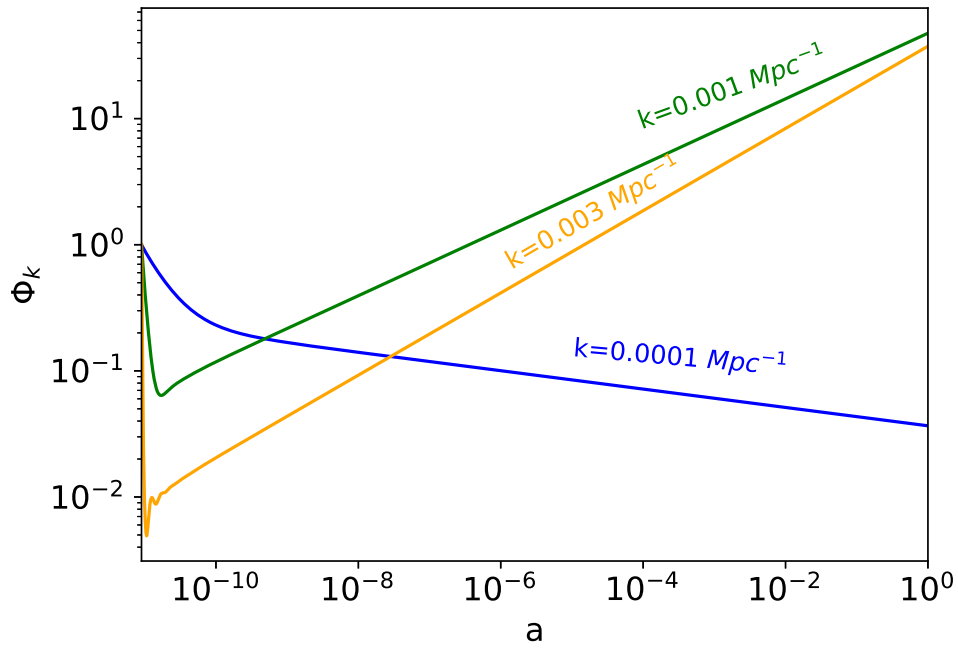

FIG. 4: Numerical solution of the perturbed potential Φ_k in $R_{\rm h} = ct$, for modes $k = 0.0001$, 0.003 and 0.001 Mpc^{-1}.

A. A Possible Failure of the Mechanism Generating the Matter Power Spectrum

The exit and re-entry of modes across the Hubble horizon are paramount for generating the observed matter power spectrum in ΛCDM. This mechanism, however, relies on the existence of an inflationary epoch. Should inflation eventually be disfavoured by the observations, ΛCDM would be unable to account for the observed matter power spectrum. It is worth mentioning in this regard that the angular correlation function measured by the Cosmic Background Explorer (COBE [115, 116]), *Wilkinson* Microwave Anisotropy Probe (WMAP [7, 8]) and particularly *Planck* [117], have indicated a rather strong tension with the prediction of ΛCDM. Slow-roll inflation predicts significant large-angle correlations in the CMB fluctuations which, however, are not seen by these instruments. Large-angle correlations are disfavoured by the data at a confidence level exceeding 8σ [118]. Cosmic variance could mitigate this problem only partially, so a resolution to this flaw in the model is still elusive. Should this failure persist, it would herald, not only an internal inconsistency of ΛCDM, but also its inability to account for the observed matter power spectrum.

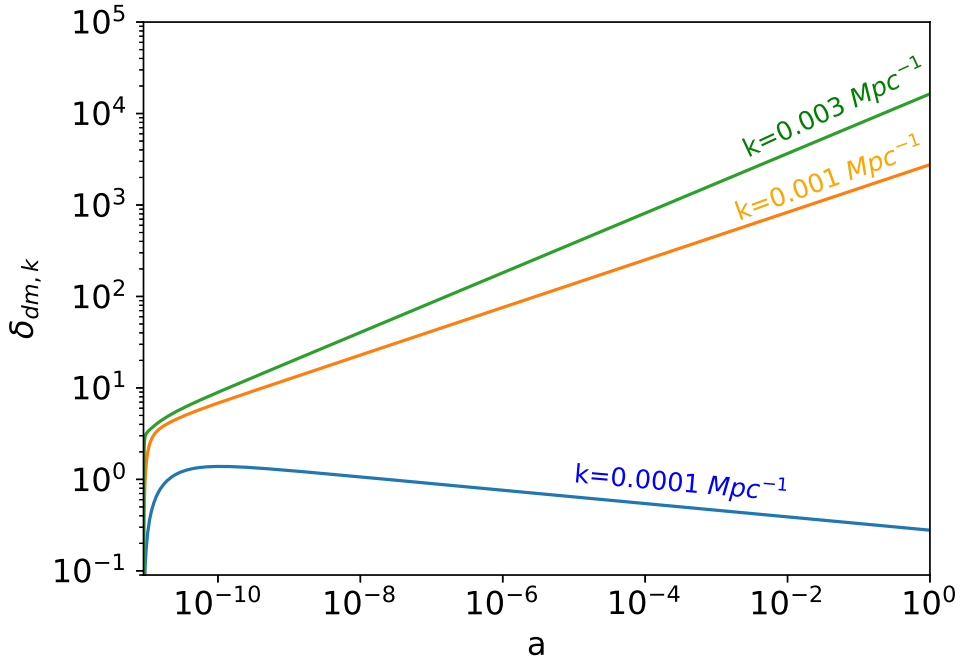

FIG. 5: Numerical solution of the perturbed $\delta_{dm,k}$ in $R_{\rm h} = ct$ for modes $k = 0.0001$, 0.003 and 0.001 Mpc^{-1}.

VIII. THE MATTER POWER SPECTRUM IN $R_{\rm h} = ct$

The fluctuations in $R_{\rm h} = ct$ involve coupled species. The density $\delta\rho$ in Equation (37) includes both dark energy and dark matter, i.e., $\delta\rho = \delta\rho_{\rm dm} + \delta\rho_{\rm de}$. Radiation and baryons are not directly coupled to dark matter, so we ignore their contribution in this paper. The relevant equations describing the growth of dark-matter fluctuations in $R_{\rm h} = ct$ may be derived as follows.

We convert the η derivatives in the coupled first-order differential Equations (37), (61), (63), (71) and (72) into derivatives with respect to the expansion factor a, and evolve them starting from $a_i = 10^{-12}$ to $a = 1$. The evolution of Φ_k over this range is shown in Figure 4 for several modes. This plot is to be compared with the corresponding potential growth for ΛCDM in Figure 1. The principal difference between these two evolutions may be understood via an inspection of Equation (37). After introducing the model dependence through $\mathcal{H}$, $\rho_{\rm dm}$ and $\rho_{\rm de}$ in $R_{\rm h} = ct$, this expression may be written

$$\frac{d\Phi_k}{da} = -\left(1 + \frac{k^2c^2}{3H_0^2}\right)\frac{\Phi_k}{a} + \frac{1}{2a}\left(\varpi(a)\delta_{\rm dm,k} + \Upsilon(a)\delta_{\rm de,k}\right), \tag{81}$$

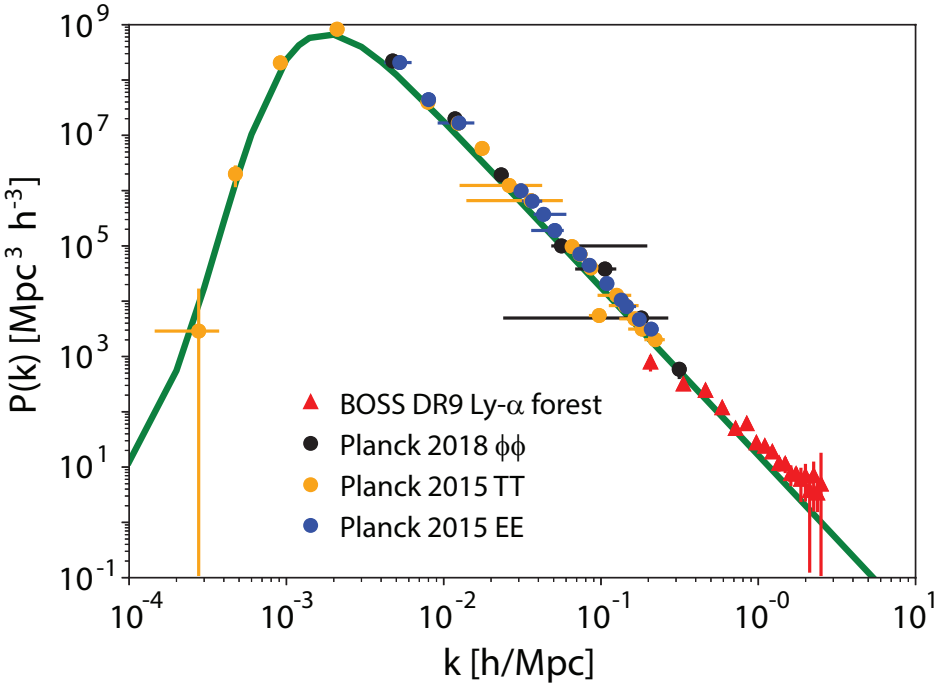

FIG. 6: The matter power spectrum observed in the CMB (orange, blue and black dots), and the Ly-α survey (red triangles), compared with the power spectrum predicted by $R_{\rm h} = ct$.

where $\varpi(a) = 0.3 \exp\left[-\frac{a_*}{a}\frac{(1-a)}{(1-a_*)}\right]$ and $\Upsilon(a) = 1 - \varpi(a)$. The corresponding expression in ΛCDM may be written

$$\frac{d\Phi_k}{da} = -\left(1 + \frac{k^2c^2}{3a^2H^2}\right)\frac{\Phi_k}{a} + \frac{3H_0^2}{2H^2a^2}\frac{\Omega_{\rm m}}{a^3}\delta_{\rm dm}\ , \tag{82}$$

where $H = H_0\sqrt{\Omega_{\rm m}a^{-3} + \Omega_{\rm r}a^{-4} + \Omega_\Lambda}$. The Hubble friction term k^2c^2/H_0^2 in $R_{\rm h} = ct$ may be written as $4\pi^2R_{\rm h}^2/\lambda^2$, where $R_{\rm h}$ is the Hubble horizon and λ is the proper wavelength of the mode. The primary difference between Equations (85) and (86) enters via the ratio $R_{\rm h}/\lambda$. This factor is constant throughout the history of the Universe in $R_{\rm h} = ct$ for each given mode, while it evolves as a function of $a(t)$ in ΛCDM for every mode.

The solution for $\delta_{dm,k}$ as a function of $a(t)$ in $R_{\rm h} = ct$ is shown in Figure 5, which is to be compared with Figure 2 for ΛCDM. The behavior of these solutions may be understood quite easily because the only 'forces' acting on the modes is the inward pull of gravity and the outwardly directed Hubble friction due to the expansion of the Universe. As one can see in Figure 4, the gravitational potential decays more rapidly for the smaller mode wavelengths, i.e., the larger k's. As a result, the growth rate of a mode varies according to its wavelength—the larger ones growing more slowly compared with the smaller ones. This

happens because the modes with larger wavelengths have a longer dynamical timescale and thus grow slowly in comparison with the shorter wavelength modes. The combination of different growth rates in $\delta_{dm,k}$ and the k-dependent decay rate of the potential produces a particular shape for the power spectrum. Together with the transfer function $T(k,a)$ for $R_{\rm h} = ct$, we compute the power spectrum $P(k)$ using $P(k) = k^{n_s} T^2(k,a)$, where $n_s = 0.967$, which is clearly a function of $a(t)$.

The computed power spectrum $P(k)$ in $R_{\rm h} = ct$ is shown in Figure 6, together with the data recalibrated for this cosmological model (see § 6 above). Above the peak, the mode decay rate increases with k. As before, let us compare the behaviour of two particular modes, k_1 and k_2, with k_1 less than 0.001 Mpc^{-1} and the second mode k_2 greater than k_1 and 0.001 Mpc^{-1}. The decay rate of Φ_{k_1} is smaller than that of Φ_{k_2} and the growth rate of k_1 is less than that of k_2, but mode k_2 did not have sufficient time to cross over k_1. This may be inferred by comparing Figures 4 and 5. Hence mode k_1 acquires more power than k_2. Now consider two modes k_3 and k_4, with k_3 less than $0.001 Mpc^{-1}$ and k_4 greater than k_3, though still less than $0.001 Mpc^{-1}$. As k_3 is smaller than k_4, Φ_{k_3} undergoes less decay than Φ_{k_4}, so the growth of k_3 is less than that of k_4, because the growth rate of k_4 exceeds that of k_3 and it had enough time to cross over. It ends up with more power than k_3. These effects all combine to produce the particular shape of the power spectrum seen in Figure 6, particularly the height and location of the peak.

An inspection of Figure 7 demonstrates another important difference between the matter power spectrum produced in $R_{\rm h} = ct$ versus its counterpart in ΛCDM. The location of its peak is time dependent. The qualitative shape of this distribution remains unchanged, but its turning point shifts as the Universe ages. The peak shifts slowly towards higher k with time. Its predicted location at $a(t_0) = 1$ (i.e., today) matches the data very well. When viewed at $a = 10$ (which in $R_{\rm h} = ct$ corresponds to a Universe ten times older than today), however, the peak will have shifted from its current k by a factor of almost 2. In contrast, the peak's location does not change as the ΛCDM Universe ages.

A second important factor to be noted in the case of $R_{\rm h} = ct$ is that the initial scale factor a_i for evolving the modes is arbitrary in this approach; it does not pertain to any particular epoch in the Universe's early expansion, such as the time at which the modes re-enter the horizon, which does not happen in this model. In reality, the initial value of $a(t)$ should correspond to the epoch at which the modes transitioned from the quantum realm to the

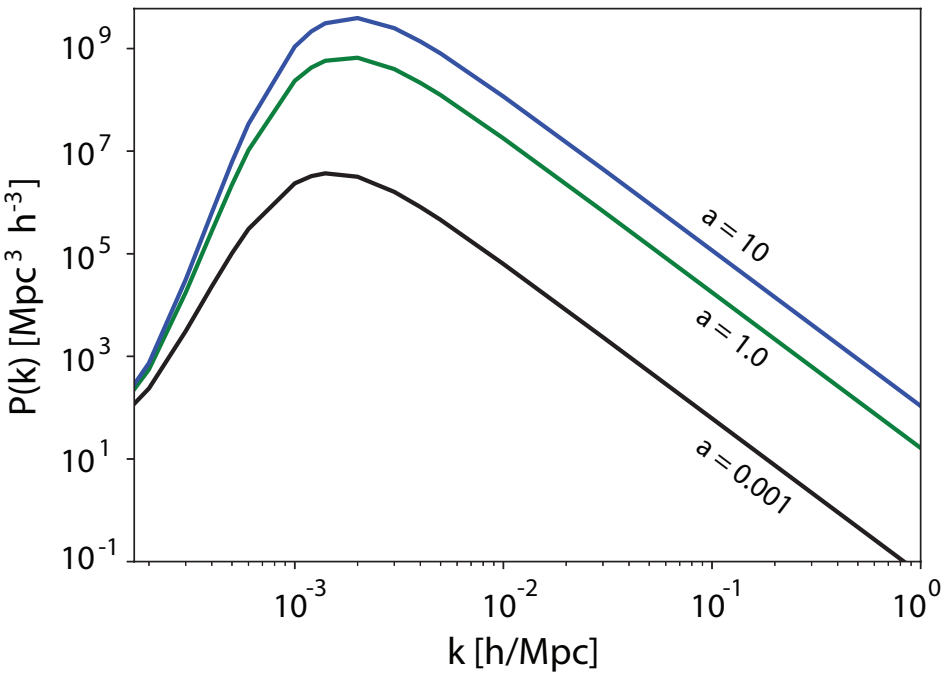

FIG. 7: The matter power spectrum in $R_{\rm h} = ct$ calculated at different values of the expansion factor, specifically $a = 10$, 1.0 and 0.001. Though the shape remains qualitatively the same, the peak of the distribution shifts slowly towards higher values of k as the Universe ages.

classical realm. But the 'classicalization' of these quantum fluctuations is still far from being completely understood. We have chosen the value $a_i = 10^{-12}$ to ensure that it does in fact lie beyond this transition. Of course, there is a wide range of possible values it could have this condition. To examine how sensitive our results are on the choice of a_i, we have therefore repeated the calculation varying the starting point, using $a_i = 10^{-14}$ and $a_i = 10^{-9}$. The results of this comparison are summarized in Figure 8. Though the amplitude does change with a_i, the shape is very minimally dependent on it. But the amplitude is normalized to obtain the measured σ_8 today, so this difference cannot be distinguished from one case to another. As one may see from this figure, the predicted result is not at all dependent on the choice of a_i. The principal physical reason behind this is that the transition from dark energy/radiation domination to dark energy/matter domination was optimized for $a_* = 10^{-9}$ in this work. The growth of the modes is therefore dominated by what takes place after this point. One may turn this approach around and view the 'fitting' of the power spectrum as a way to identify the transition point a_*.

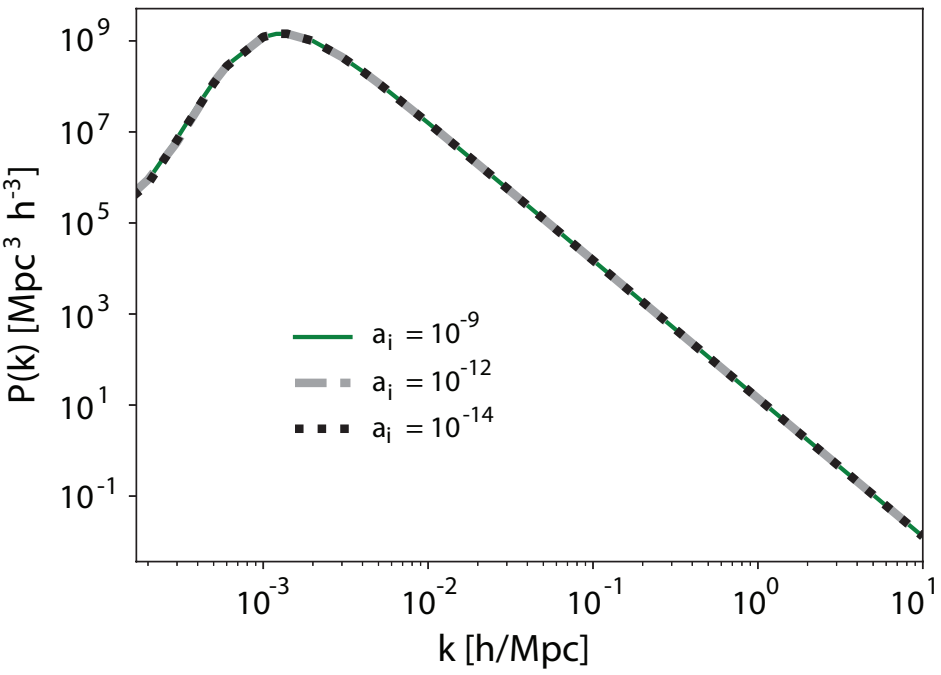

FIG. 8: A comparision of the computed matter power spectrum for different values of the starting point a_i in $R_{\rm h} = ct$.

IX. CONCLUSION

The mechanism responsible for the matter power spectrum in $R_{\rm h} = ct$ is quite different from that developed for ΛCDM, primarily because the fluctuations in this cosmology include a coupled dark matter–dark energy fluid. The formation of this spectrum in $R_{\rm h} = ct$ is quite simple, largely influenced by the strong dependence of the perturbed gravitational potential's (Φ_k) decay rate on the size of the modes: the smaller the scale size, the larger the decay rate. Coupled to the k dependence of the mode growth rate, this trend shapes the matter power spectrum, producing a distribution consistent with the observations.

It is important to stress that this mechanism does not require inflation at all, even to generate quantum fluctuations in the first place, since the presence of any scalar field at the Planck scale would suffice [119]. In contrast, the formation of the matter power spectrum in ΛCDM requires the modes to exit and re-enter the Hubble horizon at specific times in order to produce the necessary growth and decay rates as functions of k. The physics of inflation is still unknown, however, so this mechanism is arguably more speculative than

its counterpart in $R_{\rm h} = ct$. If the inflationary paradigm turns out to be correct, then the principal effect responsible for shaping the matter power spectrum is the k dependence of the time at which modes re-enter the horizon, with the smaller ones returning first, during the radiation-dominated epoch, and the larger ones re-entering later, when matter was dominant. The different growth rates during these epochs is the explanation for the peak and shape of the distribution. The fact that such a complicated process is not needed in $R_{\rm h} = ct$ is comforting to see, particularly since inflation is also not needed to solve the temperature horizon problem, which does not exist in this model.

This distinction is important in view of the growing tension between ΛCDM and the data in other areas. For example, with the discovery of the Higgs particle, the standard model is now facing a second major horizon problem, this time having to do with the electroweak phase transition [120]. While the inflationary (GUT) scale expansion may fix the temperature horizon problem, it cannot under any known circumstance fix the subsequent electroweak horizon inconsistency. Coupled to this, is the problem with the timeline in ΛCDM, which has significant difficulty accounting for the 'too early' appearance of massive halos and supermassive black holes. With its much simpler structure formation process, the $R_{\rm h} = ct$ universe is able to solve "the impossibly early galaxy problem" and the too early appearance of high-z quasars.

The fact that the cosmic fluid is dominated by dark energy throughout the Universe's history in $R_{\rm h} = ct$, comprising $\approx 80\%$ of ρ at early times and 2/3 of ρ towards the present, means that a coupling of dark matter and dark energy is unavoidable in this cosmology. But though these fractions are constrained quite tightly, the redshift at which this transition took place, gradual or otherwise, is not known. In this paper, we have optimized the fit to the matter power spectrum by treating the time at which this transition occurred as an adjustable parameter, reflected in the value of a_* in Equation (55). Eventually, higher precision high-z observations will be required to better constrain this process. Gamma-ray bursts (GRB) from Pop III stars [121–123] may provide such a diagnostic. In particular, the rate of gamma-ray bursts to be observed is strongly dependent on the growth rate, which itself depends on the transition redshift (from dark energy/radiation to dark energy/matter dominated epochs). The observation of GRB's by the James Webb Space Telescope (JWST) may prove to be critical to a proper comparison and evaluation of these two models.

Acknowledgements: We are grateful to Andreu Font-Ribera, David Weinberg and Arthur

Kosowsky for very informative discussions regarding the observed matter power spectrum from Ly-α, and the CMB. We are also thankful to Solèene Chabanier for sharing the matter power spectrum data with us. FM is grateful to the Institutode Astrofisica de Canarias in Tenerife and to Purple Mountain Observatory in Nanjing, China for their hospitality while part of this research was carried out.

---

[1] A. H. Guth, PhRvD **23**, 347 (1981).

[2] V. F. Mukahnov and G. V. Chibisov, JETP Lett **33**, 532 (1981).

[3] A. H. Guth and S.-Y. Pi, PhRvL **49**, 1110 (1982).

[4] S. W. Hawking, PLB **115B**, 295 (1982).

[5] A. A. Starobinsky, PLB **117B**, 175 (1982).

[6] V. F. Mukhanov, Physical Foundations of Cosmology, Cambridge University Press: Cambridge, England (2005).

[7] C. L. Bennett et al., ApJS **148**, 97 (2003).

[8] D. N. Spergel et al., ApJS **148**, 175 (2003).

[9] M. Tegmark et al., ApJ **606**, 702T (2004).

[10] F. Zwicky, ApJ **86**, 217 (1937).

[11] Y. Sofue et al., ApJ **523**, 136 (1999).

[12] P. Combes, NewAR **46**, 755 (2002).

[13] F. Hammer, P. Teyssandier, E. J. Shaya, I. M. Gioia and G. A. Luppino, ApJ **491**, 477 (1997).

[14] J.-P. Kneib, R. S. Ellis, I. Smail, W. Couch and R. M. Sharples, ApJ **471**, 643 (1997)

[15] I. M. Gioia, E. J. Shaya, O. Le Favre, E. E. Falco, G. Luppino and F. Hammer, ApJ **497**, 573 (1998).

[16] J. A. Tyson, G. P. Kochanski and I. P. Dell'Antonio, ApJL **498**, L107 (1998).

[17] F. Katherine, IJMPD **26**, 1730012 (2017)

[18] W. H. Press and P. Schechter, ApJ **187**, 425 (1974).

[19] X.-B. Wu et al., Nature **518**, 512 (2015).

[20] F. Melia and T. M. McClintock, AJ **150**, 119 (2015).

[21] X. Fan et al., Astron. J **125**, 1649 (2003)

[22] L. Jiang et al., Astron. J **134**, 1150 (2007).

[23] C. J. Williott et al., Astron. J **134**, 2435 (2007).

[24] L. Jiang et al., Astron. J **135**, 1057 (2008).

[25] C. J. Williott et al., Astron. J **139**, 906 (2010).

[26] D. J. Mortlock et al., Nature **474**, 616 (2011).

[27] E. Banados et al., Astron. J **148**, 14 (2014).

[28] E. Banados et al., ApJS **227**, 11 (2016).

[29] L. Jiang et al., ApJ **833**, 222 (2016).

[30] Y. Matsuoka et al., ApJ **828**, 26M (2016).

[31] C. Mazzucchelli et al., ApJ **849**, 91M (2017).

[32] J. J. Tang et al., MNRAS **466**, 4568 (2017).

[33] F. Wang et al., ApJ **839**, 27 (2017).

[34] B. Chehade et al., MNRAS **478**, 1649C (2018).

[35] Y. Matsuoka et al., PASJ **70**, 35M (2018).

[36] E. Pons, R. G. McMahon, R. A. Simcoe, M. Banerji, P. C. Hewett and S. L. Reed, MNRAS **484**, 4 (2019).

[37] Y. Shen et al., ApJ **873**, 1 (2019).

[38] Z. Haiman, A. A. Thoul and A. Loeb, ApJ **464**, 523 (1996).

[39] M. Tegmark et al., ApJ **474**, 1 (1997).

[40] T. Abel, G. L. Bryan and M. L. Norman, Science **295**, 93 (2002).

[41] V. Bromm, P. S. Coppi and R. B. Larson, ApJ **564**, 23 (2002).

[42] N. Yoshida, V. Bromm and L. Hernquist, ApJ **605**, 579 (2004).

[43] J. L. Johnson, T. H. Grief and V. Bromm, ApJ **665**, 85 (2007).

[44] E. Barkana and A. Loeb, Phys. Rep **349**, 125 (2001).

[45] J. Miralda-Escudé, Science **300**, 1904 (2003).

[46] V. Bromm and R. B. Larson, ARAA **42**, 79 (2004).

[47] B. Ciardi and A. Ferrara, Space Sci. Rev **116**, 625 (2005).

[48] S. Glover, Space Sci. Rev **117**, 445 (2005).

[49] T. H. Grief, J. L. Johnson, V. Bromm and R. S. Klessen, ApJ **670**, 1 (2007).

[50] J. H. Wise and T. Abel, ApJ **685**, 40 (2008).

[51] V. Bromnn, N. Yoshida, L. Hernquist and C. F. McKee, Nature **459**, 49 (2009).

[52] F. Salvaterra, A. Ferrara and P. Dayal, MNRAS **424**, 399 (2011).

[53] T. H. Grief et al., MNRAS **424**, 399 (2012).

[54] J. Jaacks, K. Nagamine and J.-H. Choi, MNRAS **427**, 403 (2012).

[55] N. Yoshida, T. Hosokawa and K. Omukai, Prog. Theor. Exp. Phys **01A**, 305 (2012).

[56] N. A. Gorgin et al., ApJS **197**, 35 (2011).

[57] A. M. Koekemoer et al., ApJS **197**, 36 (2011).

[58] P. Capak et al., in preparation (2016).

[59] C. L. Steinhardt, P. Capak, D. Masters and J. S. Speagle, ApJ **824**, 1 (2016).

[60] M. K. Yennapureddy and F. Melia, PDU **20**, 65 (2018).

[61] M. K. Yennapureddy and F. Melia, EPJ **79**, 571Y (2019).

[62] F. Melia, The Edge of Infinity: Supermassive Black Holes in the Universe, Cambridge University Press: Cambridge, UK (2003).

[63] F. Melia, MNRAS **382**, 1917 (2007).

[64] F. Melia, AJ **144**, 110 (2012).

[65] F. Melia, ApJ **764**, 72 (2013).

[66] F. Melia, Frontiers of Physics **11**, 119801 (2016).

[67] F. Melia, Frontiers of Physics **12**, 129802 (2016).

[68] S. Perlmutter et al., Nature **391**, 51 (1998).

[69] A. G. Riess et al., AJ **116**, 1009 (1998).

[70] B. P. Schmidt et al., ApJ **507**, 46 (1998).

[71] Planck Collaboration, A&A **594**, A13 (2016).

[72] R. Penrose, The Road to Reality, Vintage Books: USA (2004).

[73] A. Perez, H. Sahlmann and D. Sudarsky, CQG **23**, 2317 (2006).

[74] S. Weinberg, Cosmology, Oxford University Press: USA (2008).

[75] D. H. Lyth and A. R. Liddle, The Primordial Density Perturbation, Cambridge University Press: Cambridge, UK (2009).

[76] G. R. Bengochea, P. Canate and D. Sudarsky, PLB **743**, 484 (2015).

[77] F. Melia and M. Abdelqader, IJMPD **18**, 1889 (2009).

[78] G. Kauffmann and M. Haehnelt, MNRAS **311**, 576 (2000).

[79] J. S. B. Wyithe and A. Loeb, ApJ **595**, 614 (2003).

[80] F. Melia, JCAP **1**, 027 (2014).

[81] F. Melia, J.-J. Wei and X. Wu, AJ **149**, 2 (2015).

[82] F. Melia and M. K. Yennapureddy, JCAP **02**, 034M (2018).

[83] Z. G. Dai, E. W. Liang and D. Xu, ApJ **612**, L101 (2004).

[84] G. Ghirlanda, G. Ghisellini, D. Lazzati and C. Firmani, ApJ **613**, L13 (2004).

[85] J.-J. Wei, X.-F. Wu and F. Melia, ApJ **772**, 43 (2013).

[86] R. Jimenez and A. Loeb, ApJ **573**, 37 (2002).

[87] J. Simon, L. Verde and R. Jimenez, PhRvD **71**, 123001 (2005).

[88] J.-J. Wei, X.-F. Wu, F. Melia and R. S. Maier, AJ **149**, 102 (2015).

[89] C. Inserra and S. J. Smartt, ApJ **796**, 87 (2014).

[90] J.-J. Wei, X.-F. Wu and F. Melia, AJ **149**, 165 (2015).

[91] J. S. Alcaniz and J. A. S. Lima, ApJ **521**, 87 (1999).

[92] J. A. S. Lima and J. S. Alcaniz, MNRAS **317**, 893 (2000).

[93] J.-J. Wei, X.-F. Wu, F. Melia, F.-Y. Wang and H. Yu, AJ **150**, 35 (2015).

[94] M. K. Yennapureddy and F. Melia, EPJC **78**, 258 (2018).

[95] K. Leaf and F. Melia, MNRAS **474**, 4507 (2018).

[96] F. Melia, A&A **553**, 76 (2013).

[97] F. Melia and R. S. Maier, MNRAS **432**, 2669 (2013).

[98] F. Melia and T. M. McClintock, Proc. R. Soc. A **471**, 20150449 (2015).

[99] F. Melia and M. Fatuzzo, MNRAS **456**, 3422 (2016).

[100] S. Weinberg, Gravitation and Cosmology, Wiley: NY (1972)

[101] L. D. Landau and E. M. Lifshitz, The Classical Theory of Fields, Pergamon Press: Oxford (1975).

[102] P. J. E. Peebles, The Large-scale Structure of the Universe, Princeton University Press: NY (1980)

[103] W. H. Press and E. T. Vishniac, ApJ **239**, 1 (1980).

[104] E. W. Kolb and M. Turner, The Early universe, Addison-Wesley: Reading MA (1990)

[105] T. Padmanabhan, Structure Formation in the Universe, Cambridge University Press: Cambridge, England (1993).

[106] P. J .E Peebles, Principles of Physical Cosmology, Princeton University Press: NY (1993).

[107] P. Coles and F. Lucchin, Cosmology: The Origin and Evolution of Cosmic Structure,Wiley: N (1995).

[108] J. A. Peacock, Cosmological Physics, Cambridge University Press: Cambridge, England (1999).

[109] A. R. D. Liddle and K. A. Lyth, Cosmological Inflation and Large-Scale Structure, Cambridge University Press: Cambridge, England (2000).

[110] C. G. Tsagas, A. Challinor and R. Maartens, Phys. Reports **465**, 61 (2008).

[111] J. M. Bardeen, PhyRvD **22**, 1882B (1980).

[112] M. Tegmark and M. Zaldarriaga, PhRvD **66**, 3508 (2002).

[113] E. Bertschinger, arXiv:astro-ph/9506070 (1995).

[114] S. Dodelson, Modern Cosmology, Academic Press: Amsterdam, Netherlands (2003)

[115] E. L. Wright et al., ApJL **464**, L21 (1996).

[116] G. Hinshaw et al., ApJL **464**, L25 (1996).

[117] Planck Collaboration., A&A **571**, A12 (2014).

[118] F. Melia and M. López-Corredoira, A&A **610**, A87 (2018).

[119] F. Melia, CQGra **34**, 5011M (2017).

[120] F. Melia, EPJ-C **78**, 739 (2018).

[121] V. Bromm and A. Loeb, AIPC **937**, 532B (2007).

[122] V. Bromm and A. Loeb, ApJ **642**, 382B (2006).

[123] V. Bromm and A. Loeb, AIPC **836**, 503B (2006).

CHAPTER-6

A comparison of the R_h = ct and ΛCDM cosmologies based on the observed halo mass function

Manoj K. Yennapureddy, Fulvio Melia

Published In: European Physics Journal C
DOI: 10.1140/epjc/s10052-019-7082-z

In chapter-4, we have shown the predicted halo mass function in Rh=ct universe is consistent with the observations, but it overpredicts the number of halos by one to two orders of magnitude at redshifts z > 7. As mentioned in chapter 5, this might be due to the breakdown of the linear perturbation theory at higher redshifts which was developed assuming that dark energy is homogeneous and does not clump.

In chapter 5, we have described the formation of structures in Rh=ct universe using the interacting dark matter - dark energy model and showed that the predicted matter power spectrum is consistent with observations.

In this chapter, we predict the halo mass function in Rh=ct universe using the growth equations obtained in chapter -5 and show that the predicted halo mass function is consistent with the data throughout the range 10 > z > 4 very well at the low and intermediate mass end, and overpredicts by one to two orders of magnitude at the high mass end.

Eur. Phys. J. C (2019) 79:571
https://doi.org/10.1140/epjc/s10052-019-7082-z

THE EUROPEAN PHYSICAL JOURNAL C

Regular Article - Theoretical Physics

A comparison of the $R_h = ct$ and ΛCDM cosmologies based on the observed halo mass function

Manoj K. Yennapureddy[1,a], **Fulvio Melia**[2,3,b]

[1] Department of Physics, The University of Arizona, Tucson, AZ 85721, USA
[2] The Applied Math Program, Department of Physics, The University of Arizona, Tucson, AZ 85721, USA
[3] Department of Astronomy, The University of Arizona, Tucson, AZ 85721, USA

Received: 5 June 2019 / Accepted: 27 June 2019 / Published online: 8 July 2019

Abstract The growth of structure may be traced via the redshift-dependent halo mass function. This quantity probes the re-ionization history and quasar abundance in the Universe, constituting an important probe of the cosmological predictions. Halos are not directly observable, however, so their mass and evolution must be inferred indirectly. The most common approach is to presume a relationship with galaxies and halos. Studies based on the assumption of a constant halo to stellar mass ratio M_h/M_* (extrapolated from $z \lesssim 4$) reveal significant tension with ΛCDM – a failure known as "The Impossibly Early Galaxy Problem". But whether this ratio evolves or remains constant through redshift $4 \lesssim z \lesssim 10$ is still being debated. To eliminate the tension with ΛCDM, it would have to change by about 0.8 dex over this range, an issue that may be settled by upcoming observations with the James Webb Space Telescope. In this paper, we explore the possibility that this major inconsistency may instead be an indication that the cosmological model is not completely correct. We study this problem in the context of another Friedmann–Lemaître–Robertson–Walker (FLRW) model known as the $R_h = ct$ universe, and use our previous measurement of σ_8 from the cosmological growth rate, together with new solutions to the Einstein–Boltzmann equations, to interpret these recent halo measurements. We demonstrate that the predicted mass and redshift dependence of the halo distribution in $R_h = ct$ is consistent with the data, even assuming a constant M_h/M_* throughout the observed redshift range ($4 \lesssim z \lesssim 10$), contrasting sharply with the tension in ΛCDM. We conclude that – if M_h/M_* turns out to be constant – the massive galaxies and their halos must have formed earlier than is possible in ΛCDM.

1 Introduction

The central principle behind the theory of structure formation is that large-scale assemblies, such as galaxies and clusters, formed via the growth of gravitational instabilities in the primordial density field, comprised of dark matter, radiation and baryonic matter. By assumption, dark matter is weakly interacting, so it decoupled from the radiation quite early and its fluctuations grew gravitationally to form the halos. Baryonic matter subsequently accreted into these potential wells once it also decoupled from the radiation, forming bound objects that would become stars and galaxies. Although this latter process is not yet fully understood, there is better consensus concerning the halo evolution itself, codified through the so-called halo mass function [1–3]. As it turns out, the halo mass function is highly sensitive to the cosmological parameters in ΛCDM, including the mass fraction $\Omega_{\rm m}$, the dark energy equation of state parameter $w_{\rm de}$, and σ_8 [4] – at least at lower redshifts (i.e., $z \lesssim 2$), where it plays a vital role in constraining standard cosmology. At higher redshifts, the halo mass function plays a vital role in probing the re-ionization history of the Universe [5] and the quasar abundance and formation sites [6]. It goes without saying that constraining and evaluating the halo mass function is therefore critical to the evaluation of structure formation in the Universe.

The standard model predicts a rapid evolution in the number density of massive halos throughout the redshift range $10 \gtrsim z \gtrsim 4$. If a strong connection exists between the halos and galaxies they host, one should expect to see a comparably rapid evolution in the number density of galaxies via their luminosity and mass distributions, implying that one should see in ΛCDM a sharp decline in the number density of luminous galaxies at constant luminosity, or a rapid decrease in luminosity for a fixed number density, towards high redshifts. Although the halo mass function has been evaluated using numerical and N-body simulations at high

F. Melia: John Woodruff Simpson Fellow.

[a] e-mail: manojy@email.arizona.edu
[b] e-mail: fmelia@email.arizona.edu

redshifts, only recently has it been tested observationally. The halos themselves are not directly observable, so they must be probed indirectly, e.g., through the measured galaxy mass distribution assuming a close relationship between the two.

Data gathered recently with the Cosmic Assembly Near-Infrared Deep Extragalactic Survey (CANDELS; [7]), and the Spitzer Large Area Surveys (SPLASH; [8]), allow us to now infer the halo mass function and its evolution with redshift. Past analyses of the halo mass function and galaxy luminosity function from these surveys have generated significant tension between the observations and predictions in the context of ΛCDM [9]. These studies derived the halo mass from the UV luminosity function by assuming a relationship between UV luminosity and stellar mass which was then used to infer the halo mass function assuming another relationship between the stellar mass and halo mass. The outcome of this work [10] indicated that the halo to stellar mass ratio is constant throughout the redshift range $0 \lesssim z \lesssim 4$, but it is not yet clear whether this ratio evolves or remains constant at $z \gtrsim 4$.

In their analysis, Behroozi et al. [11], Behroozi & Silk [12] and Finkelstein et al. [13] concluded that in order to alleviate the tension with ΛCDM, this ratio needs to evolve by as much as ~ 0.8 dex. An opposing view [9,14,15] maintains that such an evolution is not supported by existing data, and that this ratio is instead roughly constant at redshifts $4 \lesssim z \lesssim 10$, continuing the trend seen at $z \lesssim 4$. In this case, the halo distribution would be inconsistent with ΛCDM by at least 2–4 orders of magnitude at redshifts $4 \lesssim z \lesssim 10$, a disparity termed as "The Impossibly Early Galaxy Problem" [9]. It is anticipated that future observations with the NIRCam and NIRspec on the James Webb Space Telescope may settle this debate.

In this paper, we consider what would happen if this problem turns out to be real and provide a possible solution using a recently completed study of the perturbation growth in the $R_\mathrm{h} = ct$ universe [16] to describe and report the growth of structure from redshift $z \sim 10^{11}$ to 0 in this alternative Friedmann–Lemaître–Robertson–Walker (FLRW) cosmology. We shall summarize the essential features of this alternative model in Sect. 2, and then derive the growth equations in Sect. 2. We shall evaluate the halo mass function in Sects. 3 and 4, and end with our conclusions in Sect. 5.

2 The $R_\mathrm{h} = ct$ universe

The $R_\mathrm{h} = ct$ universe [17–22] has thus far been tested using a variety of observations. For a summary, see Table 2 in ref. [23]. The principal difference between ΛCDM and $R_\mathrm{h} = ct$ is that the latter model is constrained by the equation of state $\rho + 3p = 0$, i.e., the so-called zero active mass condition in general relativity. In the standard model, radiation was dominant early, followed by matter and dark energy at later times, whereas dark energy has always been present in $R_\mathrm{h} = ct$, with a significant component of radiation early on, followed by matter towards lower redshifts. Also, the dark-energy equation of state is $w_\mathrm{de} = -1$ in ΛCDM, while it is $w_\mathrm{de} = -1/2$ in $R_\mathrm{h} = ct$ (see Ref. [24] for further details).

Some additional support for the $R_\mathrm{h} = ct$ cosmology, based on an alternative theoretical concept, may also be found in Ref. [25] and the updated discussion in Ref. [26]. But in spite of the success this model has enjoyed thus far in accounting for many observations as well, if not better, than the standard model, some counter claims have also been published in recent years, so the issue of whether or not it is the correct cosmology still needs to be resolved. This is a principal reason for continuing to test it as we do in this paper. Our analysis here advances this discussion significantly by providing new insights and an important new comparison between $R_\mathrm{h} = ct$ and ΛCDM using observations over an unusually large redshift range (see Figs. 2, 3, 4, 5, 6, 7 below).

As noted above, over the past decade, $R_\mathrm{h} = ct$ has been compared to ΛCDM using data across a broad redshift range, using integrated distances and the redshift-dependent Hubble parameter, among various other measures. Still, some of these data are often associated with unknown systematics and, worse, are often dependent on the presumed background model. The analysis of Type Ia SNe is a well-known example in which the lightcurve is characterized by at least 3 'nuisance' parameters that need to be optimized along with those in the cosmological model. A different choice of assumptions (e.g., the unknown intrinsic dispersions) and techniques (e.g., χ^2 minimization versus maximization of a likelihood function and/or model selection with information criteria), can sometimes produce varying outcomes in these tests.

For example, Type Ia SNe are challenging to use for model testing when various subsamples are merged together to improve the statistics, since one must deal with different unknown systematics in each case. In his assessment, Shafer [27] merged the Union2.1 and JLA samples and found that this compilation favours the standard model. In his analysis, however, he avoided the unknown intrinsic dispersions by instead constraining the reduced χ^2 to be 1 in each subsample. In recent years, a superior statistical approach has been developed [28–30] in which these unknowns are instead estimated by maximizing the overall likelihood function. The outcome of which cosmology is preferred by the SN data changes depending on which of these assumptions and methods are chosen.

Another recent test [31] used local probes, combining SN data with measurements of the Hubble parameter $H(z)$ and baryon acoustic oscillations (BAO). This analysis also showed that ΛCDM is favoured over $R_\mathrm{h} = ct$, contrasting with other work where the opposite was reported [30,32]. The

different results may be traced to the choice of data sets in the two studies. As is the case for SN measurements, the BAO also do not provide model-independent information since the location of the BAO peak cannot easily be distinguished from redshift space distortions (RSD). As of today, only 3 such measurements have provided a clean peak location. In other cases, a cosmology must be preassumed in order to model the RSD, rendering the data highly model-dependent. Any use of these BAO data, and the of $H(z)$ measured from them, produces a biased outcome. In their assessment, Lin et al. [31] used all the data and concluded, not surprisingly, that they favour ΛCDM because the standard model was used to estimate the RSD. When only model-independent data are used instead, however, one reaches the opposite conclusion [32].

As we discuss elsewhere in this paper, the inferred halo mass function is itself subject to an important unknown: the redshift dependence of the halo to stellar mass ratio M_h/M_*, so our conclusions may also require revision once new data will have been acquired. Depending on whether or not this ratio changes by roughly an order of magnitude between redshifts 4 and 10, a factor yet to be resolved observationally, ΛCDM may or may not be favoured over $R_\mathrm{h} = ct$. Nonetheless, providing one more important comparison between these two models is essential in establishing the conditions that must be met in order for $R_\mathrm{h} = ct$ to be viewed as a viable alternative to the standard model.

3 The Einstein–Boltzmann equations for dark matter and energy fluctuations

To obtain the complete evolution of density fields starting from initial perturbations, one must solve the coupled Boltzmann/Einstein equations (see Ref. [33]). The baryons are strongly coupled with radiation until decoupling and therefore do not contribute to the growth of structure during this epoch. Once they decouple from the radiation, baryons follow the evolution of dark matter, which has preceded them in forming bound systems. Hence, the initial growth of structure is dominated by dark matter. For this paper, which is focused on the question of halo growth, we therefore concentrate solely on the growth of dark matter perturbations. Other aspects of structure growth will be presented elsewhere [16]. Thus, since we are not interested here in temperature fluctuations of the radiation field or acoustic oscillations, we justify the use of Einstein–Boltzmann equations customized solely for the purpose of describing the growth of dark matter perturbations, which we derive as follows.

The distribution function for any species (i.e., dark matter, baryons, radiation, etc.) may depend on the coordinates (x^μ) and momentum (P^μ) 4-vectors, resulting in an 8-dimensional phase space. An additional constraint emerges, however, from the invariant contraction of the momentum, $g_{\mu\nu}P^\mu P^\nu = -m^2$, which reduces the phase space to 7-dimensions. So we choose x^μ, $p \equiv |\boldsymbol{p}|$ and the direction of the momentum, $\hat{p}^i$, as our independent variables. Louisville's theorem produces the equation

$$\frac{df_s}{d\lambda} = \frac{\partial f_s}{\partial x^0}\frac{\partial x^0}{\partial \lambda} + \frac{\partial f_s}{\partial x^i}\frac{\partial x^i}{\partial \lambda} + \frac{\partial f_s}{\partial p}\frac{\partial p}{\partial \lambda} + \frac{\partial f_s}{\partial \hat{p}^i}\frac{\partial \hat{p}^i}{\partial \lambda} = C[f_s], \tag{1}$$

where $f_s(x^\mu, p, \hat{p}^i)$ is the distribution function for any species 's' (i.e., dark matter, dark energy, baryons, etc.), λ is the affine parameter, and $C[f_s]$ is a collision/source term for this species. We define $P^\mu = dx^\mu/d\lambda$, so that $dx^0/d\lambda = P^0$. Dividing the above equation by P^0, and neglecting the fourth term that is of second order, gives

$$\frac{df_s}{d\eta} = \frac{\partial f_s}{\partial \eta} + \frac{\partial f_s}{\partial x^i}\frac{P^i}{P^0} + \frac{\partial f_s}{\partial p}\frac{\partial p}{\partial \eta} = \frac{C[f_s]}{P^0}, \tag{2}$$

where η is now the conformal time, $d\eta \equiv dt/a(t)$, in terms of the expansion factor $a(t)$ and cosmic time t in the Friedmann–Lemaître–Robertson–Walker metric.

In the above equation, we may write $P^i/P^0 = (p/E)\hat{p}^i$ (where E is the energy) and, using the geodesic equation, we get

$$\frac{dp}{d\eta} = -\mathcal{H}p + E\hat{p}^l\partial_l\frac{h_{00}}{2} - \frac{p}{2}\frac{dh_{ij}}{d\eta}\hat{p}^i\hat{p}^j, \tag{3}$$

where $\mathcal{H}$ is the Hubble parameter written in terms of η, and $h_{\alpha\beta}$ are the perturbed metric coefficients. Substituting Eq. (3) into Eq. (2), we get

$$\frac{df_s}{d\eta} + \frac{p\hat{p}^i}{E}\frac{\partial f_s}{\partial x^i} + p\left(-\mathcal{H} + \frac{E}{p}\hat{p}^l\partial_l\frac{h_{00}}{2} - \frac{1}{2}h'_{ij}\hat{p}^i\hat{p}^j\right)\frac{\partial f_s}{\partial p} = \frac{a}{E}(1-\Phi)C[f_s], \tag{4}$$

where we have substituted $P_0 = \frac{E}{a}(1+\Phi)$, in terms of the perturbed gravitational potential Φ. We now separate the distribution function into its unperturbed component, $\bar{f}_s$, and the perturbed contribution, $\mathcal{F}_s$, such that

$$f_s(\eta, x^i, p, \hat{p}^i) = \bar{f}_s(\eta, x^i, p, \hat{p}^i) + \mathcal{F}_s(\eta, x^i, p, \hat{p}^i). \tag{5}$$

Then, multiplying Eq. (4) by $E(p)$, and integrating over momentum space, collecting the zeroth-order terms, gives

$$\int \frac{d^3p}{(2\pi)^3}E(p)\frac{d\bar{f}_s}{d\eta} - \int \frac{d^3p}{(2\pi)^3}\mathcal{H}pE(p)\frac{\partial \bar{f}_s}{\partial p} = \int \frac{d^3p}{(2\pi)^3}aC[f_s]. \tag{6}$$

In this expression, $C[f_s]$ is zero in the context of ΛCDM because the particle number is conserved during this phase of the fluctuation growth. But this is not the case in $R_\mathrm{h} = ct$. The early universe in this model contains approximately 80%

dark energy and approximately 20% radiation, with a small contamination of matter [24]. At late times, the $R_{\rm h} = ct$ universe contains approximately 70% dark energy and 30% matter. A coupling therefore exists between dark matter and dark energy, such that the particle number for each individual species is not conserved in this model. The right-hand side of Eq. (6) is therefore not zero in $R_{\rm h} = ct$. Integrating the second term on the left-hand side by parts and neglecting the boundary term, we arrive at the expression

$$\int \frac{d^3p}{(2\pi)^3} E(p) \frac{d\bar{f}_s}{d\eta} + 3\mathcal{H} \int \frac{d^3p}{(2\pi)^3} \left(E + \frac{p^2}{3E} \right) \bar{f}_s = \int \frac{d^3p}{(2\pi)^3} aC[f_s]. \tag{7}$$

This equation may be further reduced by using the following definitions for the (background) density and pressure:

$$\rho_s = \int \frac{d^3p}{(2\pi)^3} E(p) \bar{f}_s, \tag{8}$$

and

$$\mathcal{P}_s = \int \frac{d^3p}{(2\pi)^3} \frac{p^2}{3E} \bar{f}_s. \tag{9}$$

When applied to dark matter, Eq. (7) may thus be written as follows

$$\frac{d\rho_{\rm dm}}{d\eta} + 3\mathcal{H}(\rho_{\rm dm} + \mathcal{P}_{\rm dm}) = \int \frac{d^3p}{(2\pi)^3} aC[f_{\rm dm}]. \tag{10}$$

For this particular species (i.e., dark matter), we may also put $\mathcal{P}_{\rm dm} = 0$. In addition, we use an approximate empirical expression, $\rho_{\rm dm} = (\rho_c/3a^2) \exp\left(- \frac{a_*}{a} \frac{(1-a)}{(1-a_*)} \right)$, to model the transition from a radiation/dark-energy dominated early universe to a matter/dark-energy dominated universe at late times, where ρ_c is the critical density today, and a_* represents the scale factor at matter radiation equality. Note that we are also normalizing $a(t_0)$ to be 1 today, which is possible in a spatially flat Universe. We infer the required collision/source term in Eq. (10) by using this empirical expression for $\rho_{\rm dm}$, which yields

$$\int \frac{d^3p}{(2\pi)^3} aC[f_{\rm dm}] = \mathcal{H}\rho_{\rm dm} + \frac{H\rho_{\rm dm}}{a} \left(\frac{a_*}{1-a_*} \right). \tag{11}$$

It is not difficult to see that the above equation is satisfied to zeroth order only if

$$C[\bar{f}_{\rm dm}] = \frac{\mathcal{H}E}{a} \bar{f}_{\rm dm} + \frac{\mathcal{H}E}{a^2} \bar{f}_{\rm dm} \left(\frac{a_*}{1-a_*} \right). \tag{12}$$

This collision/source term explicitly shows the interactions between dark energy and dark matter required to sustain the zero active mass condition described above. That is, in order for the partitioning of 80% dark energy plus 20% radiation in the early Universe to transition to a balance of 70% dark energy plus 30% matter today, a fraction of the dark energy must decay/evolve into dark matter. As such, the collision/source for dark energy must be the negative of Eq. (12), so that

$$\frac{d\rho_{\rm de}}{d\eta} + 3\mathcal{H}(\rho_{\rm de} + \mathcal{P}_{\rm de}) = -\int \frac{d^3p}{(2\pi)^3} \left[\mathcal{H}E \bar{f}_{\rm dm} + \frac{\mathcal{H}E}{a} \bar{f}_{\rm dm} \left(\frac{a_*}{1-a_*} \right) \right], \tag{13}$$

where

$$C[\bar{f}_{\rm de}] = -\frac{\mathcal{H}E}{a} \bar{f}_{\rm dm} + \frac{\mathcal{H}E}{a^2} \bar{f}_{\rm dm} \left(\frac{a_*}{1-a_*} \right). \tag{14}$$

Returning now to Eq. (4), and using Eq. (12), we find for dark matter that

$$\frac{df_{\rm dm}}{d\eta} + \frac{p\hat{p}^i}{E} \frac{\partial f_{\rm dm}}{\partial x^i} + \left(-\mathcal{H} + \frac{E}{p} \hat{p}^l \partial_l \frac{h_{00}}{2} - \frac{1}{2} h'_{ij} \hat{p}^i \hat{p}^j \right) \frac{\partial f_{\rm dm}}{\partial p} = \left[\mathcal{H} f_{\rm dm} + \frac{\mathcal{H}}{a} f_{\rm dm} \left(\frac{a_*}{1-a_*} \right) \right] (1 - \Phi) \tag{15}$$

We again multiply this equation by $E(p)$ and integrate over momentum space, but now collecting first order terms, finding that

$$\frac{d(\delta\rho_{\rm dm})}{d\eta} + (\rho_{\rm dm} + \mathcal{P}_{\rm dm}) \partial_i v^i_{\rm dm} + 3\mathcal{H}(\delta\rho_{\rm dm} + \delta\mathcal{P}_{\rm dm}) + 3(\rho_{\rm dm} + \mathcal{P}_{\rm dm}) \frac{d\Phi}{d\eta} = \left[\mathcal{H} + \frac{\mathcal{H}}{a} \left(\frac{a_*}{1-a_*} \right) \right] (1 - \Phi) \delta\rho_{\rm dm} \tag{16}$$

where, as always, Φ is the gravitational potential. Then, defining $\delta_{\rm dm} \equiv \delta\rho_{\rm dm}/\rho_{\rm dm}$ for the dark-matter perturbation, with $\mathcal{P}_{\rm dm} = \delta\mathcal{P}_{\rm dm} = 0$, we may write

$$\frac{d\delta_{\rm dm}}{d\eta} = \frac{1}{\rho_{\rm dm}} \frac{d(\delta\rho_{\rm dm})}{d\eta} - \frac{\delta_{\rm dm}}{\rho_{\rm dm}} \frac{d\rho_{\rm dm}}{d\eta}. \tag{17}$$

Substituting for $d(\delta\rho_{\rm dm})/d\eta$ in Eq. (16), and isolating the Fourier mode k, we find that

$$\frac{d\delta_{{\rm dm},k}}{d\eta} = -ku_k - 3\frac{d\Phi_k}{d\eta} - \mathcal{H} \left[1 + \frac{a_*}{a(1-a_*)} \right] \Phi, \tag{18}$$

where we have written $\partial_i v^i_k = ku_k$, in terms of the velocity perturbation u_k of the dark matter. Finally, we take the second moment of Eq. (15), multiplying it by $p\hat{p}^i$ and contracting it with $i\hat{k}_i$. Then integrating over momentum space, and collecting first order terms, we get

$$\frac{d(\rho_{\rm dm} u_{\rm dm,k})}{d\eta} + 4\mathcal{H}\rho_{\rm dm} u_{\rm dm,k} + k\Phi\rho_{\rm dm} = \mathcal{H} \left[1 + \frac{a_*}{a(1-a_*)} \right] \rho_{\rm dm} u_{\rm dm,k}, \tag{19}$$

where $u_{\mathrm{dm,k}}$ is the k^{th} velocity perturbation of dark matter. Substituting for $d\rho_{\mathrm{dm}}/d\eta$ in the above equation we thus get

$$\frac{du_{\mathrm{dm,k}}}{d\eta} = -\frac{1}{a}\frac{da}{d\eta}u_{\mathrm{dm,k}} - k\Phi_k. \tag{20}$$

Turning now to the dark-energy perturbations, we begin with Eq. (4) and the interaction term in Eq. (14), and find that

$$\frac{df_{\mathrm{de}}}{d\eta} + \frac{p\hat{p}^i}{E}\frac{\partial f_{\mathrm{de}}}{\partial x^i} + p\left(-\mathcal{H} + \frac{E}{p}\hat{p}^l\partial_l\frac{h_{00}}{2} - \frac{1}{2}h'_{ij}\hat{p}^i\hat{p}^j\right)\frac{\partial f_{\mathrm{de}}}{\partial p} = -\mathcal{H}(1-\Phi)\left[1 + \frac{a_*}{a(1-a_*)}\right]f_{\mathrm{dm}}, \tag{21}$$

where f_{de} is the distribution function for dark-energy. Thus, partitioning f_{de} into its unperturbed ($\bar{f}_{\mathrm{de}}$) and perturbed ($\mathcal{F}_{\mathrm{de}}$) components, as was done in Eq. (5), we can collect the first-order perturbed terms to find that

$$\frac{d\mathcal{F}_{\mathrm{de}}}{d\eta} + \frac{p\hat{p}^i}{E}\frac{\partial\mathcal{F}_{\mathrm{de}}}{\partial x^i} - \mathcal{H}p\frac{\partial\mathcal{F}_{\mathrm{de}}}{\partial p} + p\left(\frac{E}{p}\hat{p}^l\partial_l\frac{h_{00}}{2} - \frac{1}{2}h'_{ij}\hat{p}^i\hat{p}^j\right)\frac{\partial\bar{f}_{\mathrm{de}}}{\partial p} = -\mathcal{H}\left[1 + \frac{a_*}{a(1-a_*)}\right]\left(\mathcal{F}_{\mathrm{dm}} - \Phi\bar{f}_{\mathrm{dm}}\right). \tag{22}$$

Multiplying this equation by $E(p)$ and integrating over the momentum space then gives

$$\frac{d\delta\rho_{\mathrm{de}}}{d\eta} + \rho_{\mathrm{de}}(1+w_{\mathrm{de}})ku_{\mathrm{de},k} + 3\mathcal{H}\delta\rho_{\mathrm{de}}\left(1 + \frac{\delta\mathcal{P}_{\mathrm{de}}}{\delta\rho_{\mathrm{de}}}\right) + 3\frac{d\Phi}{d\eta}\rho_{\mathrm{de}}(1+w_{\mathrm{de}}) = \mathcal{H}\left[1 + \frac{a_*}{a(1-a_*)}\right](\rho_{\mathrm{dm}}\Phi - \delta\rho_{\mathrm{dm}}). \tag{23}$$

Defining $\delta_{\mathrm{de}} = \delta\rho_{\mathrm{de}}/\rho_{\mathrm{de}}$, and using $\mathcal{P}_{\mathrm{de}} = -\rho_{\mathrm{de}}/2$ ([24]) we may write

$$\frac{d\delta_{\mathrm{de}}}{d\eta} = \frac{1}{\rho_{\mathrm{de}}}\frac{d\delta\rho_{\mathrm{de}}}{d\eta} - \frac{\delta\rho_{\mathrm{de}}}{\rho_{\mathrm{de}}^2}\frac{d\rho_{\mathrm{de}}}{d\eta}, \tag{24}$$

so that with Eqs. (13) and (23), we find that

$$\frac{d\delta_{\mathrm{de}}}{d\eta} = -\frac{k}{2}u_{\mathrm{de},k} - 3\mathcal{H}\delta_{\mathrm{de}}\left(\frac{1}{2} + \frac{\delta\mathcal{P}_{\mathrm{de}}}{\delta\rho_{\mathrm{de}}}\right) - \frac{3}{2}\frac{d\Phi}{d\eta} + \mathcal{H}\left[1 + \frac{a_*}{a(1-a_*)}\right]\frac{\rho_{\mathrm{dm}}}{\rho_{\mathrm{de}}}(\delta_{\mathrm{de}} - \delta_{\mathrm{dm}} + \Phi). \tag{25}$$

The sound speed for our coupled dark matter/dark energy fluid is not known yet, so we write it as follows

$$c_s^2 \equiv \frac{\delta\mathcal{P}}{\delta\rho} = \frac{\delta\mathcal{P}_{\mathrm{de}}}{\delta\rho_{\mathrm{dm}} + \delta\rho_{\mathrm{de}}} = \frac{\delta\mathcal{P}_{\mathrm{de}}/\delta\rho_{\mathrm{de}}}{(1 + \delta\rho_{\mathrm{dm}}/\delta + \rho_{\mathrm{de}})}, \tag{26}$$

analogously to what is commonly done with the coupled baryon-radiation fluid in the standard model. And following the conventional approach of assuming adiabatic fluctuations, we also write

$$\frac{\delta\mathcal{P}_{\mathrm{de}}}{\delta\rho_{\mathrm{de}}} = c_s^2\left[1 + \frac{2\rho_{\mathrm{dm}}}{\rho_{\mathrm{de}}}\right]. \tag{27}$$

For the sake of simplicity, we assume the sound speed to be a constant delimited to the range $0 \lesssim (c_s/c)^2 \lesssim 1$. We have found that the actual value of this constant has a negligible impact on the solutions to the above equations since the ratio of dark matter density to dark energy is always much less than 1 in the $R_{\mathrm{h}} = ct$ universe, and we therefore adopt the simple fraction $c_s^2 = c^2/2$ throughout this work. Thus, using Eqs. (25) and (27), we get

$$\frac{d\delta_{\mathrm{de}}}{d\eta} = -\frac{k}{2}u_{\mathrm{de},k} - \delta_{\mathrm{de}}\left(\frac{3\mathcal{H}}{2} + 3\mathcal{H}c_s^2 + \frac{6\mathcal{H}c_s^2\rho_{\mathrm{dm}}}{\rho_{\mathrm{de}}}\right) - \frac{3}{2}\frac{d\Phi}{d\eta} + \mathcal{H}\left[1 + \frac{a_*}{a(1-a_*)}\right]\frac{\rho_{\mathrm{dm}}}{\rho_{\mathrm{de}}}(\delta_{\mathrm{de}} - \delta_{\mathrm{dm}} + \Phi). \tag{28}$$

Finally, we take the second moment of Eq. (21), multiply it by $p\hat{p}^i$ and contract it with $i\hat{k}_i$. Integrating over momentum space, and collecting first order terms, we thus find that

$$\frac{du_{\mathrm{de},k}}{d\eta} = -\frac{5\mathcal{H}}{2}u_{\mathrm{de,k}} - k\Phi + 2kc_s^2\left[1 + \frac{2\rho_{\mathrm{dm}}}{\rho_{\mathrm{de}}}\right]\delta_{\mathrm{de}} + \mathcal{H}\left[1 + \frac{a_*}{a(1-a_*)}\right]\frac{\rho_{\mathrm{dm}}}{\rho_{\mathrm{de}}}(u_{\mathrm{de},k} - 2u_{\mathrm{dm},k}). \tag{29}$$

Our final equation comes from perturbing the FLRW metric in Einstein's equations (see [33]), which gives

$$k^2\Phi_k + 3\frac{1}{a}\frac{da}{d\eta}\left(\frac{d\Phi_k}{d\eta} + \frac{1}{a}\frac{da}{d\eta}\Phi_k\right) = 4\pi Ga^2\left[\rho_{\mathrm{m}}\delta_{\mathrm{dm},k} + \rho_{\mathrm{de}}\delta_{\mathrm{de}}\right]. \tag{30}$$

In arriving at Eq. (30), we have chosen the Newtonian gauge for the primary reason that the independent components in this gauge have a direct correspondence to the gauge invariant Bardeen variables [33,34].

It is important to stress that the set of Eqs. (18), (20), (28) and (29) in $R_{\mathrm{h}} = ct$ differ from their counterparts in ΛCDM. This happens because dark energy and dark matter are coupled in $R_{\mathrm{h}} = ct$, while dark energy is simply a cosmological constant in the most basic ΛCDM model. The only expression that is formally common to both $R_{\mathrm{h}} = ct$ and ΛCDM is Eq. (20), though the dependence of ρ_{dm} on $a(t)$ is, of course, model dependent. Mathematically, this comes about because the collision/source term in Eq. (12) actually cancels out in the perturbation Eq. (19) for the velocity perturbations. The dependence on cosmology also enters into the growth of δ_{dm} via the model-dependent $\mathcal{H}$ and $a(t)$ functions. These quantities change with time according to the background evolution, and are therefore strongly dependent on the chosen model.

More specifically, an inspection of these equations reveals that there are three principal differences between $R_h = ct$ and ΛCDM: (1) the scale factor $a(t)$ in $R_h = ct$ is given as $a(t) = (t/t_0)$ at all epochs, whereas in ΛCDM it is proportional to $t^{1/2}$ and $t^{2/3}$ during the radiation and matter dominated phases, respectively; (2) the matter density scales as $\rho_{dm} = (\rho_c/3a^2)\exp\left(-\frac{a_*}{a}\frac{(1-a)}{(1-a_*)}\right)$ in $R_h = ct$, whereas it is given as $\rho_m = (\Omega_m \rho_c/a^3)$ in ΛCDM; and (3) the various modes of the density field in ΛCDM exited the horizon during inflation, whereas none of the modes ever crossed the horizon in $R_h = ct$ [49]. In ΛCDM, small-scale modes re-entered the horizon while radiation was dominant, while larger-scale modes entered the horizon when matter dominated, which produces a late start for the growth of structure compared with what happens in $R_h = ct$. This appears to be the principal reason why galaxies and supermassive black holes appeared earlier in $R_h = ct$ than in the standard model.

We shall formally introduce the growth function in Eq. (31) below, and plot it in Fig. 1. It is obtained by solving Eqs. (10)–(30) simultaneously (see Ref. [16] for more details). It is quite evident from this plot that the growth factor in $R_h = ct$ is significantly stronger at large redshifts than that in ΛCDM, in full agreement with the previous results of our analysis at lower redshifts [35]. In contrast, the growth function in ΛCDM indicates a strong evolution from $z \sim 10$ to $z \sim 4$. And since galaxies typically form on a dynamical timescale ~ 300 Myr [36] after halo virialization, the rapid evolution in the number density of halos from $z \sim 8$ to ~ 4 predicted by ΛCDM corresponds to a rapid evolution in the UV luminosity of galaxies at $6.0 \gtrsim z \gtrsim 3.4$. This is one of the points of contention between the two camps, since this (required) rapid evolution in the UV luminosity function conflicts with the observations [9]. The observed UV luminosity evolves much more slowly than this prediction, which would mean that these massive galaxies would have formed much earlier than expected in ΛCDM.

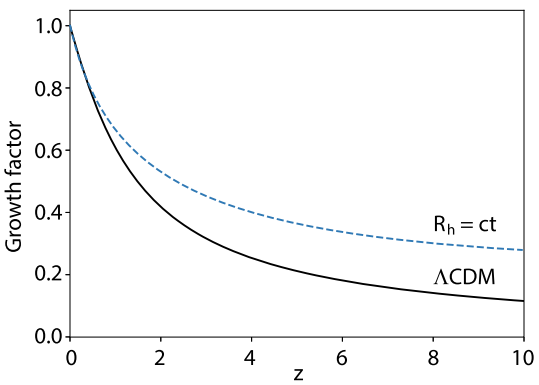

Fig. 1 Growth Factor predicted by $R_h = ct$ (dashed) and flat ΛCDM (solid)

4 Halo mass function

The halo mass function was first derived by Press and Schechter [37] assuming spherical collapse and a primordial Gaussian density field. When tested against numerical simulations, however, it became evident that the Press-Schechter formalism over-predicts the number of halos at the high mass end, and under-predicts at the low mass end. This inconsistency was resolved by introducing ellipsoidal collapse, rather than spherical, by Sheth–Tormen [1]. But the Bolshoi simulations performed by Klypin et al. [38] several years later indicated that, while discrepancies in the Sheth–Tormen mass function at $z \sim 0$ are less than 10% for halo masses in the range $5 \times 10^9 - 5 \times 10^{14}\ M_\odot$, this prescription over-predicts the density by about 50% at $z \sim 6$ for masses in the range $10^{11} - 10^{12}\ M_\odot$, getting even worse (by an order of magnitude) by $z \sim 10$. Unfortunately for the standard model, the inclusion of corrections from the Bolshoi simulations actually exacerbates the discrepancy between theory and observation. For this reason, and the fact that analogous simulations to the Bolshoi calculations have not yet been carried out for $R_h = ct$, we won't include such adjustments in this paper. We point out that if we were to add such corrections to $R_h = ct$, the comparison of this model's predictions with the data under the assumption of a constant halo mass to stellar mass ratio would be even more favourable than the Sheth–Tormen formulation on its own, as one may readily see in Figs. 2, 3, 4, 5, 6 and 7. As such, our exclusion of these corrections produces an effect more favourable to ΛCDM than $R_h = ct$, even with this assumption, which we do in order give the standard model as much benefit of the doubt as possible.

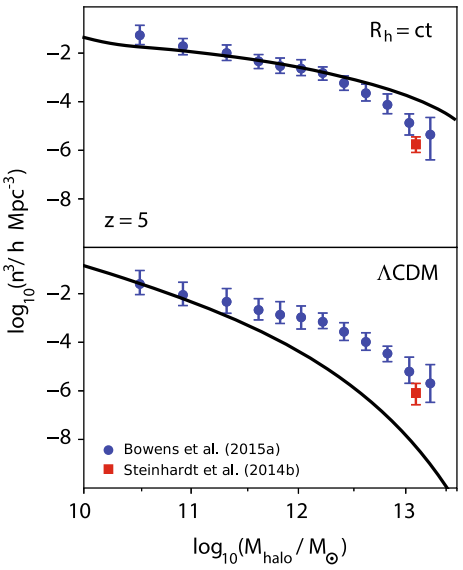

Fig. 2 Top: halo mass function inferred from galaxy surveys at $z = 5$ compared with $R_h = ct$. Bottom: same, except now for ΛCDM

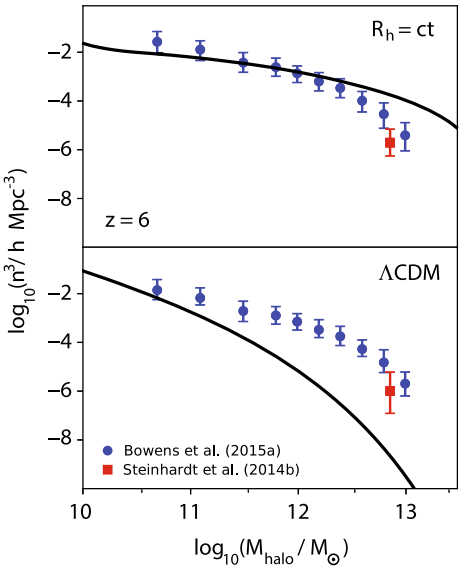

Fig. 3 Top: halo mass function inferred from galaxy surveys at $z = 6$ compared with $R_\mathrm{h} = ct$. Bottom: same, except now for ΛCDM

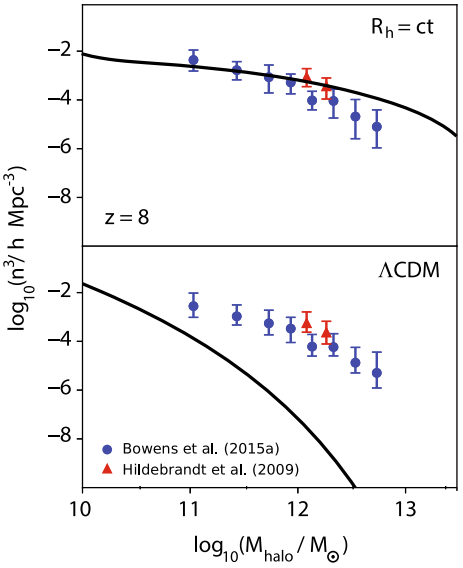

Fig. 5 Top: halo mass function inferred from galaxy surveys at $z = 8$ compared with $R_\mathrm{h} = ct$. Bottom: same, except now for ΛCDM

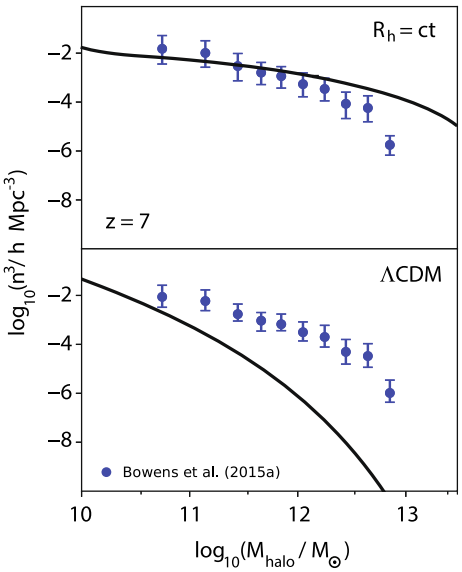

Fig. 4 Top: halo mass function inferred from galaxy surveys at $z = 7$ compared with $R_\mathrm{h} = ct$. Bottom: same, except now for ΛCDM

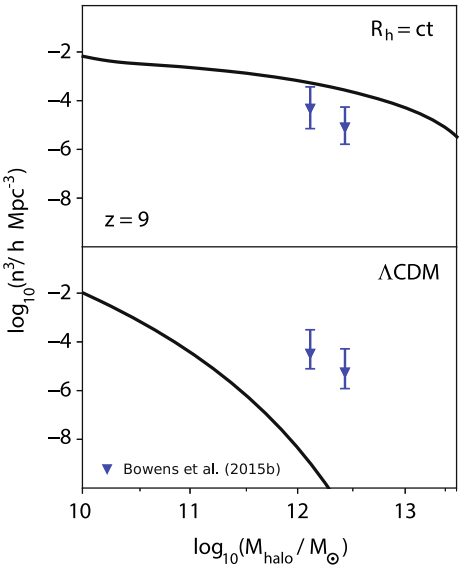

Fig. 6 Top: halo mass function inferred from galaxy surveys at $z = 9$ compared with $R_\mathrm{h} = ct$. Bottom: same, except now for ΛCDM

The Sheth–Tormen mass function is given as

$$f(\sigma) = A\sqrt{\frac{2a}{\pi}}\left[1 + \left(\frac{\sigma^2}{a\delta_c^2}\right)^p\right]\frac{\delta_c}{\sigma}\exp\left[-\frac{a\delta_c^2}{2\sigma^2}\right], \tag{31}$$

where $A = 0.3222$ is a normalization factor, and $a = 0.707$ and $p = 0.3$. Using this halo mass function, one may obtain the number of dark matter halos per comoving volume with masses less than M as follows:

$$\frac{dn}{d\ln M} = \frac{\rho_0}{M} f(\sigma)\left|\frac{d\ln\sigma}{d\ln M}\right|, \tag{32}$$

where σ is defined according to the expression

$$\sigma_R^2(R, z) = \frac{b^2(z)}{2\pi^2}\int_0^\infty k^2 P(k) W^2(k, R) dk, \tag{33}$$

and $P(k)$ is the power spectrum, $W(k, R)$ is the top-hat filter and $b(z)$ is the growth factor shown in Fig. 1 for both ΛCDM and $R_\mathrm{h} = ct$.

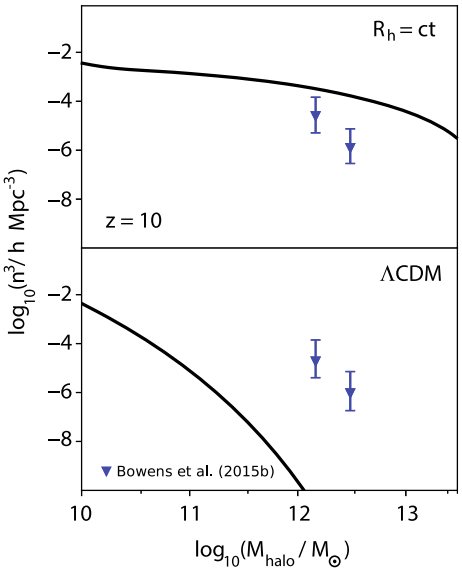

Fig. 7 Top: halo mass function inferred from galaxy surveys at $z = 10$ compared with $R_{\rm h} = ct$. Bottom: same, except now for ΛCDM

5 Observed halo mass function

The data used in this paper were assembled by Steinhardt et al. [9], based on measurements obtained using three different techniques, including the clustering method [39,43] based on the spatial distribution of galaxies to obtain the halo masses. This method doesn't assume any physical properties of the galaxies themselves, but assumes a model for the dark matter concentration. Other techniques include template fitting [40], that adopts a relationship between the luminosity and stellar masses; the abundance matching technique [13] that relates critical features in the galaxy luminosity or mass function, such as a 'knee', to crucial elements in the halo mass distribution, that can then be used to match the galaxy and dark matter densities to infer the halo mass function. The high redshift ($z \gtrsim 6$) data points are derived from the UV luminosity function, that yields halo masses by assuming that the halo mass to light ratio obtained at lower redshifts persists to higher redshifts. Most of the data used in this work were obtained assuming a constant ratio of halo to stellar-mass. The two main principles for arriving at this ratio are (1) that 10% of the baryonic matter eventually condensed into stars [41] and (2) the observation of a 6:1 ratio of dark matter to baryonic matter [42].

It is quite obvious from the progression seen in Figs. 2, 3, 4, 5, 6 and 7 that the observed halo mass function obtained via these different techniques [13,39,43,44] is entirely inconsistent with the distribution predicted by ΛCDM, if the halo to stellar-mass ratio remains constant throughout the $4 \lesssim z \lesssim 10$ redshift range [9]. Of course, the caveat is that these data were not measured directly, and were obtained using relationships derived at low redshifts. Steinhardt et al. [9] studied the possibility that these correlations could be breaking down at high-z. Their investigation indicated, however, that the star-formation rate vs. stellar mass of these high redshift galaxies lies on the extrapolation from lower redshift galaxies. In addition, the ratio of stellar mass to halo mass in these high redshift galaxies is similar to the standard value 30:1 seen at all redshifts. These two tests therefore indicate that the high redshift galaxies are quite normal, implying that the problem is real.

In addition to this, Steinhardt et al. [9] determined that an evolution of 0.8 dex in M_{Halo}/L_{UV} is needed to mitigate this problem. Such a change might occur if the stellar population in galaxies at $z = 8$ is younger than that at $z = 4$. Steinhardt et al. [9] extensively investigated whether this possibility could mitigate the disparity by modeling the halo mass to light ratio from an initial stellar population assuming they formed in one rapid burst at $z = 12$ and then evolved along the main sequence until $z = 4 - 8$, where they were observed. This resulted in a star formation rate $\propto M_*^{0.7}$, with a stellar age asymptotically approaching $50 - 150$ Myr, starting from an initially small value. But this isn't sufficient enough to remove the problem and, worse, the above approach isn't realistic considering a dynamical timescale of 300 Myr for star formation after virialization of the halo.

Steinhardt et al. [9] considered this scenario and modeled the halo mass to light ratio as described above, concluding that this too is insufficient to reconcile the problem. Another possibility is that the halo mass to stellar mass ratio evolves towards higher redshifts. An evolution of 0.8 dex in this ratio would reconcile the problem. But such a modification is only possible either by a complete absence of dark matter at redshift 8, or if 100% of the baryons condensed instantly into stars at high redshift upon halo virialization, which is quite impossible. Hence, one may reasonably conclude that this problem may be reconciled in ΛCDM only via the introduction of implausible physics. When viewed in the context of other "too early" types of problems, the disparity evident in Figs. 2, 3, 4, 5, 6 and 7 is quite damning for the standard model. For example, the early appearance of supermassive black holes at $z \sim 6$–7 [45,46] and galaxies at $z \sim 10 - 12$ (see references cited in [47], argues in favor of these problems being real, presenting a challenge to any attempt to alleviate them in the context of ΛCDM.

In contrast, the comparison between the Steinhardt et al. [9] data, under the assumption that the halo to stellar mass ratio is constant in the redshift range $4 \lesssim z \lesssim 10$, and the predictions of $R_{\rm h} = ct$, is very favourable – except at the very high mass end of the halo mass distribution, as one may see in Figs. 2, 3, 4, 5, 6 and 7. The standard model disagrees progressively more and more with this approach as the redshift increases, while $R_{\rm h} = ct$ fits the data throughout the range $10 \gtrsim z \gtrsim 4$ very well at the low and intermediate mass end, and overpredicts by one to two orders of mag-

nitude at the high mass end. This over-prediction may be due to two possible reasons: (1) as noted earlier, the Bolshoi simulation [38] has indicated that the Sheth–Tormen mass function overpredicts the number of halos by at least 10% at redshift $z \sim 0$, and overpredicts by at least 50% at redshift $z \sim 10$. Although simulations similar to Bolshoi haven't yet been carried out for $R_h = ct$, a trend analogous to this in the context of this model, would produce corrections that largely mitigate the problem at the high mass end; (2) this over-prediction may also be due in part to observational selection effects that may be 'hiding' some of the sources. Some massive galaxies may have been missed due to extinction, which future observations might be able to address. Regardless of which, if any, of these mitigating factors are at play in $R_h = ct$, none of them can resolve the disparity arising from the predictions of ΛCDM. The discrepancy seen in the standard model is extreme, ranging from one to over four orders of magnitude from low to high mass, throughout the redshift range $4 \lesssim z \lesssim 10$. The factors that may alleviate the high-mass end problem with $R_h = ct$, actually makes the comparison much worse for ΛCDM, increasing the disparity between predictions and observations. The weaker evolution in growth rate predicted by $R_h = ct$ is the vital reason for its success, indicating that massive galaxies must have formed earlier than predicted in the standard model, consistent with the observations.

The problem in ΛCDM may instead be reconciled with an evolution in the halo mass to light ratio, which could happen, e.g., if the initial mass function were top-heavy. Studies have shown, however, that this function should be the same at all redshifts $z \lesssim 8$ [48]. Hopefully, this conclusion can be tested using supernova rates in the future, which may eliminate even this last possible caveat for the significant tension between the observed halo mass function and ΛCDM. On the flip side, if it turns out that future observations with JWST support an evolution in the halo to stellar mass ratio of at least ~ 0.8 dex between $z \sim 4$ and 10, validating the predictions of ΛCDM, the inferred halo distribution will be in tension with the predictions of $R_h = ct$. The differences are so significant (at least several orders of magnitude) that a refinement of the halo distribution may produce one of the most robust comparative cosmological tests of these models.

6 Conclusion

In this paper, we have discussed an ongoing debate concerning the early appearance of massive galaxies (and their halos), which may challenge the formation of structure predicted by ΛCDM if the halo to stellar mass ratio is roughly constant in the redshift range $4 \lesssim z \lesssim 10$. This difficulty could be mitigated with a refinement of the underlying theory of star formation and galaxy evolution, but appears to require implausible modifications to the physics underlying these phenomena (Steinhardt et al. 2016). Some support for the existence of a real problem is provided by other types of "too early" problems, such as the premature appearance of supermassive black holes at $z \sim 6$–7 [45,46].

Combining our earlier measurement of σ_8 at redshift 0 [49] with our recently completed calculation of the growth function using the coupled Boltzmann and perturbed Einstein equations, we have re-analyzed "The Impossibly Early Galaxy Problem" in the context of $R_h = ct$ and showed that this problem virtually disappears in this cosmology even if the halo to stellar mass ratio is constant. Although, the $R_h = ct$ universe overpredicts the number density of halos by one to two orders of magnitude at the very high mass end, this problem may be mitigated by corrections to the Sheth–Tormen mass function, as indicated by the Bolshoi simulations [38]. Thus, once we resolve the question of whether or not this ratio evolved with redshift, the inferred halo mass distribution can clearly distinguish between the $R_h = ct$ and ΛCDM cosmologies.

The timeline in $R_h = ct$ allows both massive galaxies and supermassive black holes to form at very high redshifts without invoking exotic physics. It should also be noted that, while ΛCDM must rely on the unproven and as yet unverified physics of inflation to account for the generation of scale-invariant primordial fluctuations and a mechanism for driving the modes to exit and re-enter the horizon, thus creating an intricate mechanism for producing different growth rates at different epochs, no such complicated, fine-tuned mechanism is necessary in $R_h = ct$. This model does not have a horizon problem and does not incorporate inflation into its expansion history. As explained in more detail in Ref. [16], the growth of structure in $R_h = ct$ is simple, streamlined and does not require a different handling of small modes compared to the larger ones. Such simplicity, particularly when viewed in the context of the excellent agreement between theory and observations (Figs. 2, 3, 4, 5, 6, 7), adds considerable support for the viability of this cosmology.

Looking forward to upcoming surveys and further theoretical developments, it is already clear that observations, e.g., with JWST, will play a crucial role in determining the quasar distribution and the rate of gamma ray bursts from Pop III stars, both heavily dependent on the growth rates we have been discussing in this paper. There is therefore significant promise of improving the comparison we have made here even further, perhaps strongly ruling out one or other of these two models.

Acknowledgements We are grateful to Charles Steinhardt and Peter Behroozi for very informative discussions. FM is grateful to the Instituto de Astrofísica de Canarias in Tenerife and to Purple Mountain Observatory in Nanjing, China for their hospitality while part of this research was carried out.

Data Availability Statement This manuscript has no associated data or the data will not be deposited. [Authors' comment: All the data used in this paper have been previously published by other authors.]

Funded by SCOAP[3].

References

1. R.K. Sheth, H.J. Mo, G. Tormen, MNRAS **323**, 1 (2001)
2. V. Springel et al., Nature **435**, 629 (2005)
3. M. Vogelsberger et al., MNRAS **444**, 1518 (2014)
4. G. Holder, Z. Haiman, J. Mohr, ApJ **560**, L111 (2001)
5. S.R. Furlanetto, M. McQuinn, L. Hernquist, MNRAS **365**, 115 (2006)
6. Z. Haiman, A. Loeb, ApJ **552**, 459 (2001)
7. N.A. Grogin et al., ApJ **197**, 35G (2011)
8. P. Capak et al., A&A **558**, 67A (2013)
9. C.L. Steinhardt, P. Capak, D. Masters, J.S. Speagle, APJ **824**, 1 (2016)
10. P.S. Behroozi, R.H. Wechsler, C. Conroy, APJL **762**, L31 (2013)
11. P.S. Behroozi, R.H. Wechsler, C. Conroy, APJ **770**, 57 (2013)
12. P.S. Behroozi, J. Silk, ApJ **799**, 32 (2015)
13. S.L. Finkelstein et al., ApJ **814**, 95 (2015)
14. A. Rodríguez-Puebla, J.R. Primack, V. Avila-Reese, S.M. Faber, MNRAS **470**, 651 (2017)
15. M. Stefanon et al., ApJ **843**, 36 (2017)
16. M.K. Yennapureddy, F. Melia, PRD (to be submitted) (2019)
17. F. Melia, MNRAS **382**, 1917 (2007)
18. F. Melia, A&A **553**, A76 (2013)
19. F. Melia, Front. Phys. **11**, 119801 (2016)
20. F. Melia, Front. Phys. **12**, 121980 (2017)
21. F. Melia, M. Abdelqader, IJMP-D **18**, 1889 (2009)
22. F. Melia, A.S.H. Shevchuk, MNRAS **419**, 2579 (2012)
23. F. Melia, MNRAS **481**, 4855 (2018)
24. F. Melia, M. Fatuzzo, MNRAS **456**, 3422 (2016)
25. M.V. John, K.B. Joseph, PRD **61**, 087304 (2000)
26. M.V. John, MNRAS **484**, L35 (2019)
27. D.L. Shafer, PRD **91**, 103516 (2015)
28. A.G. Kim, Publ. Astron. Soc. Pac. **123**, 230 (2011)
29. J.-J. Wei, X. Wu, F. Melia, R.S. Maier, AJ **149**, 102 (2015)
30. F. Melia et al., EPL **123**, 59002 (2018)
31. H.-N. Lin, X. Li, Y. Sang, Chin. Phys. C **42**, 095101 (2018)
32. F. Melia, M. López-Corredoira, IJMP-D **26**, 1750055 (2017)
33. C.P. Ma, E. Bertschinger, ApJ **455**, 7 (1995)
34. J.M. Bardeen, PRD **22**, 1882B (1980)
35. M.K. Yennapureddy, F. Melia, PDU **20**, 65Y (2018)
36. T. Wong, ApJ **705**, 650 (2009)
37. W. Press, P. Schechter, ApJ **187**, 425 (1974)
38. A.A. Klypin, S. Trujillo-Gomez, J. Primack, ApJ **740**, 102 (2011)
39. H. Hildebrandt, J. Pielorz, T. Erben, L. Van Waerbeke, P. Simon, P. Capak, A&A **498**, 725 (2009)
40. O. Ilbert et al., A&A **556**, A55 (2013)
41. A. Leauthaud et al., ApJ **744**, 159 (2012)
42. Planck Collaboration et al., A&A **594**, A13 (2016)
43. K.S. Lee et al., ApJ **752**, 66 (2012)
44. K.I. Caputi et al., ApJ **810**, 73 (2015)
45. F. Melia, ApJ **764**, 72 (2013)
46. F. Melia, T.M. McClintock, Proc. R. Soc. A **471**, 20150449 (2015)
47. F. Melia, JCAP **01**, 027 (2014)
48. B. Dias, P. Coelho, B. Barbuy, L. Kerber, T. Idiart, A&A **520**, A85 (2010)
49. F. Melia, MNRAS **464**, 1966 (2017)

CHAPTER-7

Conclusion

In this thesis, we have shown through various model independent cosmological tests that R_h=ct is more likely to be a true cosmological model than ΛCDM. In the chapter-2 using HII galaxies, we have shown the R_h=ct has 69% likelihood probability of being true whereas the ΛCDM has less than 1%. These results indicate that the prediction of R_h=ct lies within about 1σ of the reconstructed curve whereas ΛCDM is excluded at over 2.6σ confidence. Similarly, in Chapter-3, using angular diameter distances inferred from strong gravitational lenses we have shown R_h=ct universe has a higher likelihood of being the correct cosmological model of the universe than ΛCDM. Also, in the Appendix- A and B we performed a similar analysis based on the angular diameter distance inferred from quasar cores and H(z) measurements inferred from cosmic chronometers and showed that these tests favour R_h=ct cosmological model than ΛCDM.

The tests in chapters - 2 and 3 based on the prediction for the homogeneous universe but the universe does contain galaxies and large scale structures which represent the inhomogeneous universe. In chapters-4 and 6 we showed that the observed timeline of structure formation favored R_h=ct. In particular, the predicted halo mass function in ΛCDM was in tension with observations; the ΛCDM cosmological model underpredicts the number of halos by at least four orders of magnitude. Whereas, the predicted halo mass function in the R_h=ct universe is consistent with observation throughout the redshift range $10 > z > 4$ very well at the low and intermediate mass end, and overpredicts by one to two orders of magnitude at the high mass end. This over-prediction may be due to two possible reasons: (1) The Bolshoi simulation has indicated that the Sheth-Tormen mass function overpredicts the number of halos by at least 10% at redshift $z \sim 0$, and overpredicts by at least 50% at redshift $z \sim 10$. Although simulations similar to Bolshoi haven't yet been carried out for R_h=ct, a trend analogous to this in the context of this model, would produce corrections that largely mitigate the problem at the high mass end; (2) This overprediction may also be due in part to observational selection effects that may be 'hiding' some of the sources. Some massive galaxies may have been missed due to extinction, which future observations might be able to address. Moreover, including these corrections for ΛCDM will make its predictions even worse rather than mitigating the problem. Besides, the

timeline in R_h=ct allows both massive galaxies and supermassive black holes to form at very high redshifts without invoking exotic physics. It should also be noted that, while ΛCDM must rely on the unproven and as yet unverified physics of inflation to account for the generation of scale-invariant primordial fluctuations and a mechanism for driving the modes to exit and re-enter the horizon, thus creating an intricate mechanism for producing different growth rates at different epochs, no such complicated, fine-tuned mechanism is necessary in R_h=ct. This model does not have a horizon problem and does not incorporate inflation into its expansion history whereas the growth of structure in R_h=ct is simple, streamlined and does not require different handling of small modes compared to the larger ones. Such simplicity, particularly when viewed in the context of the excellent agreement between theory and observations, adds considerable support for the viability of this cosmology.

All the tests shown in this thesis indicate that R_h=ct universe describes the universe better than the standard cosmological model. More importantly, the R_h=ct with its only free parameter passing through all the test better than ΛCDM (with its five free parameters) indicates that R_h=ct is more viable than the ΛCDM cosmological model. The below table summarizes all the tests performed thus far.

Tabel 7.1: Model Comparisons between R_h=ct and ΛCDM

Tests or Observational Conflict/Tension	Outcome	Reference
Angular Correlation Function of the CMB	R_h= ct fits it very well; standard inflationary ΛCDM misses by >> 3σ	Ref. [1]
Massive halo growth at $4 \lesssim z \lesssim 10$	**Data consistent with R_h= ct; ΛCDM misses by~10^4**	**Ref. [2, 3]**
Electroweak Horizon Problem	R_h= ct does not have it; ΛCDM has no solution	Ref. [4]
Missing progenitors of high-z quasars	In tension with ΛCDM, but consistent with timeline in R_h= ct	Ref. [5]
Angular-diameter distance test with quasar cores	**R_h= ct is favoured over ΛCDM with BIC likelihood 81% vs 19%**	**Ref. [6, 7]**
HII Hubble diagram	**R_h= ct is favoured over ΛCDM with BIC likelihood 93% vs. 7%**	**Ref. [8, 9]**
Alcock-Paczynski test with the BAO scale	R_h= ct is favoured over ΛCDM at a 2.6σ C.L.	Ref. [10]
FSRQ γ-ray luminosity function	R_h= ct is very strongly favoured over ΛCDM with $\Delta \gg 10$	Ref. [11]

QSO Hubble diagram + Alcock-Paczynski	R_h= ct is about 4 times more likely than ΛCDM to be correct	Ref. [12]
Constancy of the cluster gas mass fraction	R_h= ct is favoured over ΛCDM with BIC likelihood 95% vs 5%	Ref. [13]
Cosmic Chronometers	**R_h= ct is favoured over ΛCDM with BIC likelihood 95% vs 5%**	**Ref. [14, 15]**
Cosmic age of old clusters	ΛCDM can't accommodate high-z clusters, but R_h= ct can	Ref. [16]
High-z quasars	Evolution timeline fits within R_h= ct, but not ΛCDM	Ref. [17, 18, 19]
The AGN Hubble diagram	R_h= ct is favoured over ΛCDM with BIC likelihood 96% vs 4%	Ref. [20]
Age vs. redshift of old passive galaxies	R_h= ct favoured over ΛCDM with BIC likelihood 80% vs 20%	Ref. [21]
Type Ic superluminous supernovae	R_h= ct is favoured over ΛCDM with BIC likelihood 80% vs 20%	Ref. [22]
The SNLS Type Ia SNe	R_h= ct is favoured overΛCDM with BIC likelihood 90% vs 10%	Ref. [23]
Angular size of galaxy clusters	R_h= ct is favoured overΛCDM with BIC likelihood 86% vs 14%	Ref. [24]
Strong gravitational lensing galaxies	**Both models fit the data very well due to the bulge-halo 'conspiracy'**	**Ref. [25, 26]**
Time delay lenses	R_h= ct is favoured over ΛCDM with BIC likelihood 80% vs 20%	Ref. [27]
High-z galaxies	Evolution timeline fits within R_h= ct, but not ΛCDM	Ref. [28]
GRBs + star formation rate	R_h= ct is favoured over ΛCDM with AIC likelihood 70% vs 30%	Ref. [29]
High-z quasar Hubble diagram	R_h= ct is favoured over ΛCDM with BIC likelihood 85% vs 15%	Ref. [30]
GRB Hubble diagram	R_h= ct is favoured over ΛCDM with BIC likelihood 96% vs 4%	Ref. [31]

The upcoming surveys such as JWST will play a crucial role in determining the quasar distribution and the rate of gamma-ray bursts from Pop III stars which will be valuable in probing the timeline of structure formation as both are heavily dependent on the growth rates and expansion rate of the universe. Therefore, there exists significant promise of improving the comparison we have made in the thesis even further, perhaps strongly ruling out one or other of these two models.

References:

[1] Melia, F. & López-Corredoira, M., 2017, IJMP-D, 26, id. 1750055

[2] Steinhardt, C. L., Capak, P., Masters, D. & Speagle, J. S., 2016, ApJ, 824, 1

[3] Yennapureddy, M. K. & Melia, F., 2018b, PDU, 20, 65

[4] Melia, F., 2018b, EPJ-C, in press (arXiv:1809.02885)

[5] Fatuzzo, M. & Melia, F., 2017, ApJ, 846, 129

[6] Melia, F., 2018a, EPL, 123, id. 39001

[7] Melia, F. & Yennapureddy, M. K., 2018, MNRAS, 480, 2144

[8] Wei, J.-J., Wu, X.-F. & Melia, F., 2016, MNRAS, 463, 1144

[9] Leaf, K. & Melia, F., 2018b, MNRAS, 474, 4507

[10] Melia, F. & López-Corredoira, M., 2017, IJMP-D, 26, id. 1750055

[11] Zeng, H., Melia, F. & Zhang, L., 2016, MNRAS, 462, 3094

[12] López-Corredoira, M., Melia, F., Lusso, E. and Risaliti, G., 2016,IJMP-D, 25, id. 1650060

[13] Melia, F., 2016b, Proc. R. Soc. A, 472, 20150765

[14] Melia F. and Maier R. S., 2013, MNRAS, 432, 2669

[15] Melia, F. and McClintock, T. M., 2015a, AJ, 150, id. 119

[16] Yu, H. & Wang, F. Y., 2014, Eur. Phys. J. C, 74, 3090

[17] Melia, F., 2013b, ApJ, 764, 72

[18] Melia, F., 2018c, A&A, 615, A113

[19] Melia, F. and McClintock, T. M., 2015b, Proc. R. Soc. A,

[20] Melia, F., 2015, ASpSci 359, 34

[21] Wei, J.-J., Wu, X., Melia, F., Wang, F.-Y. and Yu, H., 2015a, AJ,150, id. 35

[22] Wei, J.-J., Wu, X. and Melia, F., 2015b, AJ, 149, id. 165

[23] Wei, J.-J., Wu, X., Melia, F. and Maier, R. S., 2015c, AJ, 149, id.102

[24] Wei, J.-J., Wu, X. and Melia, F., 2015d, MNRAS, 447, 479

[25] Melia, F., Wei, J.-J. & Wu, X., 2015, AJ, 149, 2

[26] Leaf, K. & Melia, F., 2018b, MNRAS, 474, 4507

[27] Wei, J.-J., Wu, X. and Melia, F., 2014a, ApJ, 788, id. 190

[28] Melia, F., 2014a, AJ, 147, 120

[29] Wei, J.-J., Wu, X., Melia, F., Wei, D.-M. and Feng, L.-L., 2014b, MNRAS, 439, 3329

[30] Melia, F., 2014b, JCAP, 01, 027

[31] Wei, J.-J., Wu, X. and Melia, F., 2013, ApJ, 772, id. 43

APPENDIX-A

The maximum angular-diameter distance in cosmology

Fulvio Melia, Manoj K. Yennapureddy

Published In: Monthly Notices of Royal Astronomical Society
DOI: 10.1093/mnras/sty1962

In chapter 2, 3, 4 and 6, we have shown using the tests based on HII galaxies Hubble diagram, and angular diameter distances inferred from strong gravitational lenses and the halo mass function favour the R_h=ct universe than the standard ΛCDM cosmological model. In this appendix, we extend this analysis and test R_h=ct and ΛCDM cosmological models using angular diameter distance inferred from quasar cores. In particular, the angular-diameter distance $d_A(z)$ uniquely reaches a maximum (at z_{max}) and then shrinks to zero towards the big bang. The location of this turning point depends sensitively on the cosmological model. By employing 140 quasar cores, we reconstruct the angular diameter distance using Gaussian processes, and compare the predictions of seven different cosmologies and showing that the measured value of z_{max} can effectively discriminate between them. We find that z_{max} = 1.70 ± 0.20 – a crucial new probe of the Universe's geometry. The most strongly favoured model is R_h=ct, followed by Planck ΛCDM. According to the results of this appendix, the R_h=ct universe, which predicts zmax = 1.718, has a 92.8% probability of being the correct cosmology whereas Planck ΛCDM has 59.6% of probability for being correct.

Monthly Notices
of the
ROYAL ASTRONOMICAL SOCIETY

MNRAS **480,** 2144–2152 (2018)
Advance Access publication 2018 July 23

doi:10.1093/mnras/sty1962

The maximum angular-diameter distance in cosmology

Fulvio Melia[1]★† and Manoj K. Yennapureddy[2]

[1]*The University of Arizona, AZ 85721, USA*
[2]*Department of Physics, The University of Arizona, AZ 85721, USA*

Accepted 2018 July 19. Received 2018 July 19; in original form 2017 November 16

ABSTRACT

Unlike other observational signatures in cosmology, the angular-diameter distance $d_A(z)$ uniquely reaches a maximum (at $z_{\rm max}$) and then shrinks to zero towards the big bang. The location of this turning point depends sensitively on the model, but has been difficult to measure. In this paper, we estimate and use $z_{\rm max}$ inferred from quasar cores: (1) by employing a sample of 140 objects yielding a much reduced dispersion due to pre-constrained limits on their spectral index and luminosity, (2) by reconstructing $d_A(z)$ using Gaussian processes, and (3) comparing the predictions of seven different cosmologies and showing that the measured value of $z_{\rm max}$ can effectively discriminate between them. We find that $z_{\rm max} = 1.70 \pm 0.20$ – an important new probe of the Universe's geometry. The most strongly favoured model is $R_{\rm h} = ct$, followed by *Planck*ΛCDM. Several others, including Milne, Einstein-de Sitter, and Static tired light are strongly rejected. According to these results, the $R_{\rm h} = ct$ universe, which predicts $z_{\rm max} = 1.718$, has a ∼92.8 per cent probability of being the correct cosmology. For consistency, we also carry out model selection based on $d_A(z)$ itself. This test confirms that $R_{\rm h} = ct$ and *Planck*ΛCDM are among the few models that account for angular-size data better than those that are disfavoured by $z_{\rm max}$. The $d_A(z)$ comparison, however, is less discerning than that with $z_{\rm max}$, due to the additional free parameter, H_0. We find that $H_0 = 63.4 \pm 1.2$ km s^{-1} Mpc^{-1} for $R_{\rm h} = ct$, and 69.9 ± 1.5 km s^{-1} Mpc^{-1} for ΛCDM. Both are consistent with previously measured values in each model, though they differ from each other by over 4σ. In contrast, model selection based on $z_{\rm max}$ is independent of H_0.

Key words: galaxies: active – cosmological parameters – distance scale – cosmology: observations – cosmology: theory.

1 INTRODUCTION

Several attempts to measure the angular diameter distance, $d_A(z)$, have been made over the past three decades, but so far only with limited success due to a lack of evident 'standard rulers' and limitations from possible size evolution with redshift. Recently, however, our understanding of compact quasar cores has improved to the point where one may now use the central, opaque regions in a luminosity-constrained sample as reliable measuring rods. These show negligible redshift evolution in the range $0 \lesssim z \lesssim 3$, allowing us to examine the geometry of the Universe over an even larger fraction of its age than is possible with Type Ia SNe.

Below, we will trace the history that has brought us to this point where we can meaningfully measure the redshift $z_{\rm max}$ at which $d_A(z)$ attains its maximum and use it to test various cosmological models. This is a unique aspect of the angular diameter distance, which none of the other observable signatures possess. To gauge its impact, consider that $z_{\rm max} = \infty$ in a model such as the Milne universe (see e.g. Vishwakarma 2013; Chashchina & Silagadze 2015), so one need only show that $z_{\rm max}$ is finite – no matter what its actual value is – in order to rule out this cosmology.

Rather than pre-assuming a parametric form for $d_A(z)$ based on each individual cosmology, we will employ Gaussian processes (GP, Rasmussen & Williams 2006; Holsclaw et al. 2010; Seikel, Clarkson & Smith 2012; Yennapureddy & Melia 2017, 2018a,b) to reconstruct the angular diameter distance to the compact quasar cores in a model-independent fashion. This has the dual benefit of (1) permitting us to compare the measured and predicted values of $z_{\rm max}$ without any bias, and (2) to reliably measure $z_{\rm max}$ even if it turns out that none of the models considered here is actually correct.

In addition, to avoid the possibility that a model may match the value of $z_{\rm max}$ rather well while still not adequately accounting for the overall reconstructed angular-diameter distance, we shall also carry out model selection based on the optimization of $d_A(z)$ over

★ E-mail: fmelia@email.arizona.edu
† John Woodruff Simpson Fellow.

the observed redshift range. Though related, these two diagnostics do not overlap completely. Note, e.g. that while fitting $d_A(z)$ to the reconstructed curve requires an optimization of the Hubble constant H_0, a determination of $z_{\max}$ is completely independent of the measured expansion rate. Thus, a consistent prioritization of the models using these two approaches will be more robust than model selection based on either of them alone. The model testing based on a comparison of the predicted and reconstructed $d_A(z)$ functions will be facilitated by our recent development of a differential area statistic introduced for this purpose in Yennapureddy & Melia (2018a,b).

In Section 2 of this paper, we will summarize the various stages of development behind the approach of measuring $d_A(z)$, highlighting the critical steps that have produced a sample of sources whose compact cores may be used as standard rulers. We then briefly describe in Section 3 the Gaussian processes approach that will allow us to analyse these data in a cosmology independent way. The data and our method of analysis are presented in Section 4, and we use the measured value of $z_{\max}$ to compare seven different models in Section 5. We will discuss the results based on the analysis of $z_{\max}$ in Section 6 and then independently carry out model selection based on how well the angular-diameter distance $d_A(z)$ compares with the GP reconstruction over the entire redshift range in Section 7. For the tests we carry out in this paper, we do not need to know the actual size of the compact structure. It will be interesting to see how its recent measurement (Cao et al. 2017b) impacts our interpretation of the Hubble constant for each model, however, and we discuss this outcome in Section 8. We end with our conclusions in Section 9.

2 BACKGROUND

An early suggestion to optimize cosmological parameters by using the angular diameter distance to compact radio sources assumed to have a fixed reference length was made by Kellermann (1993), whose analysis argued for a cosmological density close to its critical value. This claim, however, appeared to have been premature given the possible influence of source evolution with redshift. Krauss & Schramm (1993) demonstrated that the position of $z_{\max}$ depends sensitively on the parameters, particularly the density of dark energy. They concluded that even an evolution of less than 30 per cent in source size at $z \lesssim 2$ could completely alter the outcome, thereby recommending that one must conclusively rule out source evolution in order to use a measurement of $z_{\max}$ as a reliable tool for cosmology.

One possible way to mitigate the impact of source evolution is to base the standard ruler on the separation of quasar pairs (Phillipps 1994), but to establish significant constraints on the cosmological parameters one needs a sample of several hundred pairs of physically related quasars at $z > 1$. Even then, one needs to have an accurate assessment of the distribution of pair separations. Phillipps, Horleston, and White (2002) also developed a variation on this theme, considering a proximity effect based on the observed deficit of Lyα forest lines at redshifts close to that of the illuminating quasar. The size of the deficient region is presumably related to the central engine's absolute luminosity. Unfortunately, this effect is difficult to disentangle from other factors, such as the intergalactic ionizing flux.

A concerted effort to better understand the evolution of radio sources and its impact on the measurement of an angular diameter distance was therefore initiated by Gurvits (1994) and Kayser (1995), who attempted to estimate how much evolution was actually occurring as a function of redshift and to what degree this affected the optimization of the model parameters. Gurvits modelled the luminosity dependence of the compact source size as $l \sim L^{\beta}(1+z)^n$, and obtained a best fit with $\beta = 0.26 \pm 0.03$ and $n = -0.30 \pm 0.90$. As we shall see shortly, however, a persistent complication with compact radio sources is that they comprise a mixture of quasars, BL Lacs, OVVs, and others, so systematic differences among them cannot be so easily disentangled from actual cosmological variations. Not surprisingly therefore this initial attempt was not very successful in identifying the correct cosmological model. This point was amplified by Kayser, who carefully re-analysed the VLBI compact source data taking into account biasing of the sample from the limited resolution, and concluded at that time that a measurement of the angular diameter distance to these objects could not be used to differentiate between different models. Dabrowski, Lasenby, and Saunders (1995) also pointed out that relativistic beaming cannot be ignored in such sources, since a flux-limited sample of them contains a projected-size distribution that is biased. Without a more careful identification of an appropriate sample, this approach therefore has a tendency to produce null results.

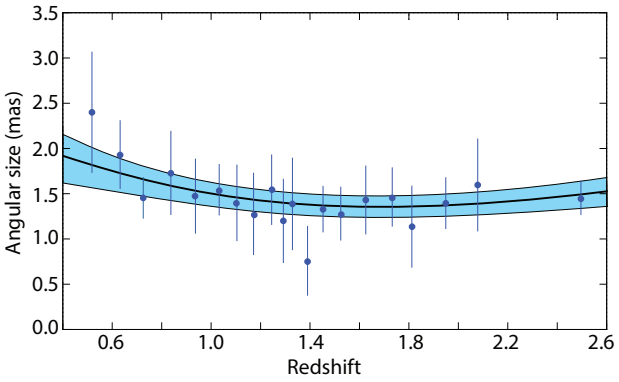

Figure 1. Angular size of 140 compact quasar cores divided into bins of seven, as a function of redshift. Each datum represents the median value in its bin. The thick solid curve is the reconstructed angular-size function using Gaussian processes, while the shaded region shows the 1σ variation.

The unknown mixture of different quasar types and their possible evolution with redshift also affected the precision with which Jackson and Dodgson (1997) could use the angular diameter distance to compact cores to identify the importance of dark matter in the expansion dynamics. None the less, their analysis of the angular diameter size versus redshift relation for 256 ultracompact sources with $0.5 < z < 3.8$ did reveal a preference for a cosmology containing dark energy over one based solely on cold dark matter.

The first evidence that $d_A(z)$ might not increase indefinitely emerged in a study of double-lobed quasars within the redshift range $1.0 \lesssim z \lesssim 2.7$ (Buchalter et al. 1998). The apparent angular size of these objects remained more or less constant with angular-diameter distance, as one might crudely expect in most Friedmann–Robertson–Walker (FRW) cosmologies without any significant evolution (see Fig. 1). The well-known exception is the Milne universe, for which $d_A(z)$ increases with redshift everywhere. Similar constraints using radio galaxies as standard rulers were obtained by Podariu et al. (2003). In both cases, however, the results were weaker than those based on other kinds of observation, e.g. Type Ia SNe.

Unlike compact cores, quasars with extended jets are subject to long-term dynamical evolution and the possible influence of environment on their structure extending over galactic scales. A more specific component within the jets, i.e. shocks whose linear diameter could in principle be a standard ruler (Wiik & Valtaoja 2001), was promising, although the need to estimate their extent by monitoring their flux density and measuring light travel times, constituted a heavy reliance on the pre-assumed cosmology. The outcome was therefore compliant to the model via a somewhat circular argument. Much of the subsequent work with radio sources since that time has therefore focused on trying to reduce the scatter in the angular diameter size versus redshift relation for compact radio sources. And one of the earliest breakthroughs in this direction was made by Gurvits, Kellermann & Frey (1999), who studied 330 5 Ghz VLBI contour maps (see also Frey 1999) in the redshift range $0.011 < z < 4.72$, demonstrating that the dispersion in this relation could be significantly reduced by restricting the sample to only those compact regions with a spectral index $-0.38 \leq \alpha \leq 0.18$ and a total luminosity density $Lh^2 \geq 10^{26}$ W Hz^{-1} (with h the Hubble constant in units of 100 km s^{-1} Mpc^{-1}). This constraint on the spectral index still appears to be valid today and we shall use it, along with more recently developed criteria, to arrive at the sample used in this paper.

Our current view of jet launching in quasars and radio galaxies suggests that the base emission is dominated by self-absorbed synchrotron emission (Blandford & Königl 1979; Melia & Königl 1989), creating optically-thick features with angular diameters in the milliarcsecond (mas) range. At typical distances, these cores extend over roughly 10 parsecs. It is therefore likely that such small features are influenced very little by the large-scale environment of the parent galaxies and kpc-scale jets, so their physical attributes should be similar from source to source and reasonably stable over the time they are seen (Kellermann 1993; Jackson 2004, 2008). It is thought that the morphology and kinematics of compact quasar cores are controlled by only a handful of parameters associated with the central engine itself, including its mass (and possibly the spin). Therefore, since opaque features in compact quasar cores typically last only tens of years (Gurvits, Kellermann & Frey 1999), they are expected to be free of long-term evolutionary effects in the active galactic nucleus (AGN), where they are found.

These theoretical ideas, along with the identification by Gurvits, Kellermann & Frey (1999) of a sub-sample of quasar cores with a reduced scatter in their apparent size, have generated increasing interest in using the latter as standard rulers. Lima and Alcaniz (2002) constrained the cosmic equation of state with this approach, assuming a flat FRW model driven by matter and dark energy. Like several other ensuing efforts, however, their model fits were characterized by rather large values of $\chi^2_{\rm dof}$ (the χ^2 per degree of freedom), indicating that the scatter in the sample was still too large to draw any definitive conclusions. In retrospect, it is not surprising that their optimized values of the model parameters are not a good match to the latest consensus (i.e. *Planck*) measurements. Similar work by Zhu and Fujimoto (2002) and Chen and Ratra (2003), using the sample of Gurvits, Kellermann & Frey (1999), attempted to constrain model parameters in cosmologies with a variable dark energy component and produced interesting limits, though weaker than those based on other methods.

An early attempt at using angular diameter distance measurements of milliarcsecond compact quasar cores to test alternative cosmological expansion scenarios was carried out by Jain, Dev, and Alcaniz (2003), who simply modelled the expansion factor as a power law in time ($a \sim t^\beta$), and concluded that the data at that time favoured a cosmic evolution with $\beta = 1$. Without the refinements we will discuss below, however, their sample had too much scatter and the errors were simply too large for them to say anything definitive about the value of $z_{\rm max}$. None the less, it is interesting to note that even with the inferior set of data at their disposal, their analysis seemed to indicate that a linear expansion was favoured by the observations. As we shall see later in this paper, our comparison of various cosmologies using compact quasar cores will demonstrate that the $R_{\rm h} = ct$ universe is favoured over the other models. This cosmology features a linear expansion, so our results appear to be consistent with those of Jain, Dev, and Alcaniz (2003).

The sample of ultracompact radio sources often used in such studies today is that assembled by Jackson and Jannetta (2006), extracted from an old 2.29 GHz VLBI survey of Preston et al. (1985) and additions by Gurvits (1994). Their own application of these data to construct the angular diameter versus redshift diagram produced results more in line with those based on observations of the CMB, including a measurement of the angular size of the acoustic horizon. We ourselves will also use this catalogue as the basis of our analysis, though with several critical improvements that we shall discuss shortly. These refinements are necessary because, as alluded to earlier, a persistent complication with ultracompact cores is that they constitute a mixed population of AGNs – quasars, BL Lacs, OVVs, etc. – making it difficult to disentangle systematic differences from true cosmological variations.

The recent introduction of an additional luminosity restriction applied to sources in the compact core sample, used in conjunction with the constraint on the spectral index α used earlier by Gurvits, Kellermann & Frey (1999), appears to have overcome this weakness. These authors, and independently Vishwakarma (2001), had already shown that the exclusion of sources with low luminosities L could mitigate the dependence of the intrinsic core size on L and redshift z. In their analysis of the Jackson and Jannetta (2006) sample, Cao et al. (2017a,b) have demonstrated a strong dependence of the core size $\ell_{\rm core}$ on luminosity, not just at the low end (as had been noted earlier), but also at the high end as well (see also Cao et al. 2015; Li et al. 2016; Zheng et al. 2017). Adopting the parametrization $\ell_{\rm core} = \ell_0\, L^\gamma (1+z)^n$, where ℓ_0 is simply a scaling constant, they showed that only a sub-sample of intermediate-luminosity radio quasars in the range 10^{27} W/Hz $< L < 10^{28}$ W/Hz have a core size with negligible dependence on luminosity and redshift. For these sources, $\gamma \approx 10^{-4}$ and $|n| \approx 10^{-3}$. Therefore, it appears that a sub-sample selected from the Jackson and Jannetta catalogue with a restricted spectral index α and luminosity L constitutes a compilation of compact radio cores with a reliable standard linear size.

This is the procedure we shall follow in this paper to measure $z_{\rm max}$ with unprecedented accuracy and to compare cosmological models in ways not previously possible using other measures of cosmological distance. In addition, we will avoid any possible biasing of the results by reconstructing the angular diameter distance of the compact cores using Gaussian processes (GP), which we now describe.

3 GAUSSIAN PROCESSES

Most fitting procedures require the pre-assumption of a parametric form for the fitting function tailored to the specific properties of the cosmological model. The Gaussian Processes (GP) approach (Seikel et al. 2012) avoids this shortcoming and is thereby not subject to the possibility that the predicted signature may, or may

not, be a reasonable representation of the actual redshift-dependence of the measurements.[1]

To model a function f(x) rigorously without relying on any prior parametric form, the GP procedure assumes that the n observations of a data set $\mathrm{y} = \{y_1, y_2, ..., y_n\}$ are sampled from a multivariate Gaussian distribution. The mean of the GP partnered to the data is taken to be zero. Note, however, that while modelling the data with GP is straightforward, one must face two potential areas of ambiguity with this technique. We describe these here and present steps we have developed to ensure that the outcome of the reconstruction is not affected significantly by our choice of GP components.

The first of these arises because the values of the function evaluated at different points x_1 and x_2 are not independent of each other. One must therefore introduce a covariance function $k(x_1, x_2)$ to deal with the linkage between neighbouring points. The difficulty is that $k(x_1, x_2)$ is not unique or well known. There is often a broad range of such covariances. Indeed, while it makes sense to pick a function that depends only on the distance between neighbouring points, this is actually not required. Most applications of this work adopt a squared exponential,

$$k(x_1, x_2) = \sigma_f^2 \exp\left(-\frac{(x_1 - x_2)^2}{2l^2}\right), \quad (1)$$

which is infinitely differentiable and useful for reconstructing both the function representing the data and its derivative.

The so-called hyperparameters σ_f and l are not parameters in the usual sense, since they do not specify the form of the function, but rather its 'bumpiness.' The length l characterizes the distance in x corresponding to a significant variation of the reconstructed function. The dependence in the ordinate direction is scaled by the signal variance σ_f. Equation (1) for $\{x_1, x_2, ..., x_n\}$ observation points leads to the covariance matrix

$$K = \begin{bmatrix} k(x_1, x_1) & k(x_1, x_2) & ..... & k(x_1, x_n) \\ k(x_2, x_1) & k(x_2, x_2) & ..... & k(x_2, x_n) \\ ..... & ..... & ..... & ..... \\ k(x_n, x_1) & k(x_n, x_2) & ..... & k(x_n, x_n) \end{bmatrix}. \quad (2)$$

The introduction of a new observation point x_* requires the evaluation of the vector

$$K_* \equiv \begin{bmatrix} k(x_*, x_1) & k(x_*, x_2) & ..... & k(x_*, x_n) \end{bmatrix}, \quad (3)$$

and the quantity $K_{**} \equiv k(x_*, x_*)$. Given that the data are assumed to be represented as a sample from a multivariate GP,

$$\begin{bmatrix} y \\ y_* \end{bmatrix} = N\left(0, \begin{bmatrix} K & K_*^T \\ K_* & K_{**} \end{bmatrix}\right), \quad (4)$$

the reconstruction entails the maximization of the conditional probability

$$p(y_*|y) \sim N(K_* K^{-1} y, K_{**} - K_* K^{-1} K_*^T). \quad (5)$$

This distribution has a mean y_*, which is given as

$$\mu(y_*) = K_* K^{-1} y, \quad (6)$$

with a corresponding uncertainty

$$\mathrm{var}(y_*) = K_{**} - K_* K^{-1} K_*^T. \quad (7)$$

[1]The full details of this implementation may be found in Seikel et al. (2012), and a catalogue of useful algorithms is maintained at http://www.acgc.uct.ac.za/seikel/GAPP/index.html

The reconstructed function shown in Fig. 1 is based on the use of the kernel in equation (1). To ensure that our measurement of $z_{\max}$ is not being unduly affected by this choice of covariance function, we also carry out a parallel set of simulations using a very different kind of kernel known as a Matérn covariance function, specifically the one called Matérn92 (Seikel et al. 2012), whose explicit form is

$$k(x_1, x_2) = \sigma_f^2 \exp\left(-\frac{3|x_1 - x_2|}{l}\right)\left(1 + \frac{3|x_1 - x_2|}{l} + \frac{27|x_1 - x_2|^2}{7l^2} + \frac{18|x_1 - x_2|^3}{7l^3} + \frac{27|x_1 - x_2|^4}{35l^4}\right). \quad (8)$$

In so doing, we confirm the results of previous workers, which show that the choice of kernel may change the p-values by a few points, though the outcome of model comparisons is not altered qualitatively. The rank ordering of models listed in Table 1 is completely unaffected by the choice of covariance function.

The second potential ambiguity is associated with the hyperparameters themselves. An often used approach is to train them by maximizing the likelihood that the reconstructed function reproduces the measured values at the data points x_i. The caveat is that for a purely Bayesian analysis, the hyperparameters should be marginalized over instead of being optimized, but for our application (as is commonly the case), the marginal likelihood is sharply peaked, so optimization is a good approximation to marginalization. The bottom line is that for a set of data such as we have here (see Fig. 1), there is actually no freedom to choose σ_f and l separately once we carry through with the optimization procedure described above.

4 DATA AND ANALYSIS

As we have seen from the above discussion, we may now choose from the many hundreds of available VLBI images a reduced sample of quasar cores with manageable scatter and little, if any, evolutionary effects by excluding those sources with low and high luminosities, L, and extreme spectral indices, α. Specifically, the dispersion in (linear) core size ℓ_{core} is significantly mitigated by selecting only sources with $-0.38 < \alpha < 0.18$ (Gurvits, Kellermann & Frey 1999; Cao et al. 2017a,b), and an intermediate-luminosity $10^{27}\,\mathrm{W/Hz} < L < 10^{28}\,\mathrm{W/Hz}$ (Cao et al. 2017). These two criteria result in a compact quasar-core catalogue with robust standard linear sizes.

The data we use here are drawn from the 613 sources assembled by Jackson and Jannetta (2006) using the 2.29 GHz VLBI survey of Preston et al. (1985) and additions by Gurvits (1994). We use the *Planck* optimized parameters (Planck Collaboration XIII 2016) to estimate the luminosity distance which, together with the measured total flux density at 2.29 GHz, gives the luminosity L, which may be used to extract the subsample with intermediate-luminosities. In doing so, we are giving *Planck*ΛCDM the benefit of the doubt, but note that this procedure is used merely to estimate L; these parameters are not used in any other way during the model comparisons described below, so the results are not biased by this approach. Reducing the sample further by restricting the range of α produces a final catalogue of 140 sources for our analysis. We bin these sources into groups of seven and select the median value in each bin to represent the angular size (Santos & Lima 2008). We take this step to partially minimize an additional degree of scatter that would otherwise appear using the individual data points. The resulting 20 data points are plotted in Fig. 1, along with their 1σ errors estimated

Table 1. $z_{\rm max}$ for seven cosmological models.

Model	$z_{\rm max}$	$\mid z_{\rm max} - z_{\rm max}^{\rm obs} \mid / \sigma$	Probability (%)
$R_{\rm h} = ct$	1.718	0.09	92.8
*Planck*ΛCDM	1.594	0.53	59.6
Einstein-de Sitter	0.682	5.09	∼0
Milne universe	∞	∞	0
Static Euclidean	∞	∞	0
Static Euclidean tired light	∞	∞	0
Static Euclidean plasma tired light	∞	∞	0

assuming Gaussian variation within each bin. The caveat with this approach is that the scatter may not be purely Gaussian, e.g. if there is some contribution from an unspecified systematic effect. In future work, we will address this question using a two-point diagnostic method we have already applied to other kinds of data, such as $H(z)$ versus z (Leaf & Melia 2017a) and the HII galaxy Hubble diagram (Leaf & Melia 2017b). As we have shown in these previous applications, the two-point diagnostics very effectively indicate the quality of the errors and their likely contributions.

The angular-diameter distance (solid curve) reconstructed with Gaussian processes (GP, Rasmussen & Williams 2006; Holsclaw et al. 2010; Seikel et al. 2012; Yennapureddy & Melia 2017, 2018a,b) allows us to study the geometry of the Universe in a new, unique way. Compact radio cores have been mapped with VLBI as far out as $z \sim 4$, allowing us to probe the geometry of the Universe over 80 per cent of its existence. This happens to be the redshift range within which $d_A(z)$ first increases, reaches a maximum at some $z_{\rm max}$, and then shrinks to zero as $z \to \infty$. The physics behind this phenomenon is actually easy to understand (Melia 2013). The angular-diameter distance is based on the measurement of a lateral proper size, so we see the object in projection as it was when it emitted the light approaching us today. But all sources were closer to us as we look back in cosmic time, so the *apparent* angular size $\theta_{\rm core}$ of compact quasar cores actually increases as $z \to \infty$, meaning that $d_A(z)$ ($\sim\theta_{\rm core}^{-1}$) therefore gets smaller.

We emphasize that as long as $\ell_{\rm core}$ is a true standard ruler, at least in an average sense, we do not need to know its actual value to identify $z_{\rm max}$ because we are simply sampling the ratio of scales at different redshifts. We also do not need to know the Hubble constant, H_0, which does not affect the location of the turning point in $d_A(z)$. The net result is that the GP reconstruction shown in Fig. 1 is completely free of any cosmological model and assumptions. The turning point $z_{\rm max}$ may then be used unambiguously to test the predictions of the models described below.

To find the error associated with this measurement of $z_{\rm max}$, we adopt the following procedure. We use the data and their 1σ errors shown in Fig. 1 to create mock samples of 20 values of the core size, $\theta_i \equiv \theta(z_i)$, with the same redshifts, z_i ($i = 1, ..., 20$), as the actual measurements, but with Gaussian randomized values $\theta_{\rm mock}(z_i) = \theta(z_i) + r\sigma_i$, where r is a Gaussian random variable with mean 0, and variance 1, and σ_i is the dispersion at z_i.

Then, for each mock sample, we redo the Gaussian-process reconstruction to find its corresponding $z_{\rm max}$, and repeat this process 50 000times. The distribution of $z_{\rm max}$ values thus constructed is shown as a histogram in Fig. 2. This distribution approximates a Gaussian, but not completely given that the data are truncated at $z \sim 2.6$. Its mean redshift is consistent with our measured value $z_{\rm max} = 1.70$ at the maximum d_A (i.e. the minimum $\theta_{\rm core}$). Crucially, approximating this distribution as a Gaussian (shown as a solid black curve in Fig. 2), we find that 68.2 per cent of the realizations occur within a standard deviation $\sigma_{z_{\rm max}} = 0.20$, which we adopt as a reasonable estimate of the measurement error for $z_{\rm max}$.

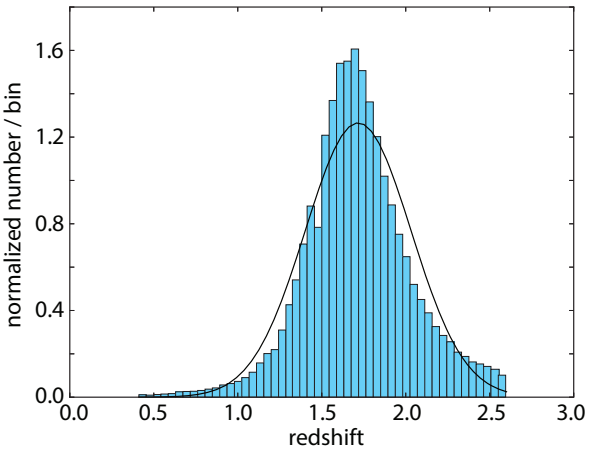

Figure 2. Distribution of $z_{\rm max}$ values calculated from 50 000 mock samples generated from the data and errors shown in Fig. 1 (see the text). The histogram is truncated at $z \sim 2.6$ due to a lack of data beyond this point. Modelling this distribution as an approximate Gaussian, we find that 68.2 per cent of the realizations lie within a standard deviation $\sigma_{z_{\rm max}} = 0.20$ of the measured value $z_{\rm max} = 1.70$.

5 COSMOLOGICAL MODELS

We will compare the measured value of $z_{\rm max}$ with the prediction of seven different cosmological models, each with its unique expression for the angular-diameter distance, $d_A(z)$. As noted, the Hubble constant does not affect $z_{\rm max}$, so we do not need to specify its value.

(i) The flat *Planck*ΛCDM model, with parameters $\Omega_{\rm m}$, Ω_Λ and a dark-energy equation of state $w_\Lambda = -1$. In the following expressions, Ω_i is the energy density of species i, scaled to today's critical density, $\rho_c \equiv 3c^2H_0^2/8\pi G$. For this model,

$$d_A(z) = \frac{c}{H_0}\frac{1}{1+z}\int_0^z \frac{{\rm d}u}{\sqrt{\Omega_m(1+u)^3 + \Omega_\Lambda(1+u)^{3(1+w_\Lambda)}}}. \qquad (9)$$

For the *Planck* parameters (Planck Collaboration XIII 2016) $\Omega_{\rm m} = 0.308 \pm 0.012$ and $\Omega_\Lambda = 1.0 - \Omega_{\rm m}$, we find that $z_{\rm max} = 1.594$ for this model.

(ii) Einstein–de Sitter (i.e. equation 1 with $\Omega_{\rm m} = 1$ and $\Omega_\Lambda = 0$):

$$d_A(z) = 2\frac{c}{H_0}\frac{1}{1+z}\left(1 - \frac{1}{\sqrt{1+z}}\right). \qquad (10)$$

As with several other models introduced below, this cosmology is disfavoured by many other observations (though see Vauclair et al. 2003; Blanchard 2006), but we include it in this list because the measurement of $z_{\rm max}$ provides an important complementary (and unique) measure of the Universe's geometry. The angular-diameter distance in this model attains its maximum value at $z_{\rm max} = 0.682$.

(iii) The $R_{\rm h} = ct$ Universe (a Friedmann–Robertson–Walker cosmology with zero active mass, Melia 2016a, 2017a). In this model, the total equation of state is $\rho + 3p = 0$, in terms of the energy density ρ and pressure p (Melia 2007; Melia & Shevchuk 2012). In this case,

$$d_A(z) = \frac{c}{H_0}\frac{1}{1+z}\ln(1+z), \tag{11}$$

and $z_{\rm max} = 1.718$.

(iv) The Milne Universe. This (well known) solution is also an FRW cosmology, though with an energy density, pressure, and cosmological constant, all equal to zero. Its spatial curvature is negative ($k = -1$). It follows from the Friedmann equations that the scale factor is linear in time (see e.g. Vishwakarma 2013; Chashchina & Silagadze 2015). Note, however, that although it shares this linear expansion with the $R_{\rm h} = ct$ universe, the observable signatures in these two models are different because – unlike Milne – the latter is not an empty universe. In Milne, the angular-diameter distance is

$$d_A(z) = \frac{c}{H_0}\frac{1}{1+z}\sinh\left[\ln(1+z)\right], \tag{12}$$

which should be contrasted with equation (11) for $R_{\rm h} = ct$. Note that this expression for the angular-diameter distance has no turning point, so for Milne $z_{\rm max} = \infty$.

(v) Static Euclidean cosmology with a linear Hubble law at all redshifts:

$$d_A(z) = \frac{c}{H_0}z. \tag{13}$$

This model, which assumes that the Universe is static, has been applied to certain specific observations (Lerner, Falomo & Scarpa 2014). Of course, there are significant challenges in finding consistency between this scenario and other kinds of data, but in this paper, our goal is simply to test its predicted value of $z_{\rm max} = \infty$ (like Milne) against the measurement.

(vi) Static Euclidean cosmology with tired light:

$$d_A(z) = \frac{c}{H_0}\ln(1+z). \tag{14}$$

This phenomenological model assumes that photons lose energy due to some interaction along their trajectory, and that this loss of energy scales as the path length, i.e. $dE/dr = -(H_0/c)E$ (LaViolette 2012). Of course, as in the previous model, this ansatz is not very successful in accounting for many other observations, but our goal here again is to simply focus on the unique observational signature $z_{\rm max} = \infty$ (again, like Milne).

(vii) Static Euclidean model with plasma tired light:

$$d_A(z) = \frac{c}{H_0}\ln(1+z). \tag{15}$$

In this plasma redshift application, there is an additional Compton scattering that is double that of the plasma redshift absorption (Brynjolfsson 2004; Section 5.8). As in Milne and the previous tired light models, we find that $z_{\rm max} = \infty$.

6 RESULTS BASED ON $z_{\rm max}$

Table 1 compares each model's prediction with the measured $z_{\rm max}$, along with the difference as a fraction of $\sigma_{z_{\rm max}}$ (the so-called z-value), and the corresponding probability that the predicted turning point is consistent with its measured value. Note that these percentages are absolute; in other words, we are not comparing relative probabilities, so they do not necessarily add up to one. Each individual model's comparison with the data is independent of the relative merits of the other cosmologies.

The surprising feature of Table 1 is how strongly the various models are differentiated on the basis of $z_{\rm max}$ alone, even without considering other kinds of data. One of the most important aspects of the expansion dynamics tested by Type Ia SNe is the hypothesized transition from deceleration to acceleration at $z \sim 0.7$. Now we see that compact quasar cores play an equally important role in examining the geometry of the Universe at another critical transition redshift, $z_{\rm max}$, where the angular-diameter distance turns over. This characteristic redshift is so different between competing cosmologies that its measurement already favours only two of the models we examine here, principally $R_{\rm h} = ct$, followed by *Planck* ΛCDM.

But in spite of *Planck* ΛCDM not being the preferred model, there is enough flexibility in the expression for $d_A(z)$ in ΛCDM (equation 1) that we should consider whether an alternative set of parameter values might raise its standing to that of $R_{\rm h} = ct$. Indeed, a variation of flat ΛCDM with $\Omega_{\rm m} = 0.23$ predicts a turning point at $z_{\rm max} = 1.70$, consistent with the measured value, and a probability exceeding 92.8 per cent. This scaled matter density, however, would be in tension at more than 6.5σ with the *Planck* optimized value. Additional flexibility could be introduced by relaxing the constraint that dark energy is a cosmological constant, so that $w_{\rm de} \neq -1$. But with each such modification to the standard model, we recede further and further from the concordance *Planck* cosmology, calling into question whether finding consistency with the measured value of $z_{\rm max}$ is worth damaging the optimization of fits to other data, including the cosmic microwave background.

Aside from this head-to-head comparison between $R_{\rm h} = ct$ and ΛCDM, the results in Table 1 also strongly support other observations that have disfavoured – or even rejected – the other five models examined here. For example, note how different the outcome is for Milne compared to $R_{\rm h} = ct$. Given that both of these models predict a linear expansion rate, they are still sometimes confused with each other in the literature. On occasion, Milne is compared to ΛCDM to 'demonstrate' that $R_{\rm h} = ct$ is disfavoured by the data (see e.g. Melia 2015, and references cited therein). But as is clearly demonstrated here, the observational signatures associated with Milne are very different from those in $R_{\rm h} = ct$, and while the latter is favoured by the data, the former is strongly ruled out.

Finally, we comment on one of the issues highlighted in Section 3 concerning a possible influence due to the choice of covariance function $k(x_1, x_2)$, while using Gaussian processes. As we alluded to earlier, the choice of k in equation (1) is not unique, though this particular function has found widespread appeal with GP applications (see e.g. Rasmussen & Williams 2006; Holsclaw et al. 2010; Seikel et al. 2012; Yennapureddy & Melia 2017, 2018a,b). What determines whether or not a particular function is appropriate is how far the correlation extends to either side of each datum, and whether the chosen k adequately models this correlation in terms of the hyperparameter l (and to a lesser degree σ_f). We have therefore tested the correlation in our data set by reconstructing the angular size function in Fig. 1 using the very different kernel in equation (8). The results are virtually identical to those shown in Table 1, except

that the individual percentages change by a few points or less. Very importantly, the rank ordering of these seven models remains exactly the same as that shown here. We are therefore confident that the GP method has been applied correctly to these data.

7 RESULTS BASED ON $d_A(z)$

One of the strengths of the $z_{\rm max}$ diagnostic is that its determination is completely independent of the Hubble constant H_0. Thus all models may be compared with each other on level ground. But as we alluded to above, there is always the possibility that a model's prediction may match the turning point rather well, while its angular-diameter distance $d_A(z)$ is overall a poor match to the GP reconstructed curve in Fig. 1. To compare the predicted and measured $d_A(z)$ functions, however, it is necessary to optimize the vertical scaling (proportional to c/H_0) in equations (9–15) individually for each cosmology. We do this by writing the theoretical angular size of the compact quasar core as

$$\theta^{\rm th}_{\rm core}(z) = \frac{\ell_{\rm core}}{d_A(z)}, \tag{16}$$

where $\ell_{\rm core}$ is the physical core size, assumed to be more or less constant from source to source in the reduced quasar sample. To carry out the analysis in this paper, we do not need to know the actual value of $\ell_{\rm core}$ and H_0, and we may combine them by merging the expression for $\theta_{\rm core}(z)$ and $d_A(z)$ for each model, writing

$$\theta^{\rm th}_{\rm core}(z) = \frac{\eta}{\mathcal{I}(z)}, \tag{17}$$

where $\eta \equiv \ell_{\rm core} H_0/c$ and

$$\mathcal{I}(z) \equiv \left(\frac{H_0}{c}\right) d_A(z). \tag{18}$$

As we shall see shortly, however, a recent measurement of $\ell_{\rm core}$ by Cao et al. (2017b) allows us to see what the optimized value of η implies for the Hubble constant in each cosmology. In order to cast each model in its best possible light, we optimize the parameter η individually in each case to yield the best match with the GP reconstructed curve, following a procedure described in Yennapureddy and Melia (2018a,b), and briefly summarized below.

The best-fitting curves for the models we test in this paper are shown in comparison with the GP reconstruction and its confidence region (shaded swath) in Figs 3 and 4. Even a quick inspection by eye shows that Einstein-de Sitter, Milne, and especially static Euclidean, static tired light and static plasma, extend beyond the 1σ region and are therefore not well matched to the data. *Planck* ΛCDM and $R_{\rm h} = ct$ do much better, as reflected also in the probabilities displayed in Table 2.

When comparing two continuous functions, i.e. the reconstructed $\theta_{\rm core}(z)$ curve in Fig. 1 with $\theta^{\rm th}_{\rm core}(z)$ in equation (17), one may not use discrete sampling statistics because sampling at random points to obtain the differences between the two curves would lose information, whose importance is difficult to ascertain. We have recently introduced a new diagnostic, called the 'Area Minimization Statistic,' to estimate the probability that a model is consistent with the data. Assuming that the measurement errors are Gaussian, one generates a mock sample of GP reconstructed curves covering the likely variation of $\theta_{\rm core}(z)$ away from the function representing the actual data. This is done by using the Gaussian randomization

$$\theta^{{\rm mock},i}_{\rm core}(z) = \theta^{i}_{\rm core}(z) + r\sigma_{\theta^{i}_{\rm core}}, \tag{19}$$

where $\theta^{i}_{\rm core}(z)$ are the actual measurements and $\sigma_{\theta^{i}_{\rm core}}$ are the corresponding errors. Also, r is a Gaussian random variable with zero

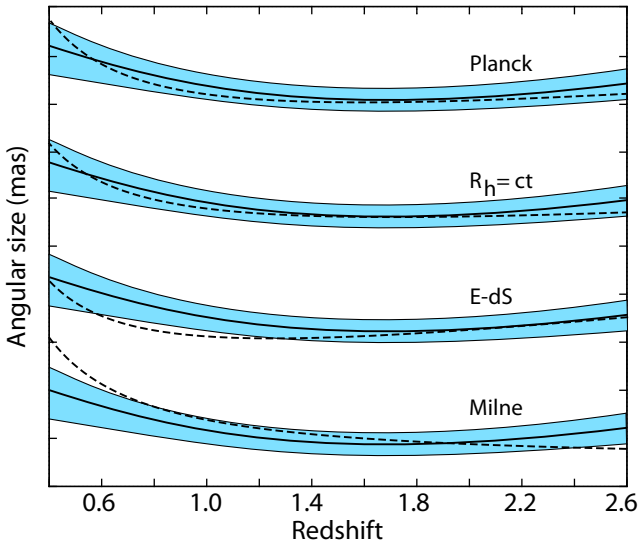

Figure 3. Comparison of the GP reconstructed quasar core size $\theta_{\rm core}(z)$ (solid curve, from Fig. 1) with the model prediction (dashed) for the *Planck*ΛCDM, $R_{\rm h} = ct$, Einstein-de Sitter and Milne cosmologies. The four plots have been staggered vertically for clarity. In each case, the shaded swath represents the 1σ confidence region for the reconstruction (see Fig. 1). The cumulative distribution is shown in Fig. 5, and the values of η (equation 17) for the optimized fits, along with the corresponding probabilities, are listed in Table 2.

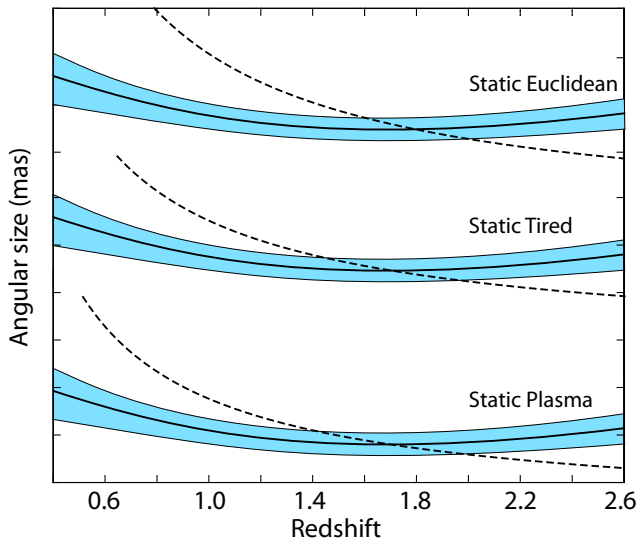

Figure 4. Same as Fig. 3, except now for the static Euclidean, static tired light, and static plasma tired light cosmologies. As indicated in Fig. 5 and Table 2, these three models are disfavoured by the data in comparison with the *Planck* ΛCDM and $R_{\rm h} = ct$ models.

Table 2. DA statistics for seven cosmological models.

Model	η	Probability (%)
PlanckΛCDM	0.53	81
$R_{\rm h} = ct$	0.48	76
Einstein-de Sitter	0.19	52
Milne universe	0.57	50
Static Euclidean	2.23	0
Static Euclidean tired light	1.31	0
Static Euclidean plasma tired light	1.31	0

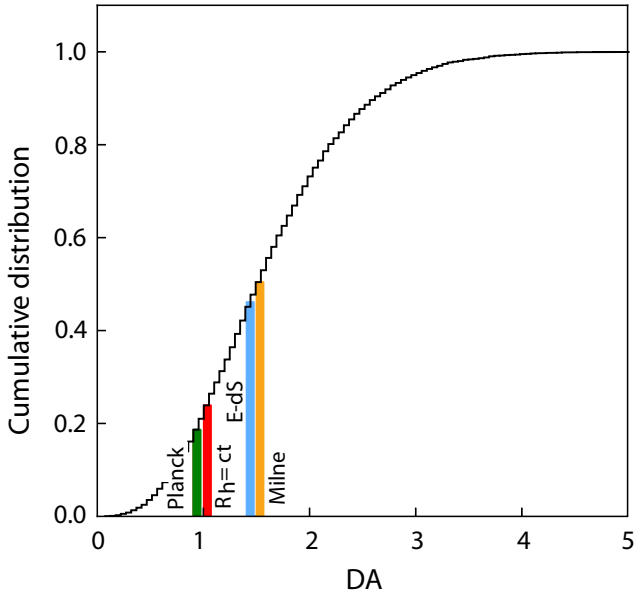

Figure 5. Cumulative probability distribution for the area differential *DA* (equation 20), and the estimated values for the cosmological models considered in this paper. The two cosmologies favoured by this test are *Planck* ΛCDM and $R_h = ct$, all with a probability ∼0.8, as indicated in Table 2. The other 3 (static) models are off the chart to the right, consistent with zero probability (see Table 2).

mean and a variance of 1. GP are then used with these $\theta_{\rm core}^{{\rm mock},i}(z)$ mock data and their errors $\sigma_{\theta_{\rm core}^i}$ to reconstruct the function $\theta_{\rm core}^{\rm mock}(z)$ representing each mock sample. In the final step, we determine the weighted absolute area difference

$$DA = \int_{z_1}^{z_2} {\rm d}z \, \frac{\left|\theta_{\rm core}^{\rm mock}(z) - \theta_{\rm core}(z)\right|}{\sigma_{\rm GP}(z)}. \quad (20)$$

Here, z_1 and z_2 are the minimum and maximum redshifts, respectively, of the data range, and $\sigma_{\rm GP}(z)$ is the calculated dispersion (corresponding to the shaded region in Fig. 1) associated with the GP reconstructed curve $\theta_{\rm core}(z)$. Repeating this procedure 10 000times, we build the probability distribution for the area differential *DA*, which is shown in Fig. 5, along with the individually measured values of *DA* for each model we test. With the assumption that a smaller *DA* corresponds to a better match to $\theta_{\rm core}(z)$, the cumulative distribution may then be used to estimate the likelihood that the difference between a model's prediction and $\theta_{\rm core}(z)$ is due principally to Gaussian randomness, rather than the model being wrong. A comparison of the likelihoods then prioritizes the models according to their probability of matching the data. Many statistical approaches utilize this basic concept, but unfortunately none of the existing methods may be used for the comparison of two continuous curves, as we have here.

The model selection based on the angular-diameter distance supports the outcome of the $z_{\rm max}$ diagnostic. The two models favoured by a comparison of the reconstructed and predicted $d_A(z)$ functions, i.e. *Planck*ΛCDM and $R_h = ct$, are also those most strongly selected according to how well they account for the observed turning point in $d_A(z)$. But while *Planck*ΛCDM and $R_h = ct$ are virtually indistinguishable from each other in Fig. 5 and Table 2, their prioritization based on $z_{\rm max}$ is much stronger (see Table 1). This is largely due to the fact that, while $\ell_{\rm core}$ and H_0 are not used in the identification of the turning point $z_{\rm max}$, one needs to optimize the ratio of these two unknowns in order to find the best fit for $d_A(z)$. This freedom to optimize η makes it easier for a model to fit the angular-size data, so the differences between the two favoured models are somewhat mitigated. This is the principal reason we highlighted the $z_{\rm max}$ diagnostic as being superior to $d_A(z)$ for model selection, given that it requires no optimization of free parameters, allowing all of the models to be compared on level ground.

8 DISCUSSION

We have emphasized throughout this paper that knowing the actual value of $\ell_{\rm core}$ and H_0 is not necessary to conduct the model comparisons based on the quasar compact core data. Attempts at measuring $\ell_{\rm core}$ have already met with some success (Cao et al. 2017b), however, so it would be interesting to see what impact this result ($\ell_{\rm core} = 11.03 \pm 0.25$ pc) has on the implied value of the Hubble constant H_0 via the optimized η in Table 2. From the definition of η (near equation 18), we infer that $H_0 = 63.4 \pm 1.2$ km s^{-1} Mpc^{-1} in the case of $R_h = ct$, and $H_0 = 69.9 \pm 1.5$ km s^{-1} Mpc^{-1} for ΛCDM. Both of these are completely consistent with previously measured values of the Hubble constant in each cosmology. The confirmation is provided by the latest Planck release (Planck Collaboration XIII 2016), and the four previous measurements reported for $R_h = ct$: 63.2 ± 1.6 km s^{-1} Mpc^{-1} (Melia & Maier 2013), 63.3 ± 7.7 km s^{-1} Mpc^{-1} (Melia & McClintock 2015), $62.3^{+1.5}_{-1.4}$ km s^{-1} Mpc^{-1} (Wei, Melia & Wu 2017), and 63.0 ± 1.2 km s^{-1} Mpc^{-1} (Melia & Yennapureddy 2018).

Aside from actually obtaining a value for $\ell_{\rm core}$, Cao et al. (2017b) showed through their analysis, based on measurements of $H(z)$ using cosmic chronometers, that this length-scale is independent of redshift, making it a true standard ruler. As long as these measurements are fully model-independent and free of any systematic effects, the use of compact structure in quasar cores with this $\ell_{\rm core}$ may constitute a powerful diagnostic for cosmological measurements, such as H_0. Already, we have found complete consistency between this approach and previous measurements, including the *Planck* optimization of model parameters.

It should also be remarked that in both cases (i.e. $R_h = ct$ and ΛCDM), the inferred value of H_0 disagrees with the local measurement based on Cepheid variables (Riess et al. 2018). It is not yet clear why this happens, but some authors have speculated on the possibility that a local 'Hubble Bubble' (Shi 1997; Keenan, Barger & Cowie 2013; Romano 2018; Wei et al. 2017) may be influencing the dynamics within a distance ∼300 Mpc (i.e. $z < 0.07$). If true, such a fluctuation might lead to anomalous velocities within this region, causing the nearby expansion to deviate somewhat from a pure Hubble flow. Until this issue is resolved, we must rely on the large-scale measurement of H_0 individually for each model.

9 CONCLUSION

Our ability to measure $z_{\rm max}$ has created an entirely new probe of the Universe's geometry. In this paper, we have shown that the predicted value of this turning point changes considerably between different models, allowing existing measurements, e.g. of compact quasar-core sizes, to disfavour all but two of the models we examined. The model preferred by these data is $R_h = ct$, which also happens to be the cosmology with the fewest parameters. Indeed, for the purpose of comparing values of $z_{\rm max}$, this cosmology has no parameters at all, which makes the consistency between its prediction ($z_{\rm max}^{R_h=ct} = 1.718$) and the measured value ($z_{\rm max} = 1.70 \pm 0.20$) quite compelling. *Planck*ΛCDM is not yet ruled out by these observations, but in order to bring its prediction in line with the observations,

one must adopt a scaled matter density $\Omega_{\rm m} = 0.23$ in tension with *Planck* at over 6.5σ.

We have highlighted the measurement of $z_{\rm max}$ as the most probative diagnostic for model selection based on angular sizes, principally because it relies on fewer parameters than the angular-diameter distance itself. But to ensure that the predicted $d_A(z)$ is consistent with the GP reconstructed function for the preferred models, we have also compared the overall angular-diameter distance to the data. The two models most highly favoured by this comparison, *Planck*ΛCDM and $R_{\rm h} = ct$, are also those most strongly preferred by $z_{\rm max}$. But unlike the latter, a comparison of $d_A(z)$ with the data is less discerning for these two models, mainly due to the additional free parameter, H_0, which provides more flexibility with the best fit. For example, the optimized value of H_0 is $63.4 \pm 1.2\,{\rm km\ s^{-1}\ Mpc^{-1}}$ for $R_{\rm h} = ct$, and $69.9 \pm 1.5\,{\rm km\ s^{-1}\ Mpc^{-1}}$ for ΛCDM. Both are fully consistent with previously measured values of the Hubble constant in each model, though they differ from each other at about 4σ. In contrast, model selection based on $z_{\rm max}$ is independent of H_0.

All of the comparative tests completed thus far (see e.g. table 1 in Melia 2017b for a summary and references) suggest that the zero active mass condition in general relativity is the influence guiding the Universe's expansion. Several exciting new tests are under development, including the measurement of redshift drift (Melia 2016b) and the detection of progenitors to high-z quasars (Fatuzzo & Melia 2017). Within a few years, we should know for certain whether or not $R_{\rm h} = ct$ is the correct cosmology. The consequences are far reaching. Chief among them is the fact that, while inflation is necessary to maintain the internal self-consistency of ΛCDM, it is not required for (and is actually inconsistent with) the zero active mass condition (Melia 2014).

ACKNOWLEDGEMENTS

We are grateful to the anonymous referee and Louis Marmet for providing a helpful set of comments and suggestions that have led to a significant improvement in this manuscript. FM is also grateful to Amherst College for its support through a John Woodruff Simpson Lectureship, and to Purple Mountain Observatory in Nanjing, China, for its hospitality while part of this work was being carried out. This work was partially supported by grant 2012T1J0011 from The Chinese Academy of Sciences Visiting Professorships for Senior International Scientists, and grant GDJ20120491013 from the Chinese State Administration of Foreign Experts Affairs.

REFERENCES

Blanchard A., 2006, in Pecker J.-C., Narlikar J. V., eds, Current issues in Cosmology. Cambridge Univ. Press, Cambridge, p. 76
Blandford R. D., Königl A., 1979, ApJ, 232, 34
Brynjolfsson A., 2004, preprint (astro-ph/0401420)
Buchalter A., Helfand D. J., Becker R. H., White R. L., 1998, ApJ, 494, 503
Cao S., Biesiada M., Zheng X., Zhu Z.-H., 2015, ApJ, 806, 66
Cao S., Biesiada M., Jackson J., Zheng X., Zhao Y., Zhu Z.-H., 2017a, J. Cosmol. Astropart. Phys., 02, 012
Cao S., Zheng X., Biesiada M., Qi J., Chen Y., Zhu Z.-H., 2017b, A&A, 606, 17
Chashchina O., Silagadze Z., 2015, Universe, 1, 307
Chen G., Ratra B., 2003, ApJ, 582, 586
Dabrowski Y., Lasenby A., Saunders R., 1995, MNRAS, 277, 753
Fatuzzo M., Melia F., 2017, ApJ, 846, 129
Frey S., 1999, New Astron. Rev., 43, 761
Gurvits L. I., 1994, ApJ, 425, 442
Gurvits L. I., Kellermann K. I., Frey S., 1999, A&A, 342, 378
Holsclaw T., Alam U., Sanso B., Lee H., Heitmann K., Habib S., Higdon D., 2010, Phys. Rev. Lett., 105, 241302
Jackson J. C., 2004, J. Cosmol. Astropart. Phys., 11, 007
Jackson J. C., 2008, MNRAS, 390, L1
Jackson J. C., Dodgson M., 1997, MNRAS, 285, 806
Jackson J. C., Jannetta A. L., 2006, J. Cosmol. Astropart. Phys., 11, 002
Jain D., Dev A., Alcaniz J. S., 2003, Class. Quantum Gravity, 20, 4485
Kayser R., 1995, A&A, 294L, L21
Keenan R. C., Barger A. J., Cowie L. L., 2013, ApJ, 775, 62
Kellermann K. I., 1993, Nature, 361, 134
Krauss L. M., Schramm D. N., 1993, ApJ, 405, L43
LaViolette P. A., 2012, Subquantum kinetics: The Alchemy of Creation, 4th edn. Starlane Publication, New York
Leaf K., Melia F., 2017a, MNRAS, 470, 2320
Leaf K., Melia F., 2017b, MNRAS, 474, 4507
Lerner E. J., Falomo R., Scarpa R., 2014, Int. J. Mod. Phys. D, 23, 1450058
Li X.-L. et al., 2016, Res. Astron. Astrophys., 16, 84
Lima J. A. S., Alcaniz J. S., 2002, ApJ, 566, 15
Melia F., 2007, MNRAS, 382, 1917
Melia F., 2013, Class. Quantum Gravity, 30, 155007
Melia F., 2014, A&A, 561, 9
Melia F., 2015, MNRAS, 446, 1191
Melia F., 2016a, Frontier Phys., 11, 119801
Melia F., 2016b, MNRAS, 463, L61
Melia F., 2017a, Frontier Phys., 12, 129802
Melia F., 2017b, MNRAS, 464, 1966
Melia F., Konigl A., 1989, ApJ, 340, 162
Melia F., Maier R. S., 2013, MNRAS, 432, 2669
Melia F., McClintock T. M., 2015, AJ, 150, 119
Melia F., Shevchuk A. S. H., 2012, MNRAS, 419, 2579
Melia F., Yennapureddy M. K., 2018, J. Cosmol. Astropart. Phys., 02, 034
Phillipps S., 1994, MNRAS, 269, 1077
Phillipps S., Horleston N. J., White A. C., 2002, MNRAS, 336, 587
Planck Collaboration, 2016, A&A, 594, 63
Podariu S., Daly R. A., Mory M. P., Ratra B., 2003, ApJ, 584, 577
Preston R. A., Morabito D. D., Williams J. G., Faulkner J., Jauncey D. L., Nicolson G., 1985, AJ, 90, 1599
Rasmussen C., Williams C., 2006, Gaussian Processes for Machine Learning. MIT Press, Cambridge
Riess A. G. et al., 2018, ApJ, 861, 13
Romano A. E., 2018, Int. J. Mod. Phys. D, 27, 1850102
Santos R. C., Lima J. A. S., 2008, Phys. Rev. D, 77, 083505
Seikel M., Clarkson C., Smith M., 2012, J. Cosmol. Astropart. Phys., 06, 036S
Shi X., 1997, ApJ, 486, 32
Vauclair S. C. et al., 2003, A&A, 412, L37
Vishwakarma R. G., 2001, Class. Quantum Gravity, 18, 1159
Vishwakarma R. G., 2013, Phys. Scr., 87, 055901
Wei J.-J., Melia F., Wu X.-F., 2017, ApJ, 835, 6
Wiik K., Valtaoja E., 2001, A&A, 366, 1061
Yennapureddy M. K., Melia F., 2017, J. Cosmol. Astropart. Phys., 11, 029
Yennapureddy M. K., Melia F., 2018a, Eur. Phys. J. C, 78, 9
Yennapureddy M. K., Melia F., 2018b, Phys. Dark Univ., 20, 65
Zheng X., Biesiada M., Cao S., Qi J., Zhu Z.-H., 2017, J. Cosmol. Astropart. Phys., 10, 030
Zhu Z.-H., Fujimoto M. K., 2002, ApJ, 581, 1

This paper has been typeset from a TEX/LATEX file prepared by the author.

APPENDIX-B

Model selection using cosmic chronometers with Gaussian Processes

Fulvio Melia, Manoj K. Yennapureddy

Published In: Journal of Cosmology and Astroparticle Physics
DOI:10.1088/1475-7516/2018/02/034

Throughout the thesis, we have compared R_h=ct and ΛCDM using various observations and showed that R_h=ct is favored than ΛCDM in all the tests. In this appendix, we extend this analysis using cosmic chronometers and test R_h=ct and ΛCDM using the model independent technique. By employing cosmic chronometers, we reconstruct the H(z) using Gaussian Processes and test six different cosmologies show that the data favours the R_h=ct universe, which has only one free parameter (i.e., H_0) over other models, including Planck ΛCDM. The results of this appendix show that the R_h=ct universe has a ~93.0% probability of being the correct cosmology whereas Planck ΛCDM has 74.2% of probability of being correct.

Journal of Cosmology and Astroparticle Physics
An IOP and SISSA journal

Model selection using cosmic chronometers with Gaussian Processes

Fulvio Melia[a,1] **and Manoj K. Yennapureddy**[b]

[a]Department of Physics, the Applied Math Program, and Steward Observatory,
The University of Arizona,
Tucson, AZ 85721, U.S.A.
[b]Department of Physics, The University of Arizona,
Tucson, AZ 85721, U.S.A.

E-mail: fmelia@email.arizona.edu, manojy@email.arizona.edu

Received July 13, 2017
Revised October 21, 2017
Accepted February 7, 2018
Published February 19, 2018

Abstract. The use of Gaussian Processes with a measurement of the cosmic expansion rate based solely on the observation of cosmic chronometers provides a completely cosmology-independent reconstruction of the Hubble constant $H(z)$ suitable for testing different models. The corresponding dispersion σ_H is smaller than $\sim 9\%$ over the entire redshift range ($0 \lesssim z \lesssim 2$) of the observations, rivaling many kinds of cosmological measurements available today. We use the reconstructed $H(z)$ function to test six different cosmologies, and show that it favours the $R_h = ct$ universe, which has only one free parameter (i.e., H_0) over other models, including *Planck* ΛCDM. The parameters of the standard model may be re-optimized to improve the fits to the reconstructed $H(z)$ function, but the results have smaller p-values than one finds with $R_h = ct$.

Keywords: cosmology of theories beyond the SM, galaxy evolution, cosmic flows, star formation

ArXiv ePrint: 1802.02255

[1]John Woodruff Simpson Fellow.

https://doi.org/10.1088/1475-7516/2018/02/034

JCAP02(2018)034

Contents

1 Introduction

Two recent developments have made it possible for us to measure the Hubble constant $H(z)$ without having to assume any particular model, thereby providing a truly model-independent probe of the expansion dynamics. The first of these is the development of a technique used to measure the differential ages of adjacent galaxies out to a redshift $z \sim 2$ [1, 2]. The second is the introduction of Gaussian Processes to the analysis of the variables, such as $H(z)$, allowing us to reconstruct their functional form without having to assume any *a priori* parametric dependence on redshift or other theoretical constraints [3–5].

Galaxies evolving passively over a time much longer than their age difference allow us to measure the expansion rate $H(z)$ solely as a function of the redshift-time derivative dz/dt. These ages are inferred from the observed 4,000 Å break in the passively evolving spectra, based on our understanding that, for old stars, this break is due to metal absorption lines whose amplitude scales linearly with stellar age. So when the metallicity of these stars is known, the age difference of two adjacent galaxies is proportional to the difference of their 4,000 Å amplitudes [2]. In previous applications [2, 6–8], these cosmic chronometers (as they are called) have been used successfully to compare the predictions of various cosmological models, such as the standard model ΛCDM and another Friedmann-Robertson-Walker cosmology known as the $R_{\rm h} = ct$ universe [9–11]. Quite surprisingly, *a constant expansion rate is preferred when the Hubble constant $H(z)$ is measured using cosmic chronometers on their own,* without the bias introduced via the inclusion of other data at low z, such as the measurement of H_0 using Cepheid variables, whose peculiar velocities associated with the influence of a local "Hubble Bubble" are comparable to those in the Hubble flow [12]. First attempts at identifying the distance beyond which the Hubble flow dominates noticeably over local, peculiar velocities yielded an estimate of $\sim 80h^{-1}$ Mpc, where h is the Hubble constant scaled to 100 km s^{-1} Mpc^{-1} [13]. More recent studies [14] of the local expansion rate have found a significant local under-density that persists out to ~ 300 Mpc, corresponding to a redshift $z \sim 0.07$ (see also ref. [15]). This effect may partly be the source of tension between cosmological parameters optimized at low redshifts compared to the values obtained by *Planck*. Instead, the expansion rate measured with cosmic chronometers appears to favour the $R_{\rm h} = ct$ model, in which the Universe expands at a constant rate.

JCAP02(2018)034

This situation clearly calls for more in-depth analysis of the cosmic chronometer measurements, preferably using several different approaches for model selection. Our goal in this paper is to follow an alternative means of using cosmic chronometers to comparatively test these cosmologies. The use of Gaussian Processes to reconstruct $H(z)$ avoids the need of "fitting" the data with pre-determined parametric functions. This non-parametric technique for reconstructing the expansion history is a fully Bayesian approach for smoothing data. The procedure results not only in a truly model-independent determination of $H(z)$ as a function of z, but the associated errors reconstructed along with the function itself strike a balance between very smooth and rapidly oscillating variations (see, e.g., ref. [5]). Having said this, an important caveat to consider along with the results presented later in this paper is that the use of Gaussian Processes necessitates the adoption of two hyperparameters whose values are not known a priori. As discussed in greater detail in section 2 below, the common approach is to train them by maximizing the likelihood that the reconstruction matches the measured values at the data points themselves. Nonetheless, this choice of parameters affects the smoothness of the function and its errors.

In section 2 of this paper, we describe the calculation of $H(z)$ in more detail and use Gaussian Processes to "measure" this quantity out to a redshift ~ 2. We then introduce the six models we will test using this metric, and carry out the comparative analysis in section 3. Finally, we will discuss our results and provide our conclusions in section 4.

2 Reconstructing $H(z)$

In recent years, several kinds of measurement of $H(z)$ have been used to optimize the parameters in ΛCDM. In some cases [7, 8], they have also been used to compare the predictions of the standard model with those of another Friedmann-Robertson-Walker (FRW) cosmology known as the $R_h = ct$ universe [9–11, 16, 17]. But one must be wary of combining measurements of $H(z)$ using different techniques because not all of these approaches are truly model independent. For example, measurements based on the identification of baryon acoustic oscillations (BAO) and the Alcock-Paczyński distortion from galaxy clustering depend on how 'standard rulers' evolve with redshift, rather than how cosmic time changes with z (see, e.g., ref. [18]). The values of $H(z)$ measured using these different approaches are sometimes merged together to form an overall $H(z)$ versus z diagram, but the BAO approach must necessarily adopt a particular cosmology and is therefore model-dependent. Up to this point, observations based on the cosmic chronometer idea are the only ones we are aware of that do not rely on the assumption of a particular cosmology, so they are suitable for testing and comparing different models. As we explain below, however, there is a lingering concern regarding whether or not the assumption of a single, dominant bout of star formation is valid in these galaxies, and the resolution to this question may depend on the expansion dynamics associated with each particular model.

2.1 Cosmic chronometers

The cosmic chronometer approach is based on the notion that the expansion rate $H(z)$ may be measured using solely the redshift-time derivative dz/dt between galaxies evolving passively over a time much longer than their age difference [1]. These massive ($\gtrsim 10^{11}\ M_\odot$) early-type galaxies are thought to have formed $\gtrsim 90\%$ of their stellar mass at $z > 2-3$, over a period of only $\sim 0.1-0.3$ Gyr, when the Universe was only ~ 4 Gyr old. A more recent study of early star formation in these galaxies, however, raises some doubt about whether or not a

JCAP02(2018)034

single bout of star formation can fully account for the observed stellar population [25]. In this paper, we will adopt the conventional view that these galaxies experienced only minor subsequent episodes of star formation, and are thus the oldest objects at all redshifts [19], though our analysis will need to be updated when these issues are better understood. So, for example, the stellar population in such a galaxy at $z \sim 1$ (i.e., when the Universe was ~ 7 Gyr old) formed during the first $\sim 2 - 10\%$ of its evolution. And since one measures only the local difference in redshift between these galaxies, one avoids the need of pre-assuming a cosmological model, which constitutes a powerful discriminant for testing different expansion scenarios. The latest compilation using this approach includes 30 measurements of $H(z)$ over the redshift range $0 \lesssim z \lesssim 2$ [2].

These measurements are based on the observed 4,000 Å break in the passively evolving galaxy spectra. For old stars, this break is a discontinuity in the spectral continuum due to metal absorption lines whose amplitude scales linearly with the stellar age and metal abundance [2]. When the metallicity of these stars is known, one can measure the age difference Δt of two adjacent galaxies in proportion to the difference of their 4,000 Å amplitudes. The metallicity determines the slope of this relation. And introducing the redshift difference Δz of these galaxies, one can then determine the Hubble constant using the simple relation

$$H(z) = -\frac{1}{(1+z)}\frac{dz}{dt} \approx -\frac{1}{(1+z)}\frac{\Delta z}{\Delta t}\,. \tag{2.1}$$

A caveat with this procedure, however, is that several factors may limit the accuracy with which the differential age of these systems is measured. Nonetheless, extensive tests [2] have demonstrated that the 4,000 Å feature is mostly dependent on the age and metallicity of the host galaxies, relying only weakly on the star formation history, their initial mass function, along with possible progenitor biases, and (the so-called) α-enhancement. These early, passive galaxies apparently have higher ratios of α elements to iron than the Milky Way. There may also be a progenitor bias due to an evolution in the mean redshift of galaxy formation as a function of redshift.

The tests that have been conducted to this point reveal that only an uncertainty in the metallicity contributes a systematic error $\sigma_{\rm sys}$ comparable to the statistical errors in the sample. The progenitor bias contributes at most only a few percent to $\sigma_{\rm sys}$, and the initial mass function has no impact. Using a Chabrier or Salpeter initial mass function for all reasonable metallicities produces a difference of less than 0.3% between the 4,000 Å amplitudes estimated for a single stellar population. The difference is less than 0.2% for solar metallicity [2]. Likewise, the α-enhancement produces an average difference in the 4,000 Å amplitudes of only $\sim 0.5\%$.

Simulations have also shown that variations in the assumed star forming rate may produce $\lesssim 13\%$ errors in the measured value of Δz from measurements of the 4,000 Å amplitudes [2]. All these effects together contribute an overall error of about 20% to Δz, and hence the inferred value of $H(z)$. The 30 measurements of $H(z)$ based on the cosmic chronometer approach are shown in figure 1 [2, 6, 20–23]. Also shown in this figure is the function $H(z)$ reconstructed from the cosmic chronometer data using Gaussian Processes, along with the 1σ and 2σ confidence regions, which we shall discuss shortly.

Before introducing the models, however, we address an issue with the data illustrated in figure 1 that has raised some concern recently regarding whether or not the associated errors are being over-estimated (see, e.g., refs. [12, 25]). The dispersions shown here are calculated in quadrature from the statistical ($\sigma_{\rm stat}$) and systematic ($\sigma_{\rm sys}$) errors, the latter

JCAP02(2018)034

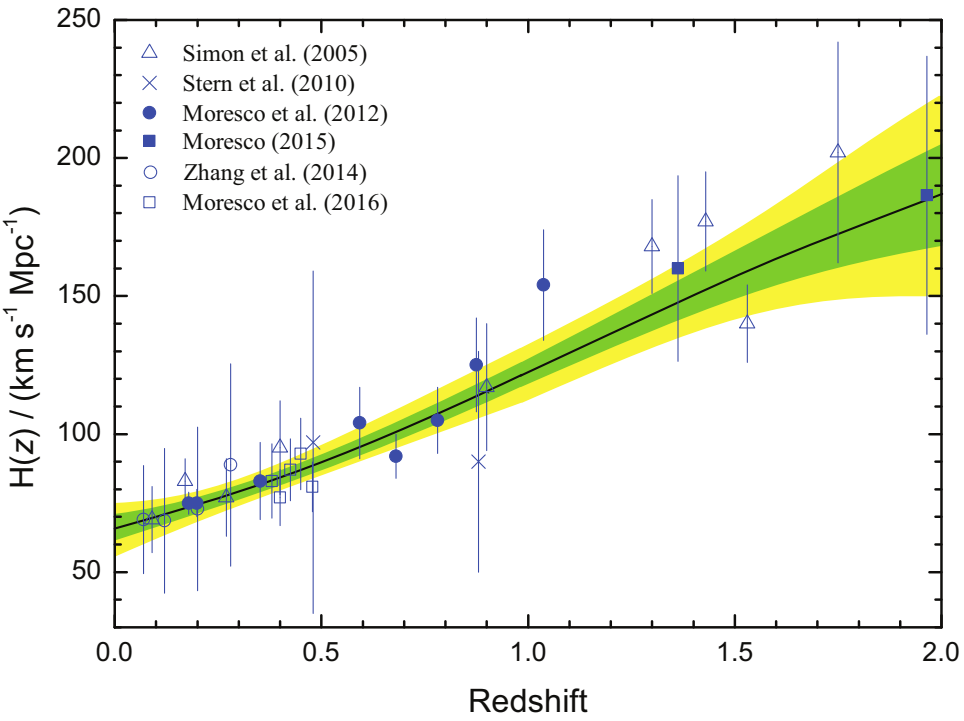

Figure 1. Thirty model-independent measurements of $H(z)$ versus z with error bars [2, 6, 20–23]. Note that these are total errors, which include both statistical and systematic contributions (see, e.g., refs. [24, 25]). Also shown here is the function $H(z)$ reconstructed with Gaussian Processes (solid black). The green and yellow shaded regions represent the 1σ and 2σ confidence regions, respectively, of the reconstruction.

of which are assumed to be uncorrelated. But this assumption may not be valid, given that some contributions to $\sigma_{\rm sys}$, e.g., the metallicity variations with redshift, are not truly random [25]. It is safe to say that, at best, $\sigma_{\rm sys}$ may have both correlated and uncorrelated components, in which case, the errors shown in figure 1 are too large. One can see this directly by comparing the published errors with the deviations of the data relative to the reconstructed $H(z)$ function, and from the fact that the reduced χ^2 is notably smaller than one ($\chi^2_{\rm dof} \sim 0.52$).

To examine the impact of this error over-estimation on model selection, in this paper we will therefore also consider a modified set of data extracted from the observations shown in figure 1 but with reduced dispersions. The ideal way to reduce the errors would be to deduce the fraction f_s representing the degree of correlation in the systematic errors with which one would then estimate the 'true' error as

$$\sigma(z_i) = \sqrt{\sigma_{\rm stat}(z_i)^2 + f_s\, \sigma_{\rm sys}(z_i)^2}\ . \tag{2.2}$$

Presumably, $f_s = 0$ corresponds to the systematic errors being fully correlated, and $f_s = 1$ totally random. As of now, however, there are several limitations that prevent us from using this approach. The first is that we do not know f_s a priori, nor whether this is even independent of redshift. Second, of the 30 data points shown in figure 1, only 17 have published values of $\sigma_{\rm stat}$ and $\sigma_{\rm sys}$. We have attempted to reconstruct the $H(z)$ function

JCAP02(2018)034

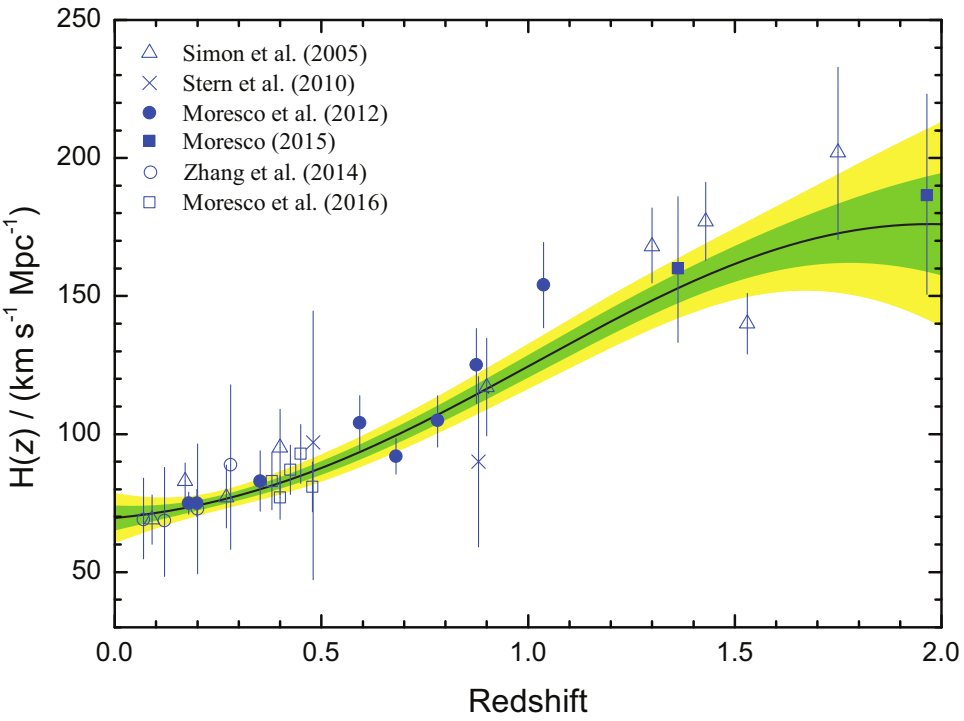

Figure 2. Same as figure 1, except that the error bars have here been reduced by an average of 25%. This modification allows a reasonable cosmological model, such as ΛCDM, to fit the data with a reduced $\chi^2_{\rm dof} \approx 1$ [12]. Also shown here is the function $H(z)$ reconstructed with Gaussian Processes (solid black). The green and yellow shaded regions represent the 1σ and 2σ confidence regions, respectively, of the reconstruction.

using only this reduced set of measurements, but the Gaussian-process approach is unstable due to the sparseness of the data, producing unphysical oscillations with redshift. For now, we shall instead follow the simpler suggestion described in ref. [12], based on the idea that if correctly estimated, a reasonable model for the data in figure 1 (say, ΛCDM) should fit these measurements with a reduced $\chi^2_{\rm dof}$ approximately equal to one. Wei et al. [12] found that to attain this goal, the errors shown in figure 1 must be reduced, on average, by about 25%. The $H(z)$ data with their modified error bars are shown in figure 2, together with the reconstructed $H(z)$ function based on these reduced dispersions.

2.2 Gaussian processes

The principal benefit of using the Gaussian Processes (GP) approach [5] is that it avoids having to assume a parametric form of the function representing the data based on particular models that may, or may not, be reasonable representations of the true redshift-dependence of the measurements. A complete description of this method has been provided in ref. [5], and a catalog of related algorithms may be downloaded from a website maintained by these authors.[1]

Gaussian Processes can model a function f(x) rigorously without assuming any prior parametric form. One assumes that the n observations of a data set y=$\{y_1, y_2, \ldots, y_n\}$

[1] http://www.acgc.uct.ac.za/~seikel/GAPP/index.html.

JCAP02(2018)034

were sampled from a multivariate Gaussian distribution, which then allows these data to be partnered with Gaussian Processes (GP). Most often, the mean of this partner GP is assumed to be zero. But though modeling the data using Gaussian Processes is straightforward, there are nonetheless two possible areas of ambiguity with this technique, so we highlight these here and describe steps we have taken to ensure that the outcome of our reconstruction is not heavily biased by our choice of GP components. One of these has to do with the fact that the values of the function evaluated at different points x_1 and x_2 are not independent of each other. As such, one introduces a covariance function $k(x_1, x_2)$ to handle the linkage between neighboring points, though the form of $k(x_1, x_2)$ is not unique or well known. In principle, there is a broad range of such covariance functions, and while it makes sense to pick one that depends only on the distance between different data points, this is actually not required. It is common in this type of work to select a squared exponential function for this purpose,

$$k(x_1, x_2) = \sigma_f^2 \exp\left(-\frac{(x_1 - x_2)^2}{2l^2}\right) , \tag{2.3}$$

simply because it is infinitely differentiable and useful for reconstructing also the derivative of a function that represents the data. In contrast to actual parameters, the so-called hyperparameters σ_f and l do not specify the form of the function, only its "bumpiness." The characteristic length l represents a distance in x over which the reconstructed function varies significantly, while the signal variance σ_f scales this dependence in the ordinate direction. The covariance matrix obtained using equation (2.3) for $\{x_1, x_2, \ldots x_n\}$ observation points is

$$K = \begin{bmatrix} k(x_1,x_1) & k(x_1,x_2) & \ldots & k(x_1,x_n) \\ k(x_2,x_1) & k(x_2,x_2) & \ldots & k(x_2,x_n) \\ \ldots & \ldots & \ldots & \ldots \\ k(x_n,x_1) & k(x_n,x_2) & \ldots & k(x_n,x_n) \end{bmatrix} . \tag{2.4}$$

For a new observation point x_*, one also needs the vector

$$K_* \equiv \begin{bmatrix} k(x_*,x_1) & k(x_*,x_2) & \ldots & k(x_*,x_n) \end{bmatrix} , \tag{2.5}$$

and the point $K_{**} \equiv k(x_*, x_*)$. As we have pointed out, the data may be represented as a sample from a multivariate GP, such that

$$\begin{bmatrix} y \\ y_* \end{bmatrix} = N\left(0, \begin{bmatrix} K & K_*^T \\ K_* & K_{**} \end{bmatrix}\right) . \tag{2.6}$$

In obtaining this, one must maximize the conditional probability

$$p(y_*|y) \sim N(K_* K^{-1} y, K_{**} - K_* K^{-1} K_*^T) . \tag{2.7}$$

The mean of the distribution is an estimate of y_*, which is given as

$$\mu(y_*) = K_* K^{-1} y , \tag{2.8}$$

and the uncertainty of the estimate is given as

$$\mathrm{var}(y_*) = K_{**} - K_* K^{-1} K_*^T . \tag{2.9}$$

All of the results discussed in this paper, particularly those shown in figures 1–6, are based on the use of the kernel given in equation (2.3). However, to ensure that this choice of covariance function is not unduly affecting our model selection, we also carry out a parallel set of simulations in the appendix based on the use of a very different kind of kernel known as a Matérn covariance function, specifically the one called Matérn92 [5]. As described in the appendix, the choice of kernel may change the p-values by a few points, but the outcome of model selection based on this approach is not changed qualitatively. The rank ordering of models we consider here (see below) appears to be unaffected by the choice of covariance function.

A second possible area of ambiguity has to do with the values of the hyperparameters themselves. The common approach followed in this context is to train them by maximizing the likelihood that the reconstructed function has the measured values at the data points x_i. Of course, for a purely Bayesian analysis, one should marginalize over the hyperparameters instead of optimizing them, but for most applications (as we have here), the marginal likelihood is sharply peaked. Optimization is therefore a good approximation to marginalization, so for the purpose of the model selection we describe in this paper, there is no freedom to choose σ_f and l separately.

2.3 Reconstructed $H(z)$ function versus the data

Let us now pause briefly to discuss a very salient point emerging from the reconstructed $H(z)$ functions shown in figures 1 and 2. As alluded to above, cosmic chronometer measurements of the Hubble constant have themselves been used in recent years, primarily to optimize the parameters in the standard model ΛCDM, but also on occasion to compare the predictions of ΛCDM with those of the $R_{\rm h} = ct$ universe [7, 8]. In the latter, the power-law form of the expansion rate, i.e., $H(z) = H_0(1+z)$, has been shown to fit these data better than the variable rate in the standard model. But those results were the outcome of model fitting to the data. Figure 1 provides us with a new perspective on this comparison, because the Hubble constant reconstructed from the data using Gaussian Processes is entirely free of any presumed model or assumed fitting function. And this approach clearly demonstrates that the $(1+z)$ power law is a much better representation of the reconstructed $H(z)$ function than the variable rate predicted by the standard model (see figure 3 below). This outcome should not be underestimated, particularly in view of other recent attempts at showing that the cosmic chronometer data support the inference that the Universe underwent a transition from deceleration to acceleration at a redshift $z \sim 0.5 - 0.7$ [2]. These arguments are based on the adoption of specific empirical functions to fit the data, unlike the Gaussian Process reconstruction which makes no such assumptions. The reconstructed $H(z)$ in figure 1 shows no evidence of such a transition, validating the conclusions drawn earlier in refs. [7, 8]. As we shall see shortly, however, the function $H(z)$ reconstructed from the data with reduced dispersions (figure 2) is not as compelling as figure 1 in this regard, principally because none of the models fits it as well as in the first case. Nonetheless, the model rankings are not changed, so the two reconstructions agree qualitatively, if not quantitatively.

3 Model comparisons

In this section, we will now briefly introduce the 6 different cosmological models we intend to test against the reconstructed $H(z)$ functions, including the concordance model (based on

JCAP02(2018)034

the *Planck* optimized parameters) and the $R_h = ct$ universe. The models we will compare are the following:

1. The $R_h = ct$ universe (a Friedmann-Robertson-Walker cosmology with zero active mass; [16, 17]). The basis for this model is the total equation of state $\rho + 3p = 0$, where ρ and p are the total energy density and pressure of the cosmic fluid [9, 11, 16, 17]. This cosmology has only one free parameter — the Hubble constant H_0, and
$$H^{R_h=ct}(z) = H_0(1+z)\ . \tag{3.1}$$

2. The concordance model, based on the *Planck* optimization of the parameters in ΛCDM. This model has the Hubble function
$$H^{\Lambda\mathrm{CDM}}(z) = H_0\left[\Omega_m(1+z)^3 + \Omega_r(1+z)^4 + \Omega_\Lambda\right]^{1/2}\ , \tag{3.2}$$
where Ω_i is the energy density ρ_i of species i, for radiation (Ω_r), matter (Ω_m) and dark energy (Ω_Λ), scaled to the critical density, $\rho_c \equiv 3c^2H_0^2/8\pi G$. Its parameters have the (fixed) prior values $H_0 = 67.4 \pm 1.4$ km s^{-1} Mpc^{-1}, $\Omega_m = 0.314 \pm 0.020$, and $\Omega_\Lambda = 0.686 \pm 0.020$ [26]. Note that $\Omega_r \ll 1$ in the redshift range associated with cosmic chronometers, and $\Omega_m + \Omega_\Lambda$ (with $\Omega_r = 0$) was fixed to 1 because this parameter optimization represents a flat universe. We therefore do not include a spatial curvature term Ω_k in equation (3.2).

3. The flat ΛCDM (Ω_m) model, with matter and dark-energy densities fixed by the condition $\Omega_\Lambda = 1 - \Omega_m$ (when radiation is insignificant). The predictions of this model are based on equation (3.2) with the optimization of one free parameter, Ω_m.

4. The flat ΛCDM (w) model, with matter and dark-energy densities fixed by the condition $\Omega_{de} = 1 - \Omega_m$ (again, when radiation is insignificant). Here, H_0 and Ω_m have prior values (from *Planck*), but the dark-energy equation of state, $w_{de} \equiv p_{de}/\rho_{de}$, where p_{de} is the dark-energy pressure, is unconstrained. Also,
$$H^{w\mathrm{CDM}}(z) = H_0\left[\Omega_m(1+z)^3 + \Omega_r(1+z)^4 + \Omega_{de}(1+z)^{3(1+w_{de})}\right]^{1/2}\ . \tag{3.3}$$

5. The flat ΛCDM (H_0) model, with matter and dark-energy densities fixed by the condition $\Omega_\Lambda = 1 - \Omega_m$ (when radiation is insignificant). Its predictions are based on equation (3.2) with an unconstrained H_0.

6. Einstein-de Sitter space, which contains only matter. This model has only one free parameter, H_0, and
$$H^{\mathrm{EdS}}(z) = H_0(1+z)^{3/2}\ . \tag{3.4}$$

Starting with the $H(z)$ function reconstructed using the full sample of 30 measurements (figure 1), one may gauge how well it compares to model predictions by examining the theoretical best-fit curves (more on this below) in relation to the 1σ and 2σ confidence regions shown in figure 3. For the sake of clarity, the reconstructed $H(z)$ curve itself is shown as a thin dashed line in these panels. A quick inspection by eye suggests that the $R_h = ct$ curve is very close to the reconstructed function, while the other models all have some excess curvature, either at low or high redshifts, introducing at least some tension with the observations.

JCAP02(2018)034

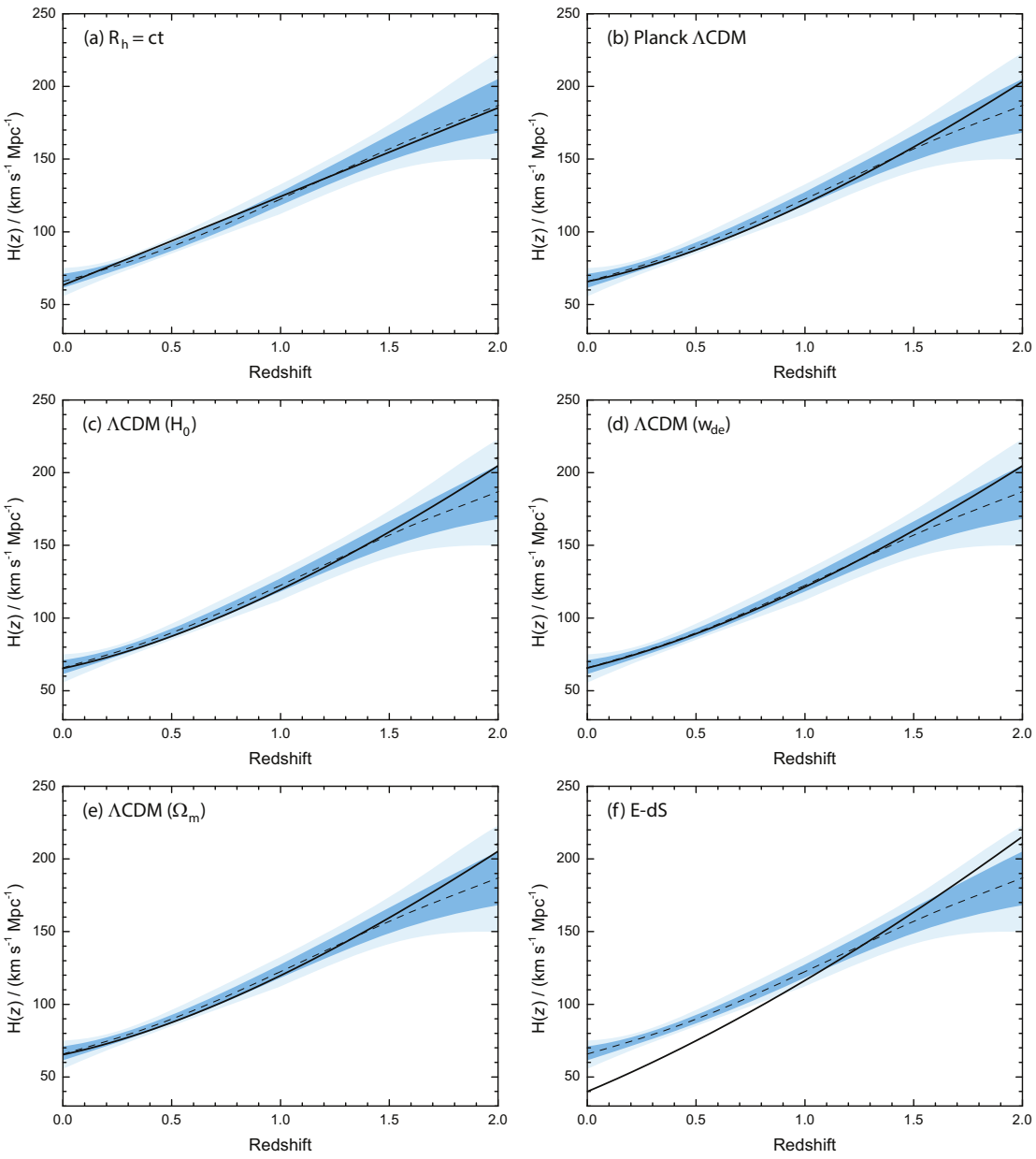

Figure 3. The Hubble constant $H(z)$ (solid curve) in various cosmologies optimized to fit the reconstructed function in figure 1 (dashed curve): (a) The $R_h = ct$ universe; (b) Planck ΛCDM; (c) ΛCDM (H_0), with a re-optimized (i.e., re-fitted) Hubble parameter; (d) flat ΛCDM (w_{de}); (e) ΛCDM (Ω_m); (f) Einstein de Sitter. The blue bands indicate the 1σ (dark shade) and 2σ (light shade) confidence regions from figure 1.

To quantify these comparisons, we will adopt the following procedure. We use the data and their 1σ errors plotted in figure 1 to create mock samples of 30 values of the Hubble constant with the same redshifts, z_i ($i = 1, \ldots, 30$), as the measurements, but with Gaussian randomized values $H^{\rm mock}(z_i) = H(z_i) + r\sigma_i$, where r is a Gaussian random variable with mean 0, and variance 1, and σ_i is the dispersion at z_i (see figure 1).

JCAP02(2018)034

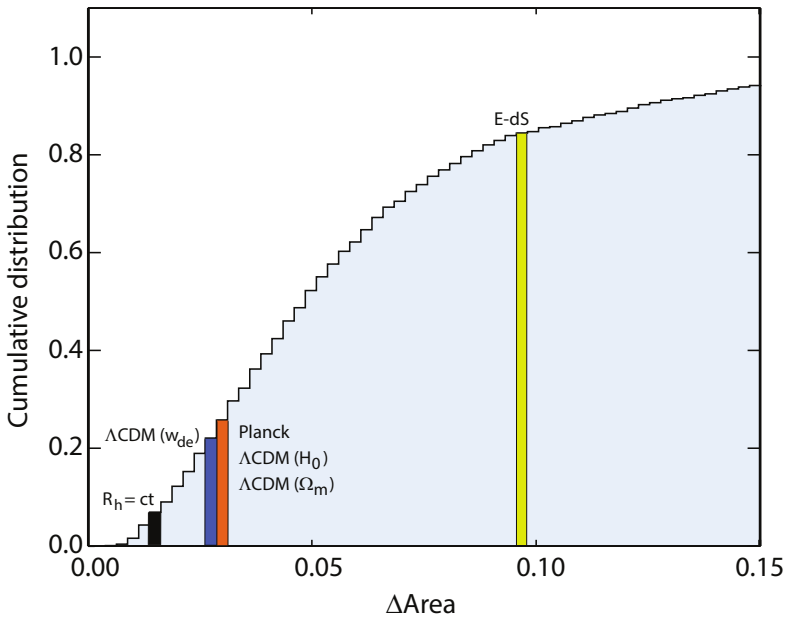

Figure 4. Cumulative probability distribution (normalized to 1) of the differential area calculated for $H(z)$ according to equation (3.5) for mock samples constructed via Gaussian randomization of the measured $H(z_i)$ values (see text preceding equation 3.5). The various models are shown according to their probabilities listed in table 1.

Using these mock data, we reconstruct a mock $H^{\rm mock}(z)$ function, and then calculate a normalized absolute area difference between this and the real function, according to

$$\Delta A = \int_0^2 dz \, \Big| H^{\rm mock}(z) - H(z) \Big| \Big/ \int_0^2 dz \, H(z) \; . \tag{3.5}$$

With this approach, we build a distribution of frequency versus differential area [27], from which we then construct the cumulative probability distribution shown in figure 4.

For each model i, we calculate the differential areas analogous to equation (3.5), replacing $H^{\rm mock}$ with its model specific function $H^i(z)$, and then estimate the probability (i.e., the p-value) of this cosmology being consistent with the reconstructed $H(z)$ function using figure 4. For a given ΔA, this figure shows what fraction of the randomized realizations had a differential area smaller than this value. Thus, a model's calculated ΔA shows the probability (the p-value) that this cosmology's prediction differs from the reconstructed $H(z)$ function due solely to cosmic variance. If a model has a free parameter, we optimize its value within its physically meaningful range by finding a minimum of the differential area ΔA. For $\Omega_{\rm m}$, this range is $(0, 1)$, while for $w_{\rm de}$ we assume $(-1, 0)$, i.e., we exclude phantom dark energy with $w_{\rm de} < -1$. The resulting probabilities and parameter values are quoted in table 1.

As we expected from a quick inspection of figure 3, the reconstructed Hubble constant prefers the $R_{\rm h} = ct$ cosmology, and provides reasonable fits for ΛCDM with either of the parameters $w_{\rm de}$, H_0 or $\Omega_{\rm m}$ re-optimized to fit the reconstructed $H(z)$ function, but with smaller probabilities. Quite coincidentally, the optimized value of $\Omega_{\rm m}$ when it is the sole parameter allowed to vary (row 5) is identical to the *Planck* value (row 4). As such, the probabilities for Planck ΛCDM and ΛCDM ($\Omega_{\rm m}$) are the same. The Einstein-de Sitter model, however, is strongly disfavoured by this comparative test.

JCAP02(2018)034

Model	H_0 (km s^{-1} Mpc^{-1})	Ω_m	Ω_{de}	w_{de}	Prob. (%) (figure 4)
$R_h = ct$	63.0	—	—	—	93.0
ΛCDM (w_{de})	67.4	0.314 (fixed)	$1 - \Omega_m$	−0.913	83.0
ΛCDM (H_0)	70.5	0.314 (fixed)	$1 - \Omega_m$	−1	78.3
Planck ΛCDM	67.4	0.314 (fixed)	$1 - \Omega_m$	−1	74.2
ΛCDM (Ω_m)	67.4	0.314 (optimized)	$1 - \Omega_m$	−1	74.2
E-dS	41.3	1.0 (fixed)	—	—	16.6

Table 1. Model comparison using the $H(z)$ function reconstructed from the 30 measurements with published errors. The value of Ω_m is fixed in every case, except for the model ΛCDM (Ω_m).

Model	H_0 (km s^{-1} Mpc^{-1})	Ω_m	Ω_{de}	w_{de}	Prob. (%) (figure 6)
$R_h = ct$	62.7	—	—	—	54.7
ΛCDM (w_{de})	67.4	0.314	$1 - \Omega_m$	−0.94	39.6
ΛCDM (H_0)	68.0	0.314	$1 - \Omega_m$	−1	39.6
ΛCDM (Ω_m)	67.4	0.319	$1 - \Omega_m$	−1	39.6
Planck	67.4	0.314	$1 - \Omega_m$	−1	15.2
E-dS	42.0	1.0	—	—	7.3

Table 2. Model comparison based on the reconstructed $H(z)$ with errors artificially reduced by 25%. The value of Ω_m is fixed in every case, except for the model ΛCDM (Ω_m), as demonstrated in table 1.

We repeat this procedure using the data with reduced dispersions (figure 2) in order to gauge the impact of correlation in the systematic errors on the reconstruction of $H(z)$. The individual model fits are shown in figure 5, with the corresponding cumulative probability distribution in figure 6. The model rankings and their probabilities are listed in table 2. We notice in this case that none of the models fit the reconstructed $H(z)$ function very well. Even $R_h = ct$, which is marginally favoured over the others, sits at roughly the halfway point of all possible Gaussian randomizations based on the reduced measurement errors, i.e., a simple variance of the reconstructed function $H(z)$ would produce a differential area ΔA smaller than that corresponding to $R_h = ct$ about half of the time. Though the two model rankings (in tables 1 and 2) are consistent with each other, one can see from figure 2 why the second reconstructed $H(z)$ is not fully consistent with the first. The scatter in the measurements increases with redshift, suggesting that a simple uniform reduction (by 25%) of the errors to account for partial correlation in the systematics may not be a reasonable approach. But attempting a more detailed mitigation of the systematic errors is not feasible, given how little is known at this stage about σ_{stat} and, particularly, σ_{sys}.

4 Conclusions

We have used Gaussian Processes to reconstruct the Hubble constant $H(z)$ and its associated 1σ and 2σ confidence regions, based exclusively on the observation of cosmic chronometers. This is an important constraint, given that other methods of measuring the Hubble constant

JCAP02(2018)034

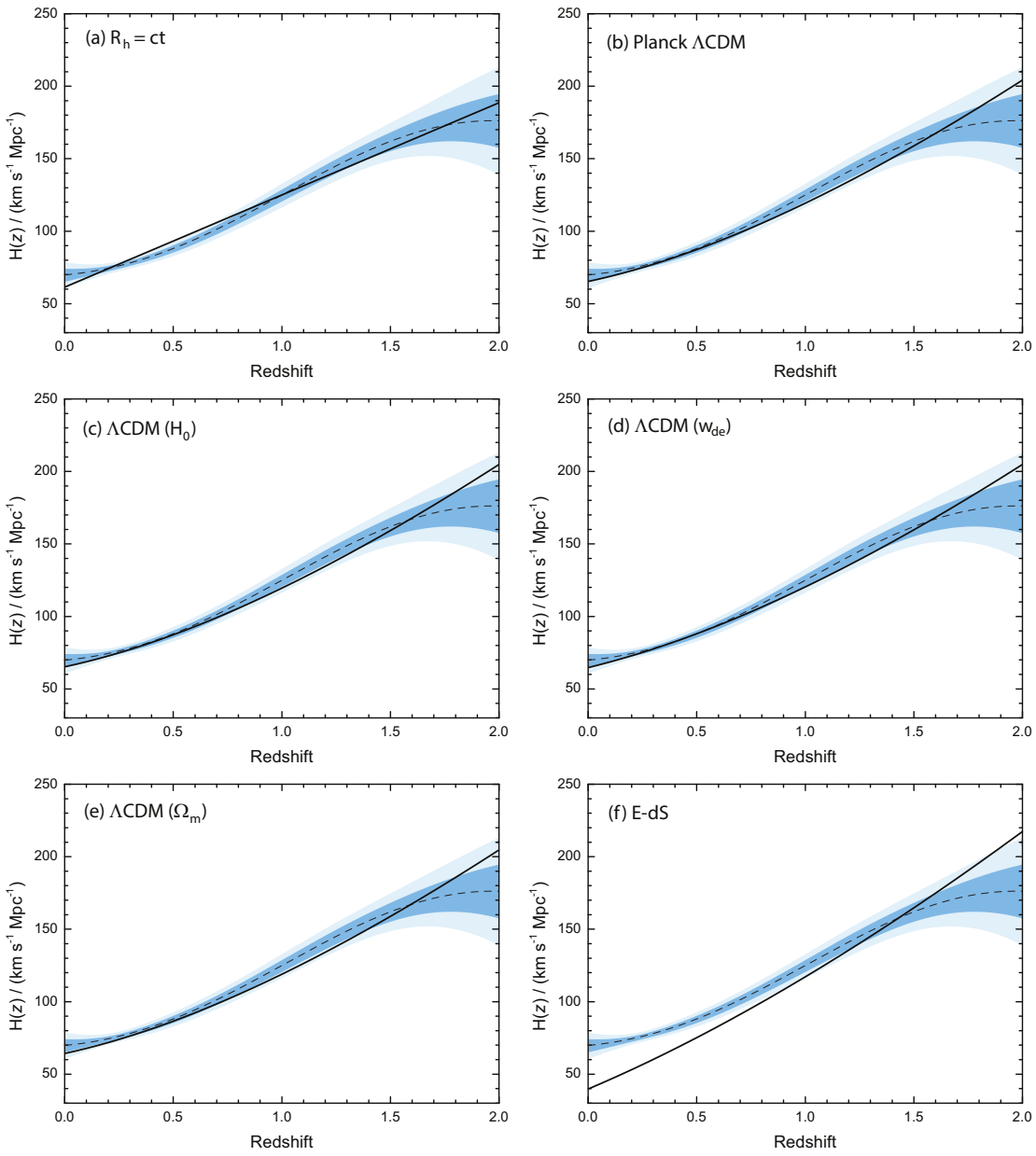

Figure 5. The Hubble constant $H(z)$ (solid curve) in various cosmologies optimized to fit the reconstructed function in figure 2 (dashed curve): (a) The $R_{\rm h} = ct$ universe; (b) Planck ΛCDM; (c) flat ΛCDM (H_0); (d) flat ΛCDM ($w_{\rm de}$); (e) ΛCDM (Ω_m); (f) Einstein de Sitter. The blue bands indicate the 1σ (dark shade) and 2σ (light shade) confidence regions from figure 2.

invariably rely on the pre-assumption of a particular cosmological model, which biases any subsequent analysis of the data for the purpose of model selection. For example, using BAO to determine the Hubble constant generally requires the assumption of a fiducial model in order to separate the cosmological redshift of the BAO peak from effects associated with internal redshift space distortions. This possible contamination arises when the positions of

JCAP02(2018)034

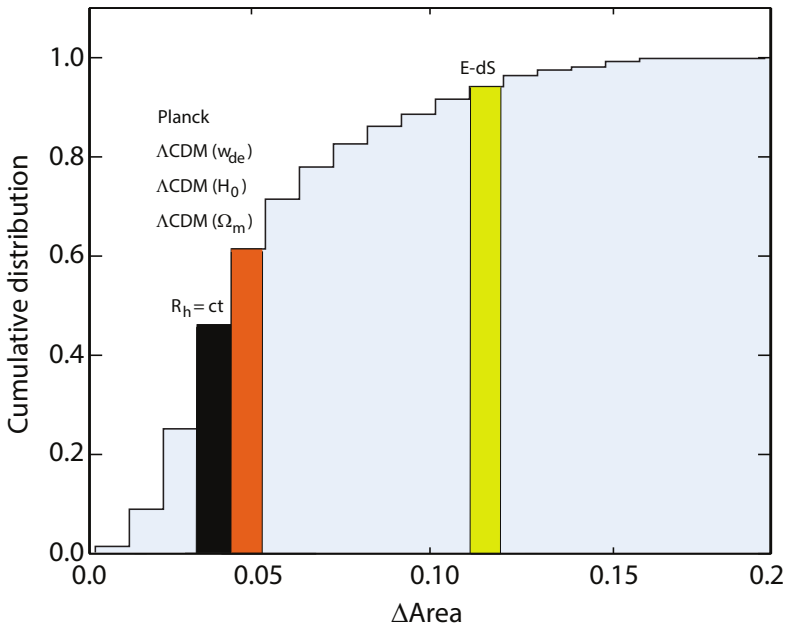

Figure 6. Cumulative distribution (normalized to 1) of the differential area ΔA calculated for $H(z)$ according to equation (3.5) for mock samples constructed via Gaussian randomization of the (modified) $H(z_i)$ values shown in figure 2. The various models are shown according to their probabilities listed in table 2.

galaxies are plotted in redshift-space rather than in terms of their angular-diameter distance, and is due to the peculiar motion of galaxies subject to their mutual gravitational attraction, contributing a Doppler shift in addition to the cosmological redshift. In order to 'measure' and subtract this Doppler effect, one must adopt a specific expansion scenario. Thus, the inferred BAO scale and $H(z)$ are relevant to that model, but not necessarily to the alternatives. And local measurements of $H(z)$, e.g., using Cepheid variables or other types of distance calibration, are often based on the parametrization in ΛCDM though, in principle, a re-calibration could be made for each individual model. The reconstructed $H(z)$ used in this paper is completely model free, and is therefore suitable for probing the expansion history without any prejudice.

The reconstructed $H(z)$ confirms the results of earlier work [7, 8], which showed that the Hubble constant measured with cosmic chronometers does not support models with a variable expansion rate, preferring instead the constant rate of expansion predicted by the $R_\mathrm{h} = ct$ universe. The earlier results were based on optimizing model fits to the $H(z)$ data. The $H(z)$ function reconstructed with the use of Gaussian Processes is, in principle, arguably better because it is obtained without reference to any model at all. Even a simple comparison by eye of the reconstructed $H(z)$ in figure 1 with the corresponding best fit curves in figure 1 of ref. [12] suggests that the cosmic chronometer data favour a constant expansion rate over a variable one.

The key results of our analysis are summarized in tables 1 and 2. Of the six models we compared here, the one favoured by the reconstructed $H(z)$ — based on both the published measurements (figure 1) and (though to a lesser extent) the data with artificially reduced dispersions (figure 2) — is $R_\mathrm{h} = ct$. ΛCDM and its variations also provide reasonably good

JCAP02(2018)034

fits — at least for $z \ll 2$ (see figures 3 and 5) — but with smaller p-values. One of the least favoured models is actually the version of ΛCDM with the *Planck* optimization of parameters. It is also important to note that the other versions of ΛCDM explored here were fitted using *Planck* priors on their free parameters, except for one of them that is different in each case, while the $R_h = ct$ model has only one free parameter (H_0), and no prior was applied to it. Information criteria provide a greater penalty to less parsimonious models (i.e., those using a larger number of free parameters), so a model comparison based, e.g., on the Bayes Information Criterion [28], would have produced an even greater disparity in probabilities than those listed in the tables.

The analysis reported in this paper continues to build the case for the $R_h = ct$ cosmology. The standard model accounts for the data at both high and low redshifts, but tension between its predictions and the observations grows as the error in the measurements drops to levels of a few percent. This is seen in the angular correlation function of the CMB, in the BAO scale measured with the Ly-α cross-correlation function, and in the growth rate at $z < 1$. In purely technical terms, the chief difference between these two models is that the former has a strictly constant equation of state, corresponding to the zero active mass condition [13, 17], while the latter has an equation of state that varies as the relative abundances of the constituents in the cosmic fluid change with redshift.

One would think that such a difference might produce only subtle changes in the expansion rate and other observable signatures. That may be true in some respects, but definitely not in others. For example, this difference in the equation of state completely eliminates the horizon problem, thereby obviating the need for an early phase of inflated expansion [29]. Considering how difficult it has been to find a completely satisfactory model of inflation, the $R_h = ct$ universe provides an acceptable alternative to the current inflationary ΛCDM paradigm. Such an outcome would bring to an end the 30-year endeavor to fix the horizon problem, which emerged from the initially misunderstood expansion history of the Universe. The observations today suggest a cosmic age consistent with a constant expansion rate since the very beginning. The non-empty $R_h = ct$ universe (as opposed to the empty, curvature-driven Milne universe) formally describes this constantly-expanding cosmos, and very interestingly permits all areas of the Universe observable today to have reached thermal equilibrium well before the cosmic microwave background was produced. If correct, the $R_h = ct$ describes a much simpler, more elegant cosmos without the pathologies (e.g., the horizon problem) requiring layers of 'fixes' to address apparent inconsistencies between the measurements at high and low redshifts.

Acknowledgments

We are grateful to the anonymous referee for very helpful, detailed comments that have led to a significant improvement in the presentation of our results. Some of this work was carried at the Instituto de Astrofísica de Canarias in Tenerife, and was partially supported by grant 2012T1J0011 from The Chinese Academy of Sciences Visiting Professorships for Senior International Scientists.

A Gaussian Processes with an alternative covariance function

The function $H(z)$ representing the 30 cosmic chronometer measurements shown in figure 1 is reconstructed here using a different covariance function $k(x_1, x_2)$ than the 'more conventional'

JCAP02(2018)034

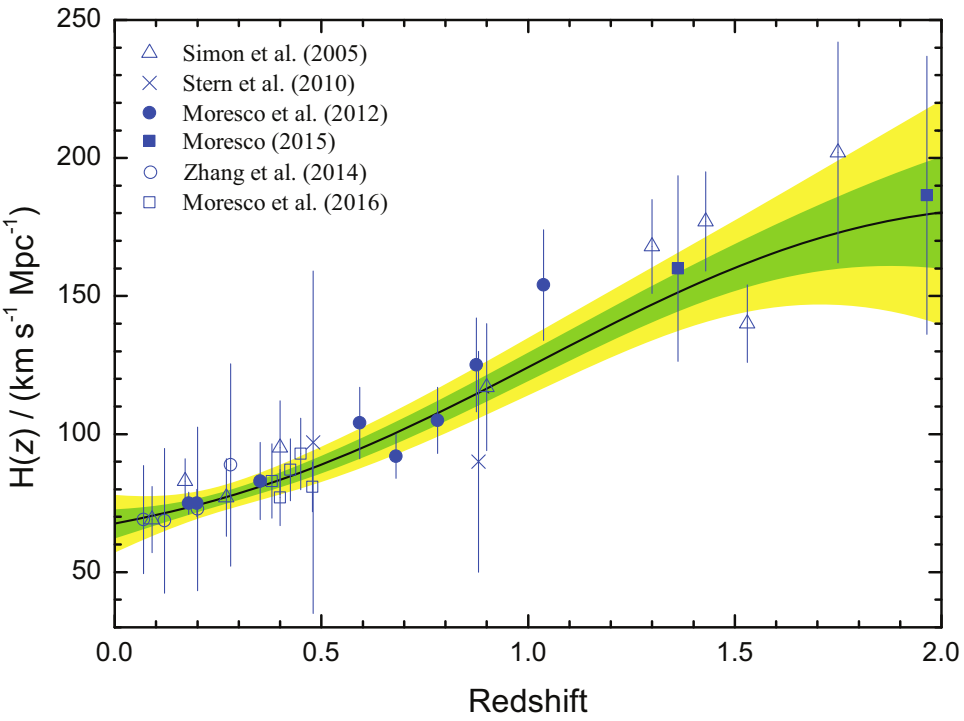

Figure 7. The function $H(z)$ reconstructed with Gaussian Processes (solid black curve), using the Matern92 covariance function (Seikel et al. 2012). The green and yellow shaded regions represent the 1σ and 2σ confidence regions of the reconstruction, respectively.

one shown in equation (2.3). Specifically, we repeat the steps followed in producing figures 1, 3 and 4, but now with the Matérn covariance function in Gaussian processes, whose explicit form is [5]

$$k(x_1,x_2) = \sigma_f^2 \exp\left(-\frac{3|x_1-x_2|}{l}\right)\left(1+\frac{3|x_1-x_2|}{l}+\frac{27|x_1-x_2|^2}{7l^2} + \frac{18|x_1-x_2|^3}{7l^3}+\frac{27|x_1-x_2|^4}{35l^4}\right) . \quad \text{(A.1)}$$

The reconstructed function is shown in figure 7, along with the 30 independent measurements of $H(z)$. This choice of covariance function produces somewhat less smoothing than that using equation (2.3), with the principal effect of creating greater tension between the predictions of ΛCDM and the data at high redshift, where the standard model requires a more rapid increase in $H(z)$ with z than the reconstruction produces. The model comparisons are made in figure 8, and the corresponding cumulative probabilities are shown in figure 9 and tabulated in table 3.

A comparison of tables 1 and 3 shows that *the choice* of $k(x_1,x_2)$ in equation (A.1) rather than equation (2.3) has resulted in slightly different p-values for the various models, but their rank ordering has remained the same. At least for cosmic chronometers, *this choice* of covariance function in Gaussian Processes does not influence model selection in any meaningful way.

JCAP02(2018)034

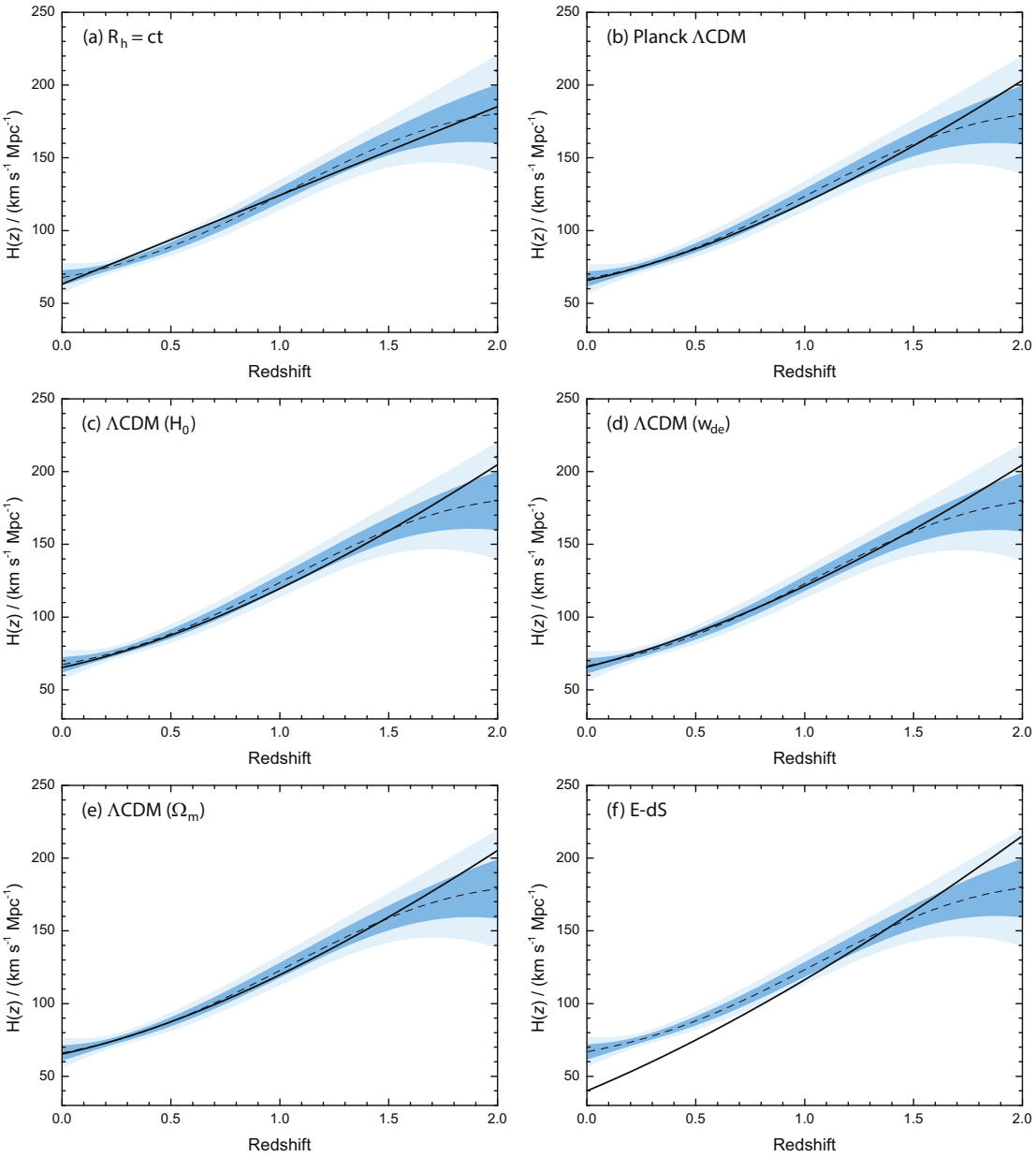

Figure 8. The Hubble constant $H(z)$ (solid curve) in various cosmologies optimized to fit the reconstructed function in figure 7 (dashed shade): (a) The $R_{\rm h} = ct$ universe; (b) Planck ΛCDM; (c) ΛCDM with a prior, $\Omega_{\rm m} = 0.314$; (d) flat ΛCDM, with prior density $\Omega_{\rm m} = 0.314$ and Hubble constant $H_0 = 67.4$ km s^{-1} Mpc^{-1}; and (e) ΛCDM (Ω_m); (f) Einstein de Sitter. The blue bands indicate the 1σ (dark shade) and 2σ (light shade) confidence regions from figure 7. See table 3 for re-optimized parameter values.

JCAP02(2018)034

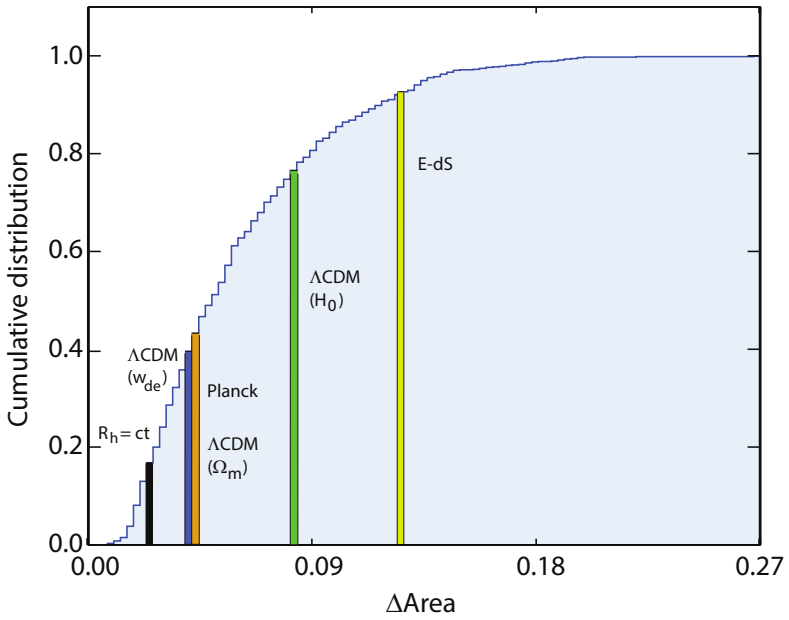

Figure 9. Cumulative probability distribution (normalized to 1) of the differential area calculated for $H(z)$ according to equation (3.5) for mock samples constructed via Gaussian randomization of the measured $H(z_i)$ values. This calculation is based on the reconstruction shown in figures 7 and 8, using the Matern92 covariance function (Seikel et al. 2012). The various models are shown according to their probabilities listed in table 3.

JCAP02(2018)034

Model	H_0 (km s^{-1} Mpc^{-1})	$\Omega_{\rm m}$	$\Omega_{\rm de}$	$w_{\rm de}$	Prob. (%) (figure 9)
$R_{\rm h} = ct$	63.0	—	—	—	83.2
ΛCDM ($w_{\rm de}$)	67.4	0.314	$1 - \Omega_{\rm m}$	-0.913	64.2
Planck ΛCDM	67.4	0.314	$1 - \Omega_{\rm m}$	-1	60.4
ΛCDM ($\Omega_{\rm m}$)	67.4	0.314	$1 - \Omega_{\rm m}$	-1	60.4
ΛCDM (H_0)	67.8	0.314	$1 - \Omega_{\rm m}$	-1	23.4
E-dS	41.3	1.0	—	—	12.3

Table 3. Model comparison using a reconstruction with the Matern92 covariance function (Seikel et al. 2012). The value of Ω_m is fixed in every case, except for the model ΛCDM (Ω_m), as demonstrated in table 1.

References

[1] R. Jimenez and A. Loeb, *Constraining cosmological parameters based on relative galaxy ages*, *Astrophys. J.* **573** (2002) 37 [astro-ph/0106145] [INSPIRE].

[2] M. Moresco et al., *A 6% measurement of the Hubble parameter at $z \sim 0.45$: direct evidence of the epoch of cosmic re-acceleration*, *JCAP* **05** (2016) 014 [arXiv:1601.01701] [INSPIRE].

[3] C. Rasmussen and C. Williams, *Gaussian Processes for Machine Learning*, The MIT Press, Cambridge U.S.A. (2006).

[4] T. Holsclaw et al., *Nonparametric Dark Energy Reconstruction from Supernova Data*, *Phys. Rev. Lett.* **105** (2010) 241302 [arXiv:1011.3079] [INSPIRE].

[5] M. Seikel, C. Clarkson and M. Smith, *Reconstruction of dark energy and expansion dynamics using Gaussian processes*, *JCAP* **06** (2012) 036 [arXiv:1204.2832] [INSPIRE].

[6] M. Moresco et al., *Improved constraints on the expansion rate of the Universe up to z 1.1 from the spectroscopic evolution of cosmic chronometers*, *JCAP* **08** (2012) 006 [arXiv:1201.3609] [INSPIRE].

[7] F. Melia and R.S. Maier, *Cosmic Chronometers in the $R_h = ct$ Universe*, *Mon. Not. Roy. Astron. Soc.* **432** (2013) 2669 [arXiv:1304.1802] [INSPIRE].

[8] F. Melia and T.M. McClintock, *A Test of Cosmological Models using high-z Measurements of H(z)*, *Astron. J.* **150** (2015) 119 [arXiv:1507.08279] [INSPIRE].

[9] F. Melia, *The Cosmic Horizon*, *Mon. Not. Roy. Astron. Soc.* **382** (2007) 1917 [arXiv:0711.4181] [INSPIRE].

[10] F. Melia and M. Abdelqader, *The Cosmological Spacetime*, *Int. J. Mod. Phys.* **D 18** (2009) 1889 [arXiv:0907.5394] [INSPIRE].

[11] F. Melia and A. Shevchuk, *The $R_h = ct$ Universe*, *Mon. Not. Roy. Astron. Soc.* **419** (2012) 2579 [arXiv:1109.5189] [INSPIRE].

[12] J.-J. Wei, F. Melia and X.-F. Wu, *Impact of a Locally Measured H_0 on the Interpretation of Cosmic-chronometer Data*, *Astrophys. J.* **835** (2017) 270 [arXiv:1612.08491] [INSPIRE].

[13] X. Shi, *Peculiar hubble flows in our local universe*, *Astrophys. J.* **486** (1997) 32 [astro-ph/9612228] [INSPIRE].

[14] R.C. Keenan, A.J. Barger and L.L. Cowie, *Evidence for a ~ 300 Megaparsec Scale Under-density in the Local Galaxy Distribution*, *Astrophys. J.* **775** (2013) 62 [arXiv:1304.2884] [INSPIRE].

JCAP02(2018)034

[15] A.E. Romano, *Hubble trouble or Hubble bubble?*, arXiv:1609.04081 [INSPIRE].

[16] F. Melia, *A Physical Basis for the Symmetries in the Friedmann-Robertson-Walker Metric*, *Front. Phys. (Beijing)* **11** (2016) 119801 [arXiv:1601.04991] [INSPIRE].

[17] F. Melia, *The zero active mass condition in Friedmann-Robertson-Walker cosmologies*, *Front. Phys. (Beijing)* **12** (2017) 129802 [arXiv:1602.01435] [INSPIRE].

[18] C. Blake et al., *The WiggleZ Dark Energy Survey: Joint measurements of the expansion and growth history at $z < 1$*, *Mon. Not. Roy. Astron. Soc.* **425** (2012) 405 [arXiv:1204.3674] [INSPIRE].

[19] T. Treu et al., *The assembly history of field spheroidals: Evolution of mass-to-light ratios and signatures of recent star formation*, *Astrophys. J.* **633** (2005) 174 [astro-ph/0503164] [INSPIRE].

[20] J. Simon, L. Verde and R. Jimenez, *Constraints on the redshift dependence of the dark energy potential*, *Phys. Rev.* **D 71** (2005) 123001 [astro-ph/0412269] [INSPIRE].

[21] D. Stern, R. Jimenez, L. Verde, S.A. Stanford and M. Kamionkowski, *Cosmic Chronometers: Constraining the Equation of State of Dark Energy. II. A Spectroscopic Catalog of Red Galaxies in Galaxy Clusters*, *Astrophys. J. Suppl.* **188** (2010) 280 [arXiv:0907.3152] [INSPIRE].

[22] C. Zhang, H. Zhang, S. Yuan, T.-J. Zhang and Y.-C. Sun, *Four new observational $H(z)$ data from luminous red galaxies in the Sloan Digital Sky Survey data release seven*, *Res. Astron. Astrophys.* **14** (2014) 1221 [arXiv:1207.4541] [INSPIRE].

[23] M. Moresco, *Raising the bar: new constraints on the Hubble parameter with cosmic chronometers at $z \sim 2$*, *Mon. Not. Roy. Astron. Soc.* **450** (2015) L16 [arXiv:1503.01116] [INSPIRE].

[24] K. Leaf and F. Melia, *Analysing H(z) data using two-point diagnostics*, *Mon. Not. Roy. Astron. Soc.* **470** (2017) 2320 [arXiv:1706.02116] [INSPIRE].

[25] M. López-Corredoira, A. Vazdekis, C.M. Gutiérrez and N. Castro-Rodríguez, *Stellar content of extremely red quiescent galaxies at $z > 2$*, *Astron. Astrophys.* **600** (2017) A91 [arXiv:1702.00380] [INSPIRE].

[26] Planck collaboration, P.A.R. Ade et al., *Planck 2013 results. XXIII. Isotropy and statistics of the CMB*, *Astron. Astrophys.* **571** (2014) A23 [arXiv:1303.5083] [INSPIRE].

[27] M.K. Yennapureddy and F. Melia, *Reconstruction of the HII Galaxy Hubble Diagram using Gaussian Processes*, *JCAP* **11** (2017) 029 [arXiv:1711.03454] [INSPIRE].

[28] G. Schwarz, *Estimating the Dimension of a Model*, *Ann. Statist.* **6** (1978) 461.

[29] F. Melia, *The $R_h = ct$ Universe Without Inflation*, *Astron. Astrophys.* **553** (2013) A76 [arXiv:1206.6527] [INSPIRE].

JCAP02(2018)034